ALPINE TURBULENCE AND BLOWING SNOW

A Thesis Submitted to the College of
Graduate and Postdoctoral Studies
In Partial Fulfillment of the Requirements
For the Degree of Doctorate of Philosophy
In the Department of Geography and Planning
(Centre for Hydrology)
University of Saskatchewan
Saskatoon

By

NIKOLAS OLSON AKSAMIT

PERMISSION TO USE

In presenting this dissertation in partial fulfillment of the requirements for a Postgraduate degree from the University of Saskatchewan, I agree that the Libraries of this University may make it freely available for inspection. I further agree that permission for copying of this dissertation in any manner, in whole or in part, for scholarly purposes may be granted by the professor or professors who supervised my dissertation work or, in their absence, by the Head of the Department or the Dean of the College in which my thesis work was done. It is understood that any copying or publication or use of this dissertation or parts thereof for financial gain shall not be allowed without my written permission. It is also understood that due recognition shall be given to me and to the University of Saskatchewan in any scholarly use which may be made of any material in my dissertation.

DISCLAIMER

Reference in this dissertation to any specific commercial products, process, or service by trade name, trademark, manufacturer, or otherwise, does not constitute or imply its endorsement, recommendation, or favoring by the University of Saskatchewan. The views and opinions of the author expressed herein do not state or reflect those of the University of Saskatchewan, and shall not be used for advertising or product endorsement purposes.

Requests for permission to copy or to make other uses of materials in this dissertation in whole or part should be addressed to:

Head of the Department of Geography and Planning
117 Science Place
University of Saskatchewan
Saskatoon, Saskatchewan S7N 1J9
Canada

OR

Dean
College of Graduate and Postdoctoral Studies
University of Saskatchewan
105 Administration Place
Saskatoon, Saskatchewan S7N 5A2

ABSTRACT

Blowing snow in mountainous terrain is a complex nonlinear phenomenon driven by turbulent eddies with length scales ranging from millimetres to kilometres. Turbulent motions across a wide spectrum of sizes are superimposed on each other, interacting through a non-stationary energy and momentum cascade. In cold regions, snow redistribution by these turbulent motions impacts hydrology, glaciology, avalanche safety, and civil engineering. Blowing snow models typically rely on relating time-averaged turbulence statistics, which may oversimplify the complexity of the flow, especially in complex mountainous terrain, to steady-state snow transport. The present research sought to improve the understanding of the dominant structures in ASL turbulence relevant to snow transport, as well as characterize the short timescale response of blowing snow to specific eddy structures. A fundamental experiment was designed utilizing high-speed videography of laser illuminated near-surface blowing snow saltation coupled with adjacent 3D sonic anemometer wind measurements at two heights. The experiments were conducted at Fortress Mountain Snow Laboratory in the Canadian Rockies of Alberta during nighttime blowing snow storms. Novel applications of particle tracking velocimetry and binarization algorithms to blowing snow recordings allowed extraction of time resolved snow particle velocities synchronized with instantaneous wind velocities, as well as time series of volumetric averages of blowing snow density in the first 30 mm above the surface.

High-speed blowing snow video and measurements revealed the importance of the often-overlooked creep mode of transport to both transport initiation and flux. Blowing snow velocity and flux profiles were found to be temporally variable and dependent on instantaneous wind speed, with dominant modes of transport varying during turbulent gusts. Sweep and ejection wind events were coupled to blowing snow responses on sub-second timescales, with each quadrant event playing a unique role in transport initiation and sustaining snow fluxes. Finally, large low-frequency turbulent motions, hypothesized to follow a top-down characterization, were found to modulate the amplitude of near-surface turbulence, as well as directly contribute to blowing snow fluxes. The role of intermittent coherent turbulent structures challenges the ability of time-averaged turbulence statistics to represent the complexity of wind-snow coupling, especially in mountainous terrain. The strong relationship found between large-scale turbulence modulating eddies and near-surface turbulence, also challenges the efficacy of applying steady-state laboratory-derived flux relationships to model transport in the ASL. The results presented here, along with recent advances on coherent turbulent structures provide an optimistic semi-deterministic avenue for improving blowing snow models in complex mountainous terrain.

ACKNOWLEDGEMENTS

I would like to thank my family for their unwavering support and consistent encouragement of introspection. Thank you to all my climbing, skiing and adventure partners throughout this process. Thank you to my friends for all the laughs. Thank you to my wife, without whom I would not have finished this degree so cheerfully.

Thank you to my advisor, John W. Pomeroy, for the support and freedom to explore this intriguing topic from many different perspectives. Thank you to my committee members for their helpful insight to improve this dissertation. Thank you to Joni Onclin and Phyllis Baynes for gracious logistical support. Thanks to Angus Duncan and May Guan for quite enjoyable field assistance and teaching me about meteorological instruments. Thank you to Don H. Tucker for helping me hone my B.S. detector for all these years.

-Nik

To all the wanderers

TABLE OF CONTENTS

LIST OF TABLES

LIST OF FIGURES

LIST OF ACRONYMS

ASL (Atmospheric Surface Layer or Above Sea Level)
AM (Amplitude Modulation)
COI (Cone of Influence)
DBSM (Distributed Blowing Snow Model)
DNS (Direct Numerical Simulation)
FMSL (Fortress Mountain Snow Laboratory)
LES (Large Eddy Simulation)
RMS (Root Mean Square)
PBSM (Prairie Blowing Snow Model)
PIV (Particle Image Velocimetry)
PTV (Particle Tracking Velocimetry)
VITA (Variable-Interval Time Averaging)
VITA+LEVEL (VITA and Quadrant Hole Threshold Analysis)

LIST OF SYMBOLS

$\overline{e_{xz}}$	Mean restitution coefficient of surface-particle impact
f_c	Separation frequency (Chapter 5)
g	Acceleration due to gravity
h_v	Height below which 75% of snow particle number flux occurred
I	Turbulence Intensity
k_v and k_Q	VITA and quadrant Thresholds (Chapter 4)
l_v	Snow concentration profile decay length (Chapter 3)
ℓ	VITA+Level lag time (Chapter 4)
m	Modulating signal (Chapter 5)
n_z	Number of blowing snow particles at height z
Q_s	Blowing snow flux (kg m^{-2} s^{-1})
Q_u, $Q_{u\uparrow}$, and $Q_{v\uparrow}$	Directional blowing snow number flux (horiz., horiz. ascending, vert. ascending)
S	Shields parameter
s	Wavelet time scale (Chapter 5)
T	VITA averaging time (Chapter 4)
u	Streamwise velocity of wind (overbar indicates temporal mean),
u_0	Particle slip velocity
u_p	Horizontal snow particle velocity (Chapter 2, 3)
u_*	Friction velocity
v	Spanwise velocity of wind (overbar indicates temporal mean)
v_p	Vertical snow particle velocity (Chapter 3)
w	Vertical velocity of wind (overbar indicates temporal mean)
u', v', w'	Fluctuating components of wind velocities after Reynolds decomposition
x, y, z	Streamwise, spanwise and vertical coordinates
z_0	Roughness length
γ	Slope of snow particle velocity profile
v_0	Exponential concentration profile parameter
ρ	Density (air, ice, or snow layer)
ρ_{bs}	Volumetric airborne blowing snow density
τ	Instantaneous Reynolds stress (u'(t)w'(t)) (overbar indicates temporal mean)

LIST OF EQUATIONS

CHAPTER 1

INTRODUCTION

1.1 Motivation and relevance

Snowmelt provides up to 40% of the world's population with drinking water (Meehl et al., 2007). Understanding the location and mass of snow available for melt is critical for informing policy decisions on water consumption for municipal, agricultural and industrial use, as well ecosystem needs and flood forecasting. Wind transport of snow causes variability in snow depth and density (Guyomarc'h et al., 1994), and influences the timing of alpine runoff (Winstral et al., 2013). Wind redistribution can heterogeneously scour ridgelines and deposit snow on leeward faces in alpine terrain aiding in the growth or ablation of small mountain glaciers (Dyunin and Kotlyakov, 1980). Over moderate terrain, such as relatively level tundra and prairie landscapes, topography, vegetation height and shrub cover drive snow accumulation (Fang and Pomeroy, 2009; Ménard et al., 2014). In both regions, deep snowdrifts caused by seasonal wind loading help snow act as a reservoir for downstream summer water supply. However, wind can also deplete frozen water reserves through sublimation. Recent observations suggest as much as 19% of an alpine snowpack can sublimate back into the atmosphere and become unavailable as melt water (Macdonald et al., 2010).

Current blowing snow models (e.g. Essery et al., 1999; Lehning et al., 2006; Winstral et al., 2013; Vionnet et al., 2014) are based on averaged approximations of particle transport that do not represent the modern understanding of multiphase flow physics (e.g. Marchioli and Soldati, 2002; Soldati, 2005; Lavezzo et al., 2010; Ho et al., 2012, 2014; Li et al., 2014) and cannot be accurately extrapolated to non-steady flows typical in mountainous terrain (Groot Zwaaftink et al., 2013). Complex phenomena, such as particle entrainment, rebound, turbulence and transport intermittency govern sediment flux rates and influence the substantial spatial variability in transport (Kaftori et al., 1995; Horender et al., 2013; Martin et al., 2013). Limitations in blowing

snow models are directly related to inaccurately representing or neglecting the large spatial and temporal variability arising from the nonlinear nature of the multiphase flow characteristics (Sørensen, 1997; Groot Zwaaftink et al., 2013; Horender et al., 2013; Groot Zwaaftink et al., 2014).

Blowing snow wind models have evolved through the years, but still rely heavily on rudimentary boundary layer theory and use crude meteorological adaptations to represent fully-developed wind profiles. In mountainous regions, the resulting errors can be significantly magnified by the non-steady, turbulent flow resulting from steep and varied alpine terrain (Helgason and Pomeroy, 2012). An accurate description of wind-snow interactions in the lowest metres in the atmosphere is required to compute snow mass flux (Vionnet et al., 2014). The remainder of this section will provide background on the field of aeolian transport, the standard blowing snow measurement techniques, and the current state of models derived from such data. Relevant aspects of atmospheric boundary layer flows that cannot be represented with current methods are then discussed, along with novel measurement and analysis techniques introduced to understand the impact of these insufficiencies. The remainder of this thesis specifically addresses the role of coherent turbulent structures at an alpine treeline observation site for near-surface blowing snow to better understand the non-stationary coupling of an alpine snowpack and atmospheric flows.

1.2 Background – Aeolian Transport

Blowing snow research has benefited greatly from the larger field of aeolian transport, the movement of dust and sand by wind. Many fundamental concepts describing blowing snow had their origin in aeolian research. The modern focus of aeolian research dates back to the 1930's with the sand transport studies of R.A. Bagnold in North African deserts and soil erosion work of W.S. Chepil near Swift Current, Saskatchewan (Chepil and Milne, 1939; Bagnold, 1941). They sought to explain the physics governing particle transport at both the near surface and upper extent of atmospheric dispersion. Bagnold's definitions of the three main transport processes have been slightly adapted over the years, but the concepts remain intact:

Reptation/Creep: This is the rolling of grains on the bed surface never rising more than a grain diameter in height above the ground. Creep is often neglected in blowing snow models as cohesive properties are usually quite high on the snow surface. Additionally, snow grains are thought to transition to saltation quickly because of their low inertia (Gauer, 1998b).

Saltation: This idealized motion involves grains following ballistic trajectories after being ejected from the surface and accelerated horizontally by the wind. They reach a maximum height, usually below 20 cm, before returning to the ground (Schönfeldt and von Löwis, 2003). This is often described as a skipping or hopping motion.

Suspension: Grains in suspension are lifted high above the surface by vertical gusts and are transported over long time periods (up to days) before returning to the surface (if at all). Suspended grains follow wind streamlines much more closely than saltating or creeping grains (Zhang et al., 2008).

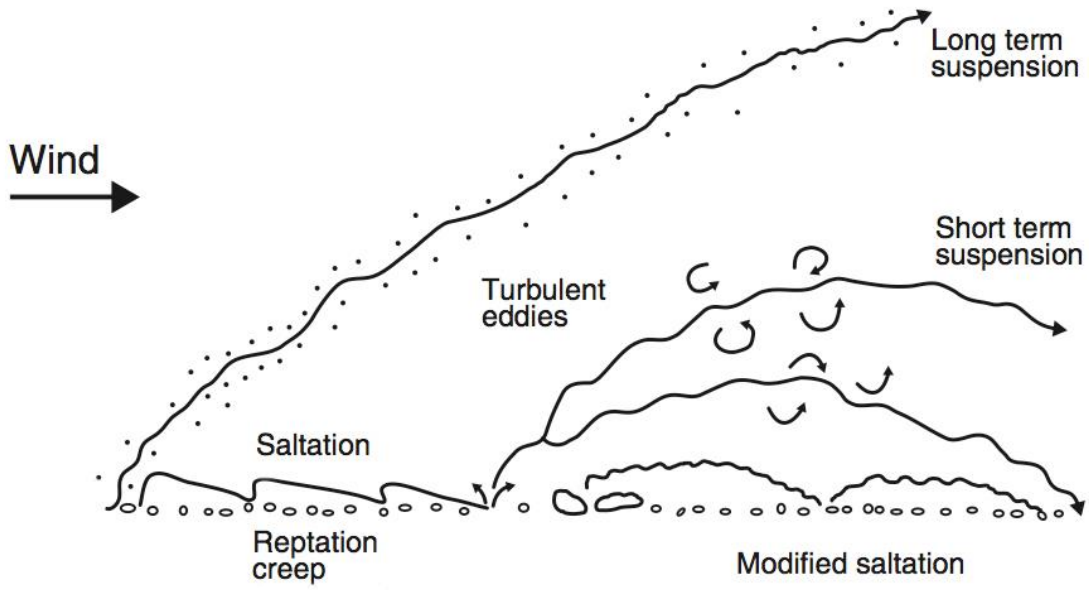

Figure 1-1: Modes of Inertial Particle Transport, adapted from Nickling and McKenna Neumann (1994)

It is in the saltation layer that mass concentration is highest for both sand and snow transport (Chepil, 1959; Gauer, 1998b; Zhang et al. 2007a). In addition, all transported particles must travel through the saltation layer at least once. As such, much work has been done in the field (e.g. Bagnold, 1941; Zhang et al., 2007a; Shi and Huang 2012) and in wind tunnels (e.g. Anderson and Haff 1988, 1991; Anderson et al., 1991; Nishimura and Hunt 2000; Guo and Huang 2013) describing sub-processes of saltation. To further understand this mode of transport, two ways in which a particle may begin saltation have been defined: aerodynamic entrainment and splash. Aerodynamic entrainment is the process of resting grains mobilizing purely from lift and drag forces. The splash sub-process describes an incoming grain, already in transport, impacting the surface, rebounding and/or ejecting other grains. There is currently no consensus on which sub-process dominates blowing snow initiation as the sub-process dominating transport initiation changes with wind speed (Nishimura and Hunt, 2000).

The classic approach to modeling initiation of particle transport has been by determining threshold friction velocities for specific grain diameters. Mass flux is then approximated as a function of mean wind speed, averaged over a period of time ranging from 15 minutes to 1 day, assuming a fixed carrying capacity for the wind (Bagnold, 1941; Chepil, 1959). This carrying capacity is dependent on both the wind strength, and the conditioning of the bed (Li and Martz, 1995). Previous work has been conducted to statistically predict the dominance of splash versus entrainment (Anderson and Haff, 1988) and create numerical splash functions (McElwaine et al., 2004), but these functions are based on sandy wind tunnel observations and were developed for use with time averaged wind speeds. This core idea remains in many snow and sand transport models to the present day even though early studies in snow transport by A.K. Dyunin in the 1950's highlighted many contrasts between snow and sand behavior, and suggested several fundamental differences in the natural phenomena including sublimation and surface cohesion (Dyunin, 1967). For example, Budd et al. (1966) were able to fit the probability of blowing snow grain diameters to a two-gamma variate that does not apply for sand. Their measurements are still widely used when a reference for blowing snow particle size distribution is desired.

Saltation and entrainment functions based on particle diameters in aeolian work have proven effective, but adaptation to snow has occurred only with extensive calibration, and with

varying levels of success (e.g. Clifton et al. 2006, Groot Zwaaftink et al., 2014). This is largely because the physical properties of a resting snowpack make representing snow particle transport considerably more complex than sand. Depending on temperature and humidity during snowflake formation and snowpack metamorphism, crystals may evolve into a variety of shapes (Libbrecht, 2005). Additionally, wet and dry metamorphism of snow grains (Sommerfeld and LaChappelle, 1970) can change the physical properties of a snowpack from day to day (see Figure 1-2). Instead of a bed of individual grains, a snowpack consists of a crystal matrix with bonds that must be broken for an individual particle to be identified (Li and Pomeroy, 1997a, Greene et al., 2008; Heggli et al., 2011).

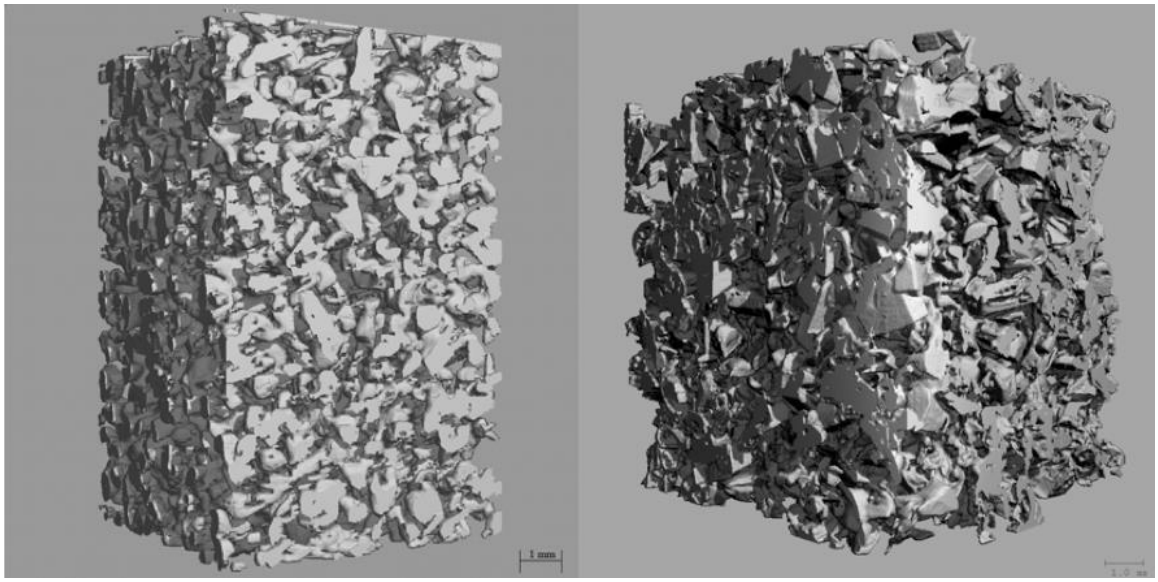

Figure 1-2: Snowpack Crystal Lattice Structure before (L) and after (R) 5 days of dry snow metamorphism (Greene et al., 2008)

The work of R.A. Schmidt (1980, 1982) in the early 1980's also displayed the importance of granular surface cohesion on the threshold wind speed needed to initiate blowing snow transport. Li and Pomeroy (1997a) used an approach similar to the wet and hardened soil crust models of Chepil and Woodruff (1963), relying on meteorological history to determine crystal matrix bond structure. The snow history was a vital component to modeling surface erosion as the formation of windcrusts during prolonged saltation hardens the surface, increasing cohesion

(Guyomarc'h et al., 1994; Guyomarc'h and Merindol, 1998). During a multiple-month transport simulation, inclusion of cohesion in a blowing snow model resulted in model errors of 7-8% of annual snowfall (Li and Pomeroy, 1997a), but on shorter timescales and in more complex terrain, the complications arising from modeling surface cohesion still persist for soil and snow transport.

1.2.1 Blowing Snow Measurement

Historically, measurements of mass flux have been long time averages or approximated by particle counting. Classic mechanical traps have been used for decades to collect average snow fluxes during wind events such as the Mellor (1965) rocket-shaped snow trap (Budd et al., 1966). Takeuchi (1980) designed a snow sock frame with multiple traps to compare mass flux against height (Figure 1-3), but was unable to derive an empirical relationship unless measuring during fully developed saturated flow. Schmidt et al. (1982) improved on the Takeuchi design but the long-time scale-averaged flux data collected was still based on an uncertain collection efficiency (Budd et al., 1966; Schmidt et al., 1984).

Beginning in the 1980's, electronic particle detectors were developed of varying design and compared against mechanical traps (Schmidt et al., 1984). Gubler (1981) and Schmidt et al. (1984) developed photo-electric sensors using infrared light and incandescent lamps respectively (Figure 1-3). Brown and Pomeroy (1989) improved on this design with an LED for particle detection and a quicker response. While this development enabled counting individual snow particles in transport over shorter time scales, the simplicity of the technique made it difficult to calculate snow flux. None of these methods provided a velocity-measurement of particles, all were susceptible to complications from only a fraction of the light being obstructed, and all relied on using an assumed particle size distribution (such as (Budd et al., 1966)) to estimate mass flux.

The latest style of snow flux measurement introduced was FlowCapt, an acoustic sensor which uses microphones to listen for snow particle impacts on a metal enclosure (Chritin et al., 1999). While the idea was novel, it relies on assumptions of constant wind gradients, uses empirical relationships between mass flux and wind speed, and performs poorly under high winds. As such, FlowCapt was shown to be unsuited for use in scientific research (Cierco et al., 2007), though still useful for avalanche forecasting.

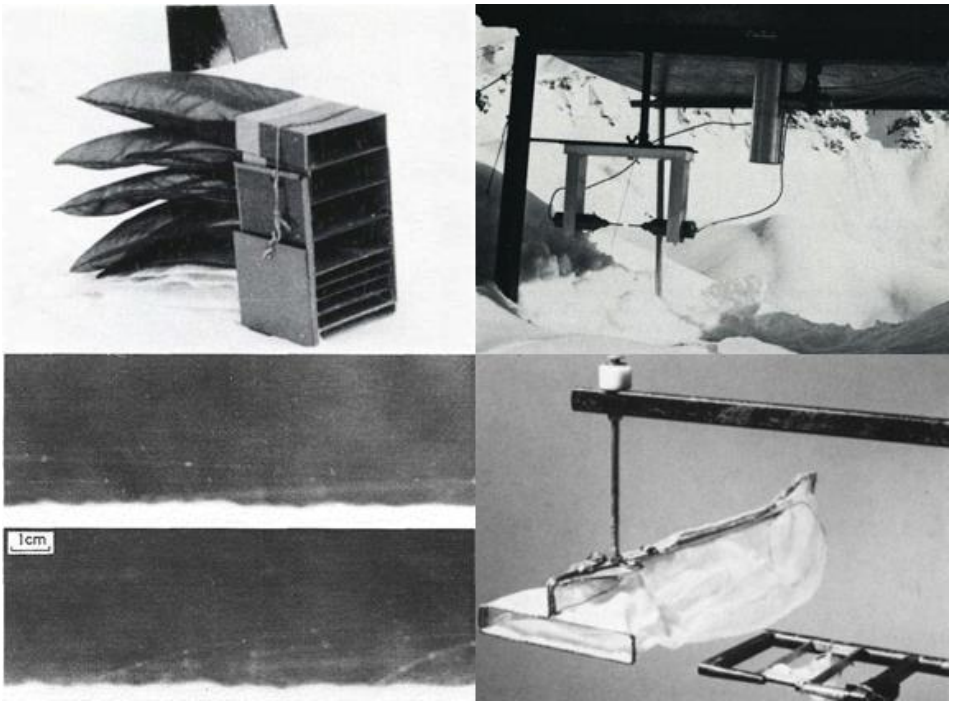

Figure 1-3: CW from top Left, Takeuchi (1980) sock trap, Gubler (1981) drift gauge, Schmidt et al. (1984) particle counter and sock, Kobayashi (1972) saltation images.

Most relevant to the proposed research is the photography of Kobayashi (1972) (Figure 1-3) who was able to obtain qualitative information on snow transport mechanics and the first photographic evidence of snow saltation. Used in wind tunnels and in natural environments, both fast and slow shutter speeds provided new information on splash and entrainment behavior as well as particle trajectories. Kobayashi (1972) was unable to acquire any quantitative data, but did lay the groundwork for more sophisticated applications with digital photography this research will propose to implement. Recently, Gordon and Taylor (2009) developed a novel backlit camera system to measure blowing snow particle size and shape parameters in a 9 mm^2 frame. Gordon et al. (2009) modified this technique to image a 124 mm x 101 mm frame and applied a black and white binarization algorithm to estimate time averaged particle density profiles. Unfortunately, particle velocity measurements were unavailable from either study.

1.2.2 Blowing Snow Modeling

Particle transport components of blowing snow models typically rely on steady-state assumptions, with few exceptions (e.g. Nemoto and Nishimura, 2004). The fully saturated flows and constant rates of entrainment that are often assumed do not apply in mountain terrain (Schmidt, 1982). In areas with sufficient flat upwind fetch, over frozen lakes and in the Canadian prairies, these assumptions have shown their effectiveness for calculating snow flux (Marsh, 1999), but have only worked with extensive model calibration, or at very low resolution, in the alpine (e.g. Liston et al., 2007). As mentioned previously, there is uncertainty in the mathematical representations of each of the transport sub-processes, calling into further question the calibrations necessary to make a model work. A precise understanding of the time dependency of erosion and deposition rates is crucial to creating a widely applicable, high-resolution blowing snow model.

1.2.2.1 Large Area Models

One of the first widely used blowing snow models is the Prairie Blowing Snow Model (PBSM) (Pomeroy and Male, 1987; Pomeroy, 1989; Pomeroy et al. 1991, 1993; MacDonald et al., 2010). The model is physically based but includes calibration of internal coefficients from detailed observations of blowing snow fluxes. Transport and deposition values are dependent on upwind fetch, and roughness elements (such as agricultural grain stalks). For wind, the model assumes a logarithmic velocity profile and includes terms for sublimation, but does not include any thermodynamic feedback on the environment (Pomeroy et al., 1993).

Saltation rates, F_{salt}, in PBSM and many other models (e.g. Doorschot and Lehning, 2002; Liston et al., 2007) are estimated through some adaptation of Bagnold's original ideas of shear-stress partitioning, such as

$$\boldsymbol{F_{salt} = \frac{c_1 e \rho u_t^*}{g}(u^{*2} - u_n^{*2} - u_t^{*2})} \tag{1-1}$$

where c_1 is the ratio of friction velocity to saltation velocity, e is the efficiency of saltation, ρ is atmospheric density, u_t^* is shear velocity at threshold of saltation, g is the acceleration due to

gravity, and u_n^* is the portion of shear stress applied to non-erodible roughness elements (Pomeroy and Gray, 1990). Equations for u_t^* and u_n^* are then based on 2-metre air temperature and soil erosion equations for exposed vegetation, respectively (Pomeroy and Li, 2000).

Following the ideas of Bagnold further, a suspension layer is calculated above the saltation layer, of distinct mass concentration. To calculate rates of transition to suspension, the sublimation, vertical diffusion, and settling velocities of snow are balanced, maintaining steady state conditions (Pomeroy and Male, 1992). To account for the effect of sublimation on suspended mass concentration, rates of change are calculated by numerically integrating the wind tunnel ice sphere sublimation rates quantified by Thorpe and Mason (1966). Upscaling these estimates to distributed models is conducted through the application of probability distribution functions based on snow age and temperature (e.g. Li and Pomeroy, 1997b). Snow sublimation is most efficient for suspended particles when there are high particle ventilation rates and large values of turbulence kinetic energy (Schmidt, 1972; Lee, 1975; Bintanja, 2000).

The simplicity of the model has led to some of its success, but also introduces limitations. PBSM performs best over flat terrain with several kilometres of upwind fetch to fully develop the wind turbulence and obtain saturated transport conditions. PBSM divides transport into spatially homogeneous layers of suspension and saltation, and uses a probability distribution for temporal and spatial upscaling of sublimation and mass flux estimates (Li and Pomeroy, 1997b). PBSM has been successfully applied in prairie and arctic environments, though Pomeroy and Li (2000) warn about application in different, untested climates. Additionally, the one-dimensional, wind input eliminates the possibility of a physically driven solution in complex terrain (i.e. not horizontally homogeneous and flat, >10° slope (Rotach et al., 2008)).

There have been several improved versions of PBSM, including the Distributed Blowing Snow Model (DBSM) for complex terrain (Essery et al., 1999). Parts of PBSM have been pieced together in conjunction with other concepts to create new models as well. Stephen Déry used the PBSM model for saltation and created several incarnations of the PIEKTUK model (Xiao et al., 2000). Liston, Sturm and others developed SNOWTRAN3D, another adaptation of PBSM equations to complex terrain (Liston et al., 2007). Over large spatial and temporal ranges, the steady-state PBSM assumptions may balance, resulting in reasonably accurate statistical values

of snow water equivalent (SWE). However, these same assumptions prevent higher spatial or temporal resolution accuracy.

Other researchers have developed empirical and semi-empirical snow distribution models on a multitude of scales, all including their own assumptions and approximations. Gallee et al. (2001) represented circumpolar snow transport in the Antarctic by using 40 km grids and a rotational wind flow. In mountainous and prairie terrain, topographic index models, such as those used by Winstral et al. (2013) and Lapen and Martz (1996), avoid the complexities of non-linear turbulent snow transport and calculate areas of high likelihood for snow deposition to determine drifts during peak snow water equivalent. The evolution of empirical blowing snow models have come with improvements in accuracy, but the core equations that govern mass flux rates of saltation and suspension are physically based, but not physically driven. Improved understanding of blowing snow at high spatial and temporal resolution requires a thorough consideration of atmospheric turbulence at small scales.

1.2.2.2 Turbulence-Driven Models

Approaches to more accurately representing turbulence in blowing snow models began with the introduction of a Reynolds-averaged Navier Stokes wind model by Uematsu et al. (1991). In his Ph.D thesis, Peter Gauer improved on this model and treated blowing snow as two layers (suspension and saltation) of continuous wind-snow mixtures (Gauer, 1998a, 1998b, 1999). He used CFX, a commercial fluid dynamics computer program, and was able to implement a k-ε closure for his wind model. The k-ε closure is a method to approximate the effects of turbulence by estimating turbulence kinetic energy (k) and turbulence dissipation (ε). Though Liston had used this approach in the past (Liston et al. 1993 a,b), Gauer did not limit his focus to wind speeds below those needed for suspension. This was a large step forward in complex wind approximation, especially over alpine terrain.

While building his numerical model, Gauer extensively considered impact and ejection angles for saltating particles. At the time of his dissertation, his work was the first to design a non-steady, three-dimensional, two-way coupled blowing snow model including saltation and

suspension layers. However, he limited the physical accuracy of his work by assuming all particles were spherical and uniform in size, disregarding drag forces and sublimation, and assuming particles had the same horizontal velocity as the estimated wind profile. Additionally, Gauer did not include a vertical velocity for his turbulent eddies among other smaller forces. These assumptions have been regarded as inaccurate since the 1950's (Dyunin, 1967), and ultimately Gauer faced difficulty verifying his simulations in the field.

The modeling and wind-tunnel work of Nemoto and Nishimura (2004) and Nishimura et al., (2004) has recently allowed the combination of saltation and suspension layers into one continuum through the use of vertical wind fluctuations. While limited to steady-state wind-tunnel measurements winds, the model was able to accurately represent the initiation and changes in mass flux prior to reaching equilibrium transport after 10 seconds. This is a promising development as blowing snow transport may not always reach equilibrium in nature and representing the onset of transport is critical for adjusting flow during gusty conditions.

At a similar time, Bintanja (2000) followed the k-ε approach and created a model of suspended snow transport incorporating explicit forces from the particle back onto the atmospheric flow. He included terms for turbulent fluxes and reduction of turbulence kinetic energy as momentum lost to transporting particles (in contrast to the future results of Zhang et al., (2008)). His treatment of turbulence was another step towards the current edge of understanding in aeolian transport, but his snow particles were assumed to be non-cohesive, spherical, rigid and inertia-free objects.

Doorschot and Lehning (2002) cultivated some of Gauer's innovations and introduced the particle-bed functions of Anderson and Haff (1991). Parameters for aerodynamic entrainment, splash, and particle trajectory height all depend on grain size. Doorschot and Lehning (2002) also included terms for the critical momentum sink in the wind flow caused by snow particle transport, similar to Bintanja (2000). Initial conditions for saltation simulation came from wind tunnel snow and ice estimates of Nishimura and Hunt (2000).

Particle size assumptions may have an especially large effect on transport rates as their entrainment model is based on particle diameter. Doorschot et al., (2004) sought to verify the 2002 model using snow particle counters, acoustic sensors and mechanical traps. In contrast to Schmidt

(1982), they found aerodynamic entrainment was the dominant process in all experiments and attributed this to the dendricity of the surface snowflakes and their inability to rebound. Critical insight was gained through the work of Doorschot and Lehning, especially evidence supporting that the prevalence of turbulent gusts over short timescales indicated snowdrift processes are better modeled more locally in time. Doorschot et al. (2004) stated that field measurements of saltation and suspension on varying slopes should be carried out, suspecting that at crests, suspension rates may outweigh saltation.

The Doorschot and Lehning (2002) saltation model was incorporated with a suspension and sublimation model in the snow surface process model Alpine3D with varying degrees of success (Lehning et al., 2006). Some modeled areas have predicted snow depth with errors up to 1-metre, mainly caused by topographic complications (Mott et al., 2010, Groot Zwaatfink et al., 2013). The location of drifts and mechanics of transport are thought to vary over complicated topography. For example, for downhill motion, splash may outweigh entrainment as particles will have higher trajectories and accelerate more by the wind. While Schmidt and Randolph (1981) performed calculations of effects on snow particle trajectories over abrupt walls with these effects in mind, a thorough investigation has yet to be conducted. As with all operational blowing snow models, major deficiencies are attributed to the use of steady state wind fields, steady state transport over hourly time steps, limited variability in wind fields and low spatial resolution (Groot Zwaatfink et al., 2013).

In an attempt to further improve wind components of blowing snow models, adapting large eddy simulations (LES) for snow transport recently began through the work of Groot Zwaaftink et al. (2014) over small scales (12.8 x 6.4 m) and flat terrain. Initial results have shown this to be an insightful and necessary innovation. The improvement of wind field models and inclusion of non-uniform snow characteristics has allowed visualization of snow streamers and spatio-temporal variability. While this model is the most sophisticated short timescale snow transport model to date, Groot Zwaaftink et al. (2014) have left open several gaps in the sub-processes governing transport.

Groot Zwaaftink et al. (2014) drove transport initiation with threshold friction velocity as determined by particle diameter relationships from the wind tunnel studies of Clifton et al. (2006),

using a calibration scalar to account for snow lattice cohesion. The LES driving the transport model is acknowledged to be misrepresentative of natural wind, and a log-law extrapolation is performed for the bottom 10 cm of the boundary layer, assuming instantaneous shear stress is constant in the region. It is also unknown whether the periodic boundary conditions skew turbulence characteristics or if the subgrid scale model influences particle transport.

Spatial variability in snow transport was shown to be largely dependent on the shear stress used in the entrainment function, not transport redistribution by wind as in Direct Numerical Simulations (DNS) (e.g. Lavezzo et al., 2010; Marchioli et al., 2006; Marchioli and Soldati, 2002; Soldati, 2005). The calculated variability in transport is therefore largely dependent on particle diameter, a characteristic of a cohesive snow matrix without rigorous definition. The work of Groot Zwaaftink et al. (2014) is a significant development, and the results suggest complementary high-resolution field measurements may aid in operational blowing snow model advancement in the atmospheric boundary layer. However, improved field measurements are necessary as the large vortical structures and natural turbulence characteristics cannot develop in a wind tunnel (Narasimha and Kailas, 1987, 1990; Narasimha et al., 1990; Sherman and Farrell, 2008; Horender et al., 2013; Groot Zwaaftink et al., 2014), thus providing a limited or erroneous picture of environmental turbulence and its interaction with two-phase flow.

1.2.3 Structured Turbulence and Aeolian Transport

Spatially or temporally averaged measurements are economical, robust and relatively easy to use, and so have been the basis for most blowing snow studies. In steady state conditions, momentum transfer from the atmosphere to a sediment bed scales with time averaged bed shear stress (Owen, 1964). However, it is becoming widely accepted that there is a growing need to characterize the phenomenon using non-steady state, non-fully developed flow characteristics (Namikas et al., 2003; Naaim-Bouvet et al., 2011; Paterna et al., 2016).

Schmidt (1980, 1982) echoed the arguments of Lee (1975) that steady-state, saturated, fully developed flows are an unrealistic ideal for snow transport in mountains. These fundamental assumptions are thought to contribute to deficiencies of many models. Observational aeolian

transport research underwent fundamental changes beginning in the 1970's and rapidly accelerated in the 1990's with DNS of wind flow and particle tracking algorithms. Researchers are no longer limited to visual qualitative descriptions of turbulent flow but are now able to quantify transient vorticity and velocity fields (e.g. Lavezzo et al., 2010; Marchioli et al., 2006; Soldati, 2005) as well as individual particle velocities in laboratory environments (e.g. Zhang et al., 2007a, 2007b, 2008; Creysells et al., 2009; Ho et al. 2011, 2012, 2014). With these new insights, the role of turbulence and fluctuations around mean flux values in aeolian transport have largely become the center of interest.

Stout and Zobeck (1997), and later Baas and Sherman (2005), argued that turbulence in wind, intermittent saltation rates, and velocity fluxes are major contributors to environmental saltation dynamics. These nonlinear mass flux dynamics are highly temporally and spatially variable and are made visible by meandering quasi-linear streamwise sand snakes (or sand streamers) (Baas, 2003) thought to be associated with "low-speed streaks" in the wind (Marchioli and Soldati, 2002; Soldati, 2005). In mountain terrain, especially in the Canadian Rockies, wind flow is also highly variable with short time scales (Helgason and Pomeroy, 2012) making snow transport susceptible to the same intermittency behavior. Turbulence-focused blowing snow studies in wind tunnels and natural environments have confirmed that wind tunnel based approximations are insufficient to realistically represent the behavior of natural turbulence (Horender et al., 2013). Thus, there is a considerable need for updated outdoor field campaigns.

Shi and Huang (2012) implemented the methods of van Boxel et al. (2004) in the field while gathering sand flux measurements in western China. They then coupled the data with a saltation model emphasizing wind flow fluctuations and observed the widely used log-law of the wall velocity profile of wind, only when averaging over intervals longer than 30 seconds. Below this timescale, the dynamic fluctuations exhibited much different mean behavior. If the mean wind speed was near threshold velocity, intermittent bursts of turbulence were shown to increase rates of bed erosion by 30%.

Recent field experiments with time averaging analysis have confirmed that non-stationarity of turbulence statistics in nature can cause errors in shear stress estimation and inaccuracies in flux calculations (Namikas et al., 2003; Martin et al., 2013). Interestingly,

observations and analysis have shown that sand flux was most dependent on the turbulent stream-wise fluctuations u', not friction velocity (Butterfield, 1991; Sterk et al., 2002; Xuan, 2004; Liu et al., 2012), as has been most often used (Bagnold, 1941; Chepil, 1959; Pomeroy, 1989; Gauer, 1999). This reinforces the need to represent wind as non-steady and not use the current methods of mean wind speed or time averaged shear stress to predict sediment transport.

Moreover, it is not only the wind fluctuation magnitudes, but also the frequency at which wind gusts occur, that govern transport rates (Spies and McEwan, 2000; Spies et al. 2000). In field studies and wind tunnels, sand transport energy has been observed to peak at periods of 6 s (Baas, 2006; Butterfield, 1998), 20 s (Butterfield, 1998) and 60 s Hz (Baas, 2006). This concept is closely tied to particle response time studies. Researchers have witnessed dust and sand particles reactions limited to wind speed fluctuations below 0.5 Hz (Spies et al., 2000), all the way up to 250 Hz (Liu et al., 2012) and measured lag times from essentially zero to 4 seconds (Li and McKenna Neuman, 2014) with an average around 1 second (Pfeifer and Schönfeldt, 2012). Therefore, particle velocities not only exhibit varying lag times in response to wind changes, but also filter higher frequency fluctuations.

To represent transport intermittency at larger scales and high Reynolds numbers, researchers have begun using LES. LES is a technique to mathematically represent turbulent motions by explicitly solving for large eddies, and statistically modeling motions below a given threshold. Interested in understanding the wind momentum lost to sand transport, Dupont et al. (2013) coupled a LES with an intermittent saltation model and observed a distinct change in the wind field upon introducing the sand particles. Saltation height was affected by turbulent fluctuations, as also observed by Baas and Sherman (2005) and Shi and Huang (2012), varying mass transport by up to 20%. Most importantly, Dupont et al. (2013) were the first to numerically represent the intermittent transport of aeolian streamers in a LES, something that had until then been neglected in snow and sand transport models.

1.2.3.1 Particle Image Velocimetry

Since 2007, some interesting sand transport results have come to light using Particle Image Velocimetry (PIV) and Particle Tracking Velocimetry (PTV). PIV and PTV are quickly improving techniques of visualizing and quantifying fluid flow fields and particle transport, respectively. The basis of both methods is the use of high-speed cameras and particle tracking. Particles are identified in pairs of images at corresponding coordinates in each frame. Particle displacement is then calculated from one frame to the next, which is converted to a particle velocity by converting pixels to a physical length, and knowing the time lapse between frames. These techniques are especially effective at quantifying turbulent motions as they are largely non-invasive and can determine high temporal- and spatial-resolution vector fields (Raffel et al., 2007).

Zhang et al. (2007a) developed a method to simultaneously use PIV and PTV in a sand-filled wind to calculate separate velocity fields for saltating sand particles and the surrounding wind flow. This provided a notable advance in understanding the effect on wind fields caused by the presence of saltating particles, especially within 20 mm of the surface (Zhang et al., 2007b). Zhang et al. (2008) confirmed that particle response times and trajectories were influenced by both wind turbulence and particle inertial forces; turbulence being dominant in suspension, and inertia dominating saltation. In another wind tunnel study, Creyssels et al. (2009) obtained promising sand transport data using PIV, Laser Doppler Anemometry and PTV. They determined that sand particle velocity varied linearly with height in contrast to the widely used logarithmic profile of wind. Again, characteristic particle height was independent of friction velocity and particle velocity profile was only slightly dependent on mean wind speed, as is often assumed. This work was continued by Ho et al. (2011, 2012, 2014) and provided more insights into the particle organization of equilibrium transport under varying steady-state conditions. While these PTV studies were conducted in low Reynolds number wind tunnels, they provide a foundation for PTV-saltation studies in natural terrain.

Rarely has PIV and PTV work been conducted in natural flows and as yet there has been no environmental boundary layer PIV or PTV with snow particle tracers. However, PIV and PTV methods have been successfully implemented in field environments, and at varying scales of interest (e.g. Morris et al., 2007; Nimmo Smith et al., 2002; Rosi et al., 2014; Toloui et al., 2014; van

Hout et al., 2007). This research has proven environmental fluid velocities and vorticity can be measured using PIV/PTV in remote locations and in turbulent boundary layers. The work of Morris et al. (2007) is especially encouraging as their focus addressed the importance of hairpin vortices in very high Reynolds number flows with near surface particle imaging over the salt flats of the Great Salt Lake. This relates very closely to the proposed coherent structure-blowing snow research as hairpin vortices have been shown to entrain and re-suspend particles in boundary layers (Prevel et al., 2013; van Hout, 2011).

1.2.3.2 Coherent structures in very high Reynolds number flows

In the high Reynolds flows of interest for natural wind, structures termed Very-Large-Scale Motions (VLSMs) in the upper boundary layer have been coupled with the surface turbulence generation not visible in DNS or wind-tunnel studies (e.g. Metzger and Klewicki, 2001; Balakumar and Adrian, 2007, Figure 1-4). Unfortunately, the spectrum of eddy sizes present in wind tunnel studies is limited when compared to those active in the atmospheric surface layer (ASL) (Guala et al., 2011; Keylock et al., 2012). While wind tunnel inner scaling variables may be of the same order of magnitude as in the ASL, outer scales in nature can be up to 40 times larger (Narasimha et al., 1990). The use of long-time mean values representing inner layer equilibrium conditions to drive blowing snow models is widely known to be physically inaccurate and obscures the transient nature of turbulent scalar and momentum transfer. Thus, shorter timescales may be better suited to capture the true nature of blowing snow mechanics (Doorschot et al., 2004). However, the large-scale time-dependent fluctuations present in the ASL that drive transport intermittency necessitate a more comprehensive characterization of the turbulence in blowing snow models than scalar, time-averaged u_* values (Sterk et al., 1998; Kok et al., 2012). This is further complicated because snow transport often occurs in mountainous terrain where topographically driven or modified flow structures are present, such as wakes, flow separations, and developing boundary layers

With the availability of high frequency observations, determining what data are relevant to sediment transport has been a focus of some significant wavelet analysis. It is widely accepted

that bursts of wind, whether described as structured turbulence or not play a vital role in sediment flux mechanics (Willets et al., 1991). The dissertation of Baas (2003), and subsequent papers (Baas and Sherman, 2005; Baas, 2006) studied the relationship between aeolian streamers and turbulence through wavelets. Baas (2006) analyzed the wavelet power spectra of acoustic sand flux data to determine what are the frequencies of peak energy for transport. Comparing this information to the power spectra of the wind gave insight into what turbulent events may be contributing most to transport. Ellis (2006) took the wavelet analysis a step further using zero-crossings of Mexican Hat wavelets at a particular scale to identify coherent structures relevant in sand flux data. This work had a similar approach to above canopy wavelet analysis conducted for latent and sensible heat flux event detection (e.g. Collineau and Brunet, 1993; Thomas and Foken, 2004).

Wavelet packets have been used to look at turbulent transport using Multi-Resolution Analysis with hotwire anemometers. Liu et al. (2012) determined that the vast majority of sand particles do not respond to wind events with a frequency higher than 250 Hz. While this is beyond the sampling capabilities of sonic anemometers, it does provide a relative upper bound for what events may be important, and what can be neglected in models. Of the relatively low frequency events identified by Liu et al. (2012), only particular gusts were important for particle transport. The gusts were periods of large instantaneous shear stress that can be classified using quadrant analysis of the Reynolds' stress tensor, $R_{ij} = \rho u_i' u_j'$ (Leenders et al., 2005).

Sweeps, wind motions with greater than average streamwise and less than average vertical velocities, may play specific roles in initiation and bed transport ('creep'), while ejections, wind motions with less than average streamwise and greater than average vertical velocities, can contribute to vertical transport of grains and the transition to suspension (Heathershaw and Thorne, 1985; Lapointe, 1992; Nelson et al., 1995; Sterk et al., 1998; Marchioli and Soldati, 2002; Leenders et al., 2005; Diplas et al., 2008; Lelouvetel et al., 2009; Chapman et al., 2012, 2013). As the bursting process associated with sweeps and ejections generates the majority of surface shear stress during sediment transport, (Grass, 1971; Jackson, 1976; Bauer et al., 1998; Li and McKenna Neumann, 2012), sweeps and ejections are of primary concern when using quadrant analysis for aeolian turbulence structure research. Outward interactions, wind motions with greater than

average streamwise and greater than average vertical velocities, may also play a critical role in aeolian transport (Heathershaw and Thorne, 1985; Nelson et al. 1995; Sterk et al., 1998, Schönfedlt and von Löwis, 2003; Leenders et al. 2005). In terrain with steep slopes, more similar to the alpine, it has been shown that aeolian transport over a simple barchan dune is sensitive to the dominant quadrant of turbulent motions, which is in turn dependent on the location of measurement on the dune (Wiggs and Weaver, 2012).

1.3 Research questions and objectives

Goal of Research: **To identify and characterize the relationships between turbulent wind structures and blowing snow events in alpine terrain.**

The micro-processes governing rates of blowing snow transport and locations of deposition have been neglected as a focus of research in recent years. During this time, advances in particle-laden boundary layer flow research have introduced new measurement techniques and turbulence models that may answer many open questions in blowing snow. Steady-state assumptions in common basin-scale models are rooted in inaccurate micro-scale assumptions, which makes their operation highly uncertain for short timescales. To improve the micro-scale understanding, the proposed research will step away from current trends and adapt new concepts from turbulent boundary layer theory. Though limited to a small spatial and temporal scale, this work focused on furthering the scientific understanding of blowing snow processes.

With this goal in mind, the proposed research addressed the following three objectives:

Objective 1) Determine snow particle motion response to time dependent atmospheric surface layer winds at varying heights in the saltation layer.

This objective will address how saltation regimes are related to time averaged winds. The first objective may also posit potential answers to the following questions:

How do uniform velocity profiles and constant rates of particle entrainment compare with real data?

What particle motion mechanisms are most important for snow particle transport initiation?

Objective 2) Identify coherent turbulence structures relevant to saltation initiation and particle entrainment.

The second objective of the proposed research is to characterize the near surface turbulence structures most important for saltation initiation and transport. The second objective may also posit potential answers to the following questions:

What types of turbulent motion (if any), as defined by quadrant analysis, preferentially impact blowing snow transport?

Do specific turbulent structures play specific roles for particle initiation or transport?

Objective 3) Improve understanding of mechanics and origins of near-surface turbulence structures most responsible for blowing snow transport.

The third objective will investigate the role of large topographically driven eddy structures in surface turbulence. The last objective may also posit potential answers to the following questions:

What are the turbulent energy frequency ranges most relevant to transport?

Are the same frequency events important for entrainment, saltation, or suspension in different topography and over different snow types?

Is near-surface motion more closely related to inner- or outer-layer atmospheric motions in alpine terrain?

1.4 Methods and thesis outline

To posit answers to the above-listed questions, a field campaign was designed to collect high frequency blowing snow and turbulence data in the lowest 2 m of the atmospheric boundary layer at an alpine study site. This included the first environmental Particle Tracking Velocimetry measurements of real blowing snow particle velocities. The data were then analyzed with signal-processing tools, many of which were applied to a blowing snow dataset for the first time. Multiple techniques were applied to the collected data, each being described more thoroughly in the associated chapter of analysis. The remainder of this chapter consists of a brief description of the data collection and analysis process, followed by the remaining thesis outline.

1.4.1 Field site, turbulence, and blowing snow measurements

Fortress Mountain Snow Laboratory (FMSL), at 50° 49′ 21″ N, 115° 11′ 54″ W, is a heavily instrumented hydrology and micrometeorology research basin in the Kananaskis Valley of the Canadian Rockies. The observation sites vary from alpine lakes and meadows, to forest clearings, and wind scoured, above-treeline ridgetops at elevations ranging from 2000 to 2600 m. FMSL receives up to 1100 mm snow water equivalent each year and can sustain wind speeds up to 35 m s^{-1}. Snow accumulation, redistribution, sublimation, and ablation in the Kananaskis valley are described by *DeBeer and Pomeroy* (2009, 2010), *Macdonald et al.* (2010), and *Harder et al.* (2016).

The blowing snow experiment site rests on a valley bench at 2040 m a.s.l. in a previously cleared ski resort base area. Winds were predominantly down-valley, from the south, providing an open, relatively flat (<10°), 400 m upwind fetch of short alpine grasses and shrubs (< 50 cm) that were buried under snow for the duration of the experiments. The area was surrounded by coniferous forest with no wind obstruction for at least 100 m in any direction (Figure 1-4). Even though the immediate surroundings of the study site are relatively flat, turbulence measurements at the study site should be considerably affected by the surrounding mountainous terrain. As such, following the classification of Stiperski and Rotach (2015), turbulence measurements in mountainous terrain refer to any site location where the influencing surroundings are classified as mountainous (e.g. Barry 2008), even if the local characteristics do not.

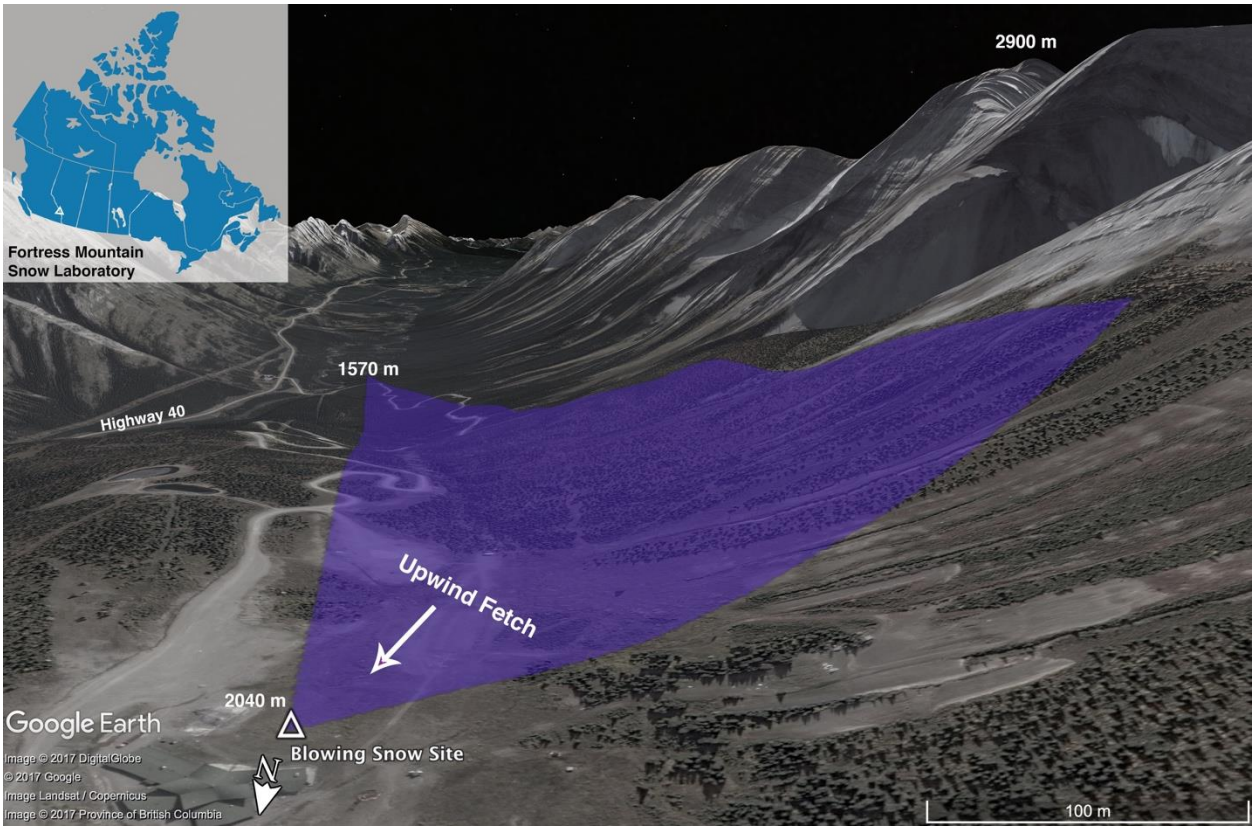

Figure 1-4: Upwind fetch in Kananaskis valley and study site location at Fortress Mountain Snow Laboratory as viewed from the North.

The site was instrumented with two Campbell Scientific CSAT3 Ultrasonic Anemometers continuously measuring 3-D wind velocity at 50 Hz during the winters of 2014-2015 and 2015-2016. The anemometers were positioned on a single 3 m mast with a distance of 1.5-2 m between them. Their respective heights above the snow surface varied with fluctuation of snow depth during the measurement campaigns. Specific heights for measurement campaigns are discussed in the following chapters.

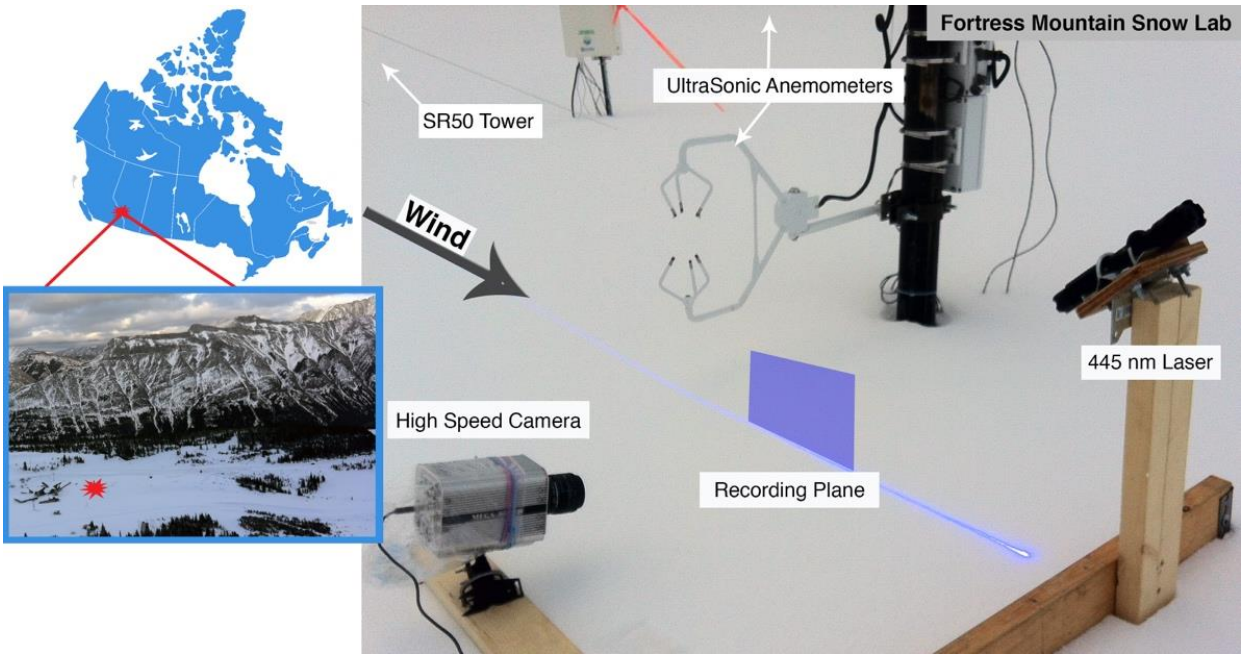

Figure 1-5: Typical blowing snow camera and laser light plane frame orientation with CSAT3 in background.

A portable camera-laser recording frame was constructed and utilized for high speed blowing snow recordings during 21 nights over the two winters of observation. The frame consisted of two arms joined at 90 degrees, with an elevated position for the laser on one arm, and near-surface position for the camera on the other. A 432 nm laser light was shone through a cylindrical lens to generate a 1 mm light plane that angled downwards and orthogonal to the snow surface. The elevated position of the laser prevented it from becoming buried during prolonged blowing snow. A Megaspeed MS85K highspeed camera was mounted on a ball swivel to obtain a perpendicular view of the 2-D illumination plane. Though the distance from the laser to camera was fixed, distance measurements were calibrated prior to each night of recording using a 1 mm square-grid positioned in the light plane for pixel to mm conversions during PTV calculations. When the laser was oriented into the predominant wind direction, a parallel view of creep and saltation trajectories provided video recordings in the first 30 mm above the snow surface (Figure 1-5).

Quality controls were implemented on both the wind and video data, restricting useable data to 7 nights of recording. Sonic anemometer data were subject to additional noise from snow

particle obstructions, data logger drift, and low voltage errors after prolonged snow storms that obscured the solar panels. However, video recordings more often fell below quality standards as streamwise wind directions rarely remained constant during an entire recording, thus becoming transverse to the plane of light. Periods of strong gusting also obscured laser illumination, essentially blacking out recordings or otherwise making individual snow particle indecipherable. Camera and laser lenses were also subjected to interference from blowing snow collecting on the cold surfaces. There were also two instances of the camera frame rate becoming non-constant during recordings because of complications at the camera-computer interface and during one night of warm wet snow that affected the camera's operation. After such videos or wind measurements were discarded, the field campaign provided nearly 5 hours of video, ranging from 50 to 2000 FPS, totaling more than 2 million frames.

An additional mast was instrumented with four SR50 sonic snow depth measurement devices approximately 10 m away to the West. The snow depth devices were arranged such that they could provide a two-dimensional view of snow dune migration but the resultant signal-to-noise ratio during blowing snow events made the data unusable.

1.4.2 Blowing Snow Video Analysis

Time-resolved sparse snow particle velocity vector fields were generated using the Particle Tracking Velocimetry package in DaVis 8 by LaVision. Significant effort was expended in ensuring particle tracking was accurate. Masking out the background and snow surface were significant hurdles. The tracking algorithms are incredibly sensitive to camera sensor hot-spots and immobile grains on the snow surface as they appear consistently in the same pixels, and thus are easily identified and tracked from one frame to the next. Sensor hot-spots are typically darker in appearance than blowing snow and can be disregarded using a strict brightness intensity threshold. However, this method was found to eliminate some small snow particles in as well as those during high density periods of saltation. Neighbourhood averaging was identified as the best method to smooth out hot-spots with the surrounding black background. Masks were generated to prevent PTV algorithms from attempting to track particles resting on the surface. As

the surface was naturally uneven and continuously evolving during recordings, this often necessitated several masks to be generated over any 20-second recording. Additionally, great care was needed to minimize the neighborhood above the surface that was masked so as to not exclude snow moving in the lowest regions of the saltation layer. The final analysis resulted in a total of 1.5×10^6 snow velocity vectors synchronized with concurrent wind conditions.

1.4.3 VITA+LEVEL Analysis

VITA+LEVEL analysis identifies the onset and end of turbulent events by looking at high variance in moving windows. The second part of the algorithm enforces a threshold on the magnitude of the signal, and then finds the regions where this threshold is first crossed on either side of the VITA spike. This delimits the entire motion. This method is further discussed in Chapter 4.

1.4.4 Wavelet coherence

Wavelet coherence (Grinsted et al., 2004) allows measurement of similar power of two signals at approximately the same frequency and times. It does not however convey strong coupling relationships or synchronicity across scales if there is a gap. This method is further discussed in Chapter 5.

1.4.5 Hilbert Transform

Hilbert Transforms allow reconstruction of the envelope of high frequency turbulence signals. This can be thought of as a convolution or as the imaginary part of the analytic signal with the real component being the original signal. Further background is provided in Chapter 5.

1.4.6 Thesis Outline

Chapter 2 adopts the concept of a three-species classification from Aeolian research and identifies the advantages and limitations of this classification with snow transport. As a first step

towards improving the understanding of snow saltation, this chapter identifies the important role that grains tumbling on the surface play in dislodging other grains as well as the difficulties associated with grain disaggregation upon impact.

Chapter 3 displays the ability of high-speed videography and particle tracking velocimetry to provide insight into the time-dependent mechanics of blowing snow saltation for the first time. Initial results from the field campaign related transport mechanisms with short timescales wind flow variations and exhibited strongly non-uniform vertical transport profiles. Initial findings also indicated blowing snow flux events were in direct response to non-steady-state motions in the atmosphere.

Chapter 4 further investigates the coupling of blowing snow flux events and non-steady state motions in the atmosphere. A method to delimit and couple active turbulent motions and blowing snow response gusts that also allows quadrant analysis gust classification is introduced and applied. Different classifications of atmospheric motions are shown to play specific roles in blowing snow initiation and transport.

Chapter 5 identifies the relevant scales of motion in the atmospheric surface layer of which blowing snow gusts most strongly respond. As well, through the lens of amplitude modulation, the origins of surface turbulence and the role of large eddies in small scale fluctuations in near-surface turbulence and snow transport are investigated to provide insight into what scale atmospheric motions are most vital to accurately resolving non-steady wind-snow coupling.

Chapter 6 provides a conclusion to the research as well as suggestions for a way forward to improve implementation of meteorological station measurements as data to drive blowing snow models.

1.4.7 Candidate Contributions to Manuscripts

It is acknowledged that I am first author on all manuscripts in this thesis with my supervisor John Pomeroy as second author. My contribution to each manuscript included conceptualization of field work experiments and analysis, conducting field work and analysis, and authoring the texts. John Pomeroy provided assistance with conceptualization, editorial assistance and connection to the broader context of this research.

1.5 References

Anderson, R. S., and P. K. Haff (1988), Simulation of eolian saltation., *Science*, *241*(4867), 820–3, doi:10.1126/science.241.4867.820.

Anderson, R. S., and P. K. Haff (1991), Wind modification and bed response during saltation of sand in air, in *Aeolian Grain Transport 1*, pp. 21–51, Springer-Vienna.

Anderson, R. S., M. Sorenson, and B. B. Willetts (1991), A review of recent progress in our understanding of aeolian sediment transport., *Acta Mech.*, *1*, 1–19.

Baas, A. C. W., and D. J. Sherman (2005), Formation and behavior of aeolian streamers, *J. Geophys. Res.*, *110*, 1–15, doi:10.1029/2004JF000270.

Baas, A. C. W. (2006), Wavelet power spectra of aeolian sand transport by boundary layer turbulence, *Geophys. Res. Lett.*, *33*, 1–4, doi:10.1029/2005GL025547.

Baas, A. C. W. (2003), The Formation and Behavior of Aeolian Streamers, University of Southern California.

Bagnold, R. A. (1941), *The Physics of Blown Sand and Desert Dunes*, 1st ed., Methuen & Co. Limited, London.

Balakumar, B. J., and R. J. Adrian (2007), Large- and very-large-scale motions in channel and boundary-layer flows., *Philos. Trans. A. Math. Phys. Eng. Sci.*, *365*, 665–81, doi:10.1098/rsta.2006.1940.

Bauer, B. ., J. Yi, S. Namikas, and D. Sherman (1998), Event detection and conditional averaging in unsteady aeolian systems, *J. Arid Environ.*, *39*, 345–375.

Barry, R. G. (2008), *Mountain Weather and Climate*, Third Edit., Cambridge University Press, Cambridge, UK.

Bintanja, R. (2000), Snowdrift suspension and atmospheric turbulence. Part I: Theoretical background and model description, *Boundary-layer Meteorol.*, *95*, 343–368.

Brown, T., and J. W. Pomeroy (1989), A blowing snow particle detector, *Cold Reg. Sci. Technol.*, *16*, 167–174.

Budd, W. F., W. R. J. Dingle, and U. Radok (1966), The Byrd snow drift project: Outline and basic results, in *Studies in Antarctic Meteorology*, edited by M. J. Rubin, pp. 59–70, American Geophysical Union, Washington D.C.

Butterfield, G. (1991), Grain transport rates in steady and unsteady turbulent airflows, in *Acta Mechanica (Supplementum)*, pp. 97–122, Springer-Verlag, Vienna, Austria.

Butterfield, G. R. (1998), Transitional behaviour of saltation: wind tunnel observations of unsteady wind, *J. Arid Environ.*, *39*, 377–394.

Chapman, C. a., I. J. Walker, P. a. Hesp, B. O. Bauer, and R. G. D. Davidson-Arnott (2012), Turbulent Reynolds stress and quadrant event activity in wind flow over a coastal foredune, *Geomorphology*, *151–152*, 1–12, doi:10.1016/j.geomorph.2011.11.015.

Chepil, W. S. (1959), Equilibrium of soil grains at the threshold of movement by wind, *Soil Sci. Soc. Am. J.*, *23*(6), 422–428.

Chepil, W. S., and R. A. Milne (1939), Comparative Study of Soil Drifting in the Field and in a Wind Tunnel, *Sci. Agric.*, *19*(5), 249–257.

Chepil, W., and N. Woodruff (1963), The Physics of Wind Erosion and its control, *Adv. Agron.*, *15*.

Chritin, V., R. Bolognesi, and H. Gubler (1999), FlowCapt: a new acoustic sensor to measure snowdrift and wind velocity for avalanche forecasting, *Cold Reg. Sci. Technol.*, *30*(1–3), 125–133, doi:10.1016/S0165-232X(99)00012-9.

Cierco, F.-X., F. Naaim-Bouvet, and H. Bellot (2007), Acoustic sensors for snowdrift measurements: How should they be used for research purposes?, *Cold Reg. Sci. Technol.*, *49*(1), 74–87, doi:10.1016/j.coldregions.2007.01.002.

Clifton, A., J. D. Rüedi, and M. Lehning (2006), Snow saltation threshold measurements in a drifting-snow wind tunnel, *J. Glaciol.*, *52*(179), 585–596, doi:10.3189/172756506781828430.

Collineau, S., and Y. Brunet (1993), Detection of Turbulent Coherent Motions in a Forest Canopy Part I: Wavelet Analysis, *Boundary-Layer Meteorol.*, *65*, 357–379.

Creyssels, M., P. Dupont, a. O. El Moctar, A. Valance, I. Cantat, J. T. Jenkins, J. M. Pasini, and K. R. Rasmussen (2009), Saltating particles in a turbulent boundary layer: experiment and theory, *J. Fluid Mech.*, *625*, 47–74, doi:10.1017/S0022112008005491.

DeBeer, C. M., and J. W. Pomeroy (2009), Modelling snow melt and snowcover depletion in a small alpine cirque, Canadian Rocky Mountains, *Hydrol. Process.*, *23*, 2584–2599, doi:10.1002/hyp.

DeBeer, C. M., and J. W. Pomeroy (2010), Simulation of the snowmelt runoff contributing area in a small alpine basin, *Hydrol. Earth Syst. Sci.*, *14*(7), 1205–1219, doi:10.5194/hess-14-1205-2010.

Diplas, P., C. L. Dancey, A. O. Celik, M. Valyrakis, K. Greer, and T. Akar (2008), The Role of Impulse on the Initiation of Particle Movement Under Turbulent Flow Conditions, *Science (80-.).*, *322*(5902), 717–720, doi:10.1126/science.1158954.

Doorschot, J., and M. Lehning (2002), Equilibrium saltation: mass fluxes, aerodynamic entrainment, and dependence on grain properties, *Boundary-layer Meteorol.*, *104*, 111–130.

Doorschot, J., M. Lehning, and A. Vrouwe (2004), Field measurements of snow-drift threshold and mass fluxes, and related model simulations, *Boundary-Layer Meteorol.*, *113*, 347–368.

Dupont, S., G. Bergametti, B. Marticorena, and S. Simoëns (2013), Modeling saltation intermittency, *J. Geophys. Res. Atmos.*, *118*(13), 7109–7128, doi:10.1002/jgrd.50528.

Dyunin, A. K. (1967), Fundamentals of the mechanics of snow storms, in *Physics of Snow and Ice: proceedings*, pp. 1065–1073.

Dyunin, A. K., and V. Kotlyakov (1980), Redistribution of snow in the mountains under the effect of heavy snow-storms, *Cold Reg. Sci. Technol.*, *3*, 287–294.

Ellis, J. T. (2006), Coherent Structures and Aeolian Saltation, PhD Dissertation, Department of Geography, Texas A&M.

Essery, R., L. Li, and J. W. Pomeroy (1999), A distributed model of blowing snow over complex terrain, *Hydrol. Process.*, *13*, 2423–2438.

Fang, X., and J. W. Pomeroy (2009), Modelling blowing snow redistribution to prairie wetlands, *Hydrol. Process.*, *23*(18), 2557–2569, doi:10.1002/hyp.

Gallée, H., G. Guyomarc'h, and E. Brun (2001), Impact of snow drift on the Antarctic ice sheet surface mass balance: possible sensitivity to snow-surface properties, *Boundary-Layer Meteorol.*, *99*, 1–19.

Gauer, P. (1998), Blowing and drifting snow in Alpine terrain: numerical simulation and related field measurements, *Ann. Glaciol.*, *26*, 174–178.

Gauer, P. (1999), Blowing and Drifting Snow in Alpine Terrain : A Physically-Based Numerical Model and Related Field Measurements, Swiss Federal Institute of Technology Zurich.

Gauer, P. (1998), Numerical Snow Drift Modeling In Complex Alpine Terrain and Comparison with Field Measurements, in *International Snow Science Workshop*, vol. 41, pp. 60–66, Sunriver, Oregon.

Gordon, M., S. Savelyev, and P. a. Taylor (2009), Measurements of blowing snow, part II: Mass and number density profiles and saltation height at Franklin Bay, NWT, Canada, *Cold Reg. Sci. Technol.*, *55*(1), 75–85, doi:10.1016/j.coldregions.2008.07.001.

Gordon, M., and P. a. Taylor (2009), Measurements of blowing snow, Part I: Particle shape, size distribution, velocity, and number flux at Churchill, Manitoba, Canada, *Cold Reg. Sci. Technol.*, *55*(1), 63–74, doi:10.1016/j.coldregions.2008.05.001.

Grass, A. J. (1971), Structural features of turbulent flow over smooth and rough boundaries, *J. Fluid Mech.*, *50*, 233, doi:10.1017/S0022112071002556.

Greene, E., M. Schneebeli, and K. Elder (2008), Recent Observations of Snow Metamorphism and Microstructure, in *International Snow Science Workshop*, pp. 129–130.

Grinsted, a., J. C. Moore, and S. Jevrejeva (2004), Application of the cross wavelet transform and wavelet coherence to geophysical time series, *Nonlinear Process. Geophys.*, *11*(5/6), 561–566, doi:10.5194/npg-11-561-2004.

Groot Zwaaftink, C. D., M. Diebold, S. Horender, J. Overney, G. Lieberherr, M. B. Parlange, and M. Lehning (2014), Modelling Small-Scale Drifting Snow with a Lagrangian Stochastic Model Based on Large-Eddy Simulations, *Boundary-Layer Meteorol.*, *153*(1), 117–139, doi:10.1007/s10546-014-9934-2.

Groot Zwaaftink, C. D., R. Mott, and M. Lehning (2013), Seasonal simulation of drifting snow sublimation in Alpine terrain, *Water Resour. Res.*, *49*(3), 1581–1590, doi:10.1002/wrcr.20137.

Guala, M., M. Metzger, and B. J. McKEON (2011), Interactions within the turbulent boundary layer at high Reynolds number, *J. Fluid Mech.*, *666*, 573–604, doi:10.1017/S0022112010004544.

Gubler, H. (1981), An electronic remote snow-drift gauge, *J. Glaciol.*, *27*(95).

Guo, L., and N. Huang (2013), Wind tunnel studies on the vertical emission of sand grains from surface, in *AIP Proceedings 1542*, vol. 1087, pp. 1087–1089.

Guyomarc'h, G., and L. Mérindol (1998), Validation of a Forecasting Application of Blowing Snow Periods, *Ann. Glaciol.*, *26*, 138–143.

Guyomarc'h, G., L. Merindol, T. Castelle, F. Sivardiere, and L. Buisson (1994), Blowing snow and avalanches, *Proc. Int. Snow Sci. Work. 1994, Snowbird, Utah*, 211–221.

Harder, P., M. Schirmer, J. W. Pomeroy, and W. Helgason (2016), Accuracy of snow depth estimation in mountain and prairie environments by an unmanned aerial vehicle, *Cryosphere*, *10*(6), 2559–2571, doi:10.5194/tc-10-2559-2016.

Heathershaw, A. D., and P. D. Thorne (1985), Sea-bed noises reveal rol of turbulent bursting phenomenon in sediment transport by tidal currents, *Nature*, *316*, 339–342, doi:10.1038/315279a0.

Helgason, W., and J. W. Pomeroy (2012), Characteristics of the Near-Surface Boundary Layer within a Mountain Valley during Winter, *J. Appl. Meteorol. Climatol.*, *51*(3), 583–597, doi:10.1175/JAMC-D-11-058.1.

Ho, T. D., P. Dupont, A. Ould El Moctar, and A. Valance (2012), Particle velocity distribution in saltation transport, *Phys. Rev. E - Stat. Nonlinear, Soft Matter Phys.*, *85*(5), 1–5, doi:10.1103/PhysRevE.85.052301.

Ho, T. D., A. Valance, P. Dupont, and A. Ould El Moctar (2014), Aeolian sand transport: Length and height distributions of saltation trajectories, *Aeolian Res.*, *12*, 65–74, doi:10.1016/j.aeolia.2013.11.004.

Ho, T. D., A. Valance, P. Dupont, and A. Ould El Moctar (2011), Scaling laws in aeolian sand transport, *Phys. Rev. Lett.*, *106*(9), 4–7, doi:10.1103/PhysRevLett.106.094501.

Horender, S., C. D. Groot Zwaaftink, B. Walter, and M. Lehning (2013), Intermittent drifting snow - combining experimental and model studies., in *Proceedings International Snow Science Workshop*, pp. 104–107, Grenoble Chamonix Mont-Blanc.

Jackson, R. G. (1976), Sedimentological and fluid-dynamic implications of the turbulent bursting phenomenon in geophysical flows, *J. Fluid Mech.*, *77*(3), 531–560, doi:10.1017/S0022112076002243.

Kaftori, D., G. Hetsroni, and S. Banerjee (1995), Particle behavior in the turbulent boundary layer. I. Motion, deposition, and entrainment, *Phys. Fluids*, *5*, 1095–1106, doi:10.1016/S0301-9322(97)88513-8.

Keylock, C. J., K. Nishimura, and J. Peinke (2012), A classification scheme for turbulence based on the velocity-intermittency structure with an application to near-wall flow and with implications for bed load transport, *J. Geophys. Res.*, *117*(F1), F01037, doi:10.1029/2011JF002127.

Kobayashi, D. (1972), Studies of Snow Transport In Low-Level Drifting Snow, *Contrib. from Inst. Low Temp. Sci.*, *A24*, 1–58, doi:10.1017/CBO9781107415324.004.

Kok, J. F., E. J. R. Parteli, T. I. Michaels, and D. B. Karam (2012), The physics of wind-blown sand and dust, *Reports Prog. Phys.*, *75*(10), doi:10.1088/0034-4885/75/10/106901.

Lapen, D. R., and L. W. Martz (1996), An investigation of the spatial association between snow depth and topography in a Prairier agricultural landscape using digital terrain analysis, *J. Hydrol.*, *184*, 277–298.

Lapointe, M. (1992), Burst-like sediment suspension events in a sand bed river, *Earth Surf. Process. Landforms*, *17*, 253–270.

Lavezzo, V., a. Soldati, S. Gerashchenko, Z. Warhaft, and L. R. Collins (2010), On the role of gravity and shear on inertial particle accelerations in near-wall turbulence, *J. Fluid Mech.*, *658*, 229–246, doi:10.1017/S0022112010001655.

Lee, L. W., and L. Wah (1975), Sublimation of Snow In Turbulent Atmosphere, PhD Dissertation, Department of Mechanical Engineering, University of Wyoming.

Leenders, J. K., J. H. van Boxel, and G. Sterk (2005), Wind forces and related saltation transport, *Geomorphology*, *71*, 357–372, doi:10.1016/j.geomorph.2005.04.008.

Lehning, M., V. Ingo, D. Gustafsson, T. A. Nguyen, M. St, and M. Zappa (2006), ALPINE3D : a detailed model of mountain surface processes and its application to snow hydrology, *Hydrol. Process.*, *20*, 2111–2128, doi:10.1002/hyp.

Lelouvetel, J., F. Bigillon, D. Doppler, I. Vinkovic, and J.-Y. Champagne (2009), Experimental investigation of ejections and sweeps involved in particle suspension, *Water Resour. Res.*, *45*(2), doi:10.1029/2007WR006520.

Li, B., and C. McKenna Neuman (2012), Boundary-layer turbulence characteristics during aeolian saltation, *Geophys. Res. Lett.*, *39*(11), 1–6, doi:10.1029/2012GL052234.

Li, L., and L. Martz (1995), Aerodynamic dislodgement of multiple-size sand grains over time, *Sedimentology*, *42*, 683–694.

Li, L., and J. W. Pomeroy (1997), Probability of occurrence of blowing snow, *J. Geophys. Res.*, *102*(D18), 21955–21964, doi:10.1029/97JD01522.

Li, L., and J. W. Pomeroy (1997), Estimates of Threshold Wind Speeds for Snow Transport Using Meteorological Data, *J. Appl. Meteorol.*, *36*, 205–213.

Li, Z., Y. Wang, and Y. Zhang (2014), A numerical study of particle motion and two-phase interaction in aeolian sand transport using a coupled large eddy simulation - discrete element method, edited by S. Dey, *Sedimentology*, *61*(2), 319–332, doi:10.1111/sed.12057.

Libbrecht, K. G. (2005), The physics of snow crystals, *Reports Prog. Phys.*, *68*(4), 855–895, doi:10.1088/0034-4885/68/4/R03.

Liston, G. E., R. L. Brown, and J. Dent (1993), Application of the E-e turbulence closure model to separated atmospheric surface-layer flows, *Boundary-Layer Meteorol.*, *66*(3), 281–301, doi:10.1007/BF00705479.

Liston, G., R. Brown, and J. Dent (1993), A two-dimensional computational model of turbulent atmospheric flows with drifting snow, *Ann. Glaciol.*, *18*, 281–286.

Liston, G. E., R. B. Haehnel, M. Sturm, C. a. Hiemstra, S. Berezovskaya, and R. D. Tabler (2007), Instruments and Methods: Simulating complex snow distributions in windy environments using SnowTran-3D, *J. Glaciol.*, *53*(181), 241–256, doi:10.3189/172756507782202865.

Liu, J., Y. Wang, and B. Yang (2012), Wavelet packet analysis of particle response to turbulent fluctuation, *Adv. Powder Technol.*, *23*(3), 305–314, doi:10.1016/j.apt.2011.04.002.

MacDonald, M. K., J. W. Pomeroy, and A. Pietroniro (2010), On the importance of sublimation to an alpine snow mass balance in the Canadian Rocky Mountains, *Hydrol. Earth Syst. Sci.*, *14*(7), 1401–1415, doi:10.5194/hess-14-1401-2010.

Marchioli, C., and A. Soldati (2002), Mechanisms for particle transfer and segregation in a turbulent boundary layer, *J. Fluid Mech.*, *468*, 283–315, doi:10.1017/S0022112002001738.

Marsh, P. (1999), Snowcover formation and melt: recent advances and future prospects, *Hydrol. Process.*, *13*(February), 2117–2134.

Marsh, P. (1999), Snowcover formation and melt: recent advances and future prospects, *Hydrol. Process.*, *13*, 2117–2134.

Martin, R. L., T. E. Barchyn, C. H. Hugenholtz, and D. J. Jerolmack (2013), Timescale dependence of aeolian sand flux observations under atmospheric turbulence, *J. Geophys. Res. Atmos.*, *118*(16), 9078–9092, doi:10.1002/jgrd.50687.

Matzl, M. et al. (2011), Measuring snow in 3-D using X-ray tomography : assessment of visualization techniques, *Ann. Glaciol.*, *52*(58), 231–236.

Mcelwaine, J. N., N. Maeno, and K. Sugiura (2004), The Splash Function for Snow From Wind-Tunnel Measurements, *Ann. Glaciol.*, *38*, 71–78.

Meehl, G. A. et al. (2007), Global Climate Projections, in *IPCC, 2007: Climate Change 2007*, pp. 747–846.

Mellor, M. (1965), *Cold Regions Science and Engineering, Part III, Section A3c: Blowing Snow*, Hanover, New Hampshire.

Ménard, C. B., R. Essery, and J. W. Pomeroy (2014), Modelled sensitivity of the snow regime to topography, shrub fraction and shrub height, *Hydrol. Earth Syst. Sci.*, *18*(6), 2375–2392, doi:10.5194/hess-18-2375-2014.

Metzger, M., and J. C. Klewicki (2001), A comparative study of near-wall turbulence in high and low Reynolds number boundary layers, *Phys. Fluids*, *13*(3), 692–701, doi:10.1063/1.1344894.

Morris, S. C., S. R. Stolpa, P. E. Slaboch, and J. C. Klewicki (2007), Near-surface particle image velocimetry measurements in a transitionally rough-wall atmospheric boundary layer, *J. Fluid Mech.*, *580*, 319–338, doi:10.1017/S0022112007005435.

Mott, R., M. Schirmer, M. Bavay, T. Grünewald, and M. Lehning (2010), Understanding snow-transport processes shaping the mountain snow-cover, *Cryosph.*, *4*(4), 545–559, doi:10.5194/tc-4-545-2010.

Narasimha, R., and S. V. Kailas (1990), Turbulent bursts in the atmosphere, *Atmos. Environ. Part A, Gen. Top.*, *24*(7), 1635–1645, doi:10.1016/0960-1686(90)90497-B.

Narasimha, R., and S. V. Kailas (1987), Energy Events in the Atmospheric Boundary Layer, , 43.

Narasimha, R., S. V. Kailas, and J. Kaimal (1990), Turbulent Bursts in a Near - neutral Atmospheric Boundary Layer - Part I, , 70.

Nelson, J. M., J. M. Nelson, R. L. Shreve, R. L. Shreve, S. R. McLean, S. R. McLean, T. G. Drake, and T. G. Drake (1995), Role of near-bed turbulence structure in bed load transport, *Water Resour. Res.*, *31*(95), 2071–2086, doi:10.1029/95WR00976.

Nemoto, M., and K. Nishimura (2004), Numerical simulation of snow saltation and suspension in a turbulent boundary layer, *J. Geophys. Res. Atmos.*, *109*(18), doi:10.1029/2004JD004657.

Nemoto, M., K. Nishimura, S. Kobayashi, and K. Izumi (2004), Numerical study of the time development of drifting snow and its relation to the spatial development, *Ann. Glaciol.*, *38*, 343–350, doi:10.3189/172756404781815202.

Nimmo Smith, W., P. Atsavapranee, J. Katz, and T. Osborn (2002), PIV measurements in the bottom boundary layer of the coastal ocean, *Exp. Fluids*, *33*(6), 962–971, doi:10.1007/s00348-002-0490-z.

Nishimura, K., and J. C. R. Hunt (2000), Saltation and incipient suspension above a flat particle bed below a turbulent boundary layer, *J. Fluid Mech.*, *417*, 77–102, doi:10.1017/S0022112000001014.

Owen, P. R. (1964), Saltation of uniform grains in air, *J. Fluid Mech.*, *20*(2), 225, doi:10.1017/S0022112064001173.

Pfeifer, S., and H.-J. Schönfeldt (2012), The response of saltation to wind speed fluctuations, *Earth Surf. Process. Landforms*, *37*(10), 1056–1064, doi:10.1002/esp.3227.

Pomeroy, J. W. (1989), A process-based model of snow drifting, *Ann. Glaciol*, *13*, 237–240.

Pomeroy, J. W., T. Davies, and M. Tranter (1991), The impact of blowing snow on snow chemistry, in *Seasonal Snowpacks*.

Pomeroy, J. W., D. M. Gray, and P. G. Landine (1993), The Prairie Blowing Snow Model : characteristics, validation, operation, *J. Hydrol.*, *144*, 165–192.

Pomeroy, J. W., and D. Gray (1990), Saltation of snow, *Water Resour. Res.*, *26*(7), 1583–1594.

Pomeroy, J. W., and D. H. Male (1992), Steady-state suspension of snow, *J. Hydrol.*, *136*(1–4), 275–301, doi:10.1016/0022-1694(92)90015-N.

Pomeroy, J. W., and D. Male (1987), *Wind transport of seasonal snowcovers*.

Pomeroy, J. W., P. Marsh, and D. Gray (1997), Application of a distributed blowing snow model to the Arctic, *Hydrol. Process.*, *11*, 1451–1464.

Pomeroy, J. W., and D. M. Gray (1995), *Snowcover: Acumulation, Relocation, and Management*, Saskatoon, SK.

Prevel, M., I. Vinkovic, D. Doppler, C. Pera, and M. Buffat (2013), Direct numerical simulation of particle transport by hairpin vortices in a laminar boundary layer, *Int. J. Heat Fluid Flow*, *43*, 2–14, doi:10.1016/j.ijheatfluidflow.2013.03.015.

Raffel, M., C. Willert, J. Kompenhans, Markus Raffel, Christian E. Willert, Steve T. Wereley, and Jürgen Kompenhans (2007), *Particle Image Velocimetry, A Practical Guide*, 2nd Ed., Springer-Verlag.

Rosi, G. a., M. Sherry, M. Kinzel, and D. E. Rival (2014), Characterizing the lower log region of the atmospheric surface layer via large-scale particle tracking velocimetry, *Exp. Fluids*, *55*(5), 10, doi:10.1007/s00348-014-1736-2.

Rotach, M. W., M. Andretta, P. Calanca, A. P. Weigel, and A. Weiss (2008), Boundary layer characteristics and turbulent exchange mechanisms in highly complex terrain, *Acta Geophys.*, *56*(1), 194–219, doi:10.2478/s11600-007-0043-1.

Schmidt, R. A. (1972), *Sublimation of wind-transported snow : a model*, Fort Collins, CO.

Schmidt, R. A. (1982), Vertical Profiles of Wind Speed, Snow Concentration, and Humidity in Blowing Snow, *Boundary-Layer Meteorol.*, *23*, 223–246, doi:10.1016/j.soncn.2013.06.001.

Schmidt, R. A. (1980), Threshold Wind-Speeds And Elastic Impact In Snow Transport, *J. Glaciol.*, *26*(94), 453–467.

Schmidt, R. a., R. Meister, and H. Gubler (1984), Comparison of snow drifting measurements at an alpine ridge crest, *Cold Reg. Sci. Technol.*, *9*(2), 131–141, doi:10.1016/0165-232X(84)90005-3.

Schmidt, R. A., and K. L. Randolph (1981), Prediction Deposition of Blowing Snow in Trenches From particle trajectories, in *Western Snow Conference*, pp. 34–42, St. George, Utah.

Schmidt, R. A., R. Tabler, and R. L. Jairell (1982), A new device for sampling mass flux of blowing snow, in *Proceedings of the Western Snow Conference 1982*.

Schönfeldt, H.-J., and S. von Löwis (2003), Turbulence-driven saltation in the atmospheric surface layer, *Meteorol. Zeitschrift*, *12*(5), 257–268, doi:10.1127/0941-2948/2003/0012-0257.

Sherman, D. J., and E. J. Farrell (2008), Aerodynamic roughness lengths over movable beds: Comparison of wind tunnel and field data, *J. Geophys. Res.*, *113*, 1–10, doi:10.1029/2007JF000784.

Shi, F., and N. Huang (2012), Measurement and simulation of sand saltation movement under fluctuating wind in a natural field environment, *Phys. A Stat. Mech. its Appl.*, *391*(3), 474–484, doi:10.1016/j.physa.2011.08.053.

Soldati, A. (2005), Particles turbulence interactions in boundary layers, *Zamm*, *85*(10), 683–699, doi:10.1002/zamm.200410213.

Sommerfeld, R. A., and E. LaChapelle (1970), The Classification of Snow Metamorphism, *J. Glaciol.*, *9*(55), 3–17.

Sørensen, M. (1997), On the effect of time variability of the wind on rates of aeolian sand transport, *Aarhus Geosci.*, *7*, 73–77.

Spies, P.-J., I. K. McEwan, and G. R. Butterfield (2000), One-dimensional transitional behaviour in saltation, *Earth Surf. Process. Landforms*, *25*(5), 505–518, doi:10.1002/(SICI)1096-9837(200005)25:5<505::AID-ESP78>3.0.CO;2-D.

Spies, P.-J., and I. K. McEwan (2000), Equilibration of saltation, *Earth Surf. Process. Landforms*, *25*(4), 437–453, doi:10.1002/(SICI)1096-9837(200004)25:4<437::AID-ESP69>3.0.CO;2-5.

Sterk, G., a. F. G. Jacobs, and J. H. Van Boxel (1998), The effect of turbulent flow structures on saltation sand transport in the atmospheric boundary layer, *Earth Surf. Process. Landforms*, *23*(10), 877–887.

Sterk, G., J. Van Boxel, and R. Zuurbier (2002), Interactions between turbulent wind flow and saltation sand transport, *Proc. ICAR5/GCTE– …*, 63–65.

Stiperski, I., and M. W. Rotach (2015), On the Measurement of Turbulence Over Complex Mountainous Terrain, *Boundary-Layer Meteorol.*, (Barry 2008), doi:10.1007/s10546-015-0103-z.

Stout, J., and T. Zobeck (1997), Intermittent saltation, *Sedimentology*, *44*, 959–970.

Takeuchi, M. (1980), Vertical profile and horizontal increase of drift snow transport, *J. Glaciol*, *26*(94).

Thomas, C., and T. Foken (2004), Detection of long-term coherent exchange over spruce forest using wavelet analysis, *Theor. Appl. Climatol.*, *80*(2–4), 91–104, doi:10.1007/s00704-004-0093-0.

Thorpe, A. D., and B. J. Mason (1966), The evaporation of ice spheres and ice crystals, *Br. J. Appl. Phys.*, *17*(4), 541, doi:10.1088/0508-3443/17/4/316.

Toloui, M., S. Riley, J. Hong, K. Howard, L. P. Chamorro, M. Guala, and J. Tucker (2014), Measurement of atmospheric boundary layer based on super-large-scale particle image velocimetry using natural snowfall, *Exp. Fluids*, *55*(5), 14, doi:10.1007/s00348-014-1737-1.

Uematsu, T., T. Nakata, K. Takeuchi, Y. Arisawa, and Y. Kaneda (1991), Three-dimensional numerical simulation of snowdrift, *Cold Reg. Sci. Technol.*, *20*(1), 65–73, doi:10.1016/0165-232X(91)90057-N.

van Boxel, J. ., G. Sterk, and S. . Arens (2004), Sonic anemometers in aeolian sediment transport research, *Geomorphology*, *59*(1–4), 131–147, doi:10.1016/j.geomorph.2003.09.011.

van Hout, R., W. Zhu, L. Luznik, J. Katz, J. Kleissl, and M. B. Parlange (2007), PIV Measurements in the Atmospheric Boundary Layer within and above a Mature Corn Canopy. Part I: Statistics and Energy Flux, *J. Atmos. Sci.*, *64*(8), 2805–2824, doi:10.1175/JAS3989.1.

Vionnet, V., E. Martin, V. Masson, G. Guyomarc'h, F. Naaim-Bouvet, A. Prokop, Y. Durand, and C. Lac (2014), Simulation of wind-induced snow transport and sublimation in alpine terrain using a fully coupled snowpack/atmosphere model, *Cryosph.*, *8*(2), 395–415, doi:10.5194/tc-8-395-2014.

Wiggs, G. F. S., and C. M. Weaver (2012), Turbulent flow structures and aeolian sediment transport over a barchan sand dune, *Geophys. Res. Lett.*, *39*(5), 1–7, doi:10.1029/2012GL050847.

Willetts, B. B., J. McEwan, and M. A. Rice (1991), Initiation of motion of quartz sand grains, *Acta Mech.*, *1*, 123–134.

Winstral, A., D. Marks, and R. Gurney (2013), Simulating wind-affected snow accumulations at catchment to basin scales, *Adv. Water Resour.*, *55*, 64–79, doi:10.1016/j.advwatres.2012.08.011.

Xiao, J., R. Bintanja, and S. Déry (2000), An intercomparison among four models of blowing snow, *Boundary-Layer Meteorol.*, *97*, 109–135.

Xuan, J. (2004), Turbulence factors for threshold velocity and emission rate of atmospheric mineral dust, *Atmos. Environ.*, *38*(12), 1777–1783, doi:10.1016/j.atmosenv.2003.12.030.

Zhang, W., J. Kang, and S. Lee (2007), Visualization of Saltating Sand Particle Movement near a Flat Ground Surface, *J. Vis.*, *10*(1), 39–46.

Zhang, W., Y. Wang, and S. J. Lee (2008), Simultaneous PIV and PTV measurements of wind and sand particle velocities, *Exp. Fluids*, *45*(2), 241–256, doi:10.1007/s00348-008-0474-8.

Zhang, W., Y. Wang, and S. J. Lee (2007), Two-phase measurements of wind and saltating sand in an atmospheric boundary layer, *Geomorphology*, *88*(1–2), 109–119, doi:10.1016/j.geomorph.2006.10.017.

CHAPTER 2
SALTATING SNOW MECHANICS: THREE-SPECIES CLASSIFICATION FROM HIGH SPEED VIDEOGRAPHY

ABSTRACT

The current understanding of blowing snow transport is derived from coupling time-averaged measurements of particle saltation and suspension with nearby wind measurements. Recently, two-phase aeolian flow studies have benefited from high frequency turbulence measurements and particle tracking, allowing a deeper comprehension of particle flow dynamics. However, these sand-based transport observations cannot be directly adopted for saltating snow because they assume an underlying bed of discrete particles and so neglect the bonds and structural metamorphism unique to snow crystal matrix structures. To examine the potential distinctive nature of snow saltation, this study employs laser illuminated high-speed videography and ultrasonic anemometry to examine snow transport over a natural snowpack in detail. A saltating snow measurement site was established at the Fortress Mountain Snow Laboratory, Alberta, Canada and instrumented with two Campbell CSAT3 ultrasonic anemometers sampling at 50 Hz and a two-dimensional Particle Tracking Velocimetry (PTV) system. The experiment has demonstrated the applicability of PTV methods to outdoor environments for blowing snow studies. A three species sub-classification of saltation from blowing sand studies allows for description of overlooked snow transport and initiation processes. However, complex behaviour that is specific to blowing snow such as the tumbling and disintegration of aggregate snow crystals, which eject smaller grains and feed disintegrating grains into the atmosphere has also been documented, complicating direct sand subspecies application. This unique avenue of data informs a new conceptualization of saltating snow transport mechanisms.

This manuscript has been modified for inclusion in this thesis. It was originally published as: Aksamit, N., and J. W. Pomeroy (2015), Saltating Snow Mechanics: Three-Species Classification from High Speed Videography, in *Proceedings of the 72nd Eastern Snow Conference*.

2.1 Introduction

Wind transport of snow influences the variability of alpine summer runoff (Winstral et al., 2013), is a large contributor to the growth or ablation of small mountain glaciers (Dyunin and Kotlyakov, 1980), and affects snow stability for avalanche forecasting (Schweizer et al., 2003). Blowing snow field measurements often present an oversimplified view of the stochastic natural phenomenon. Trap mechanisms such as snow socks provide averaged mass flux measurements over a prolonged collection period and therefore little possibility to relate fluxes to turbulence, whereas snow particle counters provide little to no information about what type of particle is in transport or its trajectory and velocity (Kinar and Pomeroy, 2015). Neither device elicits information about individual particle transport mechanics. As such, currently only a basic understanding of blowing snow exists with a lack of detailed particle velocity observations.

Kobayashi (1972) pioneered blowing snow recordings with outdoor, 1/8-second shutter speed images. This was the first visual evidence of particle mechanics in the snow saltation layer, but the photographs consisted of blurred snow particle streaks or were saturated with particles, leaving many unanswered questions (Figure 2-3). Gromke et al. (2014) and Lü et al. (2012) utilized faster frame rates in recent years but were limited to wind tunnels for their blowing snow studies and were not focused on the mechanics of transport.

Current theory represents blowing snow in two layers, saltation and suspension with a poorly understood creep mechanism recognised at the lower boundary of saltation (Pomeroy and Gray, 1990). Saltating particles are thought to exist below 20 cm and follow ballistic trajectories, rebounding off the ground. Suspended particles begin in saltation and disperse upwards. Closely following wind streamlines, suspended snow particles rarely encounter the ground (Pomeroy and Male, 1992).

Two proposed modes of saltation initiation are *aerodynamic lift*, the direct drag-induced ejections of grains, and *splash*, the ejection of grains by rebounding saltating particles (Doorschot and Lehning, 2002). However there are substantial uncertainties about these mechanisms; Schmidt (1986) showed that direct aerodynamic lift was not possible under average flow conditions over a level snow surface due to strong snow particle bonding. Subsequently, Pomeroy (1988) showed that lower saltation threshold (initiation) wind speeds due to splash

could not be observed in the field and was unable to relate threshold wind speeds to physical properties of the snowpack such as hardness and density. As a result, these two modes of initiation have not been parameterized in saltating snow models (Pomeroy and Gray, 1990) and empirical techniques have been required to account for crystal bond strength effects on threshold conditions for snow transport and saltation efficiency (Li and Pomeroy, 1997a; Pomeroy and Li, 2000). However, few blowing snow transport studies have focused on direct measurements within the first 10 cm above the snow surface, the region responsible for rebound and ejection dynamics.

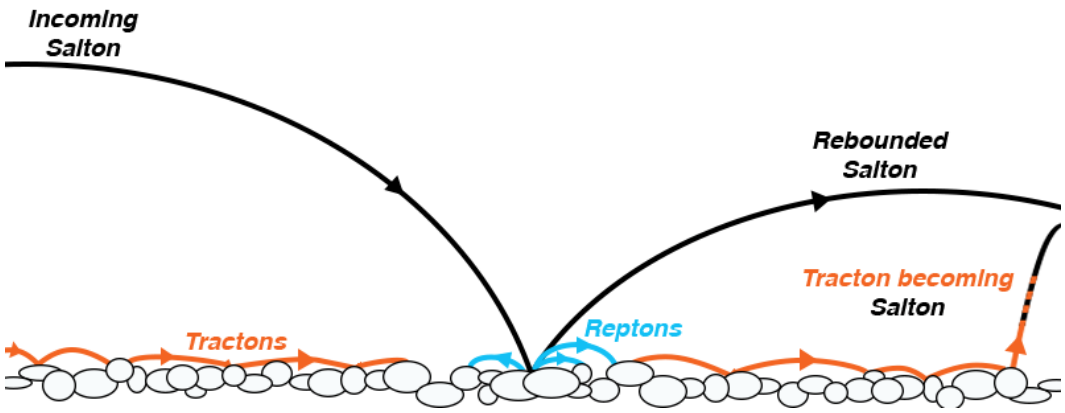

Figure 2-1: Schematic of three species of motion: Reptons, Saltons, and Tractons

While Anderson and Haff (1988) utilized a computationally expensive continuous spectrum of particle motion in a two-phase saltating sand model, recent sand saltation research has highlighted a variety of distinct transport modes for saltating particles. Andreotti (2004) introduced a simple conceptual three species classification of saltating sand particles, which was implemented by Lämmel et al. (2012) into a more economical saltation model. In this model particles are distinguished by kinetic energy rather than physical properties such as grain size. These saltation particle species are saltons, reptons, and tractons (Figure 2-1).

High-energy saltons are particles that impact the surface with great momentum, rebounding and ejecting lower-energy reptons into motion. Reptons are particles gaining fewer than several grain diameters in height above the snow surface upon ejection, existing for only one

hop. Tractons, also known as creeping particles, roll and tumble across the surface, bouncing along the way. Tractons that gain sufficient kinetic energy bounce higher into saltation, becoming further accelerated by the wind. Saltons often begin motion as reptons or tractons (Willets et al., 1991), and are reclassified upon acceleration.

At sufficiently high wind speeds, splash is known to be exponentially more effective at entraining sand particles than wind drag alone (Willetts et al., 1991). The transition to a splash dominated snow initiation regime and the role of crystal cohesive forces is not yet well understood. Additionally, the role of tractons and reptons in initiation of snow transport has not yet been investigated in detail and may play a crucial role in setting transport threshold wind speeds.

To improve the physical theory governing snow erosion, transport and deposition in a turbulent boundary layer, this study focussed on the short timescale mechanisms of snow saltation initiation and transport in order to examine variability in snow surface impact mechanics for natural meteorological and snow surface conditions. To accomplish this a unique field research campaign was designed to measure 3D wind velocity and individual snow particle velocities at frequencies of 50 and 1000 Hz, respectively. In doing so, the approach introduces high-speed laser-light illuminated videography to an alpine setting and to the outdoor study of blowing snow particle motion.

2.2 Study site and methods

Fieldwork was conducted from February to April, 2015 at the Fortress Mountain Snow Laboratory (FMSL), Kananaskis Valley, Alberta, Canada. FMSL is home to several well-instrumented high-altitude, wind-swept observation sites. Meteorological stations include precipitation and standard measurements, as well as specialized eddy correlation, and acoustic and dielectric snow water equivalent measurement systems. The area is topographically interesting in that there is access to relatively flat terrain, a modest ridgeline and very pronounced steep slopes.

The blowing snow site (2000m A.S.L.) is located in a clear-cut base area of the Fortress Mountain ski area. The area was lightly used, allowing for clear upwind fetch, with a moderate

ridge flanking the west. The ground was snow covered and shrub vegetation buried for the duration of the experiment with snow depths fluctuating from 70 to 120 cm. The measurement location was equipped with two Campbell Scientific CSAT3 three-dimensional ultrasonic anemometers positioned at varying heights on a single mast. The anemometers were typically situated 40 and 200 cm above the snow surface, though heights varied during snow accumulation and wind erosion events. The anemometer heights were reset once during the field campaign due to snowfall burying the lower instrument.

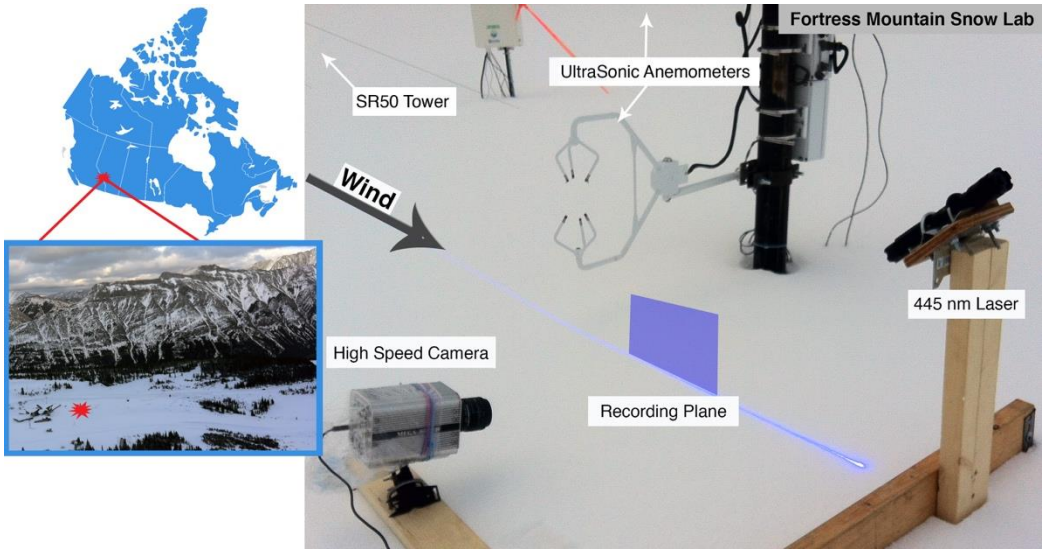

Figure 2-2: Field Site Location and High Speed Videography Setup

The most unique aspect of this experiment was the implementation of high-speed videography for nighttime particle tracking observations. A rigid frame equipped with a Megaspeed MS85K high-speed camera and a 445 nm wavelength 1.5-Watt continuous-wave laser was placed on the snow surface, typically 1 m downwind from the anemometer mast. The frame sat flush on the snow allowing the camera a nearly tangent view of the surface, perpendicular to the flow of saltating particles. Laser light was projected through a cylindrical lens to create a 2 mm wide plane orthogonal to both the snow surface and the view of the camera (Figure 2-2). The light plane was oriented in the direction of the prevailing winds, such that the plane illuminated saltating snow particles and allowed recordings in the lowest 10 cm of the atmosphere with minimal foreground shadowing and background reflection.

The camera was controlled by a laptop located downwind in a nearby portable office trailer. Nighttime campaigns typically lasted from four to eight hours over a variety of wind directions. A wide spectrum of snow crystal types was imaged, sometimes changing during the course of one night. At the beginning of each recording session, the camera and data logger timestamps were synchronized to minimize drift for future analysis.

The resolution of the images captured by the MS85K varied depending on snow conditions and particle behaviour. Typical resolutions allowed a recorded region of interest averaging 30 mm x 120 mm. Frame rates varied from 870 to 1300 FPS depending on the selected image resolution. The frames rates possible in this campaign have not previously been achieved in blowing snow field research and are critical for observing the natural mechanics of particle ejection and saltation. This non-intrusive method of observation also allows measurements in the lowest mm of the atmosphere, a region typically impossible to monitor with snow particle counters.

One major complication for 2D recordings is the inherently three-dimensional nature of turbulence. Though positioned with respect to the prevailing wind, particle motion did not always stay parallel to the laser light sheet. As well, wind direction would change throughout a night of recordings. This necessitated the rigid frame to be portable to allow reorientation of the laser into the wind.

Particle Tracking Velocimetry (PTV) provides measurements of snow particle velocities by way of tracking algorithms that match individual particles in subsequent frames imaged by a high-speed camera. Calculations must then be made to convert pixels to the mm displacement of each particle. In this study, the laser light plane creates a two-dimensional projection of saltation preventing the need for additional cameras and three-dimensional displacement calculations. Knowing the time step between pairs of frames then allows sparse velocity vector field creation.

DaVis 8 software by LaVision calculated PTV vector fields to quantify the blowing snow subprocesses displayed in the high-speed recordings. PTV, and Velocimetry in general, is most often used for wind tunnel studies, with few applications, in any discipline, in an outdoor environment (e.g. Rosi et al., 2014; Zhu et al., 2007). This is the first known application of PTV for boundary-layer blowing snow studies in a natural environment.

2.3 Observations

The high-speed saltation recordings provide a degree of clarity of particle motion impossible to attain at lower frame rates or without the use of 2D laser illumination (i.e. Kobayashi, 1972). As the camera was focused close to the snow surface, hundreds of thousands of rebound and splash events were recorded over the season. Video was later reviewed with playback reduced 100 times, providing insight to the mechanics of saltating particle motion and bed interactions.

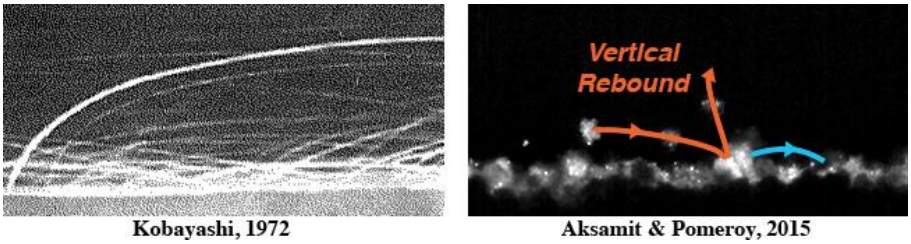

Figure 2-3: 1/8 s exposure Kobayashi image and vertical rebound diagram overlaid on 21:38 Mar 23, 2015 particle images

For example, it has been speculated as to the source of vertical ejections of snow particles from the surface as seen in Kobayashi's photographs (Figure 2-3). The vast majority of vertical trajectories in this measurement campaign are easily ascribed to particles rebounding off the complex and rough snow surface at odd angles while reptating, tractating or in saltation (Figure 2-3). Vertical aerodynamic lift of snow particles as suggested by Doorschot and Lehning (2002) was not evident.

Many classic sand saltation models rely heavily on grain diameter based statistics. Adapting these ideas to snow is problematic as identifying snow particle size is inherently subjective because the snowpack is not a bed of distinct grains. Snow is a matrix with an ice crystal lattice structure that must be shattered to produce measureable grains (Schmidt, 1982). In addition, snow particles are often non-spherical and are sintered during transport due to impact and ablated due to sublimation. Over the course of this field campaign, the applicability of diameter-based theories was challenged as particle size was found to be an extremely dynamic characteristic. Focussing exclusively in the first 30 mm above the surface, the present observations

challenge the classic entrainment framework, showing that a new conceptual model including subcategories of saltation and additional initiation sub-processes should be considered.

The nights of February 5 and 11 provided fresh, warm (~ 0°C) concurrent snowfall with large (~ 5 mm diameter) aggregate crystals and moderate 6 ms^{-1} wind speeds at 0.4 m height. Both nights of recording spanned four hours, providing ample evidence of large snow particles tumbling as tractons, resembling tumbleweeds – something not observed in other aeolian materials. Their relatively large mass contributed to ejecting many smaller grains into reptation and saltation upon impact (Figure 2-4). After gaining sufficient momentum, the large particles fractured into smaller crystals, themselves ejecting into saltation. This does not fit the Doorschot and Lehning (2002) "splash versus entrainment" theory of initiation and does not allow for permanent definitions of particle size.

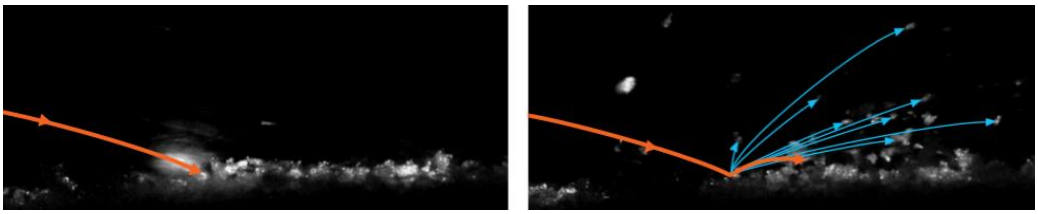

Figure 2-4: Splash and Inbound Salton Collapse. Timestep 11.4 ms, Feb 5, 2015 21:22

In agreement with Willetts et al. (1991), all recordings show many saltons beginning motion as reptons and tractons. While rolling on the uneven snow surface, tractons may bounce into saltation after impacting a well-lodged particle and quickly accelerate from wind drag as they rise above the surface (Figure 2-1 & 2-3). Extensive review of the field recordings suggests particles accelerating out of an active creep layer are needed as a third component of initiation in blowing snow theories. Reptons and tractons provide an efficiently entrained source of blowing snow particles as they have already broken their snow surface bonds and supply their own momentum prior to vertical ejection. This lowers the drag forces necessary for tracton and repton entrainment, all the while the stationary bed concurrently undergoes classic aerodynamic drag and splash initiation.

Particle flow observations of different snow crystal types provided insights into the variable nature of snow saltation mechanics, sometimes closely resembling blowing sand theory,

but other times diverging in important ways. In contrast to sand, snow saltation initiation and rebound changed dramatically as snow particles shattered, sintered and sublimated and the snow surface hardened. The elasticity of blowing snow particles and ability of the snow surface to absorb momentum upon impact appeared to change substantially over a two-hour span of recordings on April 1 (Figure 2-5). Over this period, 0.4 m wind speeds varied from 0 to 8.6 ms^{-1}, with a mean of 1.4 ms^{-1}, resulting in a decrease in blowing snow particle size. Eventually a hard wind crust masking an old radiation crust was revealed by the next day.

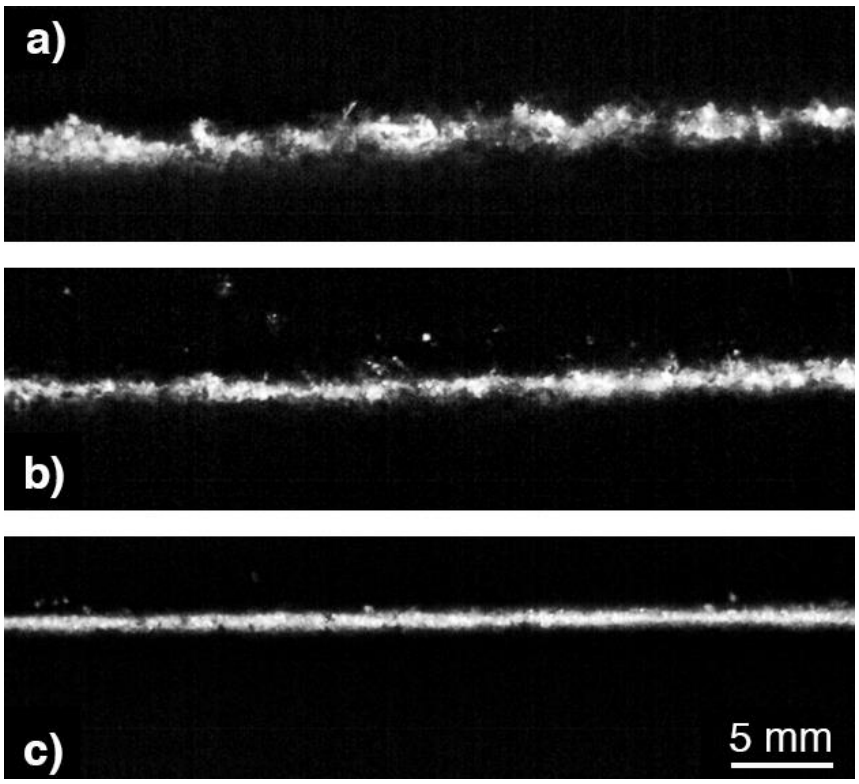

Figure 2-5: Reducing surface roughness and particle size on April 1, 2015

Figure 2-5 exhibits wind conditioning of the saltating and surface snow crystals shortly after cessation of snowfall at precisely the same location over a 105-minute period beginning 20:15. Frame 'a)' displays initial conditions with large fresh stellar crystals and a rough snow surface with many exposed snow crystal structures. The subsequent frame 'b)' is five minutes later, after 2.44 ms^{-1} 0.4 m wind speed, showing a variety of sizes of sintering and shattering grains in motion and a relatively smoother snow surface. Frame 'c)' was captured after 100 more minutes

elapsed, exhibiting mostly small, rounded snow grains in saltation and a much smoother surface. The wind-scoured snow surfaces upwind contained a low percentage of loose grains available to be dislodged, greatly reducing the effectiveness of splash actions. This left many saltons rebounding out of frame without ejecting any reptons or tractons, effectively reducing the particle number concentration. As well, there was an obvious change in surface roughness.

Li and Pomeroy (1997b) documented trends similar to the snow surface evolution on April 1 and developed a probability function of blowing snow transport that depends on wind hardening. In the present data set, the average threshold velocity did not appear to increase as particles are still in transport at relatively low wind speeds. A decrease in number concentration with increasing wind speed appears to be a more physically accurate description of the April 1 trend and is consistent with the Li and Pomeroy (1997b) theory of reduced probability of transport with wind hardening.

This temporal evolution of entrainment and transport dynamics cannot be ascribed to particle diameter alone as evolving bed structures played a significant role. As well, the April 1 two-hour transition in grain size was relatively quick compared with other nights of recording exhibiting no apparent change in particle size. This reveals more variability in blowing snow dynamics that may be snow type or even storm specific. Further research into wind hardening and slab formation may elucidate the evolution of grain availability for blowing snow.

2.4 Analysis

The recordings allow visual qualitative analysis of blowing snow processes previously invisible to researchers, and the ability to quantify individual 2D projected particle velocities over a variety of time scales through PTV. Certain particle behaviour trends reappear in all PTV conducted for the February-April field campaign. Example PTV data calculated from March 23 recording #6 is displayed in Figure 2-6. The saltating snow consisted of graupel-like spherical grains with a mean 0.4 m wind speed of 4.78 m s^{-1}. The recording comprises 16,000 frames spanning 13 seconds of continuous transport in non-constant winds beginning 21:38. For clarity, the vector field displayed was calculated from only 4 seconds of recorded video. The highlighted

green area indicates an uneven region of surface topography providing unreliable statistics for particle motion.

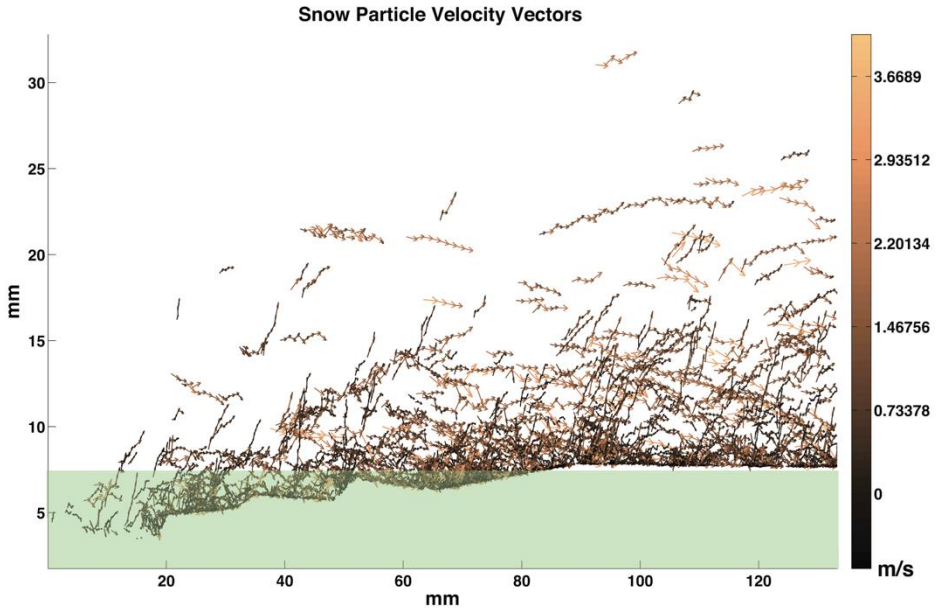

Figure 2-6: Sparse Snow Particle Velocity Vector Field from recording 3-23 #6. The green area indicates an uneven region of surface topography providing unreliable statistics for particle motion.

When comparing regions above and below 10 mm, the vector field visualization (Figure 2-6) shows the relatively high concentration of particles near the surface. Figure 2-7 further corroborates this observation. The left graph shows the percentage of total particles $P_z = \frac{n_z}{\sum_z n_z}$, where n_z is the number of particles identified in a horizontal 0.1 x 130 mm slice at height z. The right graph shows the influence of increasing particle velocity with height on particle flux. At a given height z, the percentage of particle flux F_z was calculated as

$$\boldsymbol{F_z} = \frac{\boldsymbol{n(z)} * \boldsymbol{u_p(z)}}{\sum_{\boldsymbol{z}}(\boldsymbol{n(z)} * \boldsymbol{u_p(z)})} \tag{2-1}$$

where v_z is the average velocity at height z. The highlighted green region is consistent in Figures 2-6, 2-7 and 2-8. For the 3-23 #6 recording, the percentage of particles approaches zero above $z = 15mm$ whereas in the flux profile, concentrations are notable until $z = 20mm$. In both plots of Figure 2-7, the maximum exists immediately above the unmoving snow surface.

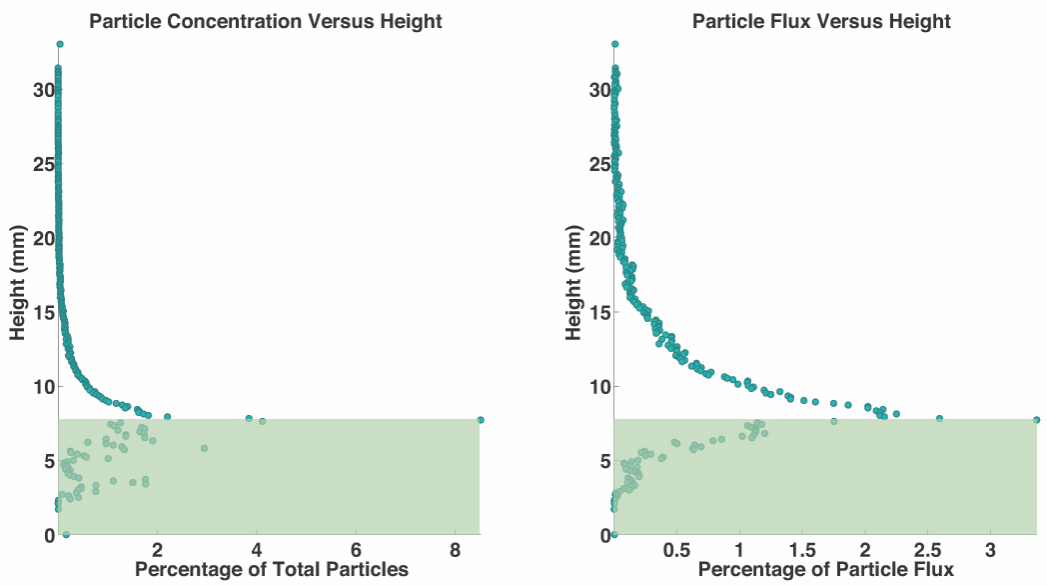

Figure 2-7: Snow Concentration Profiles for 0.1mm slices from 3-23 #6

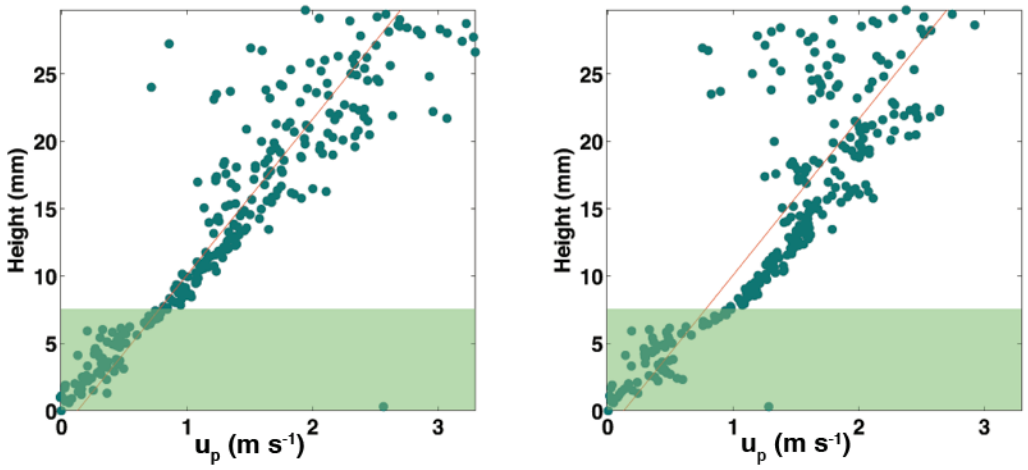

Figure 2-8: Velocity Profiles for 3-23 #6. Left: Ascending Particles. Right: Ascending and Descending

Figure 2-8 consists of mean velocity profiles for ascending particles (left) and both ascending and descending grains (right). Heights of $7 < z < 10\ mm$ consists of saltons at either the beginning or end of a ballistic trajectory, as well as the reptons and tractons. This 3 mm thick layer contains 50% of total particles tracked, but constitutes only 10% of the layer of investigation. The number of low-energy particles with velocities $u_p < 0.75\ ms^{-1}$ vastly outweighs the number

of high-energy saltons in this region, contributing 70% of particle velocities calculated. For the layer $z > 15mm$ particles with velocities $u_p > 1.5\ ms^{-1}$ constitute 70% of particles tracked. This shows a transition in both particle number density and particle motion mechanics within a 20 mm thick layer.

There is general agreement between the shape of velocity profiles for the ascending and total particle plots in Figure 2-8. Deviations from characteristic profiles are found in the layers influenced by microtopography, and in the lower density upper salton layer. There is a tight fit to the characteristic profile in the layer $7 < z < 15\ mm$ though noticeably more linear for ascending particles. This is consistent with particles being ejected from the surface with an initially small horizontal velocity that increases linearly with jump height and therefore transport-time. The linear fit could also be attributed to a layer of constant shear stress ($du/dz = \alpha$) and momentum transfer by the wind immediately above the surface. The layer of tight fit below 15 mm coincides with high particle concentrations. The velocity of grains in this layer provide less variance from mean profile values and show the strong prevalence of tracton and repton motion over saltons, whereas upper regions appear to be more influenced by turbulence.

2.5 Discussion

The existence of creeping snow particles has been previously recognized but neither their importance nor prevalence was understood (Gauer, 1998). Several common traits in snow particle motion, previously neglected in blowing snow literature, were found in this study. Three species of motion were distinguished in saltating snow. Salton, repton, and tracton behaviours were evident in the majority of recordings, regardless of snow crystal size and shape. The prevalence of low energy particles was further corroborated by initial PTV analysis. Thus far, creeping particles have been largely overlooked as a source of saltation initiation, mass transport and wind momentum deficit. At the wind speeds observed, blowing snow particle density has been found to be highest in the lowest 15 mm of the saltation layer. The significant proportion of moving particles that reptons and tractons constitute in this layer suggests they may indeed play a critical role in snow saltation dynamics.

Including reptons could also present an improvement to wind components of two-phase snow saltation models. Classical single trajectory models of saltation assume a uniform trajectory in the saltation layer (e.g. Pomeroy and Gray, 1990) and force an unstable or non self-consistent momentum transfer from wind to particles (Andreotti, 2004). Utilizing reptons in a two-species model allowed Lämmel et al. (2012) to achieve a stable wind momentum deficit during saltation. As well, repton creation helps balance the reduced velocity of a rebounding salton. These momentum balances have not been investigated for blowing snow.

The large concentration of slow moving grains in the first 3 mm above the snow surface has not been previously measured and likely impacts the lower boundary condition for wind flow. For instance, the no-slip assumptions for momentum transfer calculations may need to be re-evaluated to better represent the snow surface as a porous wall under a dense moving bed of particles during saltation. Tractation and reptation motions are responsible for breaking most snow surface bonds, but how they break these bonds is not yet known. Neither of these issues have been investigated for snow saltation.

Over the course of the field campaign, some snow particle trajectories exhibited classic sand-like behaviour. However, when enormous aggregate crystals, decomposing grains, and mixed grain types were present, particle behaviour unique to snow was exhibited. Further observations will show to what degree saltating snow can be described using saltating sand-like motions. New blowing snow particle motion descriptions may also need to be considered.

2.6 Conclusions

For the first time, high-speed video employed outdoors has been used to investigate the motion of saltating snow in great detail. Over short timescales, snow particle behaviour appears to be influenced by complex initiation and rebound dynamics, including reptation and tractation, which have not previously been described for snow. The ability of the snow surface to absorb impact momentum into the bed, or through repton and tracton generation, and the elasticity of particles were all found to be temporally variable and heavily dependent on snow crystal type. Sintering, shattering, and sublimation of saltating snow particles appear to be factors influencing mass flux and turbulent momentum transfer that should be further investigated.

The first environmental PTV computations for snow have proven to be a viable avenue for exploring complex wind-snow interactions at millisecond timescales. Initial results have supported a new three species conceptual model of snow saltation, though exact initiation and rebound dynamics are dependent on snow crystal characteristics. PTV shows potential to solve many unanswered problems in blowing snow research allowing quantification of energy dispersal in very near surface particle motion. In addition, the high temporal resolution measurements may prove useful in future work for understanding the turbulent influences on blowing snow processes.

Key Points for Next Chapters

- What are the impacts of a dense creep layer on particle transport velocities and concentrations?
- Can one quantify the evolving initiating mechanisms during the onset of a wind gust?
- Can one characterize different responses of particle saltation under varying wind conditions?

2.8 Acknowledgements

The authors wish to acknowledge field assistance from students and staff of the Centre for Hydrology, often in very inclement conditions. Financial assistance from NSERC through the Changing Cold Regions Network, Research Tools and Instruments and Discovery grants programme, the Canada Research Chair and Canada Excellence Research Chairs programme, the Canada Foundation for Innovation, and Alberta Environment and Sustainable Resource Management is gratefully acknowledged. Fortress Mountain Resort is thanked for their support of snow science and particularly this study.

2.9 References

Anderson, R. S., and P. K. Haff (1988), Simulation of eolian saltation., *Science*, *241*(4867), 820–3, doi:10.1126/science.241.4867.820.

Andreotti, B. (2004), A two species model of aeolian sand transport, *J. Fluid Mech.*, *510*, 47–70.

Bagnold, R. A. (1941), *The Physics of Blown Sand and Desert Dunes*, 1st ed., Methuen & Co. Limited, London.

Doorschot, J., and M. Lehning (2002), Equilibrium saltation: mass fluxes, aerodynamic entrainment, and dependence on grain properties, *Boundary-layer Meteorol.*, *104*, 111–130.

Dyunin, A. K., and V. Kotlyakov (1980), Redistribution of snow in the mountains under the effect of heavy snow-storms, *Cold Reg. Sci. Technol.*, *3*, 287–294.

Gauer, P. (1999), Blowing and Drifting Snow in Alpine Terrain : A Physically-Based Numerical Model and Related Field Measurements, Swiss Federal Institute of Technology Zurich.

Gromke, C., S. Horender, B. Walter, and M. Lehning (2014), Snow particle characteristics in the saltation layer, *J. Glaciol.*, *60*(221), 431–439, doi:10.3189/2014JoG13J079.

Kinar, N. J., and J. W. Pomeroy (2015), Measurement of the physical properties of the snowpack, *Rev. Geophys.*, *53*, doi:10.1002/2015RG000481.

Kobayashi, D. (1972), Studies of Snow Transport In Low-Level Drifting Snow, *Contrib. from Inst. Low Temp. Sci.*, *A24*, 1–58, doi:10.1017/CBO9781107415324.004.

Lämmel, M., D. Rings, and K. Kroy (2012), A two-species continuum model for aeolian sand transport, *New J. Phys.*, *14*, 24, doi:10.1103/PhysRevLett.83.5170.

Li, L., and J. W. Pomeroy (1997), Probability of occurrence of blowing snow, *J. Geophys. Res.*, *102*(D18), 21955–21964, doi:10.1029/97JD01522.

Li, L., and J. W. Pomeroy (1997), Estimates of Threshold Wind Speeds for Snow Transport Using Meteorological Data, *J. Appl. Meteorol.*, *36*, 205–213.

Lü, X., N. Huang, and D. Tong (2012), Wind tunnel experiments on natural snow drift, *Sci. China Technol. Sci.*, *55*(4), 927–938, doi:10.1007/s11431-011-4731-3.

Pomeroy, J. W. (1988), Wind transport of snow, University of Saskatchewan.

Pomeroy, J. W., and D. Gray (1990), Saltation of snow, *Water Resour. Res.*, *26*(7), 1583–1594.

Pomeroy, J. W., and L. Li (2000), Prairie and Arctic areal snow cover mass balance using a blowing snow model, *J. Geophys. Res. …*, *105*(D21), 26619–26634.

Pomeroy, J. W., and D. H. Male (1992), Steady-state suspension of snow, *J. Hydrol.*, *136*(1–4), 275–301, doi:10.1016/0022-1694(92)90015-N.

Rosi, G. a., M. Sherry, M. Kinzel, and D. E. Rival (2014), Characterizing the lower log region of the atmospheric surface layer via large-scale particle tracking velocimetry, *Exp. Fluids*, *55*(5), 10, doi:10.1007/s00348-014-1736-2.

Schmidt, R. A. (1986), Transport Rate of Drifting Snow and the Mean Wind Speed Profile, *Boundary-Layer Meteorol.*, *34*, 213–241.

Schmidt, R. (1982), Properties of Blowing Snow, *Rev. Geophys. Sp. Phys.*, *20*(1), 39–44.

Schweizer, J., B. Jamieson, and M. Schneebeli (2003), Snow avalanche formation, *Rev. Geophys.*, *41*(4), doi:10.1029/2002RG000123.

Willetts, B. B., J. McEwan, and M. A. Rice (1991), Initiation of motion of quartz sand grains, *Acta Mech.*, *1*, 123–134.

Winstral, A., D. Marks, and R. Gurney (2013), Simulating wind-affected snow accumulations at catchment to basin scales, *Adv. Water Resour.*, *55*, 64–79, doi:10.1016/j.advwatres.2012.08.011.

Zhu, W., R. van Hout, and J. Katz (2007), PIV Measurements in the Atmospheric Boundary Layer within and above a Mature Corn Canopy. Part II: Quadrant-Hole Analysis, *J. Atmos. Sci.*, *64*(8), 2825–2838, doi:10.1175/JAS3990.1.

CHAPTER 3
NEAR-SURFACE SNOW PARTICLE DYNAMICS FROM PARTICLE TRACKING VELOCIMETRY AND TURBULENCE MEASUREMENTS DURING ALPINE BLOWING SNOW STORMS

Abstract

Many blowing snow conceptual and predictive models have been based on simplified two-phase flow dynamics derived from time-averaged observations of bulk flow conditions in blowing snow storms. Measurements from the first outdoor application of Particle Tracking Velocimetry (PTV) of near-surface blowing snow yields new information on mechanisms for blowing snow initiation, entrainment, and rebound, whilst also confirming some findings from wind tunnel observations. Blowing snow particle movement is influenced by complex surface flow dynamics, including saltation development from creep that has not previously been measured for snow. Comparisons with 3D atmospheric turbulence measurements show that blowing snow particle motion immediately above the snow surface responds strongly to high frequency turbulent motions. Momentum exchange from wind to the dense near-surface particle-laden flow appears significant and makes an important contribution to blowing snow mass flux and saltation initiation dynamics. The more complete and accurate description of near-surface snow particle motions observed by PTV may prove useful for improving blowing snow model realism and accuracy.

This manuscript has been modified for inclusion in this thesis. It was originally published as: Aksamit, N. O., and J. W. Pomeroy (2016), Near-Surface Snow Particle Dynamics from Particle Tracking Velocimetry and Turbulence Measurements during Alpine Blowing Snow Storms, *Cryosph.*, *10*, 3043–3062, doi:10.5194/tc-10-3043-2016.

3.1 Introduction

Wind transport of snow influences the variability of alpine summer runoff (Pomeroy et al., 2012; Winstral et al., 2013), is a large contributor to the growth or ablation of small mountain glaciers (Dyunin and Kotlyakov, 1980), and can contribute snow loading to avalanche prone areas (Schweizer et al., 2003). Time-averaged blowing snow field measurements often present an oversimplified view of a highly variable and unsteady natural phenomenon. Physical snow trap mechanisms only provide mass flux averages over prolonged collection periods (Budd et al.,

1966). Snow particle counters only recently began providing point measurements of particle speed (Nishimura et al., 2014) along with particle size and number flux values (Schmidt, 1984; Brown and Pomeroy, 1989; Kinar and Pomeroy, 2015). Snow traps and particle counters can neither measure the mechanisms of transport initiation nor provide continuous vertical profiles of particle concentration or transport. Yet, most current blowing snow model development has been informed from time-averaged measurements from such devices. Accordingly, simplified models of blowing snow persist in the literature that do not contain self-consistent wind-snow momentum balances, as demonstrated by Andreotti (2004) for sand. As well, there is a current lack of detailed measurements of particle-surface interactions in natural conditions.

Recent progress in blowing snow research has been accelerated by novel applications of high-speed imaging systems. Kobayashi (1972) pioneered blowing snow recordings with outdoor, 1/8-second shutter speed images. This was the first visual evidence of particle mechanics in the snow saltation layer and was extremely informative in the development of saltation theory (Pomeroy and Gray, 1995), but the photographs consisted of blurred snow particle streaks or were saturated with particles, disguising individual particle motions. More recently, Gordon and Taylor (2009) designed a novel and effective halogen backlit camera system to effectively obtain particle size and shape parameters in the Arctic, but were limited to an imaging area on the order of 9 mm^2. In a further study, Gordon et al. (2009) modified this technique to image an area of 124 mm x 101 mm with a black and white binarization algorithm to obtain continuous particle density profiles. Unfortunately, particle velocity measurements were unavailable from either study.

In laboratories, several wind tunnel studies have examined drifting snow with Particle Image Velocimetry (PIV) (Lu et al., 2012; Tominaga et al., 2012), shadowgraphy (Gromke et al., 2014) and shadowgraphic Particle Tracking Velocimetry (PTV) (Groot Zwaaftink et al., 2014; Paterna et al., 2016), providing valuable insights into saltating snow velocity distributions, average relative wind and saltating snow velocities, particle size distributions, qualitative comparisons to Large Eddy Simulation driven transport, and equilibrium wind-blowing snow decoupling. Blowing snow transport model development continues to address small-scale variability (e.g. Nemoto and Nishimura, 2004; Groot Zwaaftink et al., 2014), and requires advanced measurement techniques to understand the physics driving such multi-scale

heterogeneities as well as evaluate the uncertainties and assumptions inherent in proposed models.

Of the multitude of blowing snow models that have been developed, many implement components of earlier aeolian saltation or initiation models, e.g. the work of Bagnold (1941), Owen (1964), Schmidt (1980), Pomeroy and Gray (1990), and Nishimura and Hunt (2000). In what follows, effort has been made to refer only to the original work containing the model component or measurement campaign under discussion, but comments generally apply to all derivatives. In a similar vain to the work of Bagnold (1941), current theory often represents blowing snow in two layers, saltation and suspension, with a neglected and poorly understood creep mechanism at the lower boundary of saltation (Pomeroy and Gray, 1990; Nishimura and Hunt, 2000; Doorschot and Lehning, 2002). Once the wind surpasses a transport threshold velocity, saltating particles follow ballistic trajectories, and rebound off the surface, rising no higher than 10 cm. As wind speeds increase, saltating particles become suspended by turbulence and disperse upwards. Closely following wind streamlines, suspended particles rarely encounter the ground (Pomeroy and Male, 1992; Bintanja, 2000).

The two most commonly modeled modes of saltation initiation are aerodynamic lift, the direct drag induced ejections of grains, and splash, the ejection of grains by rebounding saltating particles (Doorschot and Lehning, 2002, McElwaine et al., 2004). However, there are substantial disagreements about these mechanisms; Schmidt (1986) calculated that direct aerodynamic lift was not possible under average flow conditions over a level snow surface due to strong snow particle bonding. Doorschot et al. (2004) argued the fragile dendritic snow in their study resulted in aerodynamic lift dominance. It is likely that both mechanisms are possible and that the prevalent mechanism depends on the wind conditions and snow surface structure and cohesion. There is a growing pool of blowing snow models parameterizing these two initiation mechanisms, including the work of Doorschot and Lehning (2002), Nemoto and Nishimura (2004) and Groot Zwaaftink et al. (2014), all adapting the blowing sand initiation model of Anderson and Haff (1991) through wind tunnel measurements.

In contrast to representing saltation as a layer of particles moving with uniform trajectories (e.g. Owen, 1964) as is common in snow saltation studies (Pomeroy and Gray, 1990;

Tabler, 1991; Doorschot and Lehning, 2002), recent wind tunnel studies and numerical simulations of wind transport of sand have shown the benefit of representing saltation with continuous grain velocity distribution functions (Creysells et al., 2009; Ho et al., 2012, 2014). From these observations, two populations of saltating particles are distinguishable by kinetic energy rather than by physical properties such as grain size. High-energy particles have higher and longer trajectories that are influenced by changes in wind strength. However, these particles only constitute the long tails of velocity distribution functions (Ho et al., 2012). The bulk of sand saltation observed in these studies consists of low-energy splashed 'ejecta' and tractating (bed transport) grains undergoing very short hops. These grains generate the majority of mass flux and govern the mean properties of equilibrium saltation (Ho et al., 2014).

As saltation develops, transport mechanics evolve. For instance, in sand, saltation and creep transport modes are often coupled when saltation begins (Willets et al., 1991): as low-energy surface particles accelerate, they begin feeding upper regions of saltation. Allowing variability of motion in blowing snow saltation models permits consideration of additional mechanisms of saltation initiation and momentum transfer to the snow surface.

It remains unknown how well recent advances in conceptualization of blowing sand transport can improve descriptions of blowing snow because detailed observations of outdoor blowing snow particle transport processes near the snow surface have not been conducted. Perhaps due to this, current theories of snow saltation are inconsistent with each other and conceptualize a limited range of snow motions and initiation mechanisms. To improve the physical theory of blowing snow initiation and transport, this study demonstrates PTV as a tool for measuring short timescale blowing snow surface motions in an outdoor environment. The objectives of this study are to examine the mechanics of snow particle motion initiation, the detailed interactions between wind speed fluctuations and snow particle dynamics, and the role of turbulent burst mechanisms that are common in mountain environments in generating shear stress to modify snow saltation. In doing so, the potential for adapting a continuum sand transport model for describing snow saltation particle motions is assessed.

3.2 Methods

Fieldwork was conducted during blowing snow events in March 2015 and February-March 2016 at the Fortress Mountain Snow Laboratory (FMSL), Kananaskis Valley, Alberta, Canada. FMSL receives at least 800 mm water equivalent of snowfall each winter, can sustain wind speeds exceeding 35 m s^{-1} and is home to several well-instrumented high-altitude, wind-swept observation sites. The blowing snow site (2000 m.a.s.l.) was located in an open base area of the Fortress Mountain ski area (Fig. 3-1). The area was lightly used, allowing for a 350 m upwind fetch of undisturbed open snowfield, with the foot of a moderate ridge flanking the west 200 m away. The ground was snow-covered and shrub vegetation buried for the duration of the experiment with snow depths fluctuating from 60 to 120 cm. Two Campbell Scientific CSAT3 three-dimensional ultrasonic anemometers positioned at varying heights depending on snow depth on a single mast (10-40 cm and 140-200 cm) measured wind speed at 50 Hz in three axes.

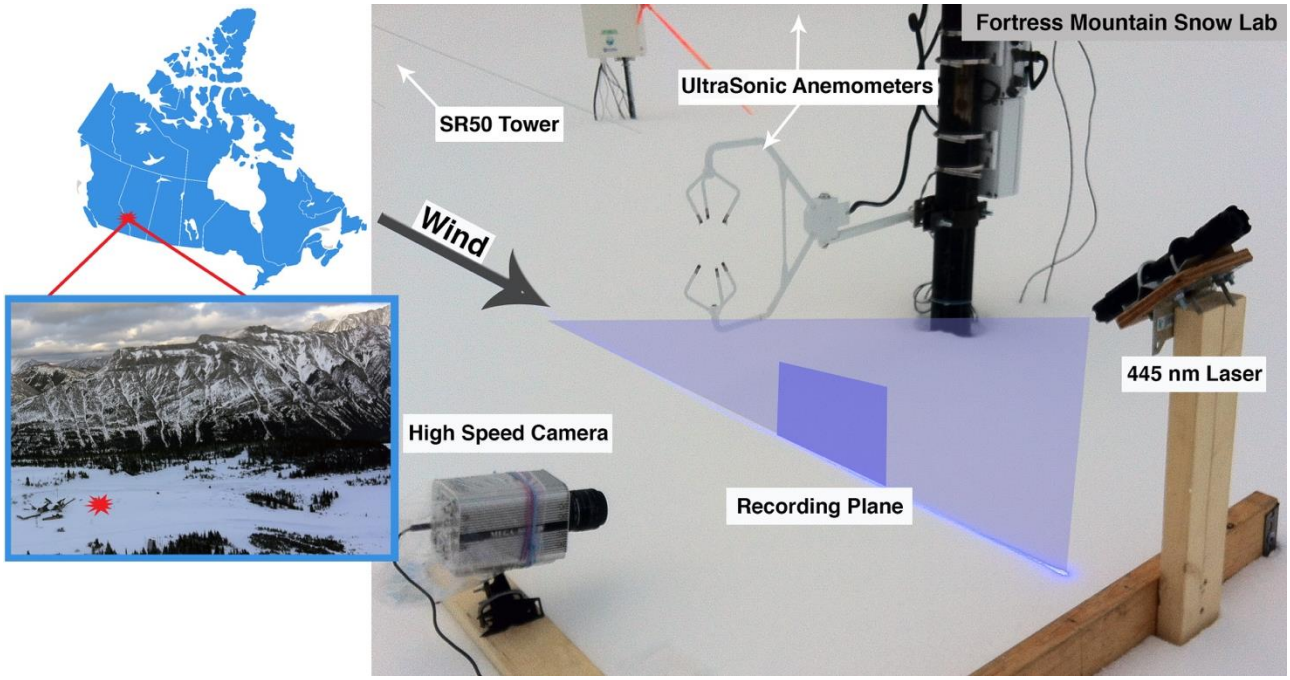

Figure 3-1: Blowing snow instrument setup and location of field site, Fortress Mountain Snow Laboratory, Alberta, Canada

A unique aspect of this experiment was the implementation of laser-illuminated high-speed videography for outdoor nighttime snow particle tracking observations. A portable rigid frame equipped with a Megaspeed MS85K high-speed camera and a 445 nm wavelength 1.5 W

continuous-wave laser was situated on the snow surface less than 1 m downwind from the anemometer mast (March 23, 2015) or 33 cm away perpendicular to the flow (February 3, March 3, 2016). Dennis and Nickels (2008) suggest reasonable application of Taylor's hypothesis up to downstream distances of up to six times the boundary layer depth δ. While there are no measurements of δ for the present data set, it is safe to assume an extreme value of 1 m is less than 6δ which is often $\mathcal{O}(10-100\,\mathrm{m})$ in the Atmospheric Surface Layer (ASL). Thus, using Taylor's frozen turbulence hypothesis and mean wind speed of the two anemometers as a surrogate for convection velocity, the effect of the downwind separation on the representativeness of anemometer mast turbulence statistics for the actual location of snow transport is assumed negligible with lag times < 0.25 s. Similarly, for the crosswind orientation, the size of energy containing eddies (discussed in Section 3), even over short recordings, are large compared to the separation. Lags between instantaneous wind and particle velocities are mentioned in the Section 4.

The frame was positioned on the snow surface allowing the camera a perpendicular 30 x 140 mm view of the flow of saltating snow. Laser light was projected through a cylindrical lens to create a 2 mm wide plane orthogonal to both the snow surface and the view of the camera (Fig. 3-1). The light plane illuminated a 2D projection of saltating snow particles. This allowed recordings in the lowest 5 cm of the atmosphere, with minimal foreground shadowing and no background reflection. Particle Tracking Velocimetry (PTV) measurements were calculated by DaVis 8 (LaVision) software and estimated individual snow particle velocities using tracking algorithms that match discrete particles in subsequent frames imaged by the high-speed camera. Particle velocimetry techniques are normally used for wind tunnel studies (e.g. Zhang et al., 2007; Creyssels et al., 2009; Ho et al., 2011, 2012; Lu et al., 2012; Tominaga et al., 2012; Groot-Zwaaftink et al., 2014; Paterna et al., 2016), with few applications, in any discipline, in an outdoor setting (e.g. Morris et al., 2007; Zhu et al., 2007; Rosi et al., 2014; Toloui et al., 2014). This is the first known application of PTV for boundary-layer blowing snow studies in a natural environment.

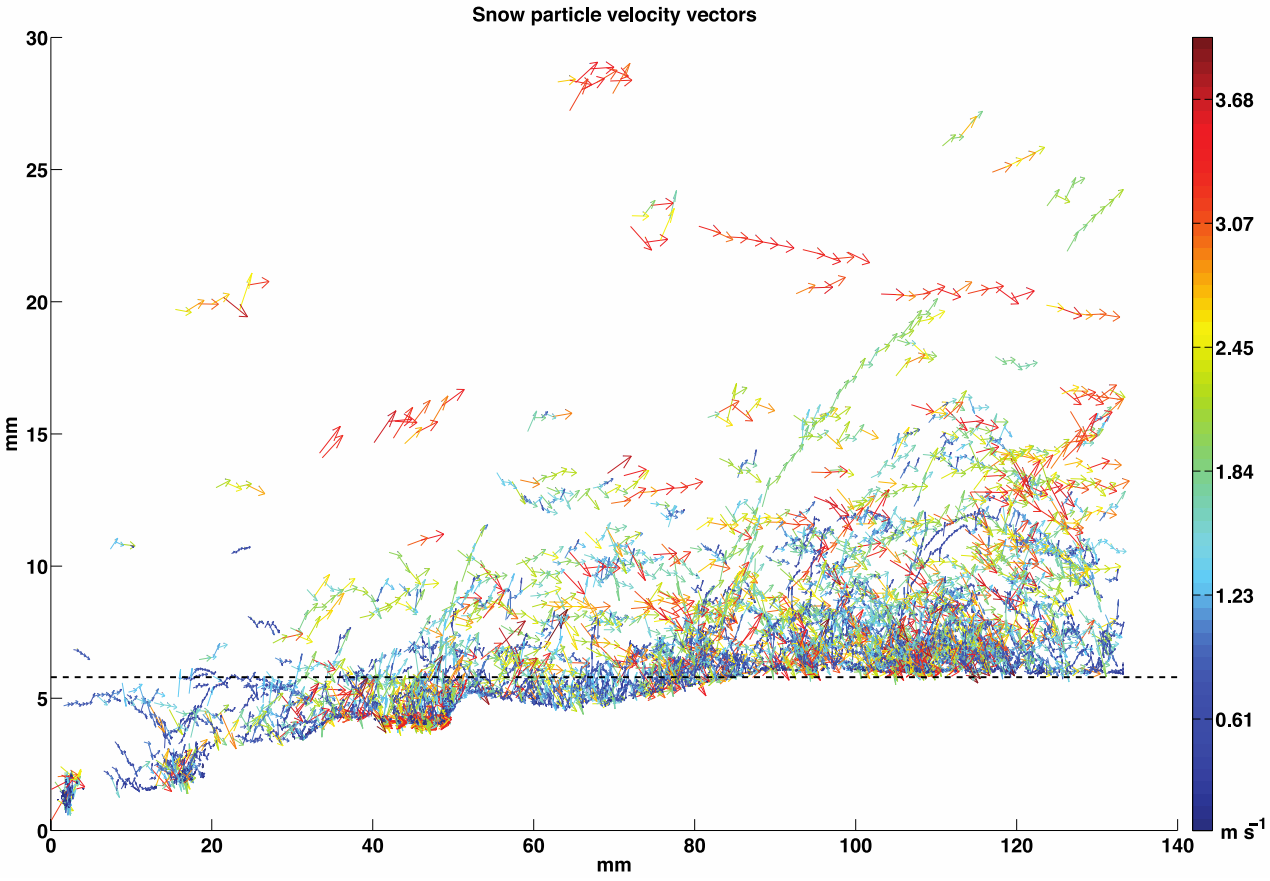

Figure 3-2: Sparse snow particle velocity vector field during one second of recording on 23 March, vector colors scaled according to total particle speed. The dashed line shows reference below which particles are influenced by microtopography.

The high-speed saltation recordings provided a great degree of visual distinction of surface particle motion and the use of 2D laser illumination minimized particle overlap (e.g. Kobayashi, 1972). As the camera was focused close to the snow surface, hundreds of thousands of rebound and splash events were recorded over the winter field seasons. In addition to PTV, videos were later reviewed with playback reduced 40-70 times, providing qualitative insight to the mechanics of near-surface saltating particle motion and bed interactions.

Figure 3-2 displays an example of velocity vectors calculated from 1 second of 23 March 2015 (recording #3). The stationary snow surface was masked out. The dashed black line indicates

the height (h_0) of the upper limit of particles whose velocities were heavily influenced by surface microtopography and contributed uncharacteristic velocity and concentration profile statistics. In order to account for gradual changes in surface topography, an orthogonal terrain following coordinate system such that $y = 0$ is always at the snow surface and the y-direction is parallel to gravity was adopted to calculate vertical profiles of mean projected horizontal particle velocity u_p, and particle number flux concentrations F_z

$$\boldsymbol{F_z} = \frac{\boldsymbol{n(z)} * \boldsymbol{u_p(z)}}{\sum_{\boldsymbol{z}} \left(\boldsymbol{n(z)} * \boldsymbol{u_p(z)} \right)} \tag{3-1}$$

where n(z) is the number of particles identified at height z. This allowed a consistent reference frame along subtle inclines like that found in Fig. 3-2. Immersed boundary coordinates based on the camera frame (x_f, y_f) are not representative of height above the complex surface, (e.g. $(x_f, y_f) = (5, 100)$ is below the surface whereas $(x_f, y_f) = (1, 5)$ is above the snow) and caused statistical values to become increasingly dubious as one approaches the roughness layer. This can result in misrepresenting surface fluxes. For example, immersed boundary coordinates indicate a flux maximum of 7 mm for Figure 3-2 because of the lack of vectors present below this height on the right side of the frame. Additionally, the height of surface microtopography varied as recordings were made over hours of active erosion and deposition, changing the surface structure, and subsequently the relative height of measurements with an immersed coordinate system. Terrain-following coordinates allowed observations to be made over a natural snowpack, crucial for improving the realism of blowing snow measurements, while still accurately defining the near-surface region.

The improved realism afforded by PTV over a natural snowpack in the ASL was counterbalanced by increased difficulty in obtaining valuable data from this methodology and from sonic anemometry during blowing snow storms. Ultrasonic wind speed measurements sometimes included spikes, "NaN" readings or were flagged for skewness/kurtosis (Vickers and Marht, 1997); these concurrent video recordings were used only for qualitative comparison. Spanwise fluctuations in wind caused snow particles to travel transverse to the plane of light, and

the streamwise wind direction usually varied at the blowing snow site over the course of an evening's observations. PTV relies on particles to remain in the plane of light for illumination and tracking through multiple frames. While the frame could be adjusted for slow variations in wind direction, directional variations during wind gusts were a significant complication. To reduce particle mismatch errors and improve velocity calculation accuracy, initial visual quality controls were implemented, discarding video that contained particles obviously moving transverse to the plane of light.

Post-processing required individual particles to be evident in at least five subsequent frames and limitations were imposed on velocity vector tracks to discard physically unrealistic acceleration or direction change from one frame to the next. The camera depth of field and light plane thickness limited out-of-plane particle velocity components to $\pm 0.5 \mathrm{ms}^{-1}$. Further uncertainty derives from the limited ability of PTV software to match individual snow particles at high wind speeds (> 9 m s^{-1} at 40 cm height). The particle matching interrogation area becomes larger as wind speeds increase and particles travel further from one frame to the next. This exponentially increases the number of particles that may be incorrectly matched.

To verify particle enumeration, a dual-threshold black and white binarization technique adapted from Otsu (1979) was used to estimate particle concentration in each frame. This complementary method of particle identification used algorithms that, unlike PTV, are not affected by transverse particle motion or particle matching limitations in gusty conditions. Binarization estimates of blowing snow concentration profiles were in sufficient agreement with concentration profiles generated by PTV, lending confidence to the measurements of particle trajectories. Additionally, with the binary image and PTV time series, it was possible to use a flood-fill algorithm to identify the connected components of blowing snow particles. Making an assumption of grain sphericity and constant density (917 kg m^{-3}) and using instantaneous mean particle velocities, the equivalent diameters of the particles were used to estimate blowing snow volume fractions and instantaneous density flux Q_s (kg $\mathrm{m}^{-2}\mathrm{s}^{-1}$). Particle diameter measurements

generated gamma-distributions of particle size (Fig. 3-3) consistent with other blowing snow literature (Budd, 1966; Schmidt, 1982).

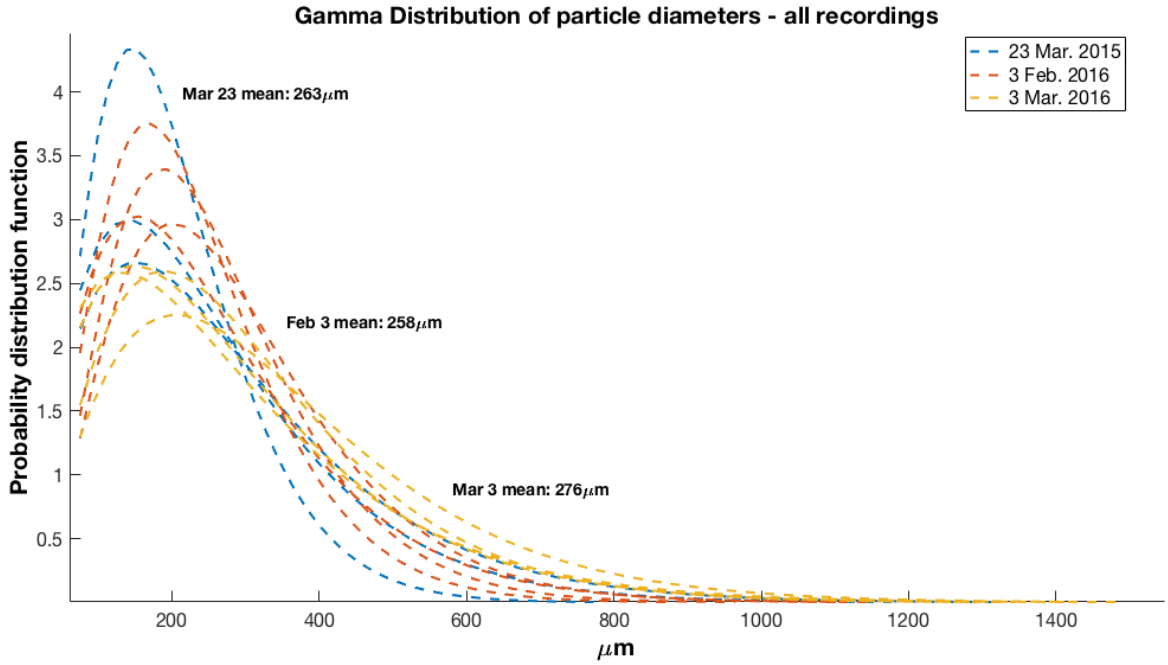

Figure 3-3: Two parameter Gamma distributions of particle diameters from each recording. Diameter measurements were obtained through black and white video binarization and equivalent diameter calculations of flood-fill identified connected components.

PTV measurements in exceptionally high wind speeds (> 10 m s^{-1}) were not possible because the laser light became blocked by particles. Therefore the dataset used in this analysis is focused on observations taken during relatively low mean wind speeds for blowing snow (mean $4 - 7$ m s^{-1}, Table 3-2); these sometimes included periods of intermittent turbulent bursts and intermittent snow transport. After all post-processing, three nights of recording satisfied all quality controls requirements. This included twelve recordings spanning 266 seconds of raw video and 470,000 frames.

3.3 Results

Examination of data calculated from 23 March, 2015, 3 February and 3 March, 2016 demonstrated the value of PTV measurements over varying wind speeds during periods of

natural variation in saltating grain shape, type, and size. Descriptions of the snowpacks following the designations of the International Classification for Seasonal Snow on the Ground (Fierz et al., 2009) for each night can be found in Table 3-1, with particle size gamma distributions for each recording in Fig. 3-3. Sample videos from each night can also be found in the document supplement. During all three nights, transport was highly intermittent, implying wind speeds were near threshold conditions. This was a necessary condition for accurate particle tracking in aeolian systems as images can become easily saturated (Ho et al., 2014).

Date	Snow surface conditions and weather	Density of loose surface grains	2 m Air/Snow Surface Temp	Surface Hardness (HHI)	Blowing Snow Grain Size (μm)
Mar. 23	5 cm graupel over old snow with light flurries	~350* (kg m^{-3})	-1C/(-)*	Fist over Melt-Freeze Crust (1 - 4)	263 (Max: 1200)
Feb. 3	Fine decomposing grains on windslab/sastrugi. No precip.	228 (kg m^{-3})	-10C/-10C	1 Finger-Pencil (3 - 4)	258 (Max: 850)
Mar. 3	Fresh snow. No precip.	156 (kg m^{-3})	-2C/-5C	Fist (1)	276 (Max: 2500)

Table 3-1: Descriptions of the snowpack for each night of recording including a description of the condition of the snow surface and concurrent precipitation, bulk density of the top 5 cm of grains, mean air temperature at the upper anemometer, snow surface temperature, hand surface hardness and HHI values following Fierz et al. (2009), as well as snow grain size as determined from the blowing snow video. *Density and Snow Surface temperature not available on March 23 with density estimated from Pruppacher and Klett (1997).

3.3.1 Wind Characteristics

Near-neutral (slightly stable) stability conditions were found during all nights using flux and gradient based methods (document supplement Fig. S1-3), however, steady-state wind conditions $\left(\frac{\partial \bar{u}}{\partial t} = 0\right)$ did not occur during the field campaign. The less strict steady-state requirements of Foken and Wichura (1996) were also tested to further confirm steady-state conditions were not evident. Recording and wind characteristics encompassing the three nights are displayed in Table 3-2. Fifteen minute and recording time period mean wind speed $\bar{u}$, friction velocity $u_*^2 = \left[\overline{u'w'}^2 + \overline{v'w'}^2\right]^{1/2}$ (Stull, 1988), and covariance based roughness length $z_0 =$

$z\,e^{-0.4\bar{u}/u_*}$ are shown for both anemometer measurements as they are the parameters most often used in blowing snow models. Additional values of turbulence intensity $I = \sqrt{\overline{u'^2} + \overline{v'^2} + \overline{w'^2}}/\sqrt{\overline{u^2} + \overline{v^2} + \overline{w^2}}$; and Shields number $S = \rho_{air} u_*^2 / \rho_{ice}\, gd$ (based on mean particle size for each video) over both time periods are provided, as well as mean blowing snow flux (Q_s kg m^{-2}s^{-1}) for the recordings.

If wind measurements are close to the surface, such as during the 3 March 2016 recordings, the physical path length of the sonic anemometers can result in losses of high frequency turbulence. Following the guidelines of van Boxel et al., (2004), the Nyquist frequency (25 Hz) is a limiting factor for mean wind speeds greater than 3 m s^{-1}, and may also contribute to some discrepancy of low and upper anemometer turbulence measurements. Additionally, the lower anemometer measurements during Recording #2 on March 23, 2015 appears to have been contaminated as there is a significant change in covariance derived u_* and z_0 values between the two heights.

The Prandtl-von Kármán logarithmic-law fitting parameters (z_0 and u_*) were unrealistic for the ASL over long periods during the storms, most likely due to violations of horizontal-homogeneous-flat (HHF) terrain and stationarity requirements. Recording period log-law based roughness lengths $z_0 = e^{\frac{u_1 \ln(z_2) - u_2 \ln(z_1)}{u_1 - u_2}}$ and friction velocities $u_* = \frac{\kappa \bar{u}(z)}{\ln(z/z_0)}$ were loosely comparable to lower anemometer fluctuation-based measurements with z_0 errors less than $\pm$ 100% (except March 3 #9), and u_* errors less than $\pm$ 70%, often slightly underestimating.

The 15-minute roughness lengths that were generated by covariance methods resulted in inaccurate log-linear wind profiles that indicated a zero-velocity zone for the wind well above the snow saltation layer and often at extremes values of tens to hundreds of mm (Table 3-2). High roughness lengths appear characteristic of this mountain region. At a nearby site 14 km northeast and 600 m lower in elevation, Helgason and Pomeroy (2005) attributed similar large covariance derived z_0 values at varying heights to the effects of surrounding topography and the non-stationary and non-steady state nature of the wind. The modified "focal-point" log-linear wind profile proposed by Bagnold (1941) for aeolian transport was not recognized in this study, with estimates of focal lengths fluctuating from several mm up to 6 m.

Recording	Duration/Frames	$\bar{u}$ m s^{-1}	u_* m s^{-1}	z_0 mm	I %	S (non-dim)	Q_s kg m^{-2} s^{-1}
23/3/15 #1	7.3 s/9147						0.0146
200 cm		1.2 (5.5)	0.61 (0.23)	910.1 (0.1)	1.10 (0.22)	0.169 (0.028)	
40 cm		1.1 (4.7)	0.46 (0.26)	126.9 (0.3)	1.13 (0.27)	0.096 (0.034)	
23/3/15 #2	11.4 s/14299						2.54e-4
200 cm		1.9 (4.3)	0.48 (0.22)	410.6 (0.8)	1.04 (0.24)	0.139 (0.039)	
40 cm		1.7 (4.2)	0.40 (0.08)	69.9 (1.3 e-4)	1.04 (0.16)	0.096 (0.007)	
23/3/15 #3	13.1 s/16404						0.0237
200 cm		1.4 (5.3)	0.28 (0.55)	312.2 (42.4)	0.80 (0.40)	0.037 (0.148)	
40 cm		1.3 (4.8)	0.24 (0.57)	116.5 (8.0)	0.79 (0.45)	0.027 (0.122)	
3/2/16 #1	27.8 s/ 43075						0.0179
155 cm		4.67 (5.78)	0.27 (0.26)	1.7 (0.3)	0.39 (0.22)	0.038 (0.036)	
25 cm		3.96 (4.9)	0.29(0.22)	1.6 (0.06)	0.41 (0.21)	0.044 (0.026)	
3/2/16 #2	28.0 s/ 57487						0.0375
155 cm		3.91 (5.35)	0.22 (0.23)	1.8 (0.4)	0.45 (0.23)	0.025 (0.027)	
25 cm		3.33 (4.54)	0.22 (0.27)	1.0 (0.2)	0.46 (0.25)	0.025 (0.037)	
3/2/16 #3	28.1 s/ 57528						0.0547
155 cm		4.3 (5.7)	0.34 (0.45)	12.2 (12.5)	0.44 (0.27)	0.054 (0.106)	
25 cm		3.67 (4.7)	0.27 (0.3)	1.7 (0.7)	0.44 (0.27)	0.034 (0.045)	
3/2/16 #4	28.0 s/ 57409						0.044
155 cm		3.1 (6.94)	0.31 (0.33)	35.4 (0.4)	0.83 (0.17)	0.056 (0.055)	
25 cm		2.6 (5.66)	0.31 (0.33)	14.7 (0.4)	0.84 (0.2)	0.056 (0.055)	
3/3/16 #1	27.9 s/ 43182						0.0046
140 cm		5.33 (4.58)	0.30 (0.16)	1.7 (0.03)	0.28 (0.16)	0.035 (0.013)	
10 cm		4.3 (3.75)	0.23(0.21)	0.2 (0.3)	0.29 (0.19)	0.021 (0.021)	
3/3/16 #2	27.9 s/ 43182						0.1474
140 cm		4.33 (5.47)	0.25 (0.42)	1.8 (10)	0.3 (0.23)	0.030 (0.084)	
10 cm		3.57 (4.33)	0.20 (0.26)	0.3 (0.1)	0.3 (0.23)	0.019 (0.033)	
3/3/16 #3	27.9 s/ 43182						0.1561
140 cm		4.7 (5.5)	0.27 (0.23)	2 (0.04)	0.26 (0.16)	0.035 (0.02)	
10 cm		3.85 (4.6)	0.22 (0.20)	0.4 (0.1)	0.27 (0.18)	0.023 (0.026)	
3/3/16 #4	28.1 s/ 57528						0.0542
140 cm		4.6 (5.54)	0.58 (0.24)	82 (0.2)	0.53 (0.17)	0.149 (0.028)	
10 cm		3.7 (4.35)	0.45 (0.21)	15 (0.9)	0.54 (0.2)	0.09 (0.021)	
3/3/16 #5	28.1 s/ 57528						0.3467
140 cm		4.3 (6.06)	0.50 (0.31)	63 (0.8)	0.61 (0.36)	0.131 (0.046)	
10 cm		3.5 (4.73)	0.42 (0.35)	14 (2)	0.63 (0.4)	0.092 (0.06)	

Table 3-2: Wind characteristics: mean wind speed $\bar{u}$, friction velocity u_*, aerodynamic roughness height z_0, turbulence intensity I, and Shields Parameter S for recordings on Mar. 23, 2015, Feb. 3 and Mar. 3, 2016. Average values from the 15 minutes surrounding each recording (and recording-only period in parentheses) are shown for the two measurement heights. Estimates of blowing snow flux Q_s in kg m^{-2} s^{-1} are included for recording only periods.

The wind was characterized by brief moments of intense gusting separated by periods of relatively calm conditions as also noted at the Helgason and Pomeroy (2005) research site. 15-minute turbulence intensity ranged from 26 to 113%, consistently higher than the recording period values where short time series preclude larger fluctuations around mean values. As a

result, values of $\bar{u}$, u_*, and z_0 consistently differ between video recording-averaged (7.3 to 28 s) and 15-minute averaged values. Turbulent gust-driven snow transport events dominated the nights. 11 out of 12 fifteen-minute averages present lower wind speeds than the recording period with the long averages often below thresholds of transport.

Figure 3-4 shows varying instantaneous Reynolds Stress ($RS = u'(t)w'(t)$) generation during recording specific periods following the language of quadrant hole analysis (Willmarth and Lu, 1971). Sweep and ejection events (Q2 and Q4) often contributed the majority of τ at both anemometers, with a more pronounced role closer to the ground, indicating changes in the snow surface influence on wind mechanics. Q2 and Q4 stress also occupied a disproportionately small amount of time near the surface, as can be seen in the impact factors inset in the bar graphs ($IF = (\%\ \text{Reynolds Stress})/(\%\ \text{Time})$) that are greater than unity. Therefore, when strong events are captured during the recordings, τ values can be much larger than long time averages. The presence of a single pronounced sweep event in Recording #3, March 23 (discussed in Section 3.3) contributed to a high recording period turbulence intensity (40-45%), and a much higher recording friction velocity than the 15-minute values (0.48 m/s and 0.24 m/s respectively) and will be discussed in detail in Section 3.3.

Understanding the changes in the quadrants generating τ helps illuminate the differences in u_* values at the two measurement heights over these short recording timescales. The recordings with the largest discrepancy in u_* (besides March 23 #2 where low height wind measurements are questionable) are February 3 #3 ($u_* = \{0.30, 0.45\}\ \mathrm{m\ s^{-1}}$) and March 3 #2 ($u_* = \{0.26, 0.43\}\ \mathrm{m\ s^{-1}}$). This was the result of a significant decrease in the magnitude of mean τ at the lower measurements (0.27 vs 0.11 $\mathrm{m^2\ s^{-2}}$ and 0.22 vs 0.09 $\mathrm{m^2\ s^{-2}}$, February 3 and March 3, respectively), while the turbulence intensity remained nearly constant (Table 3-2). The reduced presence of Q1 and Q3 at the lower heights, and increased impact factor of Q2 and Q4 (Fig. 3-4) indicated a complex shift in boundary layer dynamics towards the snow surface that is beyond the scope of this manuscript. Other recordings exhibited much closer friction velocity and roughness length values at the two anemometers, indicating similar turbulent motions were captured.

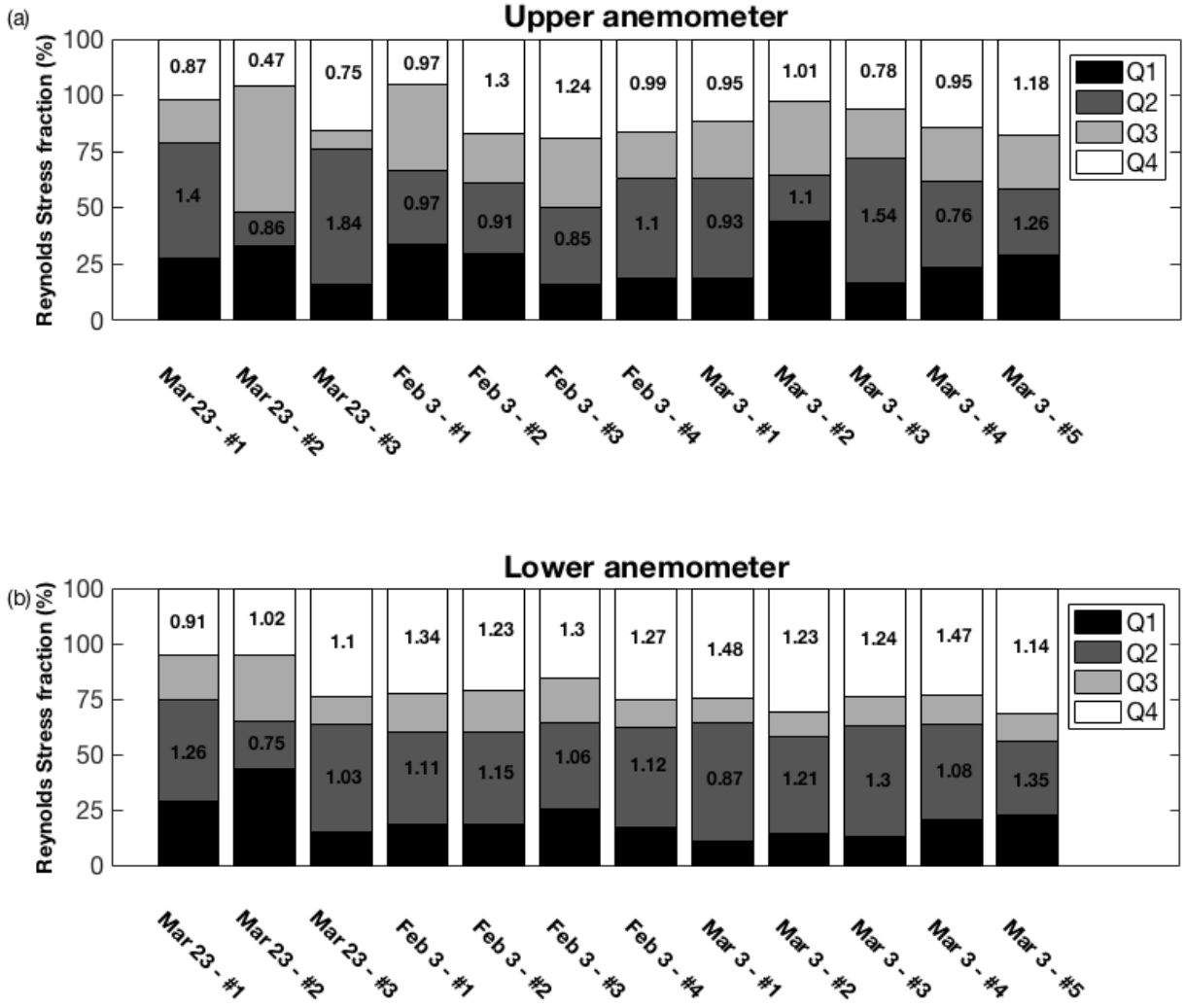

Figure 3-4: Percentage of Reynolds Stress distributed by Quadrants Analysis during 12 Blowing Snow Recordings with impact factor (% Stress/% Time) inset in Q2 and Q4 events. Note dominance of Q2 and Q4 generated stress. Mar 23 - #2 Low anemometer measurement contaminated.

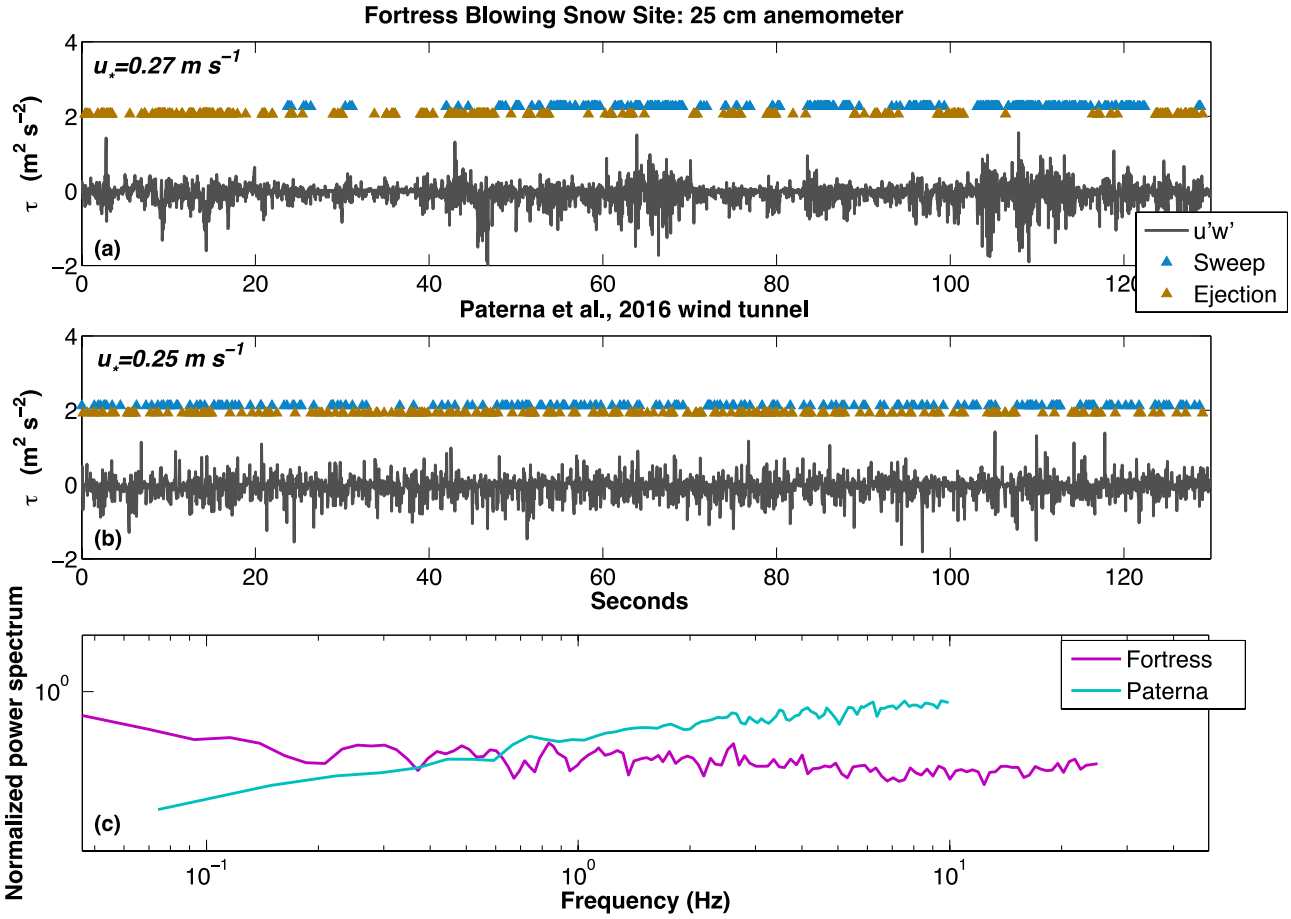

Figure 3-5: Plots a & b compare Reynolds Shear Stress signals from 3 February 2016 and Paterna et al. (2016) wind tunnel blowing snow studies. Triangles indicated Sweep and Ejection events larger than one standard deviation of Reynolds Stress. C) Normalized Power Spectral Density for streamwise velocity for the two time series.

As also seen by Bauer et al. (1998), sweeps and ejections did not immediately follow one another, rather there were prolonged clusters of sweeps and ejections with gaps in between (Fig. 3-5a). The gaps may be a result of point measurements' inability to capture a full 3D motion (Bauer et al., 1998), but nevertheless the measurements showed significantly different τ generation than that typically found in wind tunnels. For example, Fig. 3-5 a-b compares τ values in a recent blowing snow wind tunnel experiment of Paterna et al. (2016) with τ found on 3 February 2016 at FMSL at similar friction velocities (0.25 m s^{-1} and 0.27 m s^{-1}, respectively). A

sweep signal of magnitude greater than one standard deviation of τ is indicated above the given τ time series by a blue triangle, while similar ejections are marked by brown triangles. Visually, there is a noticeable shift toward clustered sweep and ejection events at FMSL (Fig. 3-5a), in which clustered pockets of sweeps alternated with ejections, while the sweep/ejection cycle and turbulent energy occurred at much a higher frequency in wind tunnel-based measurements by Paterna et al. (2016) (Fig. 3-5b). This is further confirmed in the power spectral density plots of streamwise wind speed (Fig. 3-5c), and in the discussion by Paterna et al. (2016). Reconciling these differences between motions in atmospheric boundary layers and wind tunnel flows is challenging (Hutchins et al., 2012) and the substantial differences in Reynolds number must be kept in mind when comparing blowing snow studies in wind tunnel and outdoor environments.

3.3.2 Vertical PTV Profiles

Figure 3-6 shows profiles of ascending particle horizontal velocity for the three nights of recording with linear regressions based on the lower 10 mm. Profiles were designated by their recording-specific low anemometer u_* values, except for 23 March where the lower wind measurements for recording #2 were contaminated. Thus, all 23 March recordings were compared by 2 m wind.

Particle motions begin with an initial ejection velocity at the surface and then accelerate due to fluid drag in the wind. Therefore, the height of an ascending snow particle should be a function of the time spent accelerating. The profiles of horizontal velocities of ascending particles confirmed this acceleration in Fig. 3-6. The average momentum transfer from wind to grain was estimated from the inverse slope of the plots and indicated the ability of the wind to entrain and accelerate particles. For all three nights, there is a near constant particle velocity gradient immediately above the surface, $\left(\frac{\partial u_p}{\partial z} = \gamma, \gamma \in \mathbb{R}^+\right)$. Above ~8-12 mm, depending on the night, mean particle velocities deviate from the linear profile as seen in Fig. 3-6 and confirmed by normalized root mean square error (NRMSE) changes from the order of 0.01 to 0.1 above and below 10 mm, respectively. It must be noted, this did not indicate a discrete transition height from creep to saltation but is rather evidence of a continuous spectrum of particle velocities (Anderson,

1987; Ho et al., 2012) transitioning to a higher energy population away from the surface. As these recordings captured intermittent transport, saltation is in constant readjustment to the turbulent wind, with particles falling in and out of the higher levels of saltation (discussed further in Section 3.3). This prevented a consistent adherence to the linear profile as seen by Ho et al. (2011), though both studies found linear profiles overestimate particle velocity at greater heights.

The velocity gradient (shear rate) γ, was estimated by linear regression and varied from $35 - 98\ s^{-1}$. Variations in wind speed and Q_s during each recording period indicate blowing snow transport never attained equilibrium. However, γ values are comparable to wind tunnel PTV sand velocity gradients ($39.0 - 150\ s^{-1}$) measured below 30 mm by Zhang et al. (2007), and the range $20 - 60\ s^{-1}$ found by Ho et al. (2011). For each night, γ increases with increasing friction velocity (Figs. 3-6 d-f). The Ho et al. (2011) rigid bed experiments were conducted at comparable Shields numbers to the high HHI, wind-hardened February 3 experiments (Ho et al.: [0.013, 0.043], Aksamit and Pomeroy: [0.026, 0.061]) and shared several trends discussed here and below. For example, as for Ho et al. (2011) the night of February 3 had on average the lowest γ values (mean $44\ s^{-1}$ versus $69\ s^{-1}$ for the erodible beds) and the least variation in γ though transport occurred during comparable friction velocities, and higher Shields parameters than many March 23 and March 3 recordings (Table 3-2). The erodible bed studies were performed at consistently higher Shields parameters for the Ho experiments (Ho et al.: [0.07, 0.14], Aksamit and Pomeroy: [0.01, 0.12]), yet both studies also found increases in γ with friction velocity for the erodible beds. Ho et al. (2011) found less variance in γ over all friction velocities as could be expected from consistent equilibrium conditions.

As with wind tunnel sand studies (Zhang et al., 2007; Creyssels et al., 2009; Ho et al., 2011), large non-zero particle slip velocities were observed. The influence of surface microtopography and density of the flow prevented an exact measurement of particle slip velocity u_0, because it becomes difficult to enumerate all grains at the surface (Creyssels et al. 2009). However, extrapolating the linear regression plots of constant shear rate $du_p/dz = \gamma$ one can estimate u_0. As found in the same Ho study, our February 3 "rigid bed" experiments exhibited a nearly linear increase in u_0 with u_* (Fig. 3-6h). While our u_0 measurements had a larger range for the "erodible bed" nights of March 23 and March 3 (Fig. 3-6g, 6i) than that of Ho et al. (2011) and Creyssels et

al. (2009) who found a near constant slip velocity, no definitive trend with u_* could be identified either. A purely constant slip velocity over erodible beds most likely depends on equilibrium transport conditions as has been theoretically explained by Ungar and Haff (1987) and may explain the ambiguity in these results.

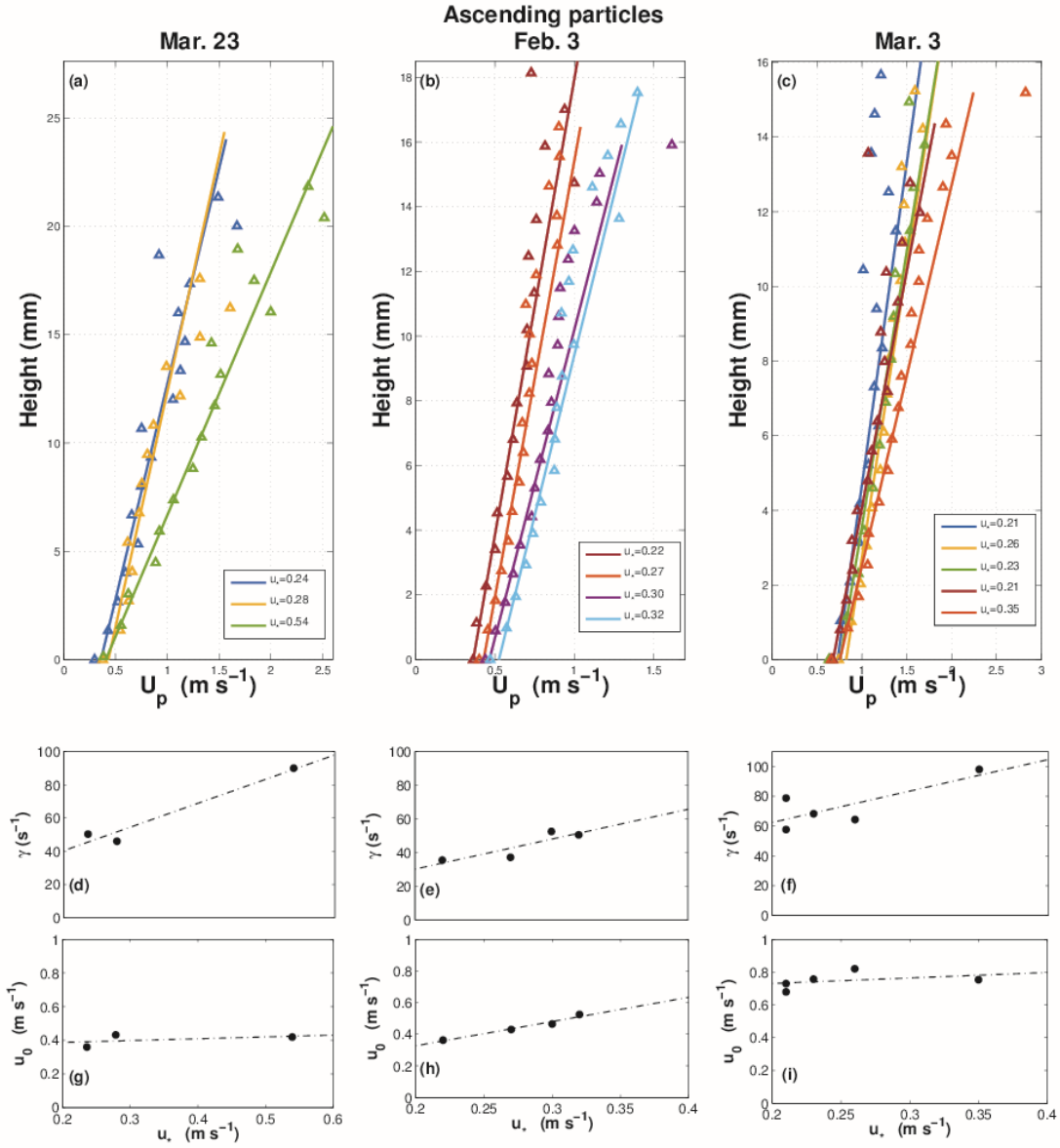

Figure 3-6: a-c) Average ascending snow particle horizontal velocities in lower saltation layer (triangles) with best fit linear profile for first 10 mm. $\boldsymbol{u_*}$ values are calculated from 200 cm, 25 cm, and 10 cm for Mar 23, Feb 3, and Mar 3, respectively. d-f) Friction velocity versus particle velocity gradient ($\boldsymbol{\gamma}$) for each recording. g-i) Friction velocity versus particle slip velocity ($\boldsymbol{u_0}$) for each recording.

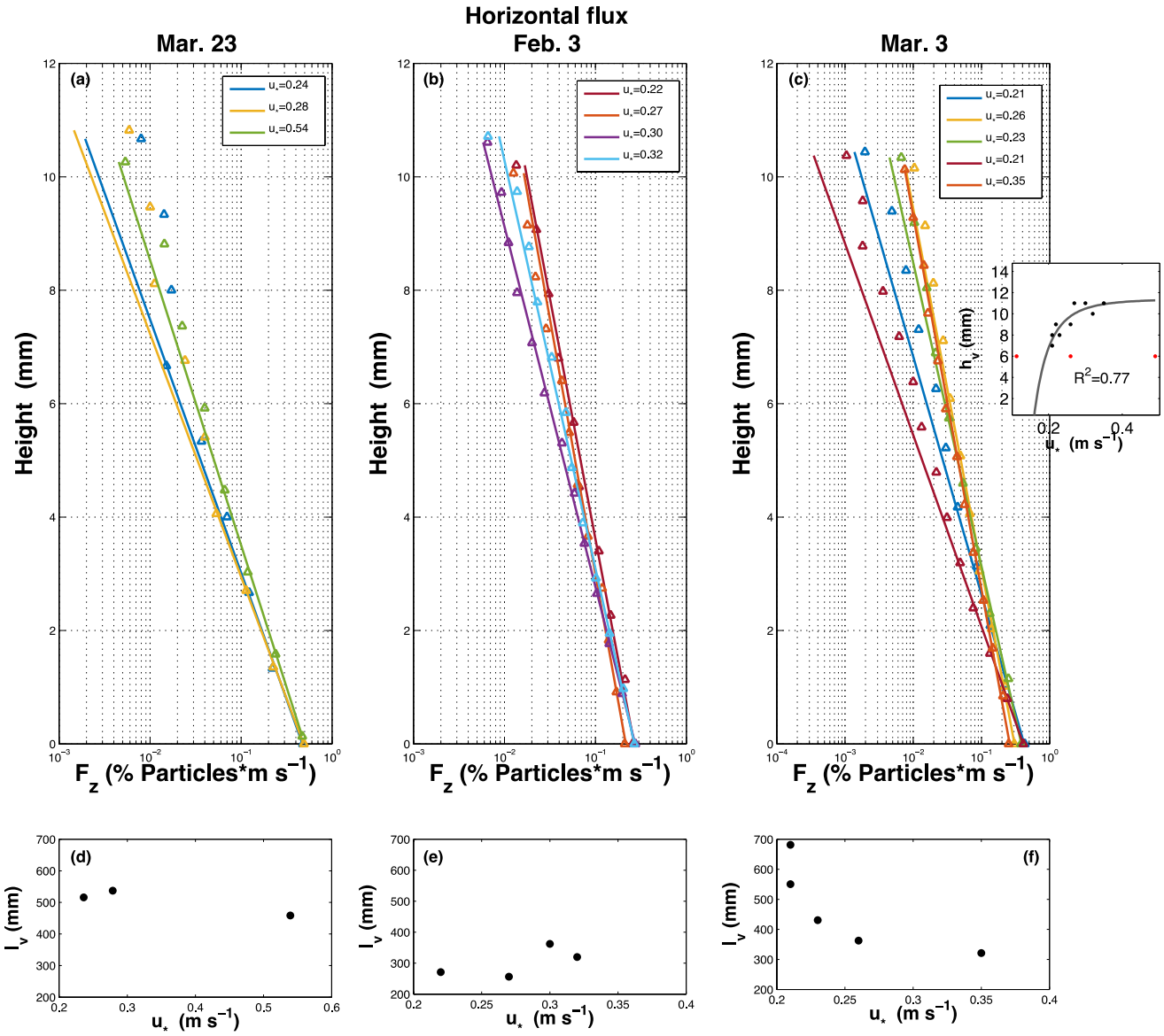

Figure 3-7: Plots a-c are mean horizontal flux measurements ($\boldsymbol{F_z}$) and best fit exponential decay. Plots d-f are friction velocity versus decay length for each night. Friction velocity versus $\boldsymbol{h_v}$ (height below which 75% number flux occurred) for all nights with power law curve fitting is seen in the right inset. Values of $\boldsymbol{h_v}$ from 23 March 2015 are marked in red.

Figure 3-7 shows the vertical profile of the normalized particle number flux calculated as Eq. (1). A normalized number flux profile was chosen instead of the volume fraction (e.g. Ho et al., 2011) or mass flux density profile (Creyssels et al., 2009) because of computational limitations of the PTV package in DaVis 8, and because of the non-equilibrium transport during the

recordings. Since it is impossible to control the rate of transport in nature, and volume fractions will change with rates of transport, wind fluctuations and snow surface conditions, it was informative to compare number flux concentrations between periods of diverse mass transport to determine differing transport mechanics over varying snow and wind conditions. As the study was focused on the dynamic role of surface transport, and not measuring mass flux, each concentration profile was renormalized by the amount of flux that occurred during a recording to compare what proportion of total particle transport is occurring at each height at suggested by Ellis et al. (2009) for aeolian transport profiles in nature. This allowed observation of changes in the relative importance of regions of transport.

The fractional number flux fits an exponential decrease of the form $\nu(z) = \nu_0 \exp(-z/l_v)$ with decreasing error as one approaches the densest flow at the surface, similar to sand and snow saltation profiles seen elsewhere (e.g. Maeno et al., 1980; Nishimura and Hunt, 2000; Creyssels et al., 2009; Ellis et al., 2009; Ho et al., 2011; Lü et al., 2012), with ν_0 and l_v being fitted parameters, the latter referred to as the decay length. The number flux decay length l_v indicated how quickly the number flux concentration approached zero (Fig. 3-7d-f), but because there were large variations in the surface concentration ν_0 in the present study, more consistent trends can be observed with the momentum deficit height h_v, the height below which 75% of particle flux occurred. As seen in the right inset of Fig. 3-7, there is a non-linear increasing relationship between friction velocity and h_v for the February 3 and March 3 recordings. After disregarding March 23, (discussed below), values of h_v followed an approximate power law relationship ($au_*^b + c, R^2 = 0.77$) with asymptotic-like behaviour towards the top of the region of interest (~11 mm). At low friction velocities, near-surface saltation was dominated by transport below 7 mm, with transport becoming gradually more uniform as h_v approached the top of the camera frame at higher friction velocities.

March 23 exhibited very little change in h_v and ν_0 with only a slight decrease in l_v. Thus, concentration was largely invariant with wind strength. This is remarkably similar to the erodible bed findings of Ho et al. (2011). Only one recording had comparable Shields numbers to Ho, but the non-cohesive graupel bed, and spherical snow grains most similarly represented sand grains and an erodible sand bed out of the three nights.

The near surface location of the maximum of F_z found over all recordings in Fig. 3-7 is in disagreement with models using Bagnold's focal height (Bagnold, 1941) to predict a peak mass flux at some distinct height above the surface (e.g. Pomeroy and Gray, 1990). This stemmed from the earlier lack of high resolution measurements of near snow surface processes outdoors, as results were in agreement with later wind tunnel observations (Sugiura et al., 1998; Nishimura and Hunt, 2000) and numerical studies (Nemoto and Nishimura, 2004) of snow flux profiles as well as the recently measured blowing snow density profiles Gordon and Taylor (2009) and Gordon et al. (2009) found over natural snowcovers in Churchill and Franklin Bay, Canada, respectively.

For the time series investigated, mean particle diameters had small temporal variance over any given recording (0.01 mm on Mar 23, 0.05 mm on Feb 3, and 0.02 mm on Mar 3). For a given time step, mean particle diameters tended to decrease with height in the field of view, typical of saltating snow studies (e.g. Sugiura et al., 1998; Gromke et al., 2014), with the most extreme variations on the order of 60 μm. From this it can be inferred that particle number concentrations were closely related to particle volume fractions through mean diameters, and one can neglect variations in particle size with wind speed changes while admittedly underestimating the relative volume concentration close to the surface.

Particles moving in the densest region of the flow, immediately above the surface, are in a zone where particle tracking by opto-electronic snow particle counters becomes impossible but PTV provides new information. Close to the surface, it is possible to observe the whole spectrum of saltating particle velocities including those considered to be moving via creep.

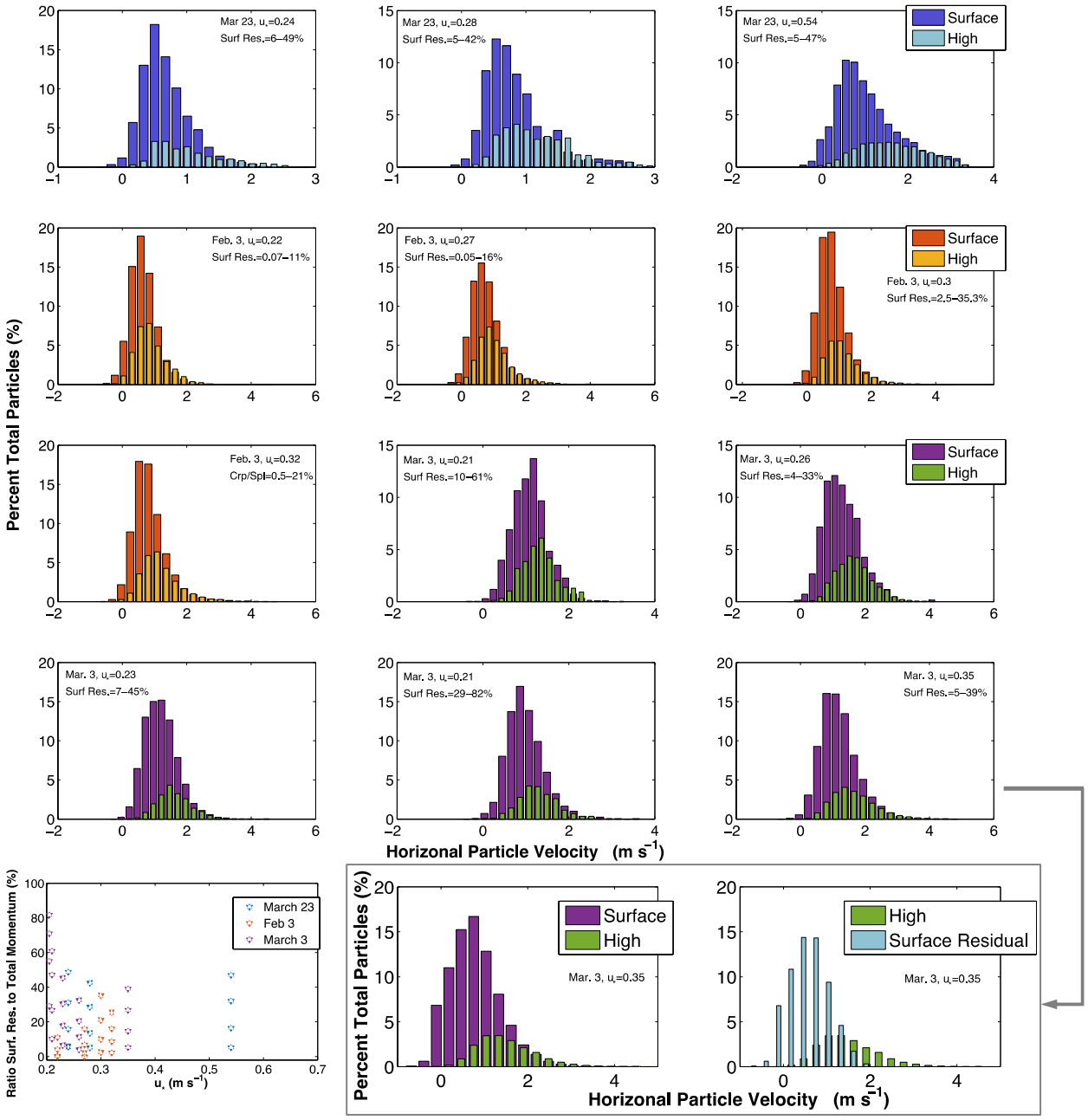

Figure 3-8: Horizontal particle velocity histograms for near-surface and upper region descending particles for each recording over the three nights (each colored differently). Near-surface residual highlighted for Mar 3 #5. The two-region delineation was set at 3 mm for Mar 23 and Mar 3, and 4 mm for Feb 3. Bottom Left: Surface residual to total momentum ratios for each recording.

Similar to the high and low-energy saltating grain populations theory of Ho et al., (2014), terrain following height bands were chosen such that two end-case populations could be delimited. Unique descending particles were separated into upper and lower regions according to a variable boundary (2 to 5 mm) so that they appear at most once in each region. Then, particles were binned into 20 equivalent size horizontal velocity bins. Figure 3-8 shows one example of histograms generated by these bins for a given height separation (3 mm for Mar 23 and Mar 3, 4 mm for February 3). Assuming that most descending particles tracked in the lowest 30 mm (frame size) will impact the surface, then most descending grains in the upper region will also be present in the lower region. This behaviour appears in Figure 3-8 where the upper region population is a subset of the lower region population, showing high and low-energy populations coexist as part of a continuous spectrum of motion at the surface. This is indicative of an inherent coupling of the creep and saltating grain motions. There is sensitivity to the selection of upper and lower regions. With a separation threshold below 2 mm, numbers of high velocity low-region particles are underestimated because tracking is increasingly difficult. With the separation threshold above 5 mm, the low density of particles and sensitivity to out of plane wind fluctuations made measurements of representative fluxes inaccurate. Thus, the separation threshold was restricted to the 2-5 mm range.

For every recording and each separation threshold chosen, there was a denser surface flow whose mean statistics are dominated by slow moving particles. This is to be expected from the particle velocity and number flux profiles in Fig. 3-6 and 3-7. The upper region histograms show saltating particles starting to transition towards higher energy trajectories, with transport dynamics dominated by larger horizontal velocities. The increasing proportion of high-energy particles with distance from the surface is likely due to the need for a greater velocity to reach greater heights on a ballistic trajectory from the surface and the subjection to higher wind speeds with increasing distance above the surface.

Subtracting the upper region particle bin numbers from the lower region bins permits an estimate of the number of particles at given velocities present solely in the lower region, hereon termed the surface residual. The sensitivity analysis showed that for nearly every separation threshold at least as many high velocity particles existed in the upper region as in the lower. This

allows conceptualization of the surface residual as the slower moving surface grains, though not necessarily creep. An example of this is shown in histograms of descending lower-region, upper-region, and surface residual particle horizontal velocities for March 3 recording #5 in Figure 3-8.

Assuming a fixed particle diameter for all particles in each recording as the mean from Figure 3-3, spherical snow grains and a grain density of 917 $kg\ m^{-3}$, snow transport momentum for each region could be estimated as the sum of momentum of particles in each velocity bin. Varying upper and lower region separation thresholds from 2 to 5 mm, the surface residual constituted between 2 – 82 %, 0.07 – 35 %, and 5 – 49 % of total transport momentum below 30 mm, on March 23, Feb 3, and March 3, respectively. Ranges of momentum contribution for individual recordings are indicated on the respective histograms in Figure 3-8 as "Surf Res," and are plotted in the bottom left panel. Surface residual momentum values complement the profiles of F_z (Fig. 3-7) as near surface F_z values also include high velocity particles that impact the surface.

In the near-surface region, the ability of the snowpack to redistribute impact momentum was estimated from PTV data derived from each recording. Mean snow particle rebound efficiency varied from night to night, and was quantified by the restitution coefficient, $\overline{e_{xz}} = \overline{\|s_r\|}/\overline{\|s_i\|}$, where $\overline{\|s_r\|}$ and $\overline{\|s_i\|}$ are mean ejection and impact speeds of particles, respectively, at 6 mm $\pm$ 2 mm such that the lower bound of the measurement band corresponds with the upper bound of the surface band generating Fig. 3-8 histograms. Because of the density of the particle flow, and transverse components of travel, a bulk statistical approach must be used to quantify momentum redistribution into the particle bed. Though these are considered different processes (Namikas et al., 2009), particle ejection speeds of both the rebounding grains and the splashed grains that reach ~20 particle diameters above the surface were averaged. Over the course of the campaign, $\overline{e_{xz}}$ varied from 0.58 to 0.84, within the bounds of the previous wind tunnel blowing snow study of Sugiura and Maeno (2000) who used a complementary particle by particle approach, separating individual rebounding and splashed grains. The mean restitution coefficient was 0.69 for the graupel grains on March 23, 0.79 for fresh snow on March 3, and 0.73 for old snow on February 3. This suggests rebound efficiency was dependent on time-sensitive saltating snow crystal and bed mechanical/material properties, as also noted in a blowing snow wind tunnel study by McElwaine et al. (2004).

3.3.3 Turbulent Event Transport

The initiation mechanisms observed at the surface during the onset of transport events differ from those proposed in single threshold velocity models (e.g. Schmidt, 1980), suggesting multiple thresholds with the dense surface flow playing a crucial role. All three transport thresholds recognized during video playback were crossed during 23 March recording #3 (Fig. 3-9) where an isolated gust was captured with minimal antecedent transport. Thus, it will be used as an example for further discussion. Concurrent streamwise wind measurements at 200 and 40 cm are plotted in Fig. 3-9a showing penetration of a turbulent sweep to the surface that is responsible for snow transport. In Fig. 3-9a, filled circles indicate sweep events with τ exceeding one standard deviation of total τ (colors corresponding to measurement heights), while triangles indicate similar moments of strong ejections. Fig. 3-9b and 3-9c show time series of spatially averaged particle velocities, and total particles tracked, respectively, in three height bands, $1 < z < 4\ mm$ (Near-Surface), $4 \leq z < 8\ mm$ (Mid), and $8 \leq z < 30\ mm$ (High). These three heights were chosen to demonstrate the subtle differences in particle transport and the continuum of motion as grains began motion and began bouncing to greater heights as wind speeds increased. These are not hard thresholds of "creep" versus "saltation" regimes. Fig. 3-9d shows the time series of instantaneous blowing snow flux Q_s in $kg\ m^{-2}s^{-1}$. These binarization based flux measurements complement PTV calculations in intense gusting when enumerating all particles through tracking became difficult.

At the end of a strong ejection event (2.5-4.5 s) at wind speeds near 4 $m\ s^{-1}$, snow particle motion began with tumbling surface movement where aerodynamic drag was barely able to directly break weak surface crystal bonds and initiate rolling (5 s in Figs. 3-9b, d). Particle-bed collisions were concurrently responsible for breaking surface snowpack matrix structures at these wind speeds, though were not yet able to initiate a splash regime. The supplementary video for March 23 begins at 5 seconds in this time series. The bonds broken by low-energy grains at low wind speeds enabled more grains to be freely available for entrainment. During this time, horizontal particle velocities remained low and in the near surface region (Fig. 3-9b), with no particles being tracked above 4 mm (Fig. 3-9c), and total mass transport remaining low (Fig. 3-9d). At this stage, the only particles in motion were those classically termed creep.

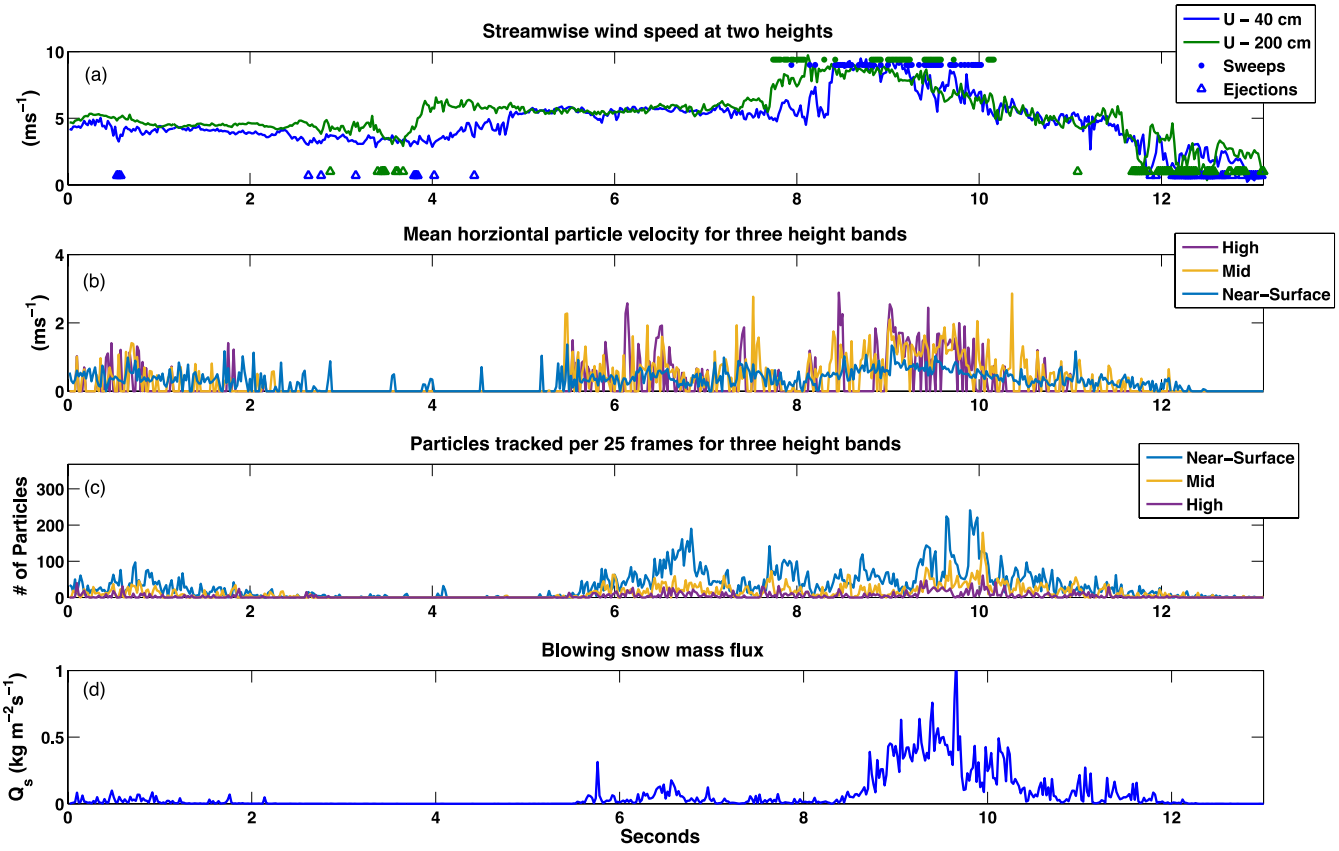

Figure 3-9: 23 March, recording #3 time series. a) 50 Hz streamwise wind speed at 40 and 200 cm above snow surface. b) 50 Hz Snow particle velocities obtained by binning particle vectors in three height bands (1<z<4 mm (Near-Surface), 4<z<8 mm (Mid), 8<z<30 mm (High)), then temporally averaged over 25 frames. c) Number of tracked particles in same height bands per 25 frames, d) Instantaneous blowing snow flux rates Q_s $(kg\ m^{-2}s^{-1})$ (1250 Hz).

As the wind speed increased (> 5 s), another threshold was crossed (~ $4.5 - 5\ m\ s^{-1}$) above which tumbling near-surface particles were sufficiently accelerated so that they could regularly bounce off the uneven surface and out of the creep layer. This initiated what is classically described as saltation, evidenced by the increasing presence of particles tracked in the "Mid" and "High" regions in Fig. 3-9c (above 4 mm), though snow mass flux remained moderate at this time (Fig. 3-9d). A continuum of motion is evidenced here as all mean particle velocities increased and velocities steadily increased away from the surface.

At 8 s, a strong sweep is present at 2 m that penetrates to the surface by 8.5 s when the last critical wind velocity threshold was crossed (~ $6\ m\ s^{-1}$); that at which saltating particles were

sufficiently accelerated to initiate an active splash regime upon rebounding. At this point snow mass flux increased exponentially (Fig. 3-9d), abruptly saturating the recording frame with snow particles and limiting illumination for successful PTV (discussed below). Similar exponential increases of sand flux during gust onset and splash commencement have been documented (Willetts et al., 1991). The increased snow mass flux (Fig. 3-9d) persisted for the duration of the gust, (until 10 s) after which both high and low streamwise velocities decreased. From 11 s onwards, the decreasing wind speed was no longer able to sustain the mass transport and particle counts dropped in the "Mid" and "High" regions of flow. A combination of inertia and wind drag prolonged transport in the creep layer, maintaining rolling crystals that continued breaking surface bonds and were available for transport during the next gust.

High region particle velocity spikes occurred with some delay after 8.5 s due to the intense snow particle density blocking the laser light illumination, making particle tracking difficult. At 9 s, the number of particles tracked in the upper region increased as particles tracked near the surface decreased. This is likely a measurement error due to the dense granular flow attenuating light penetration to the snow surface. As the gust began to subside after 9 s, PTV-observed velocities and particle numbers increased because tracking became more successful. Then, as wind speed decreased further, observed velocities and particle numbers decreased as expected. The Otsu (1979) binarization thresholds were determined over short sub-periods (0.085 s) of recording #3 (Fig. 3-9d), allowing the thresholding technique to adapt to different levels of illumination and overcome these saturation issues.

Particle impact dynamics evolved as snowpack surface conditions varied during the season with multiple melt-freeze cycles, periods of wind hardening and the appearance of mixed grain types. Warm (Air Temp: +1°C) February 2015 snowstorms precipitated enormous aggregate and rimed crystals that expanded the role of near-surface particle dynamics. Large (4 mm diameter) tumbleweed-like aggregate grains termed here "tumblons", eroded many smaller crystals from the surface or shattered themselves and immediately became saltating grains, depending on impact velocity. Overlain PTV vectors can be seen in Supplementary Video – Tumblon PTV, where an impacting tumblon shatters at the surface at seven seconds, with an impact velocity of approximately $(u_p, v_p) = (2.46, -0.43)\ m\ s^{-1}$. At 35 seconds in the PTV video,

a comparably sized tumblon with velocity $(u_p, v_p) = (0.6, 0.1)$ m s^{-1} tumbles across the screen without collapse. This type of particle motion has not been described before and would seem to be a distinctive feature of blowing snow during or shortly after snowfall of large dendritic flakes in relatively warm conditions. Uniquely large grains can also be found in the March 3 supplementary video, though shattering dynamics do not appear prevalent on that night as large grains resulted from riming and not wet grain aggregation. Decomposing and aggregate grains of extreme size have not been reported for saltating sand. This may limit the application of sand bed momentum balances and wind tunnel studies where there are no contributions of falling snow to saltation.

3.4 Discussion

Choosing the appropriate timescale to characterize turbulent energy for snow transport is vital. From Table 3-2 and Fig. 3-6 & 3-7, it is clear that recording-specific particle velocity gradients γ, and flux concentration profiles parameters did not scale with 15-minute u_* or z_0 values as is assumed on average for many existing snow saltation models (Pomeroy and Gray, 1990). Part of this lack of concurrence was due to intermittent transport and large-scale atmospheric motions generating high shear over short periods (Fig. 3-4). Also, the limited Reynolds numbers possible in wind tunnel blowing snow experiments cannot replicate the complex eddy structure of the ASL. Thus kinetic energy is contributed to mass transport at much higher frequencies in wind tunnels (Paterna et al., 2016) and the full spectrum of motion can be measured over shorter time scales. Moreover, with the influence of surrounding topography, capturing the relevant range of energy containing eddies to predict snow transport in the alpine is less straightforward. The 15-minute mean wind speeds were often below any snow transport thresholds reported in the literature (Li and Pomeroy, 1997). The significant errors arising when applying time-averaged values in a u_* driven transport model (i.e. Bagnold, 1941) in intermittent winds have been examined for sand (Sorenson, 1997; Stout and Zobeck, 1997) and equally apply for snow saltation. Pomeroy and Li (2000) accounted for the inapplicability of steady-state theory in near threshold conditions by using a probability of occurrence function to reduce transport fluxes at lower mean wind speeds, but it is unclear whether this empirical correction can account for the complex

interaction of turbulence and particle flux near the threshold. Disagreements between u_* and z_0 values at the two measurement heights, large 15-minute z_0 values, and disagreement between log-law based and covariance generated u_* values reinforces the notion that all required assumptions must be met before log-law profiles should be applied for blowing snow models (George, 2007), especially in complex terrain.

Blowing snow PTV transport profiles were clearly more related to recording-specific u_* than 15-minute values because of the non-steady state nature of the wind. As found in several wind tunnel sand studies (Creyssels et al., 2009; Ho et al., 2011), particle velocity gradients adhered to linear profiles below ~8-12 mm depending on the night. The low-energy near surface population of particles were less affected by fluctuations in wind strength (Ho et al., 2014), which resulted in more temporally consistent periods of near surface low-energy transport and lower NRMSE values. Recent blowing snow wind tunnel experiments found log-linearity present in the horizontal velocity profile (Tominaga et al., 2013), though this was not observed in the present study because of a lack of presence of a log-law for the wind.

For all recordings, the velocity gradients γ increased with increasing friction velocity estimates (Fig. 3-6d-f). Thus, even in the dense low-energy population of grains, there was noticeable adaptation to changing wind speeds. However, the role of low-energy grains diminished as surface grains became less available with increasing surface hardness. As with the rigid bed experiments by Ho et al., (2011) at similar Shields parameters, there was a much smaller variability in γ for the wind-hardened bed on February 3 than for the two nights with lower HHI and lower overall γ values. The momentum deficit height h_v was also highest for February 3 (Fig. 3-7 inset) with relatively low Shields numbers (0.026-0.061), indicating a muted role of creep and a more uniform saltation layer.

On the same night, a linear increase in particle slip velocity u_0 was observed for wind-hardened beds, similar to the findings over rigid beds by Ho et al., (2011) for sand. This showed a general acceleration of all grains in saltation when there are fewer new grains to be entrained in the flow. In comparison, there was much less variability for slip velocity for March 23 and March 3 over a wider range of Shields parameters and no clear increasing or decreasing trend. A constant slip velocity is characteristic of erodible beds in equilibrium sand transport experiments

(Creyssels et al., 2009, Ho et al., 2011). Presumably, as increasing concentration compensates for increasing friction velocity, u_0 returns to mean values over time. Snow transport was observed to be in constant readjustment to changes in wind speed, and equilibrium was never reached in the experiments, though reduced variation in u_0 may be indicative of early stages of the equilibrium process as theorized by Ungar and Haff (1987).

Particle number flux concentration profiles fit an exponential decrease model with increasing accuracy as height decreased and flow density increased, as predicted in many other sand and snow studies (Maeno et al., 1980; Nishimura and Hunt, 2000; Creyssels et al., 2009; Ellis et al., 2009; Ho et al., 2011; Lü et al., 2012). A direct comparison of decay length (l_v) between recordings and other experiments was impractical because large variations in surface concentration (ν_0) skewed the decay length, making it a poor analogue for saltation height. Instead, it was found that the momentum deficit height h_v increased for most recordings with increasing friction velocity. Lower h_v values require more particle momentum transport nearer the surface. The presence of low-energy near-surface particles at low friction velocities served as a reservoir for the transition to saltation with subsequent increases in wind speed. As the wind speed accelerates, more particles are accelerated and transported to greater heights where they are further accelerated, resulting in a more uniform vertical distribution of mass flux. This occurs gradually with increasing wind speed, rather than involving discrete transport threshold velocity values for separate modes of transport.

The notable exception for this trend in h_v were the events of March 23 (Fig. 3-7, inset – red dots) where h_v, l_v, and ν_0 values remained constant as was predicted by Ho et al. (2011) for erodible beds. This difference in behaviour can be physically justified as spherical graupel grains over a non-cohesive bed are the conditions most closely resembling sand, and so the number flux profiles behaved more similarly to sand than for the other two nights of blowing snow.

Histograms of horizontal velocity further supported the relevant and dynamic role of the low-energy surface population of blowing snow (Fig. 3-8), and the decreasing importance of near-surface mass flux with increasing surface hardness. The bottom left plot in Figure 3-8 shows that for the nights with erodible beds and lower HHI (March 23 and March 3), the ratio of surface residual to total momentum is largest for low friction velocity. This is not sensitive to the

separation threshold height chosen. During low wind speeds, particle transport for the erodible beds was largely confined to the lower region with few high-energy surface impacts. The ratio of surface residual to total momentum, and therefore number flux, was much higher over erodible beds than over the wind-hardened rigid bed recordings on February 3 (Fig. 3-7 & 3-8). This complemented the fact that the low-energy surface transport on February 3 had the smallest contribution to total number flux. Thus particle type and snow bed properties played a significant role in the surface momentum balance, changing the uniformity of saltation profiles and wind momentum lost to surface transport. Mean particle diameters remained relatively similar over all recordings and thus snow transport models need to account for snow bed hardness or erodibility as there is a connection to a variable near surface transport momentum sink.

Analyzing the instantaneous wind speeds in Fig. 3-9a helps to explain the short timescale roles of gusts, high friction velocity and turbulence intensity for snow transport in recording #3. The turbulent sweep event ($u' > 0$, $w' < 0$) from 8 to 9 s generated considerable τ; this turbulent structure is widely reported to be involved in initiating aeolian sediment transport (Grass, 1971; Jackson, 1976; Sterk et al. 1998; Chapman et al., 2012). The 1 s sweep accounted for 29% and 25% of total absolute τ at 40 and 200 cm, respectively, and contributed 56% of total snow particle flux below 30 mm, but occupied only 8% of the time. Turbulent ejections ($u' < 0$, $w' > 0$) generated 39% of total absolute shear stress during the recording and contributed the same direction of τ values to friction velocity calculations but only resulted in 3% of total snow particle flux. Varying the lag time between wind and snow measurements from 0 to 1 second to determine the resultant snow flux had no significant effect on these calculations.

In this gusty alpine environment, periodic turbulent gusts generated the majority of momentum flux as seen by impact factors greater than unity at the surface for Q2 and Q4, and small contributions from Q1 and Q3 (Fig. 3-4). More importantly, recording #3 showed that the sweep event with strong positive u' fluctuation resulted in particle entrainment and transport, whereas the large ejection event was ineffective at generating snow transport. As suggested by Sterk et al. (1998), instantaneous wind speed is a potentially better predictor of snow transport than friction velocity. However, during each night, the mass flux scaled with increasing friction velocity (Table 3-2). This unlikely performance of friction velocity may help explain some of the

robustness of u_*-based time-averaged uniform trajectory blowing snow models, but requires further investigation. The role of sweep events such as this for initiating snow saltation is potentially important for developing models that couple turbulence to snow erosion, entrainment and mass flux and may help resolve current uncertainty in estimating threshold conditions for transport. The importance of understanding snow response to instantaneous wind speed is further increased in mountainous terrain where the 300 m of clear upwind fetch or 60 s of constant wind suggested by Takeuchi (1980) for saltation to fully develop is not always available. For a more general application, this requires further investigation of turbulent snow transport over longer time series and other snow conditions.

Designating creep as distinct from saltation as originally done by Bagnold (1941) is not only unnecessary but also physically inaccurate as snow transport displays a continuous spectrum of motions, similar to that proposed for sand by Anderson (1987), and individual particles can easily transition from one form of motion to another over their trajectories. However, two populations of motion in this spectrum could be identified in the analysis of Figs. 3-6 to 3-9. While undergoing wind speed fluctuations, the region of near-surface flux has the most temporally consistent transport (Fig. 3-9). This was also the region of largest velocity variance (Fig. 3-8), yet the consistent presence of the slow particle flow allowed the best fit of particle number flux and mean particle velocity to profiles suggested in the equilibrium sand transport literature. The worst fit of both gradients always occurred at the upper regions dominated by high-energy particles (Fig. 3-8). These high-energy particles constituted the population of fast moving grains that was most susceptible to changes in wind speed (Ho et al. 2014) and most temporally intermittent (Fig. 3-9).

The lower boundary condition for momentum transfer is complex due to creep and dependent on instantaneous wind speed and turbulent motions near the surface. As a result, equilibrium conditions were never found in the field observations reported here. Non-equilibrium saltation-wind interactions cannot be described with simple uniform trajectories. The majority of particle trajectories in saltation consist of short hop lengths and times, resulting in high frequencies of particle collisions that break surface bond structures, and create dense quasi-fluidized bed characteristics. The complexity of conservation of mass, momentum, and kinetic

energy in blowing snow in natural environments, such as measured here, cannot be understated, especially when the large rimed, aggregate tumblons were present. In the alpine snowpacks investigated, variable particle restitution coefficients contributed to this complexity. While high HHI wind-hardened surfaces exhibited similar behaviour of slip velocity and particle velocity gradients as rigid bed sand studies, complexities over a natural snowpack prevented conclusive bimodal "erodible" versus "non-erodible" scale relations that appear to be viable for sand (Ho et al., 2011). Blowing snow is a distinctive two-phase flow.

Despite arguments to the contrary for other materials (e.g. Sterk et al., 1998), saltating snow models relate mass flux to surface shear stress estimated from air motions well above the surface. These estimates are often based on a momentum deficit derived from the total number of particles in transport, neglecting the vertical heterogeneity of particle concentration and momentum within the snow saltation layer (Doorschot and Lehning, 2002). As all panels in Fig. 3-6 and 3-7 show, uniform descriptions of surface shear stress calculations based on concentration and flux measurements above 10 mm overlook the substantial wind momentum transferred into the creep layer (i.e. Zhang et al., 2007, Creyssels et al., 2009; Ho et al., 2011, 2012, 2014). Disregarding this flux prevents calculation of the full momentum balance. Accounting for variability in saltation trajectories would also allow for a dense surface flow to be represented that can feed upper regions (e.g. Nemoto and Nishimura, 2004) and create a self-consistent momentum balance. Andreotti (2004) wrote a further discussion of self-consistency errors of wind feedback in single trajectory saltation models.

The wide variety of snow saltation initiation mechanisms observed in this experiment is in contrast to classic initiation models that assume that a temporally-constant fraction of saltating grains begin motion through either aerodynamic entrainment or splash (e.g. Pomeroy and Gray, 1990). As seen in Fig. 3-9 and the supplementary video, in intermittent conditions this variability is magnified, as splash regimes themselves are intermittent, and depend on sufficient wind speed for adequate particle acceleration upon ejection from the snow surface.

3.5 Conclusion

This is the first investigation to measure outdoor snow particle flux and velocity immediately above the snow surface. It provides an opportunity to test certain observations of saltating particle flux trajectories measured in wind tunnels. Though observations were restricted to moderate wind speeds and intermittent transport, they show the importance of creep to the initiation of blowing snow transport and the transition to full saltation. Being able to relate high frequency turbulent wind speed to snow transport (e.g. Guala et al., 2008) is critical in the alpine environment (Naaim-Bouvet et al., 2011) and this study makes a contribution to understanding these dynamics.

PTV has proven to be a viable avenue for exploring complex wind-snow interactions at millisecond timescales in natural, non-steady state, high Reynolds number wind conditions. These results support the need for further conceptual advancement of models of snow particle movement, including initiation, rebound, multiple types of motion and the interaction of turbulent sweeps with particle erosion and entrainment. Over short timescales, snow particle motion is influenced by complex wind speed dependent initiation and rebound dynamics, including a dense near-surface flow whose presence and variation cannot be described by scalar aerodynamic entrainment and splash parameterizations. Wind-to-snow and snow-to-snow momentum transfer in the first few mm above the surface is critical for driving mechanisms of transport initiation and providing lower boundary conditions for two-phase atmospheric flows.

The results show a wide spectrum of particle motions exist with near-surface and upper level snow particle transport intrinsically linked through momentum and mass balances. The relative contributions of near-surface and upper level transport depend on wind strength and snowpack properties. Sand saltation velocity distribution models do not comprehensively describe transport of complex snow crystal structures such as the previously undescribed tumblon motions or snow particle shattering and sintering. Low-energy near-surface particles contributed significantly to snow transport as high near-surface particle concentrations compensated for reduced particle speeds, and sustained a layer of peak particle momentum and mass flux. The low-energy grains also contributed considerably to saltation by being a reservoir

of particles bouncing into saltation and by breaking snow bed matrix bonds, thus making particles more available by reducing the wind drag required for splash and entrainment.

The ability of the snowpack surface to absorb wind and particle momentum in the dense near-surface region of particle transport appears variable and substantial. The role that low-energy near-surface particles play in the wind-snow momentum balance and mass flux appeared dependent on snow surface hardness. Wind-hardened surfaces shared several trends similar to that of rigid sand-beds, though not all wind-tunnel observations could be replicated. As saltation dynamics are dependent upon creep particle motions, which mediate exchange between the snow surface and blowing snow, creep dynamics changes over varying surface hardnesses also result in changes in saltation, such as changes in velocity gradients, particle concentration, and rebound dynamics. Therefore the near-surface snow transport has far more intricate dynamics and greater flux relevance than previously described.

In the present study, the near-surface particle velocities reflected instantaneous wind speed fluctuations and never achieved equilibrium. As the snow transport was in constant readjustment to changes in wind velocity, and short time scale turbulence characteristics did not scale with long time averages, further characterizations of the time scale of relevance or relevant turbulence scaling relations in alpine terrain need to be performed before a steady-state equilibrium type saltation model (e.g. Pomeroy and Gray, 1990; Doorschot and Lehning, 2002) can be deemed appropriate for these situations. Furthermore, as contributions of shear stress from different τ quadrants are spatially and temporally variable and the mechanics of transport vary during gusts as seen in Section 3.3, the need to account for variable shear stress in high-resolution modeling (Doorschot et al., 2004; Groot Zwaaftink et al., 2014) is reinforced.

It could be very useful to compare modeled entrainment and splash ratios with PTV datasets, however longer recording times over a larger variety of snow types would be necessary to obtain statistically significant comparisons. Specifically, whether longer time-averaged statistics can account for periods of varying initiation during intermittent saltation, or can only apply in more nearly steady-state environments would be a useful finding for high temporal resolution applications (e.g. Groot Zwaaftink et al., 2014). PTV shows potential to answer many open questions in blowing snow research through quantification of momentum redistribution in

very near-surface particle motions. The use of high temporal-resolution outdoor PTV measurements may prove useful in future work for understanding how turbulence influences blowing snow processes in natural settings.

Key Points for Next Chapters

- Can one quantify the role of each turbulent quadrant event on blowing snow transport?
- Is there evidence of top-down or bottom-up mechanics driving blowing snow motions?
- Can one better quantify the drive-response mechanisms of wind-snow coupling in the frequency domain?

3.6 Acknowledgements

The authors acknowledge funding from the Canadian Foundation for Innovation, the Natural Sciences and Engineering Research Council of Canada, the Changing Cold Regions Network, Canada Research Chairs, the Global Institute for Water Security and Alberta Agriculture and Forestry. The assistance of the Fortress Mountain Resort in logistics is gratefully noted, as are the suggestions from Nicolas Leroux and Florence Naaim-Bouvet to improve the manuscript. Data is available upon request directly from the authors, john.pomeroy@usask.ca.

The document supplement can be found at:

https://www.the-cryosphere.net/10/3043/2016/tc-10-3043-2016-supplement.zip

3.6 References

Anderson, R. S., and P. K. Haff (1988), Simulation of eolian saltation., *Science*, *241*(4867), 820–3, doi:10.1126/science.241.4867.820.

Anderson, R. S. (1987), Eolian Sediment Transport as a Stochastic Process: The Effects of a Fluctuating Wind on Particle Trajectories, *J. Geol.*, *95*(4), 497–512, doi:10.1086/629145.

Andreotti, B. (2004), A two species model of aeolian sand transport, *J. Fluid Mech.*, *510*, 47–70.

Bagnold, R. A. (1941), *The Physics of Blown Sand and Desert Dunes*, 1st ed., Methuen & Co. Limited, London.

Brown, T., and J. W. Pomeroy (1989), A blowing snow particle detector, *Cold Reg. Sci. Technol.*, *16*, 167–174.

Budd, W. F. (1966), The Drifting of Non-Uniform Snow Particles, in *Studies in Antarctic Meteorology, Antarctic Research Series 9*, edited by M. J. Rubin, pp. 59–70, American Geophysical Union, Washington D.C.

Budd, W. F., W. R. J. Dingle, and U. Radok (1966), The Byrd snow drift project: Outline and basic results, in *Studies in Antarctic Meteorology*, edited by M. J. Rubin, pp. 59–70, American Geophysical Union, Washington D.C.

Chapman, C. a., I. J. Walker, P. a. Hesp, B. O. Bauer, and R. G. D. Davidson-Arnott (2012), Turbulent Reynolds stress and quadrant event activity in wind flow over a coastal foredune, *Geomorphology*, *151–152*, 1–12, doi:10.1016/j.geomorph.2011.11.015.

Creyssels, M., P. Dupont, a. O. El Moctar, A. Valance, I. Cantat, J. T. Jenkins, J. M. Pasini, and K. R. Rasmussen (2009), Saltating particles in a turbulent boundary layer: experiment and theory, *J. Fluid Mech.*, *625*, 47–74, doi:10.1017/S0022112008005491.

Dennis, D. J. C., and T. B. Nickels (2008), On the limitations of Taylor's hypothesis in constructing long structures in a turbulent boundary layer, *J. Fluid Mech.*, *614*, 197, doi:10.1017/S0022112008003352.

Doorschot, J., and M. Lehning (2002), Equilibrium saltation: mass fluxes, aerodynamic entrainment, and dependence on grain properties, *Boundary-layer Meteorol.*, *104*, 111–130.

Doorschot, J., M. Lehning, and A. Vrouwe (2004), Field measurements of snow-drift threshold and mass fluxes, and related model simulations, *Boundary-Layer Meteorol.*, *113*, 347–368.

Dyunin, A. K., and V. Kotlyakov (1980), Redistribution of snow in the mountains under the effect of heavy snow-storms, *Cold Reg. Sci. Technol.*, *3*, 287–294.

Fierz, C., R. Armstrong, Y. Durand, P. Etchevers, E. Greene, D. M. McClung, K. Nishimura, P. K. Satyawali, and S. A. Sokratov (2009), *The international classification for seasonal snow on the ground*, International Association of Cryospheric Sciences.

Foken, T., and B. Wichura (1996), Tools for quality assessment of surface-based flux measurements, *Agric. For. Meteorol.*, *78*, 83–105, doi:10.1016/0168-1923(95)02248-1.

Foken, T. (2008), *Micrometeorology*, Springer, Berlin.

Gauer, P. (1999), Blowing and Drifting Snow in Alpine Terrain : A Physically-Based Numerical Model and Related Field Measurements, Swiss Federal Institute of Technology Zurich.

George, W. K. (2007), Is there a universal log law for turbulent wall-bounded flows?, *Philos. Trans. A. Math. Phys. Eng. Sci.*, *365*(1852), 789–806, doi:10.1098/rsta.2006.1941.

Gordon, M., S. Biswas, P. a. Taylor, J. Hanesiak, M. Albarran-Melzer, and S. Fargey (2010), Measurements of drifting and blowing snow at Iqaluit, Nunavut, Canada during the star project, *Atmosphere-Ocean*, *48*(2), 81–100, doi:10.3137/AO1105.2010.

Gordon, M., S. Savelyev, and P. a. Taylor (2009), Measurements of blowing snow, part II: Mass and number density profiles and saltation height at Franklin Bay, NWT, Canada, *Cold Reg. Sci. Technol.*, *55*(1), 75–85, doi:10.1016/j.coldregions.2008.07.001.

Gromke, C., S. Horender, B. Walter, and M. Lehning (2014), Snow particle characteristics in the saltation layer, *J. Glaciol.*, *60*(221), 431–439, doi:10.3189/2014JoG13J079.

Groot Zwaaftink, C. D., M. Diebold, S. Horender, J. Overney, G. Lieberherr, M. B. Parlange, and M. Lehning (2014), Modelling Small-Scale Drifting Snow with a Lagrangian Stochastic Model Based on Large-Eddy Simulations, *Boundary-Layer Meteorol.*, *153*(1), 117–139, doi:10.1007/s10546-014-9934-2.

Guala, M., C. Manes, a. Clifton, and M. Lehning (2008), On the saltation of fresh snow in a wind tunnel: Profile characterization and single particle statistics, *J. Geophys. Res. Earth Surf.*, *113*(3), 1–13, doi:10.1029/2007JF000975.

Helgason, W., and J. W. Pomeroy (2005), Uncertainties in estimating turbulent fluxes to melting snow in a mountain clearing, in *Proc. 62nd Eastern Snow Conf*, pp. 129–142.

Ho, T. D., P. Dupont, A. Ould El Moctar, and A. Valance (2012), Particle velocity distribution in saltation transport, *Phys. Rev. E - Stat. Nonlinear, Soft Matter Phys.*, *85*(5), 1–5, doi:10.1103/PhysRevE.85.052301.

Ho, T. D., A. Valance, P. Dupont, and A. Ould El Moctar (2014), Aeolian sand transport: Length and height distributions of saltation trajectories, *Aeolian Res.*, *12*, 65–74, doi:10.1016/j.aeolia.2013.11.004.

Ho, T. D., A. Valance, P. Dupont, and A. Ould El Moctar (2011), Scaling laws in aeolian sand transport, *Phys. Rev. Lett.*, *106*(9), 4–7, doi:10.1103/PhysRevLett.106.094501.

Hutchins, N., K. Chauhan, I. Marusic, J. Monty, and J. Klewicki (2012), Towards reconciling the large-scale structure of turbulent boundary layers in the atmosphere and laboratory, *Boundary-Layer Meteorol.*, *145*(2), 273–306, doi:10.1007/s10546-012-9735-4.

Jackson, R. G. (1976), Sedimentological and fluid-dynamic implications of the turbulent bursting phenomenon in geophysical flows, *J. Fluid Mech.*, *77*(3), 531–560, doi:10.1017/S0022112076002243.

Kinar, N. J., and J. W. Pomeroy (2015), Measurement of the physical properties of the snowpack, *Rev. Geophys.*, *53*, doi:10.1002/2015RG000481.Received.

Kobayashi, D. (1972), Studies of Snow Transport In Low-Level Drifting Snow, *Contrib. from Inst. Low Temp. Sci.*, *A24*, 1–58, doi:10.1017/CBO9781107415324.004.

Li, B., and C. McKenna Neuman (2012), Boundary-layer turbulence characteristics during aeolian saltation, *Geophys. Res. Lett.*, *39*(11), 1–6, doi:10.1029/2012GL052234.

Li, L., and J. W. Pomeroy (1997), Estimates of Threshold Wind Speeds for Snow Transport Using Meteorological Data, *J. Appl. Meteorol.*, *36*, 205–213.

Lü, X., N. Huang, and D. Tong (2012), Wind tunnel experiments on natural snow drift, *Sci. China Technol. Sci.*, *55*(4), 927–938, doi:10.1007/s11431-011-4731-3.

Maeno, N., K. Araoka, and K. Nishimura (1980), Physical Aspects of the Wind-Snow Interaction in Blowing Snow, *J. Fac. Sci. Hokkaido Univ.*, *6*(1), 127–141.

Mcelwaine, J. N., N. Maeno, and K. Sugiura (2004), The Splash Function for Snow From Wind-Tunnel Measurements, *Ann. Glaciol.*, *38*, 71–78.

Morris, S. C., S. R. Stolpa, P. E. Slaboch, and J. C. Klewicki (2007), Near-surface particle image velocimetry measurements in a transitionally rough-wall atmospheric boundary layer, *J. Fluid Mech.*, *580*, 319–338, doi:10.1017/S0022112007005435.

Naaim-Bouvet, F., M. Naaim, H. Bellot, and K. Nishimura (2011), Wind and drifting-snow gust factor in an Alpine context, *Ann. Glaciol.*, *52*(58), 223–230, doi:10.3189/172756411797252112.

Namikas, S. L., B. O. Bauer, B. L. Edwards, P. A. Hesp, and Y. Zhu (2009), Measurements of Aeolian Mass Flux Distributions on a Fine-Grained Beach: Implications for Grain-Bed Collision Mechanics, *J. Coast. Res.*, *2009*(56), 337–341.

Nemoto, M., and K. Nishimura (2004), Numerical simulation of snow saltation and suspension in a turbulent boundary layer, *J. Geophys. Res. Atmos.*, *109*(18), doi:10.1029/2004JD004657.

Nishimura, K., and J. C. R. Hunt (2000), Saltation and incipient suspension above a flat particle bed below a turbulent boundary layer, *J. Fluid Mech.*, *417*, 77–102, doi:10.1017/S0022112000001014.

Nishimura, K. et al. (2014), Snow particle speeds in drifting snow, *J. Geophys. Res. Atmos.*, *119*, 9901–9913, doi:10.1002/2014JD021686.

Otsu, N. (1979), A Threshold Selection Method from Gray-Level Histograms, *IEEE Trans. Syst. Man. Cybern.*, *SMC-9*(1), 62–66.

Owen, P. R. (1964), Saltation of uniform grains in air, *J. Fluid Mech.*, *20*(2), 225, doi:10.1017/S0022112064001173.

Paterna, E., P. Crivelli, and M. Lehning (2016), Decoupling of mass flux and turbulent wind fluctuations in drifting snow, *Geophys. Res. Lett.*, 1–7, doi:10.1002/2016GL068171.

Pomeroy, J. W., X. Fang, and C. Ellis (2012), Sensitivity of snowmelt hydrology in Marmot Creek, Alberta, to forest cover disturbance, *Hydrol. Process.*, *26*(12), 1891–1904, doi:10.1002/hyp.9248.

Pomeroy, J. W., and D. Gray (1990), Saltation of snow, *Water Resour. Res.*, *26*(7), 1583–1594.

Pomeroy, J. W., and L. Li (2000), Prairie and Arctic areal snow cover mass balance using a blowing snow model, *J. Geophys. Res. …*, *105*(D21), 26619–26634.

Pomeroy, J. W., and D. H. Male (1992), Steady-state suspension of snow, *J. Hydrol.*, *136*(1–4), 275–301, doi:10.1016/0022-1694(92)90015-N.

Pomeroy, J. W., and D. M. Gray (1995), *Snowcover: Acumulation, Relocation, and Management*, Saskatoon, SK.

Rosi, G. a., M. Sherry, M. Kinzel, and D. E. Rival (2014), Characterizing the lower log region of the atmospheric surface layer via large-scale particle tracking velocimetry, *Exp. Fluids*, *55*(5), 10, doi:10.1007/s00348-014-1736-2.

Schmidt, R. A. (1984), Measuring Particle Size and Snowfall Intensity in Drifting Snow, *Cold Reg. Sci. Technol.*, *9*, 121–129.

Schmidt, R. A. (1982), Vertical Profiles of Wind Speed, Snow Concentration, and Humidity in Blowing Snow, *Boundary-Layer Meteorol.*, *23*, 223–246, doi:10.1016/j.soncn.2013.06.001.

Schmidt, R. A. (1980), Threshold Wind-Speeds And Elastic Impact In Snow Transport, *J. Glaciol.*, *26*(94), 453–467.

Schweizer, J., B. Jamieson, and M. Schneebeli (2003), Snow avalanche formation, *Rev. Geophys.*, *41*(4), doi:10.1029/2002RG000123.

Sørensen, M. (1997), On the effect of time variability of the wind on rates of aeolian sand transport, *Aarhus Geosci.*, *7*, 73–77.

Sterk, G., a. F. G. Jacobs, and J. H. Van Boxel (1998), The effect of turbulent flow structures on saltation sand transport in the atmospheric boundary layer, *Earth Surf. Process. Landforms*, *23*(10), 877–887.

Stout, J., and T. Zobeck (1997), Intermittent saltation, *Sedimentology*, *44*, 959–970.

Stull, R. (1988), *An Introduction to Boundary layer Meteorology*, Kluwer Academic Publisher, Dordrecht, The Netherlands.

Sugiura, K., and N. Maeno (2000), Wind-tunnel measurements of restitution coefficients and ejection number of snow particles in drifting snow: determination of splash functions, *Boundary-Layer Meteorol.*, *95*(1), 123–143.

Sugiura, K., K. Nishimura, N. Maeno, and T. Kimura (1998), Measurements of snow mass flux and transport rate at different particle diameters in drifting snow, *Cold Reg. Sci. Technol.*, *27*(2), 83–89, doi:10.1016/S0165-232X(98)00002-0.

Tabler, R. D. (1991), Snow Transport as a Function of Wind Speed and Height, in *Proceedings, Cold Regions Sixth International Specialty Conference TCCP/ASCE*, pp. 729–738, Cold Regions Engineering, West Lebanon, NH.

Takeuchi, M. (1980), Vertical profile and horizontal increase of drift snow transport, *J. Glaciol*, *26*(94).

Toloui, M., S. Riley, J. Hong, K. Howard, L. P. Chamorro, M. Guala, and J. Tucker (2014), Measurement of atmospheric boundary layer based on super-large-scale particle image velocimetry using natural snowfall, *Exp. Fluids*, *55*(5), 14, doi:10.1007/s00348-014-1737-1.

Tominaga, Y., T. Okaze, A. Mochida, Y. Sasaki, M. Nemoto, and T. Sato (2012), PIV measurements of saltating snow particle velocity in a boundary layer developed in a wind tunnel, *J. Vis.*, *16*(2), 95–98, doi:10.1007/s12650-012-0156-8.

Ungar, J. E., and P. K. Haff (1987), Steady state saltation in air, *Sedimentology*, *34*(2), 289–299, doi:10.1111/j.1365-3091.1987.tb00778.x.

van Boxel, J. ., G. Sterk, and S. . Arens (2004), Sonic anemometers in aeolian sediment transport research, *Geomorphology*, *59*(1–4), 131–147, doi:10.1016/j.geomorph.2003.09.011.

Vickers, D., and L. Mahrt (1997), Quality control and flux sampling problems for tower and aircraft data, *J. Atmos. Ocean. Technol.*, *14*(3), 512–526, doi:10.1175/1520-0426(1997)014<0512:QCAFSP>2.0.CO;2.

Willetts, B. B., J. McEwan, and M. A. Rice (1991), Initiation of motion of quartz sand grains, *Acta Mech.*, *1*, 123–134.

Winstral, A., D. Marks, and R. Gurney (2013), Simulating wind-affected snow accumulations at catchment to basin scales, *Adv. Water Resour.*, *55*, 64–79, doi:10.1016/j.advwatres.2012.08.011.

Zhang, W., Y. Wang, and S. J. Lee (2007), Two-phase measurements of wind and saltating sand in an atmospheric boundary layer, *Geomorphology*, *88*(1–2), 109–119, doi:10.1016/j.geomorph.2006.10.017.

Zhu, W., R. van Hout, and J. Katz (2007), PIV Measurements in the Atmospheric Boundary Layer within and above a Mature Corn Canopy. Part II: Quadrant-Hole Analysis, *J. Atmos. Sci.*, *64*(8), 2825–2838, doi:10.1175/JAS3990.1.

CHAPTER 4
COHERENT STRUCTURES IN THE ATMOSPHERIC SURFACE LAYER DRIVING BLOWING-SNOW TRANSPORT

Abstract

Turbulent bursts are considered critical for blowing-snow transport and initiation but the interaction of wind and snow is not fully understood. To better characterize the coupling of turbulent structures and blowing-snow transport, observations collected in natural environments at the necessary high resolution timescales are needed. To address this, high frequency measurements of wind, blowing-snow density and particle velocity were made in the Canadian Rockies. During blowing-snow storms, modified variable-interval time averaging identified and coupled periods of near-surface blowing snow and shear-stress-producing motions in the lowest 2 m of the atmospheric surface layer. This has allowed the identification of turbulent motions responsible for blowing snow, and allows a better understanding of the event-driven mechanics of initiation and sustained transport. The type of coherent structures generating Reynolds stress were as important as the magnitude of Reynolds stress in initiating and sustaining near-surface blowing snow. The results suggest that blowing-snow models driven by time-averaged shear stress lack physical realism in the near-surface region. The next phase of blowing-snow model development should incorporate representations of coherent turbulent structures.

This manuscript has been modified for inclusion in this thesis with permission: Aksamit, N. O., and J. W. Pomeroy (2017), The Effect of Coherent Structures in the Atmospheric Surface Layer on Blowing-Snow Transport, *Boundary-Layer Meteorol.*, doi:10.1007/s10546-017-0318-2

4.1 Introduction

Wind transport of snow is a turbulence-driven phenomenon affecting mountain hydrology (Pomeroy et al., 2012; Winstral et al., 2013), glaciology (Dyunin and Kotlyakov, 1980), and avalanche safety (Schweizer et al., 2003). Modern concepts of turbulence in the atmospheric surface layer (ASL), the layer interacting with the snow surface, have migrated away from the

classically chaotic descriptions of Reynolds (1895) with the discovery of what have been termed coherent structures (Hussain, 1983; Narasimha and Kailas, 1990; Träumner et al., 2015). As there is still no commonly accepted definition of coherent structures, the present study continues in the vein of Robinson (1991) with the definition of "a three-dimensional region of the flow over which at least one fundamental flow variable exhibits significant correlation with itself or with another variable over a range of space and/or time that is significantly larger than the smallest local scales of the flow."

While the role of coherent structures in scalar and momentum transfer in the boundary layer has been widely studied, coupling specific turbulent motions to blowing snow mechanisms is challenging. Spatially- or temporally-averaged measurements are economical, robust and relatively easy to use, resulting in many blowing-snow models that use low resolution measurements (Pomeroy and Gray, 1990). Since the seminal work of Bagnold (1941), a single time-averaged variable, most often the friction velocity, u_*, is typically used to study and model sediment transport as a steady-state phenomenon (Bauer et al., 2013). For aeolian processes, however, non-stationary flow composed of large coherent structures enhance fluctuations in particle concentrations because of the nonlinear relationship between the flow and sediment flux (Sørensen, 1997; Shugar et al., 2010). Snow transport often occurs in mountainous terrain where topographically-driven or modified flow structures are present (Chapman et al., 2012, 2013; Helgason and Pomeroy, 2012). Additionally, severe blowing snow often occurs during the passage of frontal systems where atmospheric conditions change rapidly and steady-state conditions are not achieved. Because of this, the common use of long-time mean values representing inner-layer equilibrium conditions in blowing-snow models is known to be physically inaccurate and obscures the transient nature of turbulent scalar and momentum transfer (Naaim-Bouvet et al., 2011; Paterna et al., 2016).

From the viewpoint of quadrant analysis (Lu and Willmarth, 1973), specific structures of turbulent motions have been hypothesized to play various roles in sediment transport (Grass, 1971; Jackson, 1976; Heathershaw and Thorne, 1985; Nelson et al., 1995; Bauer et al., 1998; Sterk et al., 1998; Schönfedlt and von Löwis, 2003; Leenders et al., 2005; Diplas et al., 2008; Lelouvetel et al., 2009; Chapman et al., 2012, 2013; Li and McKenna Neumann, 2012), and it is widely

accepted that turbulent bursts, whether defined as structured or not, play a vital role in sediment flux mechanics (Willetts et al., 1991, Naaim-Bouvet et al., 2011; Bauer et al., 2013). Thus, shorter timescales, or using a more comprehensive characterization of turbulence than time-averaged u_*, may be better suited to describe the nature of blowing-snow mechanics (Sterk et al., 1998; Doorschot et al., 2004; Kok et al., 2012). Understanding the role of coherent structures in blowing snow may be a pathway to this end (Nishimura et al., 2014).

The difficulties associated with obtaining high frequency and high spatial resolution aeolian flux measurements have only recently become surmountable with the availability of high-speed videography and particle-tracking algorithms (Lü et al., 2012; Tominaga et al., 2012; Gromke et al., 2014; Groot Zwaaftink et al., 2014; Aksamit and Pomeroy, 2016; Paterna et al., 2016). Investigating the role of coherent structures in blowing-snow transport using the wind tunnel is limited because the spectrum of eddy sizes present is insufficient to represent those active in the ASL (Narasimha et al., 1990; Guala et al., 2011; Keylock et al., 2012). To date, little research has been conducted that identifies connections between aeolian transport and coherent structures (Bauer et al., 2013 and references therein); this includes blowing-snow saltation.

The purpose of the present study is to better understand the role that coherent structures in the ASL play in lowest 2 m of near-surface blowing-snow transport. High frequency turbulence and blowing-snow flux measurements are necessary to determine all relevant scales of motion in the two-phase system (Bauer et al., 2013). A field campaign was conducted using 3D ultrasonic anemometry and laser-illuminated particle tracking velocimetry (PTV) to measure turbulent motions and near-surface blowing-snow transport in alpine terrain. An objective coherent event identification scheme then delimited individual blowing-snow events in order to couple them to the responsible turbulent structures. Through this, a conceptual model of near-surface blowing-snow transport over a variety of snow and wind conditions was verified.

4.2 Methods

4.2.1 Fieldwork

Fieldwork was conducted during night time blowing-snow events between November 2015 and March 2016, at the Fortress Mountain Snow Laboratory, Kananaskis Valley, Alberta,

Canada (Figure 4-1). Measurements were taken over locally level terrain on a valley bench at 2000 m, immersed amongst steep alpine faces. Valley bottom elevations of 1500 m rise to 2900 m ridge tops over less than 5.5 km in the region. This location presented the opportunity of studying the effect of non-stationary flow, with high turbulence intensity, but no immediate ($\leq$ 200 m) bluff body interference. During the season of data collection, the ground was snow covered and the shrub vegetation was buried with snow depths fluctuating between 0.4 and 0.8 m. Two Campbell Scientific CSAT3 ultrasonic anemometers were positioned at different heights on a single mast to measure wind speed at 50 Hz in three dimensions. Measurement heights above the snow surface varied as snow depth fluctuated over the season (0.1-0.4 and 1.4-1.7 m). Wind characteristics at this site were further discussed by Aksamit and Pomeroy (2016). High frequency energy losses can be estimated using the equations of van Boxel et al. (2004). While these losses can be up 30% for the lowest measurements, the inclusion of this high frequency energy (e.g. with a hot wire anemometer) would increase small fluctuations and the event detection results would improve.

A mobile camera system collected laser-illuminated high-speed video of night time snow particle transport for the purpose of snow PTV, as described by Aksamit and Pomeroy (2016). The camera was situated 0.3 m laterally from the lower anemometer head, in a spanwise orientation to the wind (Fig. 4-1) and was rotated several times per night so that the light plane was parallel to the dominant wind direction. At the upper end of the energy spectrum, particle concentration is a stochastic process with fluctuations related to particle dynamics and surface impacts (Anderson, 1987; Liu et al. 2012), while at the lower end, large eddies drive sediment transport concentrations (Baas, 2006; Liu et al., 2009). Because camera memory limited the length of high frame rate recordings, a two-pronged recording approach was necessary to capture all relevant timescales of blowing-snow motion. Subsequent recordings alternated between short, high frame rate, PTV-capable recordings (21-28 second durations, 1350-2050 frames per second) and longer recordings (550-1150 second durations, 50-200 frames per second). Concurrent anemometer measurements were continuous throughout the nights. The camera recorded an approximately 30 mm × 140 mm plane parallel to the flow of saltating snow (Fig. 4-1) on the nights of November 20, December 4 and 8, 2015, and February 3 and March 3, 2016.

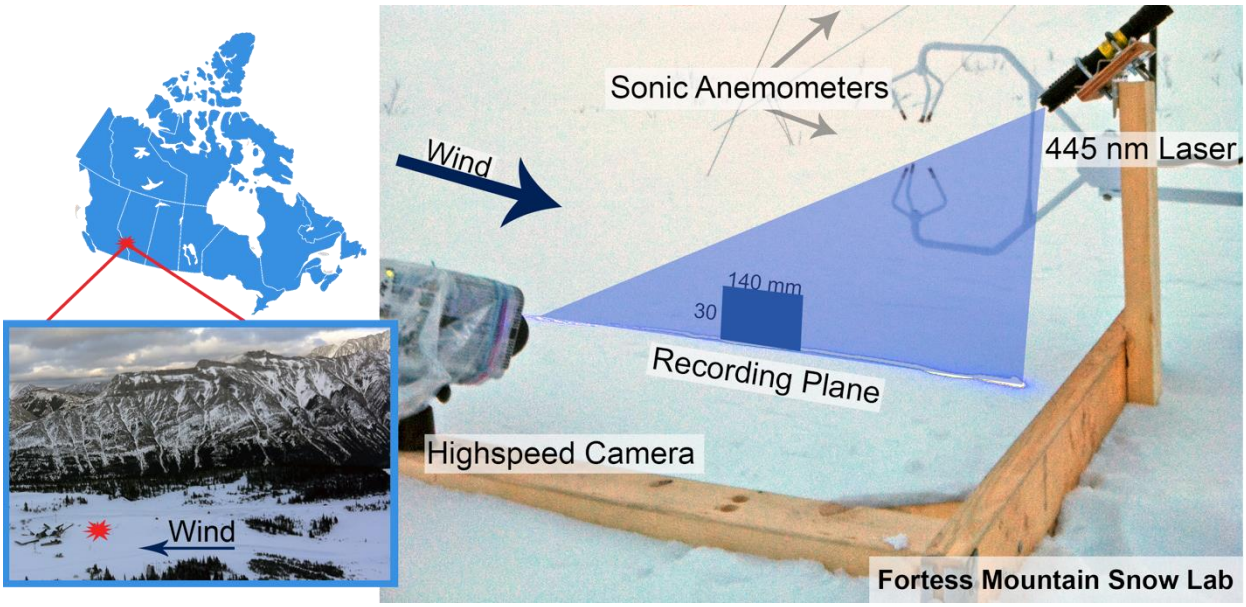

Figure 4-1: Field site location and recording apparatus setup with meteorological measurements, Fortress Mountain Snow Laboratory, Kananaskis, Alberta. The red mark indicates the location of the blowing-snow measurement devices as viewed from the West with respect to the upwind fetch.

Each blowing-snow recording consists of 2.7-5.8 × 10^4 frames, depending on frame resolution, totaling 2 million frames over 4.6 hours for 47 blowing-snow recordings, with 10.5 minutes of blowing-snow PTV. Descriptions of the snow surface, snow densities from the top 0.05 m of the snowpack, average air and snow surface temperatures, surface hand hardness indices, diameters of grains in transport, and ranges of mean wind speeds for the four nights can be found in Table 4-1.

Concurrent wind and video measurements were synchronized prior to each night of recording to minimize data logger timestamp drift. The wind was largely non-stationary during the nights of recording as also noted by Aksamit and Pomeroy (2016). For each recording, wind measurements were rotated such that the x-axis was parallel to the streamwise direction, u, and spanwise and vertical wind (v, w respectively) had a zero-mean following Kaimal and Finnigan (1994).

	Surface description	Snow surface density (kg m^{-3})	Air/Snow surf. temp	Surface hardness	Grain size range (mm)	Mean 0.4 m wind speeds (m s^{-1})	Slow/Fast recording length (s)
Nov. 20	0.02-0.03 m wind slab	N/A	-10C/ N/A	Pencil	N/A	2.7 - 3.9	4161 / 0
Dec. 4	Pockets of drifted snow on wind slab	390	-3C/-4C	Pencil	0.25-0.75	2.4 - 6.4	5422 / 266
Dec. 7	0.01 m fresh snow on wind slab	137	-3 / -3.5	4 Finger	0.5-1.5	1.5-3.0	2137 / 56
Feb. 3	Fine decomposing grains on wind slab/sastrugi	262	-10C/-10C	1 Finger-Pencil	0.5-1	3.6 – 5.7	3014 / 112
Mar. 3	Fresh snow, not snowing	156	-2C/-5C	Fist	0.5	3.5 – 4.8	1152 / 195

Table 4-1: Snow surface and meteorological conditions during each night of blowing snow. Missing values are indicated by 'N/A'. Surface hardness is measured by the hand hardness index.

4.2.2 Blowing-snow Signal Processing

Greyscale blowing-snow recordings were binarized following the algorithm of Otsu (1979) to obtain blowing-snow particle concentrations per frame. Similar techniques have been used in wind tunnel sand-transport concentration studies (e.g. Liu et al., 2012) and natural blowing-snow studies (e.g. Gordon et al., 2009). The binarization threshold varied with density of saltation in each frame and accounted for varying illumination. After binarization, quality control tests were implemented to eliminate false positive snow measurements from camera sensor "hot spots" during low transport periods as well as to adjust for low light conditions during periods of high transport when the laser was largely obscured. A flood-fill algorithm was then implemented to identify individual snow particles and estimate their equivalent particle diameters. By making the assumptions of constant snow particle density equal to ice (917 kg m^{-3}) and particle sphericity, airborne blowing-snow density ρ_{bs} was estimated per frame as by Aksamit and Pomeroy (2016).

In addition, 50 Hz PTV time series of mean horizontal particle velocity u_p, mean horizontal velocity of ascending particles, $u_{p\uparrow}$, and mean vertical velocity of ascending particles, $v_{p\uparrow}$ were generated. The particle velocity time series have increased noise and amplified fluctuations during periods of high wind speed or low particle number density, thus particle velocity time series were weighted by the number of particles tracked per frame to give the corresponding directional particle number flux values, Q_u, $Q_{u\uparrow}$, and $Q_{v\uparrow}$ in units of (number of

particles) × m s^{-1}. The PTV time series were used to investigate a conceptual model of sweeps and ejections in horizontal and vertical transport of grains (e.g. Lelouvetel et al., 2009).

4.2.3 Delimiting Turbulent Structures

The key assumption of this work is that specific strong turbulent structures can drive blowing snow and are superimposed on relatively inactive local turbulence (e.g. Sterk at al., 1998; Shih et al., 2017). Thus, an objective method able to identify and characterize active events in wind and snow time series was necessary. Two of the most widely used techniques for turbulent motion identification are variable-interval time averaging (VITA) (Blackwelder and Kaplan, 1976) and quadrant hole analysis (Lu and Willmarth, 1973; Wallace, 2016). The basis of VITA analysis is the identification of periods of high variance in a turbulent time series, $f(t)$. Define

$$\hat{f}(t,T) = \frac{1}{T}\int_{t-T/2}^{t+T/2} f(t)^2 dt - \left[\frac{1}{T}\int_{t-\frac{T}{2}}^{t+\frac{T}{2}} f(t)dt\right]^2, \tag{4-1}$$

where T is chosen as the length of an averaging neighborhood. In general, VITA analysis seeks to find all t when $\hat{f}(t) > \mathrm{k_V}\,\overline{f^2}$, where k_V is an arbitrary scalar threshold and the overbar indicates a space or time average. Depending on the choice of T, this scheme essentially detects times of high df/dt that correspond to the onset or end of a turbulent burst (Morrison et al., 1989).

Quadrant hole analysis (Lu and Willmarth, 1973) identifies times when Reynolds stress (τ) exceeds a given threshold or 'level':

$$|\tau(t)| = |-\rho_{air} u'(t)w'(t)| \geq k_Q \rho_{air}\sqrt{\overline{u'^2} + \overline{w'^2}}, \tag{4-2}$$

where ρ_{air} is the approximate density of air during recording, u' and w' are the fluctuating values of streamwise and vertical velocity components as determined by Reynolds decomposition, and k_Q is a user-defined threshold, the hole size.

As noted by Diplas et al. (2008) and confirmed by Valyrakis et al. (2010), strong fluctuations in streamwise velocity are a necessary but not sufficient condition to dislodge sediment and initiate aeolian transport. Sequences of turbulent events have a stronger association with initiation of transport than do individual high shear stress events (Shih et al., 2017). Morrison et al. (1989) coined the term "VITA+LEVEL analysis" as a combination of VITA with the level-based technique of quadrant analysis in a two-part algorithm to delimit entire turbulent events, instead of single extreme fluctuations or accelerations. The VITA+LEVEL analysis was found to be less dependent on the choice of T, k_V and k_Q than either of its component schemes and more objectively identified the full duration of turbulent motions (Morrison et al., 1989). VITA+LEVEL also more accurately delimited visually identified turbulent motions than VITA and quadrant hole analysis (Tubergen and Tiederman, 1993).

In the VITA+LEVEL analysis, a preliminary point of interest is identified when the time series exceeds both VITA and quadrant hole thresholds. The second step of the VITA+LEVEL analysis delimits the entire "active" turbulent event by including the neighboring points that exceed quadrant hole thresholds. The result of the scheme is an indicator function:

$$ID(t) = \begin{cases} 1 & \text{when conditions are met} \\ 0 & \text{otherwise} \end{cases}, \tag{4-3}$$

Separate ID functions were generated for the snow and wind, ID_{Snow} and ID_{Wind}, respectively. For the purpose of this study, the contiguous blocks of time where $ID(t) = 1$ are assumed to be coherent motions in either the wind or snow signals and are referred to as "events." In a comparison of VITA, quadrant hole, and VITA+LEVEL techniques, VITA+LEVEL applied to τ was "very accurate" at identifying the correct number and duration of turbulent events when the appropriate thresholds were chosen (Tubergen and Tiederman, 1993). Thus, τ was used in the VITA+LEVEL algorithm for comparison with snow transport signals. A variety of snow signals were used for comparison including ρ_{bs}, and directional particle number flux time series Q_u, $Q_{u\uparrow}$, and $Q_{v\uparrow}$.

For each recording, pairs of wind and snow signals were analyzed using the same k_V, k_Q and T. To verify that coupling identified in the two-phase system was not an artefact of an arbitrary choice of T, k_V and k_Q, and because there is no precedent for VITA+LEVEL analysis of any aeolian transport in complex terrain, 600 combinations of the VITA+LEVEL variables were used on each pair of wind and snow signals. Their ranges covered those commonly found in the literature: $0.4 \leq T \leq 10$ seconds spaced logarithmically, $0.01 \leq k_v \leq 0.05$ with a step of 0.004, and $0.5 \leq k_Q \leq 4$ with a step of 0.38 (Luchik and Tiederman, 1987; Morrison et al., 1989, Narasimha and Kailas, 1987, 1990; Bauer et al., 1998; Sterk et al., 1998; Wiggs and Weaver, 2012). Average trends in wind-snow coupling present over all combinations were then analyzed.

Example results of the VITA+LEVEL analysis applied to five seconds of recording from February 3 are presented in Figure 4-2. Figures 4-2a and 4-2b depict the same two time series: low anemometer τ in blue and ρ_{bs} in orange. Highlighted green regions in Fig. 4-2a cover the VITA+LEVEL events detected in the wind signal while purple regions in the Fig. 4-2b cover VITA+LEVEL snow events. Purple and yellow asterisks indicate sweep or ejection motions greater than the quadrant hole size during the wind or snow events.

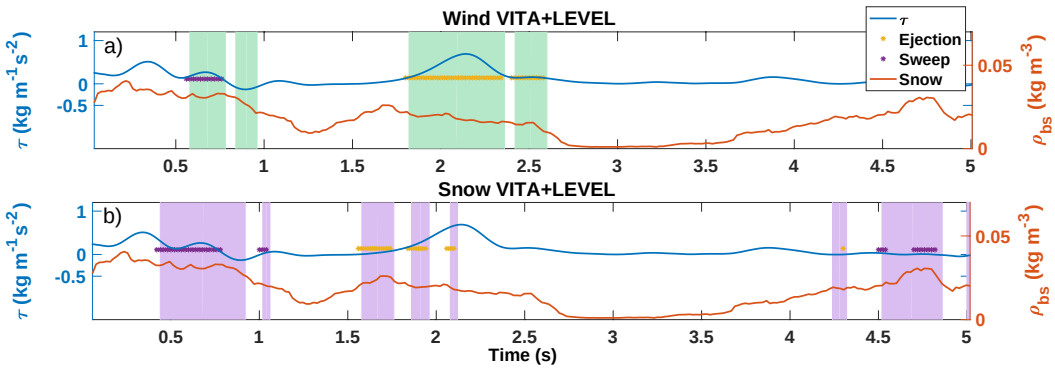

Figure 4-2: The VITA+LEVEL analysis applied to Reynolds stress and ρ_{bs} time series. 4-2a shows when $ID_{Wind} = 1$ with green highlighting, and $ID_{Snow} = 1$ is shown with purple highlighting in 4-2b. Purple (yellow) asterisks indicate moments of strong sweep (ejection) during VITA+LEVEL events.

4.2.4 Sweep- and Ejection-Driven Events

The use of the level threshold in the VITA+LEVEL analysis allows identification of coherent wind events in accordance with quadrant analysis, where each quadrant corresponds with the location of the $(u'(t), w'(t))$ signal (Q1-'outward motions': $u' > 0, w' > 0$; Q2-'ejections': $u' < 0, w' > 0$; Q3-'inward motions': $u' < 0, w' < 0$; Q4-'sweeps': $u' > 0, w' < 0$). As the majority of shear stress at the surface during sediment transport is generated by sweeps and ejections, (Grass, 1971; Jackson, 1976; Bauer et al., 1998; Li and McKenna Neumann, 2012), ID_{wind} functions were subdivided into ID_{Sw} and ID_{Ej}, and ID_{undef} if sweeps (e.g. 0.5-0.7 s, Fig. 4-2a), ejections (e.g. 1.9-2.5 s, Fig. 4-2a), or both were present during wind events, respectively. In what follows, Sw and Ej subscripts indicate sweep and ejection specific versions of the VITA+LEVEL metrics, and superscripts indicate the snow time series compared with τ.

As the camera frame was located laterally in the spanwise direction from the anemometer mast, and because of inertial lag effects in aeolian transport (Anderson and Haff, 1988; Butterfield, 1991; McEwan and Willetts, 1991; Spies et al., 2000, Arnold 2002; Baas, 2006; Wiggs and Weaver, 2012), it was assumed that significant events in the blowing-snow signal never preceded the responsible motion in the wind signal. From the onset time of a blowing-snow event, the responsible wind event was identified as the nearest preceding VITA+LEVEL block in a two second neighborhood and allowing for temporal overlap. This neighborhood follows the suggestions of multiple researchers that there is no more than a 1-2 s lag time for sand saltation to respond to changes in wind speed (Bauer et al., 2013 and references therein), and includes any delay caused by the 0.3 m distance between measurements. It should be noted that precisely identifying the lag between the onset of a wind and snow event was practically impossible because of differing timescales dominant in the two signals, such as longer active saltation periods because of particle cloud inertial effects prolonging transport between turbulent bursts (Ellis, 2006; Shih et al., 2017). ID_{Snow} was subdivided in the same manner as ID_{wind}, with subdivisions corresponding to the nearest previous wind event with which a blowing-snow event was coupled.

While the sweeps and ejections appeared to cycle on occasion, no reproducible cycle could be identified, as also noted in several of the aeolian sand studies summarized by Bauer et al.

(2013). It is unlikely that any consistent sweep-ejection cycle (e.g. Zhu et al., 2007) artificially skewed the average coupling of blowing snow and responsible wind events.

4.2.5 VITA+LEVEL Analysis Metrics

Mean time lags, ℓ_{Ej} and ℓ_{Sw}, measured the average duration between the VITA+LEVEL ejections or sweeps and subsequent blowing-snow events. The percentage of the total number of blowing-snow events coupled with either quadrant, π_{Ej} and π_{Sw}, indicated how often each quadrant was coupled with near-surface snow motions. Two metrics, the percent of the total duration of wind events overlapping with snow events, $P(W_T)$, and the percent of snow events overlapping with wind events, $P(S_T)$, were adapted from Tubergen and Tiederman (1993):

$$P(W_T) = \frac{T_{WS}}{T_W} = \frac{\sum_{t\in D} ID_{Wind} ID_{Snow}(t)}{\sum_{t\in D} ID_{Wind}(t)} \quad \text{and} \tag{4-4}$$

$$P(S_T) = \frac{T_{WS}}{T_S} = \frac{\sum_{t\in D} ID_{Wind} ID_{Snow}(t)}{\sum_{t\in D} ID_{Snow}(t)}, \tag{4-5}$$

where T_W and T_S are the length of the VITA+LEVEL identified wind and snow events, respectively, T_{WS} is the total time where the VITA+LEVEL analysis detects active motions in both signals, and D is the time domain of a given recording. T_W and T_S can be visualized in Figs. 4-2a-b as the total duration of green and purple highlighted regions, respectively. T_{WS} is the total overlap of the two regions. For each recording, ID_{Sw} and $ID_{\mathrm{E}j}$ were temporally delayed by ℓ_{Sw} and ℓ_{Ej}, respectively, to maximize T_{WS}.

To measure the performance of the VITA+LEVEL wind events to transport snow mass, $P(S_Q)$ was generated by weighting $P(S_T)$ by the concurrent blowing snow density:

$$P(S_Q) = \frac{Q_{WS}}{Q_S} = \frac{\sum_{t\in D} ID_{Wind} ID_{Snow}(t)\rho_{bs}}{\sum_{t\in D} ID_{Snow}(t)\,\rho_{bs}}, \tag{4-6}$$

where Q_{WS} is the sum of the blowing-snow density while both signals are "active," Q_S is the sum of density when only the blowing-snow signal is "active." Event specific metrics $P(W_T)_{Ej}$, $P(S_T)_{Ej}$, $P\left(S_Q\right)_{Ej}$, $P(W_T)_{Sw}$, $P(S_T)_{Sw}$, $P\left(S_Q\right)_{\mathrm{Sw}}$ were calculated by replacing ID_{Wind} with the corresponding ID_{Ej} or ID_{Sw}, and allowed comparison of the impact on snow transport of the two types of gusts.

The amount of blowing snow generated by each quadrant event was normalized by the magnitude of Reynolds stress present:

$$GS_i = \frac{\sum_{t\in D} ID_i(t)\rho_{bs}(t)}{\sum_{t\in D} ID_i(t)|\tau(t)|}, \tag{4-7}$$

where $i \in$ {Sw, Ej}. The ratio $GS_{Sw}/GS_{\mathrm{E}j}$ indicates whether sweeps or ejections are more effective at transporting blowing snow given the same absolute τ. If blowing-snow flux in these recordings is driven by the magnitude of τ, as is assumed by u_*^2 blowing-snow models through $u_* = \sqrt{\bar{\tau}/\rho_{air}}$ (e.g. Pomeroy and Gray, 1990), then the quadrant generating shear stress should be irrelevant and GS_{Sw}/GS_{Ej} should be close to unity.

4.3 Results

In Sect. 4.1 and 4.2, parameter averages and nightly averages of the VITA+LEVEL metrics are referred to with the following meanings: parameter averages indicate the mean value of a given metric for a specific recording over all 600 threshold (k_V and k_Q) and averaging time (T) combinations. Nightly averages are the mean values of parameter averages for a given night. Ranges of parameter-averaged metrics for each night of recording are detailed in Appendix 1 in Table A1 for the VITA+LEVEL analysis of τ with ρ_{bs}, Q_u, $Q_{u\uparrow}$, and $Q_{v\uparrow}$, with nightly averages in parentheses.

Sweeps and outward motions were not easily distinguishable in the observations. "Top-down" motions (cf. Hunt and Morrison, 2000) appeared in the data as w' fluctuated around zero during highly autocorrelated periods of largely positive u' originating at the high anemometer

before appearing in the lower time series. Near the snow surface, eddies are stretched predominantly in the streamwise direction, with much smaller vertical extent (Hunt and Morrison, 2000), leading to less pronounced vertical fluctuations than streamwise fluctuations. These VITA+LEVEL events will be regarded as the larger scale sweep motion instead of the local turbulence fluctuations, as in Shih et al. (2017).

Net Reynolds stress was positive during each recording, indicating mean momentum transfer towards the surface. For each recording ID_{undef} was rarely non-zero, adding confidence to the notion that the VITA+LEVEL analysis was identifying large-scale coherent turbulent structures and not brief fluctuations from local turbulence. Sweeps and ejections generated the majority of τ with mean combined contributions of ≈62% over the study period. Reynolds stress generated by sweeps was slightly larger than by ejections. There was an increased presence of ejections away from the surface for each recording, as is typical for turbulent boundary layers (Wallace et al., 1972).

All metrics had comparable values when the VITA+LEVEL analysis compared blowing-snow time series with either upper or lower anemometer signals. As well, using the VITA+LEVEL analysis to compare the two τ signals, nightly averages of $P(S_T)^\tau$ and $P(W_T)^\tau$ were as high as 72% to 92% and 75% to 84%, respectively, after assuming events would be present at the upper anemometer prior to the lower. These high values indicate the turbulent motions that coupled with blowing-snow events were often present at both heights, with a "top-down" character. Because of this strong agreement, the lower anemometer τ time series was used for all VITA+LEVEL analysis, unless otherwise noted.

4.3.1 VITA+LEVEL Analysis of Reynolds Stress and Blowing-Snow Density

Turbulent motions and blowing-snow events were coupled with varying accuracy (Table A1), largely depending on snow surface conditions. Nightly averages of $P(S_T)^\rho$ and $P(W_T)^\rho$ varied between $10-35\%$ and $11-34\%$, respectively, with results from the 600 parameter combinations spanning a much larger range. Choosing only the best performing parameters increased nightly coupling averages: $P(S_T)^\rho$ between $51-82\%$ and $P(W_T)^\rho$ between $35-87\%$.

$P(S_T)^\rho$ and $P(W_T)^\rho$ values were typically better for longer averaging times, $T \in [2-10]$ seconds, and lower thresholds $k_v \in [0.01-0.03]$ and $k_Q \in [0.5-0.8]$. The worst wind-snow coupling was found on December 4 where there was limited mobile surface snow and the most anomalous transport behavior, as will be discussed in Sect. 4.

At these low anemometer heights (≈0.2 and ≈2 m), the VITA+LEVEL scheme identifies much shorter duration events for the wind than for the blowing-snow signals. The timescales of snow and wind events consistently differed because of concurrent falling snow or inertial particle effects, as seen in the sand studies of Ellis (2006). Thus, it is useful to note that the percentage of the total number of blowing events with any overlap with wind events ranges from $72-99\%$ for low wind measurements and $69-97\%$ for upper measurements. This shows that turbulent wind events were actually identified during the vast majority of the blowing-snow events, though temporal overlap was imperfect.

Sweeps were coupled to blowing-snow events with shorter time lags than ejections during all nights (Table A1). Only 11% of total recording time (5 out of 47 recordings) resulted in shorter parameter-averaged ℓ_{Ej}^ρ. Nightly averages showed ℓ_{Sw}^ρ varying from 0.37 to 0.63 seconds, whereas ℓ_{Ej}^ρ varied from 0.77 to 1.00 seconds. These values are well within the ranges of sand and snow transport lag times (Schmidt, 1982; Anderson and Haff, 1988; Butterfield, 1991; McEwan and Willetts, 1991; Spies et al., 2000; Arnold, 2002; Baas, 2006; Naaim-Bouvet et al., 2011; Pfeifer and Schönfeldt, 2012; Wiggs and Weaver, 2012). Ejection lags may be longer because of the physical definition of ejections as periods of flow with lower than average streamwise velocities, and thus slower convection velocities. Compared with lower anemometer measurements, upper anemometer lag times were slightly longer for sweeps (up to 0.48-0.66 s), and slightly shorter for ejections, (0.7-0.91 s).

In addition to the shorter time lags, sweeps were most often found to be the nearest wind events preceding blowing snow. Parameter-averaged π_{Ej}^ρ ranged between 0-34%, with the highest values occurring on December 4. Sweep coupling rates were much higher; parameter-averaged π_{Sw}^ρ ranged from 3-90%, with the highest values on February 3 and March 3. Only 0.8% of the 4.6 observation hours consisted of recordings with higher parameter-averaged π_{Ej}^ρ. Nightly averages indicate sweeps coupled 2-58 times more often than ejections.

The temporal overlap of blowing-snow events with sweeps was also greater than that of ejections at both anemometers. Parameter averages of $P(S_T)_{Ej}^{\rho}$ were greater than $P(S_T)_{Sw}^{\rho}$ for 0.8% of the total recording times, with nightly averages always indicating a larger mean $P(S_T)_{Sw}^{\rho}$. Parameter-averaged $P(W_T)_{Ej}^{\rho}$ was greater than $P(W_T)_{Sw}^{\rho}$ for 12% of the total recording time.

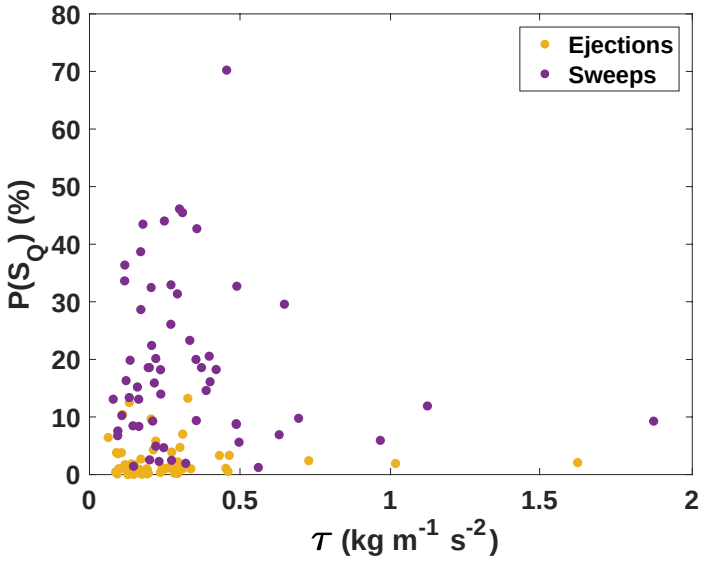

Figure 4-3: Mean Reynolds stress generated by ejections or sweeps during each recording plotted against parameter-averaged $P(S_Q)_{Ej}^{\rho}$ or $P(S_Q)_{Sw}^{\rho}$, respectively.

$P(S_Q)^{\rho}$ and $GS_{Sw}^{\rho}/GS_{Ej}^{\rho}$ provided additional information about the ability of each motion to entrain and transport snow. The parameter-averaged percent of blowing snow during sweeps, $P(S_Q)_{Sw}^{\rho}$, was considerably larger than its ejection counterpart, $P(S_Q)_{Ej}^{\rho}$, for all but 6 recordings, all of which occurred on December 4. Parameter-averaged $P(S_Q)_{Sw}^{\rho}$ and $P(S_Q)_{Ej}^{\rho}$ ranged between 2-70% and 0-13%, respectively, with sweeps contributing up to 700 times more blowing-snow flux in a single recording. Figure 4-3 displays the difference in blowing snow resulting from sweeps or ejections. Each dot relates the total Reynolds stress generated in either quadrant during a single recording with the parameter-averaged $P(S_Q)_{Sw}^{\rho}$ or $P(S_Q)_{Ej}^{\rho}$. While the ranges of τ from the two quadrants are similar, typical values $P(S_Q)_{Sw}^{\rho}$ are much greater.

The ratio GS_{Sw}/GS_{Ej} compares Reynolds-stress-normalized sweep- and ejection-driven blowing snow. Parameter-averaged $GS^{\rho}_{Sw}/GS^{\rho}_{Ej}$ dropped below unity for only 6% of the recording time at the low anemometers, indicating the existence of some exceptional ejections (Table A1). For 38 out of 47 recordings, sweep generated Reynolds stress was between 1.1 and 62 times more effective at producing blowing-snow flux than Reynolds stress during ejections. This suggests it is not solely the sign or magnitude of τ that is important to near-surface blowing snow, but also the mechanism generating the surface stress.

To verify that the VITA+LEVEL algorithm was not preferentially identifying sweep events in the wind signals, Reynolds stress time series during uncoupled blowing-snow events were also analyzed. Even when the VITA+LEVEL analysis failed to couple snow motions with a turbulent burst, it was still more likely that a $u' > 0$ event (Q1 and Q4) was present. Low anemometer Q1 or Q4 motions coincided with 57% to 85% of uncoupled blowing-snow events per night. As well, between 59% and 90% of uncoupled events had upper anemometer Q1 or Q4 signatures. The lowest values of Q1 and Q4 contribution, and highest values of Q2 contribution occurred on December 4.

4.3.2 VITA+LEVEL Analysis of Reynolds stress and PTV Time Series

PTV time series were limited to high frame rate video (1350-2050 frames per second) and represent a small portion of the total observations from each night. However, PTV allowed particle velocity and number flux time series to be analyzed in response to specific coherent structures. The VITA+LEVEL metrics analyzing τ with mean horizontal number flux, Q_u, mean horizontal number flux of ascending particles, $Q_{u\uparrow}$, and mean vertical number flux of ascending particles, $Q_{v\uparrow}$ are summarized in Table A1. PTV signals have units (number of particles) × m s^{-1} and have been block averaged to 50 Hz resolution.

Parameter-averaged ℓ_{Sw} and ℓ_{Ej} typically remained less than one-second for all three PTV analyses. $P(S_T)$ and $P(W_T)$ values were often lower than those obtained with comparisons with ρ_{bs} (Table A1). Nightly-averaged π_{Ej}, π_{Sw} and metrics of temporal sweep and ejection coupling, $P(S_T)_{Ej,Sw}$ and $P(W_T)_{Ej,Sw}$, were all lower for PTV signals than ρ_{bs} analysis. One exception is

found on March 3, where π_{Sw} is higher for nightly averages with PTV data than corresponding ρ_{bs} analysis.

For parameter averages, $\pi_{Sw}^{Q_u} < \pi_{Ej}^{Q_u}$ for 38% of the time, $\pi_{Sw}^{Q_{u\uparrow}} < \pi_{Ej}^{Q_{u\uparrow}}$ for 33% of the time, and $\pi_{Sw}^{Q_{v\uparrow}} < \pi_{Ej}^{Q_{v\uparrow}}$ for 38% of the time. This implies an increased importance of ejection events for snow particle acceleration during turbulent events when compared with blowing snow density metrics (Table A1). Interestingly, all but one of the recordings during which this occurred were on December 4. These are nights with the lowest average $P(W_T)$ and $P(S_T)$ values for all PTV and ρ_{bs} time series. The complications arising from the limited snow availability on the surface on December 4 for PTV and VITA+LEVEL analysis performance are discussed in Sect. 4. Over the span of the campaign, the VITA+LEVEL analysis coupling τ and PTV time series typically mimicked the results of that with ρ_{bs}, but provided the additional information on particle response in Sect 4.3.

4.3.3 The Roles of Ejections after Sweeps

Visual inspection of τ and blowing-snow time series suggests that ejection events are only successful in sustaining transport when there is existing blowing snow (e.g. Figure 4-4a, t between 370 and 490 s and Figure 4-5a, 6 s and 19 s). This model is consistent with the theory that ejections are responsible for vertical transport and transition to suspension of grains already active in bed load transport (Lelouvetel et al., 2009). To investigate this, two representative time series from Feb 3 (recording #7 and #8) help illuminate the roles of sweeps and ejections (Fig. 4-4 & 4-5). The upper plots in Fig. 4-4a & 4-5a show τ and concurrent ρ_{bs} with VITA+LEVEL wind events ($ID_{Wind} = 1$) highlighted in green. The lower plots depict the same two time series with blowing-snow events highlighted in purple ($ID_{Snow} = 1$), as in Fig. 4-2. The thresholds ($k_V = 0.01, k_Q = 0.5$) and averaging time ($T = 1$ s) were chosen for the two example recordings because they, on average, generated the strongest ejection coupling and helped illuminate the full mechanics of transport. Purple and yellow asterisks mark sweep and ejection events, respectively, during wind and snow VITA+LEVEL events, with magnitudes exceeding a hole size calculated for the entire recording time series.

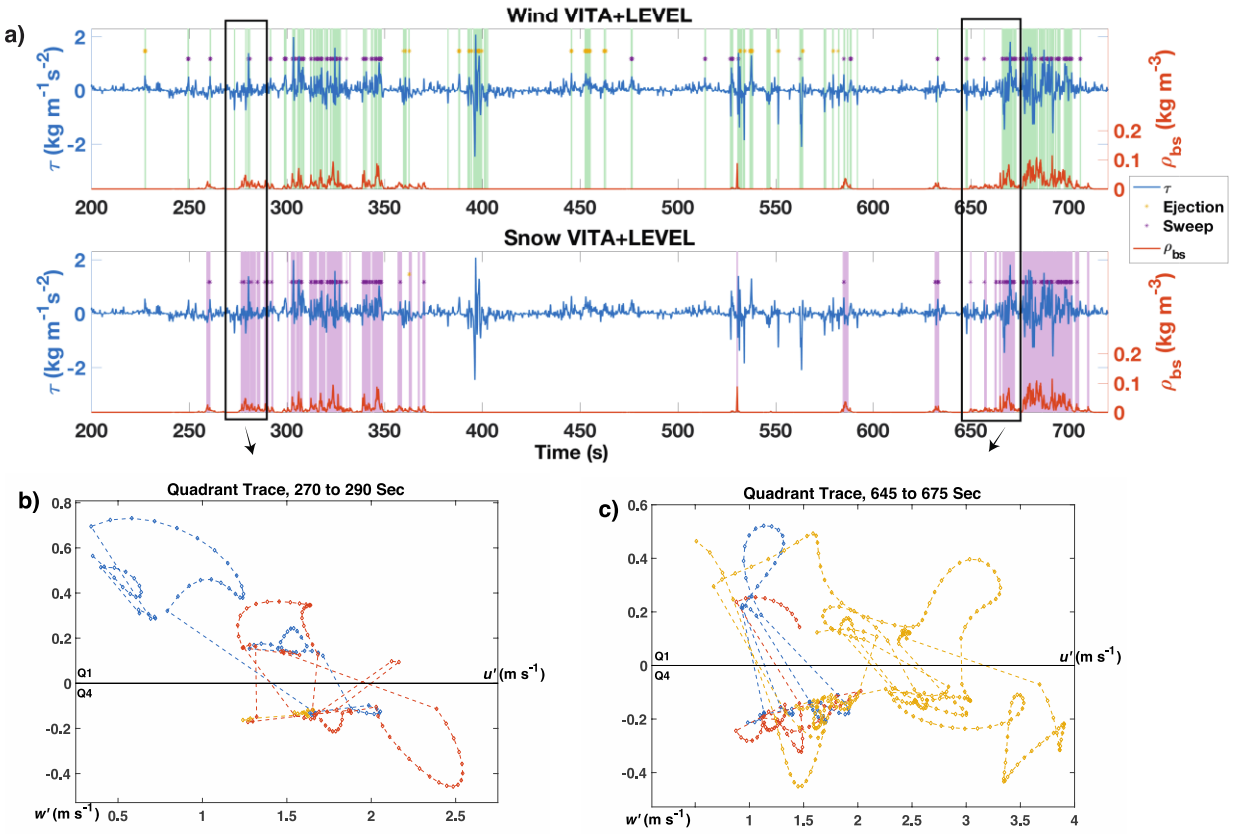

Figure 4-4: VITA+LEVEL analysis time series and highlighted sub-periods of quadrant traces for 3 February for recordings #7 (1150 s), indicating the presence of ejection- and sweep-driven transport, as well as quadrant sequencing prior to blowing-snow events. Parametric curves in b, c are sequentially coloured blue, red and yellow. Time series and quadrant traces are smoothed with a moving window of 0.1 s for clarity.

Both recordings showed a dominance of sweep-driven blowing snow as indicated by a majority of purple asterisks inside highlighted purple regions in the lower plots of Figs. 4-4a and 4-5a. While ejections during recording #7 elicit no blowing-snow response (Fig 4-4a, 400 s and 450 s), some ejections in recording #8 were identified during a VITA+LEVEL snow event (e.g. Fig 4-5a, 6 s). The sequence of turbulent events during two sub-periods of active turbulence and blowing snow from each recording were further analyzed to better understand the different blowing-snow responses to ejection events.

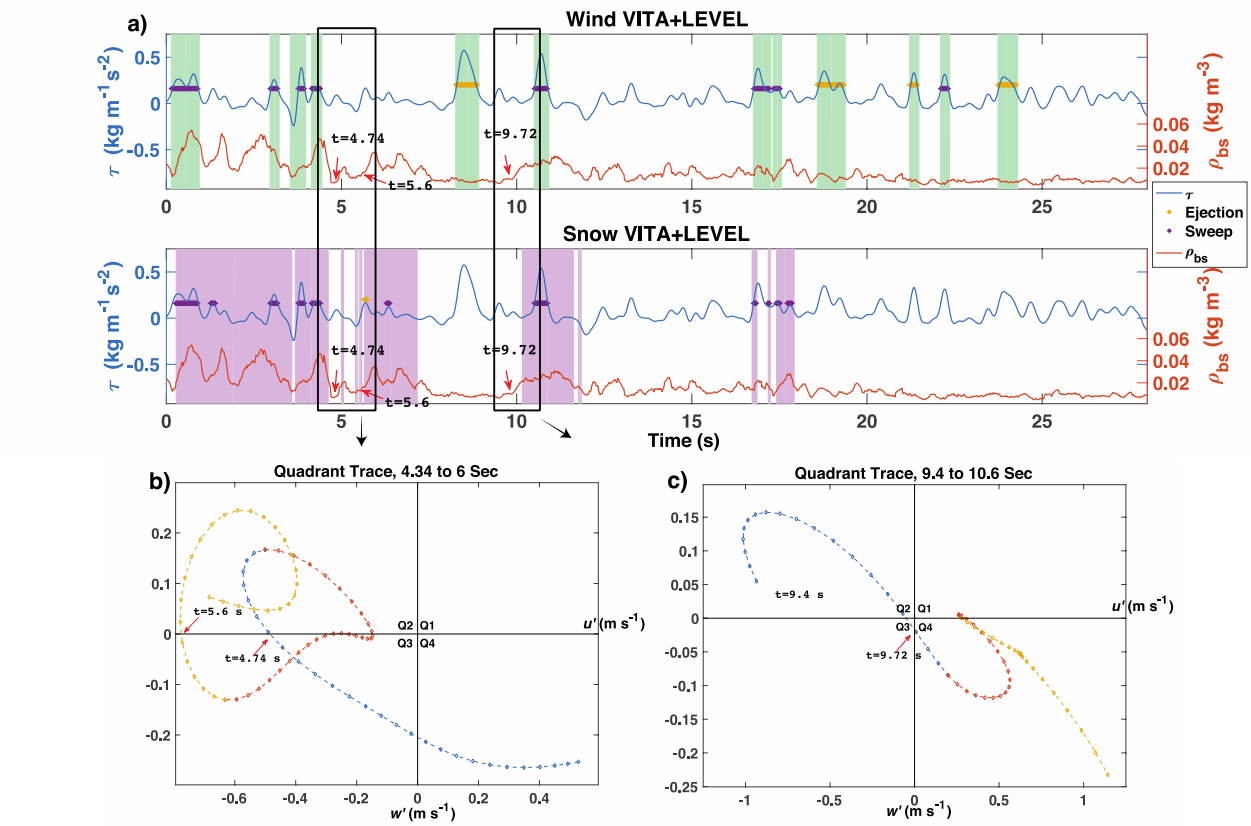

Figure 4-5: VITA+LEVEL analysis time series and highlighted sub-periods of quadrant traces for 3 February for recordings #8 (28 s), indicating the presence of ejection- and sweep-driven transport, as well as quadrant sequencing prior to blowing-snow events. Parametric curves in b, c, are sequentially coloured blue, red and yellow. Time series and quadrant traces are smoothed with a moving window of 0.1 s for clarity.

Sub-periods prior to and at the onset of transport are highlighted from 270-290 s and 645-675 s in Fig 4-4a and 4.34-6 s and 9.4-10.6 s in Fig 4-5a. Figures 4-4b-c and 4-5b-c show parametric curves, $S(t) = (u'(t), w'(t))$, during these sub-periods. An example blowing-snow video from Mar. 3 with synchronized VITA+LEVEL analysis and a parametric quadrant curve animates this style of analysis in the supplementary video. Quadrant motions outside a hole size of 1 were plotted for visual clarity in the longer time periods in Fig 4-4b-c (events with $k_Q = 0$ were still Q1 or Q4), while a hole size of 0 was used for Fig 4-5b-c. $S(t)$ curves have been smoothed with a moving average of 0.1 s to aid in visualization. The sub-periods in Figs. 4-4b-c and 4-5b-c were

divided into three equal portions of time so as to color code the curves with blue, red, and yellow corresponding to the beginning, middle, and end, respectively.

As seen in Fig. 4a, there was no snow transport immediately prior to either sub-period. For both events, initiation begins with a horizontal rush (increasing u') that oscillates between Q1 and Q4, increasing surface drag and particle lift. Transport diminishes towards the end of the sub-period in Fig. 4-4c as the yellow portion of $S(t)$ begins to meander back towards $u' = 0$. This migration of $S(t)$ back to $u' = 0$ exists, but is less pronounced in Fig. 4-4b. Both events are examples of sweep (Q4) motions dominating the coupling of sweeps and blowing snow.

Figures 4-5b-c illustrate that, given the appropriate conditions, ejections can also contribute to blowing-snow flux. The ejection-driven blowing snow peaking at $t = 6$ s is analysed in Fig. 4-5b with two moments when the wind transitions into Q3 ($t = 4.74$ and $t = 5.6$ s) marked in Fig. 4-5a and 4-5b. In contrast to ejections occurring from 375 to 500 s in Fig. 4-4a, there is sweep-driven antecedent blowing snow in Fig. 4-5a from 0.2-4.55 s. ρ_{bs} decreases as the wind moves into Q3 at 4.55 s in Fig. 4-5b, followed by an increase in blowing-snow concentration immediately after the transitions to ejection (Q2) at 4.74 and 5.6 s. Strong ejections at 8.5 s (Fig. 4-5a, top plot) sustain blowing snow until the onset of a sweep visible in Fig. 4-5c results in an increase in ρ_{bs} at 9.72 s.

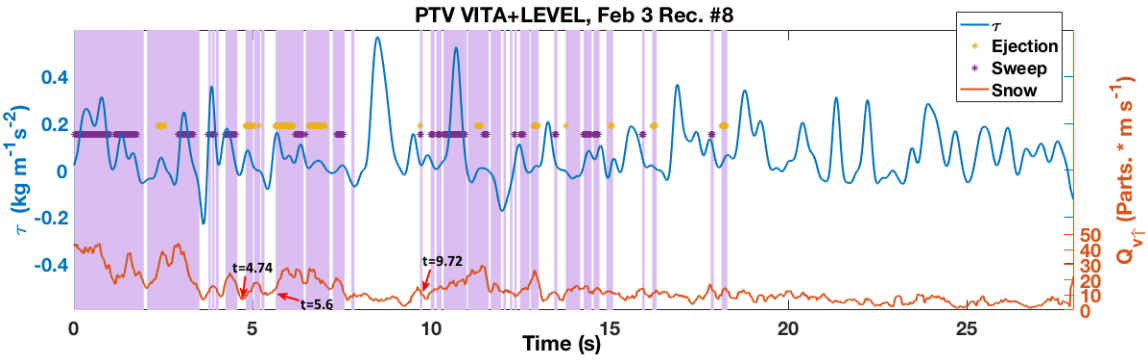

Figure 4-6: Time series of $Q_{v\uparrow}$ and Reynolds stress with highlighted $Q_{v\uparrow}$ VITA+LEVEL events and concurrent ejections and sweeps.

The VITA+LEVEL analysis of $Q_{v\uparrow}$ with a τ overlay during the same time period as Fig 4-5a is displayed in Fig. 4-6. The concurrent quadrant motions are displayed during VITA+LEVEL snow events and indicate the presence of both ejections and sweeps during strong vertical snow

particle flux. There is increased vertical flux during the ejection period from 4.74-6 s, as well as during 10-19 s when both sweeps and ejections are present.

To verify the conceptual model that ejections can enhance blowing snow through vertical transport of mobilized grains, one-second time series of the streamwise wind speed and ρ_{bs} preceding each ejection-driven blowing-snow event were analyzed for all nights. These time series are labeled u_{pre} and ρ_{pre}, respectively. Only one optimized parameter set was used to define the ejection-driven blowing-snow events ($k_V = 0.01, k_Q = 0.5,\ T = 1$ s) as it was found to result in VITA+LEVEL metrics most favorable to ejections.

For 96.7% of coupled ejections over all nights, either u_{pre}, was above transport thresholds (> 4 m s^{-1}) and/or ρ_{pre} was >30% of mean ρ_{bs}. The other 3.3% of ejections occurred in ten videos, with 2.4% occurring on December 4 alone. The December 4 case will be discussed further in Sect. 4. Thus, for more than 96% of ejections-driven blowing-snow events, there was either significant snow transport preceding the ejection or there were antecedent high wind conditions conducive to blowing snow.

	Dec. 4	Dec. 7	Feb. 3	Mar. 3
$\|\boldsymbol{v_{p,Ej}}\|$	0.96	0.86	1.02	1.02
$\|\boldsymbol{v_{p,Sw}}\|$	1.12	1.07	1.02	1.09
$\|\boldsymbol{Q_{v\uparrow,Ej}}\|$	1.16	1.00	1.00	1.29
$\|\boldsymbol{Q_{v\uparrow,Sw}}\|$	1.06	1.32	1.65	1.66

Table 4-2: Nightly averages of normalized vertical particle velocity ($\|v_p\|$) and normalized number flux ($\|Q_{v\uparrow}\|$) during sweeps (Sw) or ejections (Ej) indicating the ability of each VITA+LEVEL-identified motion to enhance vertical particle transport as compared with the recording average.

This ability of ejections to contribute to vertical transport of snow was further analyzed with PTV time series during coupled ejection events. Concurrent parameter-averaged v_p and $Q_{v\uparrow}$ during coupled ejection and sweep events were normalized by their respective recording means to identify the relative response of vertical particle motions to each quadrant. Nightly averages of these normalized values are detailed in Table 4-2. Values greater than unity indicate that VITA+LEVEL ejections typically enhance vertical transport, when compared to average vertical flux. VITA+LEVEL sweep events also enhance vertical transport near the surface, and often to a greater extent than ejections.

4.4 Discussion

Coherent structures in the ASL were coupled to blowing-snow events with varying degrees of temporal overlap depending on the choice of the VITA+LEVEL thresholds and averaging time. Nightly-averaged temporal overlap metrics rose substantially when longer averaging times and lower threshold values were used. $P(S_T)^\rho$ peaked as high as $51-82\%$ and $P(W_T)^\rho$ between $35-87\%$. Additionally, various metrics indicated that the turbulent motions present over a mountain snowpack resulted in sweeps outperforming ejections in both initiating and transporting snow. This confirms that sweeps are critical to snow transport initiation, as suggested by several investigators in aeolian sand research (Bauer et al., 1998; Sterk et al., 1998; Wiggs and Weaver, 2012).

All but four of the recordings where ejections outperformed sweeps occurred on December 4, 2015. This night coincided with the lowest temporal overlap of VITA+LEVEL wind and snow events with nightly averages of $P(W_T)^\rho$ and $P(S_T)^\rho$ being 11% and 10%, respectively. This is likely the result of the complex snow surface and variable meteorological conditions present. Air temperatures rose above freezing (up to 9° C) during the four days prior to December 4, and the subsequent snowfall was subjected to strong winds (≈30 m s^{-1}). The hardened surface modified particle impact dynamics and limited the availability of snow for transport as described by Pomeroy (1991).

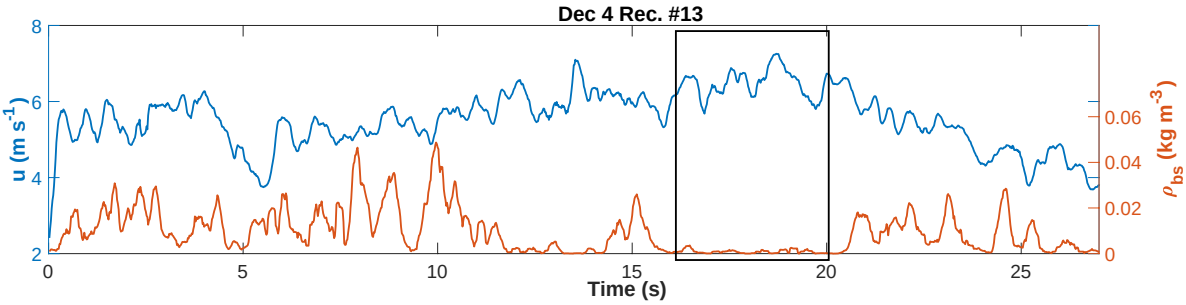

Figure 4-7: Streamwise wind speed (U) and blowing-snow density (ρ_{bs}) Dec 4, recording #13 shows decreased near-surface ρ_{bs} during strong wind in the interval from 16 to 20 s.

With fewer splashed grains, periods with high wind speed on December 4 resulted in quicker acceleration of particles, greater vertical dispersion of particles and lower particle concentrations at the surface, similar to the findings of Ho et al. (2011) and Aksamit and Pomeroy

(2016). When wind speeds decreased (Q2-ejections and Q3 events), particles became both present in larger numbers near the surface and moved at velocities trackable by PTV thus resulting in ρ_{bs} and PTV time series falsely suggesting that ejections play a more significant role in accelerating particles than sweeps.

For example, in Figure 4-7 there was increasing snow flux with increasing wind speed until $t = 10$ s, at which point the wind and snow signals began to decouple. This decoupling was maximized from t =16-20 s when there was no snow in the video frame, but wind speeds reached their peak (Q1 and Q4). After twenty seconds, the wind speeds reduced (Q2 and Q3) and blowing snow reappeared. This trend recurred sporadically in December 4 recordings around peak wind speeds. The difficulties arising during December 4 collection suggest some further refinement of the measurement processes is needed, but also demonstrate some of the confounding complexities found in natural environment observations – snow surface properties are quite dynamic.

Recordings with low parameter-averaged $P(W_T)$ were indicative of turbulent motions with significant Reynolds stress events that did not generate blowing snow (e.g. Figure 4-4a, 380-470 s). Typically, this could be accounted for by consistent low values of $P(S_T)_{Ej}$ and $P(W_T)_{Ej}$ affecting total $P(W_T)$ calculations and implies that simple magnitude thresholds of shear stress may be insufficient for predicting blowing-snow flux. The quadrant generating the Reynolds stress was as important. For all nights, ejection-driven events were predominantly identified when significant antecedent blowing-snow flux was measured, and/or antecedent surface wind speeds were well above transport threshold condition (e.g. Fig. 4-5). This complicates simple u_*-driven blowing-snow models, as contributions of τ from Q2 are ineffective at particle transport initiation, but may contribute to flux after grains are mobilized.

Ejections enhanced vertical transport of saltating particles during blowing-snow events through the upward lift of particles with positive w'. This was exhibited in Fig. 4-6 and in the normalized mean values of ejection-driven v_p and $Q_{v\uparrow}$ which were often above unity in Table 4-2. Table 4-2 also illustrates that ejections did not outperform sweeps in this role because $\|v_p\|$ and $\|Q_{v\uparrow}\|$ during sweeps were often larger. This is likely because increased horizontal particle momentum is quickly transformed to vertical momentum upon surface impacts. However, the

roles of ejections and sweeps in vertical particle transport when particle are transitioning from saltation to suspension regimes, or during concurrent snowfall, may vary substantially from the findings of this near-surface saltation study.

Outward and sweep signatures were often present in the same VITA+LEVEL blocks (Fig. 4-4b-c), and it was essentially impossible to distinguish coherent Q1 and Q4 structures. This may be because Q1 motions can represent local turbulence fluctuations superimposed on the large-scale sweep motion (e.g. Shih et al., 2017). As well, coordinate rotation corrections notably affect w' fluctuations as w is forced to have a zero-mean. An octant analyses approach (e.g. Ölçmen et al., 2006) may be a beneficial alternative for a 3D classification of coherent structures with limited influence from coordinate rotations. Regardless, the uncoupled blowing-snow events consistently coincided with $u' > 0$ events with relatively small τ values. These observations agree with those of Sterk et al. (1998) and Bauer et al. (1998) for sand transport over flat terrain, in that $u' > 0$ events appears more important for predicting initiation of particle transport than the large, positive τ contribution associated with a sweep-ejection cycle. The use of a gust factor (e.g. Chepil, 1959; Naaim-Bouvet et al., 2011) in initiation or transport models that represents a sweep-ejection bursting process may prove beneficial for blowing snow in terrain susceptible to high turbulence intensity or in intermittent conditions when near-surface turbulence is particularly important for particle dislodgement (Shih et al., 2017).

Many of the same turbulent motions were measured at both the upper (1.4-1.7 m) and lower (0.1-0.4 m) anemometer heights, with sweeps dominating blowing-snow flux transport in both velocity signals. With the scale of motions under investigation, the predictive capabilities of the VITA+LEVEL analysis performed on 1.7 m velocity signals were only slightly worse than at 0.4 m, in contrast to the results of Leenders et al. (2005) where 2 m Reynolds stress could not be correlated to coastal aeolian fluxes. This may be the result of larger topographically-driven turbulent structures or a different boundary-layer depth. The VITA+LEVEL analysis coupling structures in τ_{low} and τ_{high} indicated that strong turbulent motions resulting in snow transport often appeared at the upper anemometer before developing nearer to the surface. More detailed investigations with a greater span of wind measurement heights at this location would be needed to determine the cause of these coherent motions (e.g. Hutchins et al., 2012), their location of

origin (e.g. Bauer et al., 1998), and their relation to average u_* values commonly used in blowing-snow models.

The entwining of u_* values, coherent flow structures, and log-law profiles (e.g. Robinson, 1991) may explain the utility and performance of time-averaged, u_*-based blowing-snow models. However, for sub-minute timescales, a large positive shear stress is not a necessary, or sufficient, condition for near-surface blowing snow. On the contrary, as the magnitude of outward interactions increases, the shear stress decreases but bed load may still increase (cf. Nelson et al., 2005). At greater measurement heights, the contribution of ejections to u_* calculations increases (Wallace et al., 1972; Lykossov and Wamser, 1995) implying common meteorological station measurements may not fully reflect the relevant surface structures. Thus, it is through the application of u_* as a proxy for "burstiness" or turbulence energy that a connection to drag induced snow transport has been made. Any scaling relationship between u_* and the relevant turbulent $u' > 0$ bursts described in the present study would likely be site- and measurement-location-specific and further complicated if u_* values are log-law derived as in many time-averaged blowing-snow studies.

Topographic forcing effects may also be amplified in complex mountainous terrain and complicate the characterization of the inner- (such as time averaged u_*) and outer-layer scaling values (e.g. Townsend 1961; Hunt and Morrison, 2000). Turbulent bursts in high Reynolds number atmospheric flows tend to scale on outer variables (Narasimha and Kailas, 1987). Thus, further investigations parameterizing inner-layer scaling values in complex terrain are prudent to maintaining physical accuracy when adapting wind tunnel derived, or even flat terrain derived, blowing-snow models.

4.5 Conclusions

A laser-illuminated high-speed camera system has allowed generation of both blowing-snow PTV number flux and blowing-snow density time series near the snow surface for comparison with high frequency turbulence measurements in complex terrain. During alpine blowing-snow storms, the VITA+LEVEL analysis was effective in coupling periods of blowing

snow and turbulent bursts in the lowest 2 m of the ASL. This has allowed the identification of turbulent structures responsible for blowing snow, and allows a better understanding of the event-driven mechanics of blowing-snow initiation and sustained transport. The coupling of blowing snow and wind events was compromised when the availability of blowing-snow particles was limited in the upwind fetch.

Specific structures defined by quadrant hole analysis were linked to blowing-snow fluxes quite well in outdoor conditions. Sweeps were the dominant motion for both initiating blowing-snow transport, and increasing concentration and particle number flux near the surface. Ejections played a subordinate role, and were capable of enhancing or sustaining transport, largely through vertical transport, but were not effective in initiating snow particle motion. It was not possible to observe if ejections contributed to suspension of near-surface saltating snow.

A consistent scaling between Reynolds stress and particle flux was not observed. The type of coherent event generating Reynolds stress was as important as the magnitude of Reynolds stress in initiating and sustaining near-surface blowing snow. Blowing-snow models estimating flux from time-averaged shear stress do not differentiate between different quadrant motions and are unable to represent the separate roles of sweeps and ejections near the surface. New models that include a parameterization of coherent structures are promising as they would allow a semi-deterministic description of longer timescale behavior to estimate fluctuating mass fluxes near the surface (Bauer et al., 2013).

Future research relating turbulent structures, wind magnitude, u_*, and directional blowing-snow flux time series may aide in increasing blowing-snow model physical realism and accuracy. It would be useful to determine the relative roles of ejections and sweeps at greater wind speeds and with greater particle transition to suspension. Future improvements of the black and white binarization algorithms and the addition of multiple cameras to allow 3D particle tracking could also provide enhanced data for further development in the field of environmental high frequency blowing-snow measurements.

Key Points for Next Chapter

- What are the relative roles of large eddies and small eddies in the turbulent transport of snow?
- How do the mechanics or turbulent transport of snow in high Reynolds number mountainous terrain flows differ from wind tunnels?
- How does the coupling of high-frequency near surface turbulence with blowing snow differ from that with low-frequency "outer-region" motions?

4.6 Acknowledgements

The authors acknowledge funding from the Canadian Foundation for Innovation, the Natural Sciences and Engineering Research Council of Canada, the Changing Cold Regions Network, Canada Research Chairs, the Global Institute for Water Security and Alberta Agriculture and Forestry. The assistance of the Fortress Mountain Resort in logistics is gratefully noted as are the suggestions to improve the manuscript from Paul Whitfield and Nicolas Leroux. Data is available upon request directly from the authors, john.pomeroy@usask.ca.

The document supplement is available from the publisher at https://doi.org/10.1007/s10546- 017-0318-2.

Appendix 1

Signals	$P(S_T)$ (%)	$P(W_T)$ (%)	l_{Sw}, l_{Ej} (s)	π_{Sw}, π_{Ej} (%)	$P(S_T)_{Sw,Ej}$ (%)	$P(W_T)_{Sw,Ej}$ (%)	$P(S_Q)_{Sw,EJ}$ (%)	GS_{Sw}/GS_{Ej} (non-dim)
20-Nov								
ρ			0.23-0.62 (0.42),	39-83 (58),	14-35 (25),			3.39-61.16
	14-35 (25)	7-29 (17)	0.29-1.14 (0.86)	0-2 (1)	0-1 (0)	8-30 (19), 0-10 (3)	14-33 (24), 0-1 (0)	(38.51)
Q_u	N/A	N/A	N/A	N/A	N/A	N/A	N/A	N/A
$Q_{u\uparrow}$	N/A	N/A	N/A	N/A	N/A	N/A	N/A	N/A
$Q_{v\uparrow}$	N/A	N/A	N/A	N/A	N/A	N/A	N/A	N/A
4-Dec								
ρ_{bs}			0.18-1.24 (0.63),	4-48 (23),	2-23 (8),			0.43-49.15
	3-25 (10)	2-34 (11)	0.47-1.08 (0.83)	0-34 (12)	0-9 (3)	1-19 (9), 0-28 (8)	1-29 (9), 0-13 (3)	(5.21)
Q_u			0.07-1.48 (0.83),	2-58 (16),	0-5 (4), 1-			
	1-14 (6)	3-18 (10)	0.37-1.23 (0.76)	2-56 (20)	10 (4)	0-12 (5), 1-22 (9)	N/A	N/A
$Q_{u\uparrow}$			0.11-1.4 (0.85),	3-70 (18),	0-14 (4),			
	1-15 (6)	3-18 (10)	0.15-1.16 (0.83)	1-55 (20)	1-10 (4)	0-13 (6), 1-19 (9)	N/A	N/A
$Q_{v\uparrow}$			0.42-1.44 (0.88),	2-64 (19),	1-12 (4),			
	2-16 (7)	3-20 (10)	0.38-1.21 (0.9)	2-48 (19)	1-11 (4)	1-13 (6), 1-21 (9)	N/A	N/A
7-Dec								
ρ_{bs}			0.16-0.76 (0.37),	3-90 (40),	2-69 (32),			1.37-2.67
	2-38 (35)	11-41 (25)	0.23-1.28 (0.77)	0-12 (6)	0-5 (2)	1-41 (23), 2-19 (7)	2-70 (34), 1-6 (2)	(1.87)
Q_u	1	10	0.86, 0.8	2, 6	1, 1	1, 1	N/A	N/A
$Q_{u\uparrow}$	1	9	0.75, 0.87	2, 6	1, 1	1, 2	N/A	N/A
$Q_{v\uparrow}$	5	8	0.76, 0.81	7, 8	3, 1	5, 4	N/A	N/A
3-Feb								
ρ_{bs}			0.29-0.61 (0.42),	43-87 (69),	18-45 (32),			1.38-62.08
	19-45 (33)	24-42 (34)	0.82-1.26 (0.93)	0-26 (6)	0-10 (5)	23-53 (38), 0-10 (5)	19-46 (34), 0-3 (1)	(18.8)
Q_u			0.32-0.59 (0.47),	38-75 (54),	9-35 (20),			
	14-38 (22)	19-33 (28)	0.66-1.22 (1.01)	3-18 (11)	1-4 (2)	14-39 (29), 6-14 (10)	N/A	N/A
$Q_{u\uparrow}$			0.32-0.72 (0.53),	37-75 (53),	9-31 (18),			
	11-31 (19)	15-34 (27)	0.71-1.28 (0.98)	2-21 (10)	0-3 (2)	12-34 (28), 4-12 (8)	N/A	N/A
$Q_{v\uparrow}$			0.3-0.86 (0.58),	39-66 (50),	6-31 (17),			
	9-34 (19)	15-37 (27)	0.74-1.26 (0.94)	1-25 (12)	0-3 (2)	11-39 (27), 3-13 (7)	N/A	N/A
3-Mar								
ρ_{bs}			0.18-0.91 (0.56),	8-82 (45),	1-30 (12),			0.17-23.39
	3-24 (16)	4-27 (18)	0.66-1.15 (0.92)	3-21 (9)	1-17 (7)	3-27 (17), 1-17 (7)	2-36 (14), 0-13 (2)	(3.77)
Q_u			0.22-0.76 (0.52),	24-86 (56),	5-28 (15),			
	7-34 (19)	13-43 (21)	0.65-1.11 (0.95)	3-14 (7)	1-2 (1)	10-34 (18), 1-12 (5)	N/A	N/A
$Q_{u\uparrow}$			0.26-0.73 (0.51),	22-87 (57),	4-37 (17),			
	6-38 (20)	13-37 (20)	0.64-1.09 (0.93)	2-11 (7)	0-2 (1)	9-37 (19), 1-12 (5)	N/A	N/A
$Q_{v\uparrow}$			0.16-0.69 (0.5),	25-86 (55),	8-37 (18),			
	9-38 (22)	18-34 (23)	0.61-1.07 (0.88)	4-12 (7)	0-2 (1)	10-34 (22), 4-15 (6)	N/A	N/A

Table 4-A1: Ranges of parameter-averaged metrics (600 thresholds & averaging time combinations) for each night and each blowing-snow signal. Parenthetical values are nightly averages. Only low frame rate recordings available for November 20. $P(S_Q)$ and GS_{Sw}/GS_{Ej} not computed for PTV signals.

4.7 References

Aksamit, N. O., and J. W. Pomeroy (2016), Near-Surface Snow Particle Dynamics from Particle Tracking Velocimetry and Turbulence Measurements during Alpine Blowing Snow Storms, *Cryosph.*, *10*, 3043–3062, doi:10.5194/tc-10-3043-2016.

Anderson, R. S., and P. K. Haff (1988), Simulation of eolian saltation., *Science*, *241*(4867), 820–3, doi:10.1126/science.241.4867.820.

Anderson, R. S. (1987), Eolian Sediment Transport as a Stochastic Process: The Effects of a Fluctuating Wind on Particle Trajectories, *J. Geol.*, *95*(4), 497–512, doi:10.1086/629145.

Arnold, S. (2002), Development of the saltation system under controlled environmental conditions, *Earth Surf. Process. Landforms*, *27*(8), 817–829, doi:10.1002/esp.354.

Baas, A. C. W. (2006), Wavelet power spectra of aeolian sand transport by boundary layer turbulence, *Geophys. Res. Lett.*, *33*, 1–4, doi:10.1029/2005GL025547.

Bagnold, R. A. (1941), *The Physics of Blown Sand and Desert Dunes*, 1st ed., Methuen & Co. Limited, London.

Bauer, B. ., J. Yi, S. Namikas, and D. Sherman (1998), Event detection and conditional averaging in unsteady aeolian systems, *J. Arid Environ.*, *39*, 345–375.

Bauer, B. O., I. J. Walker, A. C. W. Baas, D. W. T. Jackson, C. M. Neuman, G. A. Hesp, and F. S. W. Patrick (2013), Critical Reflections on the Coherent Flow Structures Paradigm in Aeolian Geomorphology, in *Coherent Flow Structures at Earth's Surface*, edited by J. G. Venditti, J. L. Best, M. Church, and R. J. Hardy, pp. 111–134, Wiley Blackwell, West Sussex, UK.

Blackwelder, R., and R. Kaplan (1976), On the wall structure of the turbulent boundary layer, *J. Fluid Mech.*, *76*, 89–112.

Butterfield, G. (1991), Grain transport rates in steady and unsteady turbulent airflows, in *Acta Mechanica (Supplementum)*, pp. 97–122, Springer-Verlag, Vienna, Austria.

Chapman, C. a., I. J. Walker, P. a. Hesp, B. O. Bauer, and R. G. D. Davidson-Arnott (2012), Turbulent Reynolds stress and quadrant event activity in wind flow over a coastal foredune, *Geomorphology*, *151–152*, 1–12, doi:10.1016/j.geomorph.2011.11.015.

Chapman, C., I. J. Walker, P. A. Hesp, B. O. Bauer, R. G. D. Davidson-Arnott, and J. Ollerhead (2013), Reynolds stress and sand transport over a foredune, *Earth Surf. Process. Landforms*, *38*(14), 1735–1747, doi:10.1002/esp.3428.

Chepil, W. S. (1959), Equilibrium of soil grains at the threshold of movement by wind, *Soil Sci. Soc. Am. J.*, *23*(6), 422–428.

Diplas, P., C. L. Dancey, A. O. Celik, M. Valyrakis, K. Greer, and T. Akar (2008), The Role of Impulse on the Initiation of Particle Movement Under Turbulent Flow Conditions, *Science (80-.).*, *322*(5902), 717–720, doi:10.1126/science.1158954.

Doorschot, J., M. Lehning, and A. Vrouwe (2004), Field measurements of snow-drift threshold and mass fluxes, and related model simulations, *Boundary-Layer Meteorol.*, *113*, 347–368.

Dyunin, A. K., and V. Kotlyakov (1980), Redistribution of snow in the mountains under the effect of heavy snow-storms, *Cold Reg. Sci. Technol.*, *3*, 287–294.

Ellis, J. T. (2006), Coherent Structures and Aeolian Saltation, Texas A&M.

Frisch, U. (1995), *Turbulence. The legacy of A. N. Kolmogov*, Cambridge University Press, Cambridge, UK.

Gordon, M., S. Savelyev, and P. a. Taylor (2009), Measurements of blowing snow, part II: Mass and number density profiles and saltation height at Franklin Bay, NWT, Canada, *Cold Reg. Sci. Technol.*, *55*(1), 75–85, doi:10.1016/j.coldregions.2008.07.001.

Grass, A. J. (1971), Structural features of turbulent flow over smooth and rough boundaries, *J. Fluid Mech.*, *50*, 233, doi:10.1017/S0022112071002556.

Gromke, C., S. Horender, B. Walter, and M. Lehning (2014), Snow particle characteristics in the saltation layer, *J. Glaciol.*, *60*(221), 431–439, doi:10.3189/2014JoG13J079.

Groot Zwaaftink, C. D., M. Diebold, S. Horender, J. Overney, G. Lieberherr, M. B. Parlange, and M. Lehning (2014), Modelling Small-Scale Drifting Snow with a Lagrangian Stochastic Model Based on Large-Eddy Simulations, *Boundary-Layer Meteorol.*, *153*(1), 117–139, doi:10.1007/s10546-014-9934-2.

Guala, M., M. Metzger, and B. J. McKEON (2011), Interactions within the turbulent boundary layer at high Reynolds number, *J. Fluid Mech.*, *666*, 573–604, doi:10.1017/S0022112010004544.

Heathershaw, A. D., and P. D. Thorne (1985), Sea-bed noises reveal rol of turbulent bursting phenomenon in sediment transport by tidal currents, *Nature*, *316*, 339–342, doi:10.1038/315279a0.

Helgason, W., and J. W. Pomeroy (2012), Characteristics of the Near-Surface Boundary Layer within a Mountain Valley during Winter, *J. Appl. Meteorol. Climatol.*, *51*(3), 583–597, doi:10.1175/JAMC-D-11-058.1.

Ho, T. D., A. Valance, P. Dupont, and A. Ould El Moctar (2011), Scaling laws in aeolian sand transport, *Phys. Rev. Lett.*, *106*(9), 4–7, doi:10.1103/PhysRevLett.106.094501.

Horender, S., C. D. Groot Zwaaftink, B. Walter, and M. Lehning (2013), Intermittent drifting snow - combining experimental and model studies., in *Proceedings International Snow Science Workshop*, pp. 104–107, Grenoble Chamonix Mont-Blanc.

Hunt, J. C. R., and J. F. Morrison (2000), Eddy structure in turbulent boundary layers, *Eur. J. Mech. B-Fluids*, *19*, 673–694, doi:10.1016/S0997-7546(00)00129-1.

Hussain, A. K. M. F. (1983), Coherent structures - Reality and myth, *Phys. Fluids*, *26*(10), 2816–2850.

Hutchins, N., K. Chauhan, I. Marusic, J. Monty, and J. Klewicki (2012), Towards reconciling the large-scale structure of turbulent boundary layers in the atmosphere and laboratory, *Boundary-Layer Meteorol.*, *145*(2), 273–306, doi:10.1007/s10546-012-9735-4.

Jackson, R. G. (1976), Sedimentological and fluid-dynamic implications of the turbulent bursting phenomenon in geophysical flows, *J. Fluid Mech.*, *77*(3), 531–560, doi:10.1017/S0022112076002243.

Kaimal, J. C., and J. J. Finnigan (1994), *Atmospheric boundary layer flows: their structure and measurement*, Oxford University Press, New York, NY.

Keylock, C. J., K. Nishimura, and J. Peinke (2012), A classification scheme for turbulence based on the velocity-intermittency structure with an application to near-wall flow and with implications for bed load transport, *J. Geophys. Res.*, *117*(F1), F01037, doi:10.1029/2011JF002127.

Kobayashi, D. (1972), *Studies of Snow Transport in Low-Level Drifting Snow*, Sapporo, Hokkaido, Japan.

Kok, J. F., E. J. R. Parteli, T. I. Michaels, and D. B. Karam (2012), The physics of wind-blown sand and dust, *Reports Prog. Phys.*, *75*(10), doi:10.1088/0034-4885/75/10/106901.

Leenders, J. K., J. H. van Boxel, and G. Sterk (2005), Wind forces and related saltation transport, *Geomorphology*, *71*, 357–372, doi:10.1016/j.geomorph.2005.04.008.

Lelouvetel, J., F. Bigillon, D. Doppler, I. Vinkovic, and J.-Y. Champagne (2009), Experimental investigation of ejections and sweeps involved in particle suspension, *Water Resour. Res.*, *45*(2), doi:10.1029/2007WR006520.

Li, B., and C. McKenna Neuman (2012), Boundary-layer turbulence characteristics during aeolian saltation, *Geophys. Res. Lett.*, *39*(11), 1–6, doi:10.1029/2012GL052234.

Liu, J., Y. Wang, and B. Yang (2012), Wavelet packet analysis of particle response to turbulent fluctuation, *Adv. Powder Technol.*, *23*(3), 305–314, doi:10.1016/j.apt.2011.04.002.

Liu, J., Y. Wang, and Y. Zhang (2009), Stationary wavelet-based analysis and simulation of unsteady wind in aeolian sand transport, in *ICEMI 2009 - Proceedings of 9th International Conference on Electronic Measurement and Instruments*, pp. 3789–3794.

Lu, S. S., and W. W. Willmarth (1973), Measurements of the structure of Reynolds stress in a turbulent boundary layer, *J. Fluid Mech.*, *60*(3), 481–511.

Lü, X., N. Huang, and D. Tong (2012), Wind tunnel experiments on natural snow drift, *Sci. China Technol. Sci.*, *55*(4), 927–938, doi:10.1007/s11431-011-4731-3.

Luchik, T. S., and W. G. Tiederman (1987), Timescale and structure of ejections and bursts in turbulent channel flows, *J. Fluid Mech.*, *174*(1), 529, doi:10.1017/S0022112087000235.

Lykossov, V. N., and C. Wamser (1995), Turbulence intermittency in the atmospheric surface layer over snow-covered sites, *Boundary-Layer Meteorol.*, *72*(4), 393–409, doi:10.1007/BF00709001.

McEwan, I., and B. B. Willetts (1991), Numerical model of the saltation cloud, in *Acta Mechanica (Supplementum)*, pp. 53–66, Springer-Verlag, Vienna, Austria.

Morrison, J. F., H. M. Tsai, and P. Bradshaw (1989), Conditional-sampling schemes for turbulent flow, based on the variable-interval time averaging (VITA) algorithm, *Exp. Fluids*, *7*, 173–189, doi:10.1007/BF00272424.

Naaim-Bouvet, F., M. Naaim, H. Bellot, and K. Nishimura (2011), Wind and drifting-snow gust factor in an Alpine context, *Ann. Glaciol.*, *52*(58), 223–230, doi:10.3189/172756411797252112.

Narasimha, R., and S. V. Kailas (1990), Turbulent bursts in the atmosphere, *Atmos. Environ. Part A, Gen. Top.*, *24*(7), 1635–1645, doi:10.1016/0960-1686(90)90497-B.

Narasimha, R., and S. V. Kailas (1987), Energy Events in the Atmospheric Boundary Layer, , 43.

Narasimha, R., S. V. Kailas, and J. Kaimal (1990), Turbulent Bursts in a Near - neutral Atmospheric Boundary Layer - Part I, , 70.

Nelson, J. M., J. M. Nelson, R. L. Shreve, R. L. Shreve, S. R. McLean, S. R. McLean, T. G. Drake, and T. G. Drake (1995), Role of near-bed turbulence structure in bed load transport, *Water Resour. Res.*, *31*(95), 2071–2086, doi:10.1029/95WR00976.

Nishimura, K. et al. (2014), Snow particle speeds in drifting snow, *J. Geophys. Res. Atmos.*, *119*, 9901–9913, doi:10.1002/2014JD021686.Received.

Olçmen, S. M., R. L. Simpson, and J. W. Newby (2006), Octant analysis based structural relations for three-dimensional turbulent boundary layers, *Phys. Fluids*, *18*(2), 25106, doi:10.1063/1.2172650.

Otsu, N. (1979), A Threshold Selection Method from Gray-Level Histograms, *IEEE Trans. Syst. Man. Cybern.*, *SMC-9*(1), 62–66.

Owen, P. R. (1964), Saltation of uniform grains in air, *J. Fluid Mech.*, *20*(2), 225, doi:10.1017/S0022112064001173.

Paterna, E., P. Crivelli, and M. Lehning (2016), Decoupling of mass flux and turbulent wind fluctuations in drifting snow, *Geophys. Res. Lett.*, 1–7, doi:10.1002/2016GL068171.

Pfeifer, S., and H.-J. Schönfeldt (2012), The response of saltation to wind speed fluctuations, *Earth Surf. Process. Landforms*, *37*(10), 1056–1064, doi:10.1002/esp.3227.

Pomeroy, J. W. (1991), Transport and sublimation of snow in wind-scoured alpine terrain, in *Snow, Hydrology and Forests in High Alpine Areas (Proceedings of the Vienna Symposium)*, pp. 131–140.

Pomeroy, J. W., X. Fang, and C. Ellis (2012), Sensitivity of snowmelt hydrology in Marmot Creek, Alberta, to forest cover disturbance, *Hydrol. Process.*, *26*(12), 1891–1904, doi:10.1002/hyp.9248.

Pomeroy, J. W., and D. Gray (1990), Saltation of snow, *Water Resour. Res.*, *26*(7), 1583–1594.

Reynolds, O. (1895), On the dynamical theory of incompressible viscous fluids and the determination of the criterion, *Philos. Trans. R. Soc. …*, *186*, 123–164.

Robinson, S. (1991), Coherent motions in the turbulent boundary layer, *Annu. Rev. Fluid Mech.*, *23*, 601–639.

Schmidt, R. A. (1982), Vertical Profiles of Wind Speed, Snow Concentration, and Humidity in Blowing Snow, *Boundary-Layer Meteorol.*, *23*, 223–246, doi:10.1016/j.soncn.2013.06.001.

Schönfeldt, H.-J., and S. von Löwis (2003), Turbulence-driven saltation in the atmospheric surface layer, *Meteorol. Zeitschrift*, *12*(5), 257–268, doi:10.1127/0941-2948/2003/0012-0257.

Schweizer, J., B. Jamieson, and M. Schneebeli (2003), Snow avalanche formation, *Rev. Geophys.*, *41*(4), doi:10.1029/2002RG000123.

Sherman, D. J., B. Li, J. T. Ellis, E. J. Farrell, L. P. Maia, and H. Granja (2013), Recalibrating aeolian sand transport models, *Earth Surf. Process. Landforms*, *38*(2), 169–178, doi:10.1002/esp.3310.

Shih, W., P. Diplas, A. O. Celik, and C. Dancey (2017), Accounting for the role of turbulent flow on particle dislodgement via a coupled quadrant analysis of velocity and pressure sequences, *Adv. Water Resour.*, *101*, 37–48, doi:10.1016/j.advwatres.2017.01.005.

Shugar, D. H., R. Kostaschuk, J. L. Best, D. R. Parsons, S. N. Lane, O. Orfeo, and R. J. Hardy (2010), On the relationship between flow and suspended sediment transport over the crest of a sand dune, Río Paraná, Argentina, *Sedimentology*, *57*(1), 252–272, doi:10.1111/j.1365-3091.2009.01110.x.

Sørensen, M. (1997), On the effect of time variability of the wind on rates of aeolian sand transport, *Aarhus Geosci.*, *7*, 73–77.

Spies, P.-J., I. K. McEwan, and G. R. Butterfield (2000), One-dimensional transitional behaviour in saltation, *Earth Surf. Process. Landforms*, *25*(5), 505–518, doi:10.1002/(SICI)1096-9837(200005)25:5<505::AID-ESP78>3.0.CO;2-D.

Sterk, G., a. F. G. Jacobs, and J. H. Van Boxel (1998), The effect of turbulent flow structures on saltation sand transport in the atmospheric boundary layer, *Earth Surf. Process. Landforms*, *23*(10), 877–887.

Tominaga, Y., T. Okaze, A. Mochida, Y. Sasaki, M. Nemoto, and T. Sato (2012), PIV measurements of saltating snow particle velocity in a boundary layer developed in a wind tunnel, *J. Vis.*, *16*(2), 95–98, doi:10.1007/s12650-012-0156-8.

Townsend, A. A. (1961), Equilibrium layers and wall turbulence, *J. Fluid Mech.*, *11*, 97–120.

Träumner, K., T. Damian, C. Stawiarski, and A. Wieser (2015), Turbulent Structures and Coherence in the Atmospheric Surface Layer, *Boundary-Layer Meteorol.*, *154*, 1–25, doi:10.1007/s10546-014-9967-6.

Tubergen, R. G., and W. G. Tiederman (1993), Evaluation of ejection detection schemes in turbulent wall flows, *Exp. Fluids*, *15*(4–5), 255–262, doi:10.1007/BF00223403.

Valyrakis, M., P. Diplas, and C. Dancey (2010), Role of instantaneous force magnitude and duration on particle entrainment, *J. Geophys. …*, *115*, F02006, doi:10.1029/2008JF001247.

van Boxel, J. ., G. Sterk, and S. . Arens (2004), Sonic anemometers in aeolian sediment transport research, *Geomorphology*, *59*(1–4), 131–147, doi:10.1016/j.geomorph.2003.09.011.

Wallace, J. M. (2016), Quadrant Analysis in Turbulence Research: History and Evolution, *Annu. Rev. Fluid Mech.*, *48*(1), 131–158, doi:10.1146/annurev-fluid-122414-034550.

Wallace, J., R. Brodkey, and H. Eckelmann (1972), The wall region in turbulent shear flow, *J. Fluid Mech.*, *54*, 39–48.

Wiggs, G. F. S., and C. M. Weaver (2012), Turbulent flow structures and aeolian sediment transport over a barchan sand dune, *Geophys. Res. Lett.*, *39*(5), 1–7, doi:10.1029/2012GL050847.

Willetts, B. B., J. McEwan, and M. A. Rice (1991), Initiation of motion of quartz sand grains, *Acta Mech.*, *1*, 123–134.

Winstral, A., D. Marks, and R. Gurney (2013), Simulating wind-affected snow accumulations at catchment to basin scales, *Adv. Water Resour.*, *55*, 64–79, doi:10.1016/j.advwatres.2012.08.011.

Zhu, W., R. van Hout, and J. Katz (2007), PIV Measurements in the Atmospheric Boundary Layer within and above a Mature Corn Canopy. Part II: Quadrant-Hole Analysis, *J. Atmos. Sci.*, *64*(8), 2825–2838, doi:10.1175/JAS3990.1.

CHAPTER 5
SCALE INTERACTIONS IN TURBULENCE FOR MOUNTAIN BLOWING SNOW

Abstract

Blowing snow particle transport responds to wind motions across many length and time scales. This coupling is nonlinear by nature and complicated in atmospheric flows where eddies of many sizes are superimposed. In mountainous terrain, wind flow descriptions are further complicated by topographically influenced or enhanced flows. To improve the current understanding and modeling of blowing snow transport in complex terrain, statistically significant timing and frequencies of wind-snow coupling were identified in high frequency observations of surface blowing snow and near-surface turbulence from a mountain field site in the Canadian Rockies. Investigation of the mechanisms influencing near-surface high-frequency turbulence and snow concentration fluctuations provided strong evidence for amplitude modulation from large-scale motions. The large-scale atmospheric motions modulating near-surface turbulence and snow transport were then compared to specific quadrant analysis structures recently identified as relevant for outdoor blowing snow transport. The results suggest that large atmospheric structures modulate the amplitude of high-frequency turbulence and modify turbulence statistics typically used to model blowing snow. Additionally, blowing snow was preferentially redistributed under the footprint of these same sweep motions, with both low and high frequency coherence increasing in their presence.

This manuscript has been modified for inclusion in this thesis. Aksamit, N. O., and J. W. Pomeroy (2017), Scale Interactions in Turbulence for Mountain Blowing-Snow, *Journal of Hydrometerology*.,

5.1 Introduction

Redistribution of snow by wind is an environmental two-phase flow with great spatio-temporal variability. Blowing snow has implications for cold regions hydrology and engineering, avalanche safety, glaciology and Antarctic mass balance (Dyunin and Kotlyakov, 1980; Pomeroy et al., 1993; Freitag and McFadden, 1997; Schweizer et al., 2003; Scarchilli et al., 2010). Redistribution of snow begins when wind drag and shear stress exceed transport thresholds and

snow grains mobilize on the surface (Li and Pomeroy, 1997). Sub-second shear stress peaks can be sufficient to initiate snow transport, and may not be reflected in time-averaged mean values (Aksamit and Pomeroy, 2016). Once in motion, blowing snow is characterized by a variety of length and time scales, from centimeter hop-lengths and rebound times for grains in saltation at the surface (Nemoto et al., 2004), to turbulent eddy length scales and bursting frequencies for particles in suspension that closely follow wind streamlines (Bintanja, 1998; 2000). The choice of representative time scale has considerable effect on the performance of all aeolian transport models in the presence of multiple scales of atmospheric motions (Bisantino et al., 2010). Much is still unknown about the coupling of turbulent wind motions and snow transport in natural terrain, though the importance of turbulent gusts is widely accepted (Naaim-Bouvet et al., 2011; Paterna et al., 2016).

Instantaneous wind speed fluctuations and atmospheric structures are vital components for understanding intermittent aeolian behavior (Stout and Zobeck, 1997; Sterk et al., 1998; Leenders et al., 2005; Wiggs and Weaver, 2012). The presence of surface streamer patterns in sand, for example, have been related to frequencies of eddies penetrating towards the surface and entraining particles (Baas and Sherman, 2005; Baas, 2006). To better represent the role of turbulent motions in snow transport models, researchers are gradually moving away from traditional approaches of modeling blowing snow as a steady-state process driven by time-averaged data (e.g. Nemoto and Nishimura, 2004; Groot Zwaaftink et al., 2014), yet models continue to rely on experimentally derived relationships between wind and snow response, largely from low Reynolds number wind tunnel experiments (e.g. Nishimura and Hunt, 2000; Clifton et al. 2006).

Modeling wind-snow coupling in truly complex turbulence, such as found in alpine environments, also requires understanding the physical mechanisms generating turbulence at very high Reynolds numbers. Recent research in very high Reynolds number wind tunnels, large eddy simulations, and some limited results with atmospheric flows, have linked modulation of high-frequency surface turbulence to the passage of large-scale coherent motions (Hutchins and Marusic, 2007a; Mathis et al., 2009a, 2009b, 2011, 2013; Anderson, 2016; Jacob and Anderson, 2017). This has provided new insight into the cascade of turbulent energy and the dissipation of momentum in large coherent structure. It has been shown that the superposition of large-scale

motions on local surface turbulence does not behave as a simple shift of mean velocity (Hutchins and Marusic, 2007b), rather, the modification of high-frequency turbulence by large-scale motions directly affects turbulence statistics and surface shear stress in high Reynolds number flows (Fig. 5-1). This has not yet been investigated in mountainous terrain, but would imply fundamental differences in the mechanics driving blowing snow in wind tunnel and atmospheric studies, and the calculations used to characterize the physical process. This suggests that considerable caution and discretion must be exercised in extrapolating wind tunnel observations to outdoor blowing snow transport phenomena.

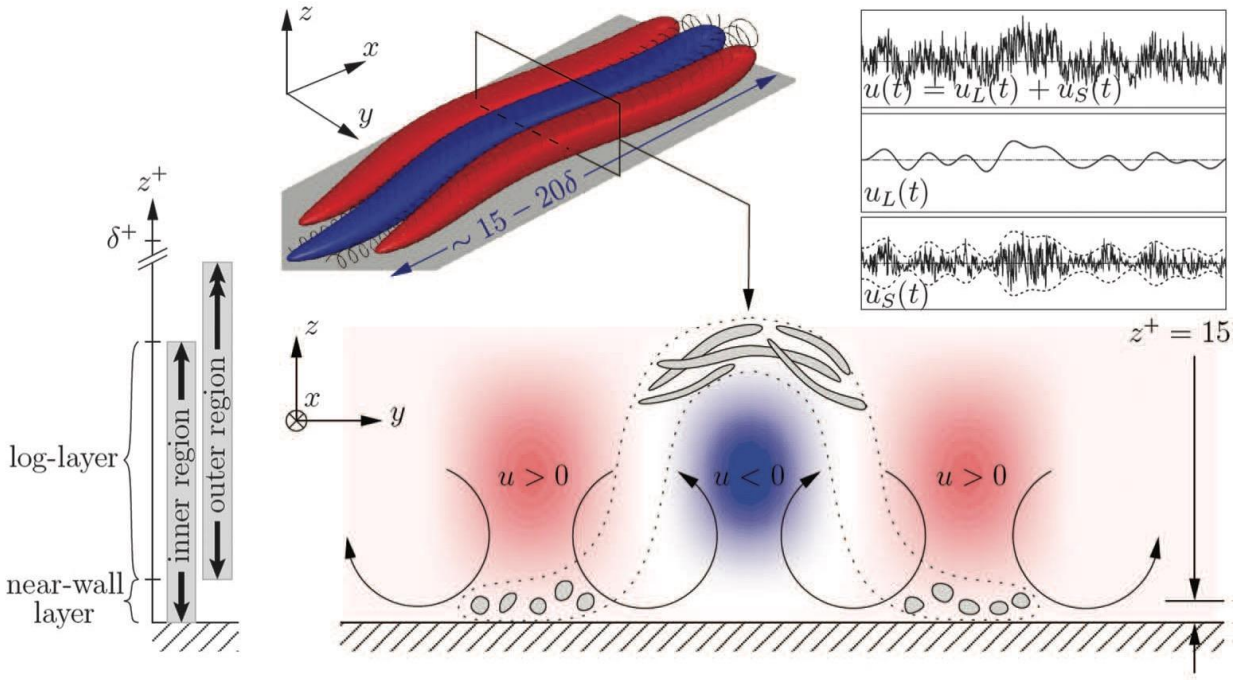

Figure 5-1: Cartoon schematic of large scale outer region structures penetrating towards the surface and interacting with surface turbulence adapted from Marusic et al., 2010. $u(t)$ is the wind signal, $u_l(t)$ and $u_s(t)$ are low-pass and high-pass components of the $u(t)$.

Most analysis connecting turbulent motions and saltation has been conducted in the time-domain (Liu et al., 2012) and has associated limitations. The temporal lag between the two signals caused by particle inertia and the superposition of a wide variety of scales of atmospheric motions result in better analysis with spectral methods (e.g. Venditti and Bennett, 2000; Schönfeldt and von Löwis, 2003; Baas, 2006; Ellis, 2006; Liu et al., 2009; 2012). Quantitative coupling of turbulent

structures with sediment response in given frequencies ranges is difficult in natural conditions, but some promising progress has been made in wind tunnels. Upon analyzing wavelet packet energy in sand saltation time series, Liu et al. (2012) found that, under steady-state conditions, sand concentrations and turbulence fluctuations can be well correlated up to ~250 Hz. High-frequency inertial decoupling with the wind increased with sand particle diameter. Similarly, using wavelet cospectra, Paterna et al. (2016, 2017) found that snow saltation in a wind tunnel was coupled with turbulence at high frequencies under "weak" steady-state saltation transport, and a turbulence-independent regime existed for "strong" transport. As the two-phase coupling in both studies was identified under steady-state conditions by detecting local energy density maxima at similar length scales in both signals, and both studies used experimental apparatuses with narrow energy spectra bandwidth, the coupling (and decoupling) they observed may not develop in natural environments with much greater Reynolds numbers, or during intermittent transport.

Rescaling these kind of steady-state wind-tunnel relationships to environmental flows is often complicated because the mechanics of transport are a function of turbulence structure, which is in turn influenced by surface topography and mesoscale winds (e.g. Wiggs and Weaver, 2012; Chapman et al., 2013). Even mass flux rates and threshold friction velocities vary with turbulence intensity which is often found to be substantially greater in complex terrain than wind tunnels or horizontally homogenous and flat terrain (Xuan, 2004). Exactly how turbulence characteristics in the atmosphere determine the variability and time averaged properties of saltation remains a critical challenge in aeolian research (Kok et al., 2012). It is still an open question whether top-down or bottom-up motions are more appropriate conceptualizations of the coherent structures driving sediment transport (Bauer et al., 1998; Sterk et al., 1998; Baas, 2008).

The objective of this study is to investigate the coherence between intermittent snow transport and turbulent gusts as a coupled nonlinear system to better inform semi-deterministic models of transport (Bauer et al. 2013). To investigate this, 50 Hz field measurements of wind and blowing snow density were collected at a study site in the Canadian Rockies. Statistically significant times and frequencies of wind-snow coupling were identified with wavelet coherence

testing. Through amplitude modulation, the role of large scale motions on high frequency wind eddies and blowing snow transport were investigated. Further analysis of the mechanics of significant large motions using quadrant analysis structures was compared to recent blowing snow-coherent structure insights (Aksamit and Pomeroy, 2017).

5.2 Methods

5.2.1 Fieldwork

Blowing snow observations were collected during night-time field experiments between November 2015 and March 2016, at the Fortress Mountain Snow Laboratory (FMSL), Kananaskis Valley, Alberta, Canada (Figure 5-1). The experimental site was surrounded by relatively flat terrain on a valley bench at 2000 m a.s.l. Nearby steep alpine faces rise from valley bottom elevations of 1500 m to 2900 m ridge tops over distances of less than 5.5 km. The site was suitable for observation of the mesoscale influence of topographically driven flows generating high turbulence intensity (26 – 189 %, cf. Section 2.4) with no immediate (≤ 200 m) bluff body interference. Surrounding ground was snow-covered and shrub vegetation buried for the duration of the experiment with snow depths varying from 40 to 80 cm depending on daily erosion and deposition. The height of snow varied no more than 5 cm during any one night of recording. Two Campbell Scientific CSAT3 ultrasonic anemometers were positioned on a single mast to measure wind speed at 50 Hz in three dimensions at two fixed heights above the ground. Measurement heights varied above the snow surface between 0.10-0.40 and 1.40-1.70 m. The location of the lower sonic anemometer, with a path length of 15 cm, can result in a certain amount of high-frequency energy that is not measured. Estimates of the high-frequency losses for each anemometer during each night of recording are provided in the document supplement.

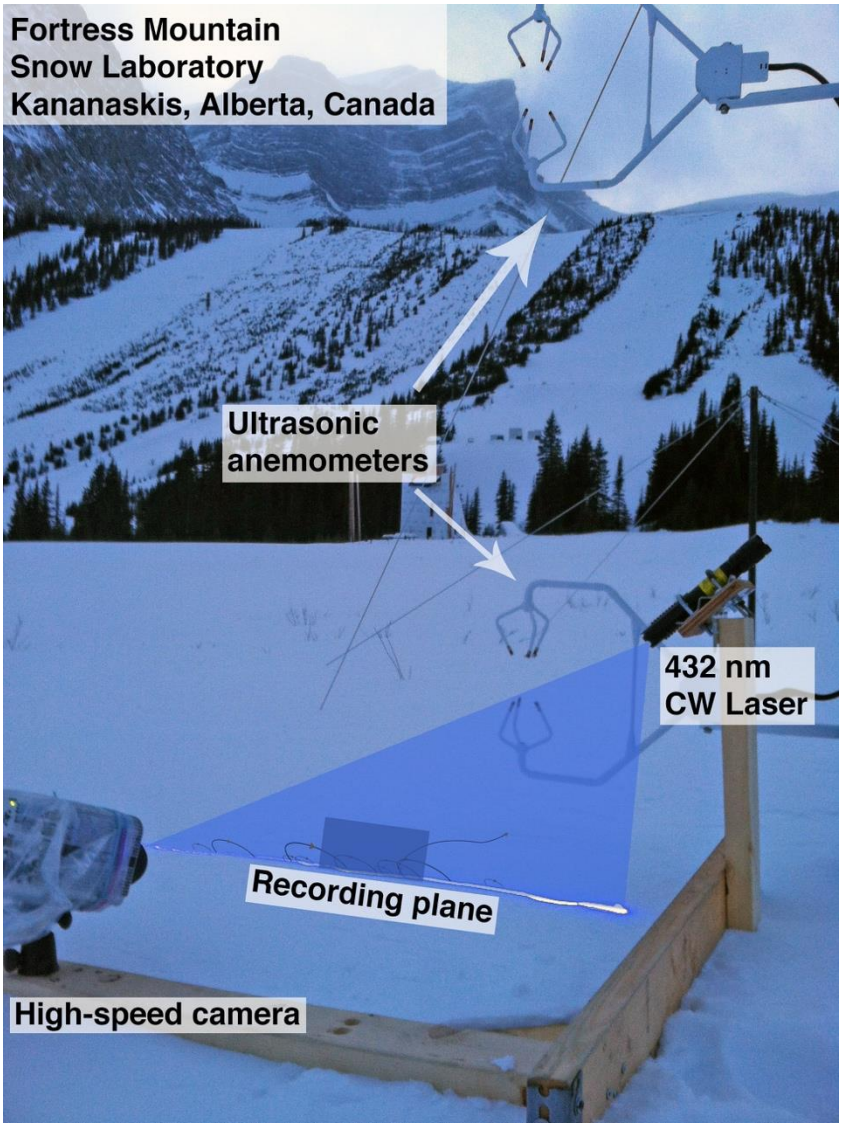

Figure 5-2: Blowing snow recording apparatus with nearby wind measurements, Fortress Mountain Snow Laboratory, Kananaskis, Alberta, Canada. The recording plane indicates the location of camera focus inside the illumination plane. The wind is oriented parallel with the plane and toward the CW laser in this schematic.

Blowing snow observations were made with the laser-video system described by Aksamit and Pomeroy (2016, 2017). The camera was situated 0.30 m from the anemometer mast, in a spanwise orientation to the wind (Fig. 5-2) and was rotated throughout the observation periods to keep the laser illumination plane parallel to the dominant wind direction. The camera then

recorded a plane (~ 30 mm x 140 mm) of the flow of saltating snow (Fig. 5-2). To capture the influence of large eddies responsible for the strongest sediment transport fluctuations (Schönfeldt and von Lowis, 2003; Baas, 2006; Liu et al., 2009), several long, 5- to 19-minute videos of night-time snow particle transport at 50-100 FPS were recorded each night. Each blowing snow video recording consisted of 2.7-5.8 × 10^4 frames, depending on aspect ratio and frame resolution, totaling 4.1 hours for 23 blowing snow recordings over 5 nights.

	Surface Description	Snow Surface Density (kg/m^3)	Air/Snow Surf. Temp (°C)	Surface Hardness (HHI)	Grain Size Range (mm)	Mean 0.4m wind speeds (m s^{-1})
Nov. 20	2-3 cm wind slab	N/A	-10 / N/A	Pencil	N/A	2.7 - 3.9
Dec. 4	Pockets of drifted snow on wind slab	390	-3 / -4	Pencil	0.25-0.75	2.4 - 6.4
Dec. 7	1 cm fresh on wind slab	137	-3 / -3.5	4 Finger	0.5-1.5	1.5-3.0
Feb. 3	Fine decomposing grains on wind slab/sastrugi	262	-10 / -10	1 Finger-Pencil	0.5-1	3.6 – 5.7
Mar. 3	Fresh snow, not snowing	156	-2 /-5	Fist	0.5	3.5 – 4.8

Table 5-1: Snow surface and meteorological conditions during each night of blowing snow. Missing values are indicated by 'N/A'.

Descriptions of the snow surface, snow densities from the top 5 cm of the snowpack, average air and snow surface temperatures, surface hand hardness indices, mobile grain diameters, and 15-minute mean wind speed ranges for the five nights are found in Table 5-1. Wind and video measurements were synchronized at the onset of nightly recording to minimize data logger drift. Each night exhibited slightly stable stratification and wind measurements for each recording were subjected to a dual-axis rotation such that u was parallel to the streamwise direction, and the spanwise and vertical winds (v, w respectively) had a zero-mean, following Kaimal and Finnigan (1994).

As amplitude modulation studies have never been conducted during blowing snow storms, it was important to consider the influence of blowing snow particles on the wind as well as the effect of large scale motions. Data from Paterna et al. (2016) were utilized for a low-Reynolds-number comparison of the role of large turbulent structures modulating surface

turbulence and blowing snow. Specifically, 20 Hz directional snow flux and wind speed fluctuations were subjected to the same analysis as the FMSL data.

5.2.2 Blowing Snow Density Estimation

Gray scale blowing snow video recordings were binarized following the algorithm of Otsu (1979), to obtain blowing snow particle concentrations per frame. A binarization threshold was determined for each frame to account for varying illumination depending on density of saltation. Similar techniques have been used in wind tunnel sand transport concentration studies (e.g. Liu et al., 2012) and environmental blowing snow studies (e.g. Gordon et al., 2009; Aksamit and Pomeroy, 2016, 2017). After binarization, quality controls were implemented to eliminate false positive snow measurements from camera sensor "hot spots" during periods of low transport as well as to adjust for low light conditions during periods of high transport when the laser was largely obscured. A flood-fill algorithm was then implemented to identify individual snow particles and estimate their equivalent particle diameters. Assumptions of particle sphericity and constant snow particle density equal to ice (917 kg m^{-3}) allowed estimation of airborne blowing snow density ρ_{bs} (kg m^{-3}) per frame as by Aksamit and Pomeroy (2016, 2017).

5.2.3 Signal Processing

5.2.3.1 Wavelet Analysis

Wavelet analysis has emerged as the standard technique to detect intermittent behavior in geophysical systems in the time-frequency domain (e.g. Foufoula-Georgiou and Kumar, 1994; Torrence and Campo, 1998; Grinsted et al., 2004). In comparison to Fourier methods, wavelets are (imperfectly) localized in time and frequency and wavelet convolution requires only local-stationarity under the image of the wavelet. This results in better identification of transient coherent structures when applied to aeolian systems (e.g. Baas, 2006; Ellis 2006). To identify statistically significant wind-blowing-snow coupling, the wavelet coherence (CH) and statistical significance testing method of Grinsted et al. (2004) is introduced for this blowing snow study. This is a complementary technique to the wavelet maps of Ellis (2006), wavelet packet decomposition of Liu et al. (2012) and wavelet cospectra of Paterna et al. (2016).

Let $W^x(n,s)$ and $W^y(n,s)$ be the continuous wavelet transforms of the time series $\{x_n\}$ and $\{y_n\}$, respectively, where n is time and s is the scaling of the mother wavelet. Further define the cross wavelet transform of the two time series as $W^{xy}(n,s) = W^x(n,s)\,W^{y*}(n,s)$, where * indicates the complex conjugate of the wavelet transform. For the present research, the Morlet wavelet was chosen as the mother wavelet as it is well localized in both frequency and time and is useful for event extraction in geophysical time series (Grinsted et al., 2004, Ellis, 2006). Following Liu (1994) and Torrence and Webster (1999), one can derive a measure, $CH_{n,s}(x,y)$, of the coherence in the cross-wavelet transform in the time-frequency domain:

$$CH^2_{n,s}(x,y) = \frac{\left|\langle s^{-1}W^{xy}_n(s)\rangle\right|^2}{\langle s^{-1}W^x_n(s)\rangle \cdot \langle s^{-1}W^y_n(s)\rangle}, \tag{5-1}$$

where $\langle\cdot\rangle$ is a smoothing operator in time and scale, and multiplication by s^{-1} converts values to energy density. The statistical significance testing of Grinsted et al. (2004) utilizing Monte Carlo simulations and background red-noise was applied at the 5 % significance level to all wavelet coherence results. The cone of influence (COI) demarcates the regions in the time-frequency domain where zero padding and edge effects from the wavelet transform improperly affect coherence calculations. To verify that significant coupling had been identified in each time series pair, CH maps for each recording were tested to determine if more than 5 % of the scale-weighted area inside the COI contained statistically significant coherence. Time-averaged $CH_{n,s}$, referred to as MCH_s, also provided a measure of mean coherence in the frequency domain for each recording. Define

$$MCH_s(x,y) = \frac{1}{\mu(n_s \in \mathrm{COI})} \int_{n_s \in \mathrm{COI}} CH_{n,s}(x,y)\,dn, \tag{5-2}$$

where $\mu(n_s \in \mathrm{COI})$ is the measure of the length of the time series intersecting the COI at scale s. Further background on the theory of wavelets can be found in Daubechies (1992). Applications and comparisons of wavelet methods are outlined by Foufoula-Georgiou and Kumar (1994) and Torrence and Campo (1998) and in the signal processing text of Mallat (2008).

5.2.3.2 Amplitude Modulation

One limitation of using Fourier or wavelet coherence tests to characterize the coupling of turbulent bursts with blowing snow is that neither method clearly captures the influence of large-

scale motions on high-frequency turbulence or snow transport energy across scales. The role of large-scale motions is being recognized as increasingly important as strong topographically-enhanced turbulent motions in this mountain region have been identified (Helgason and Pomeroy, 2012) but the power spectra likely overlap with local processes, often preventing a clear spectral separation of large and small-scale motions (Sievers et al., 2015). Thus, the relationship of large eddies (duration greater than 30 s) with high-frequency near-surface turbulence and blowing snow was further investigated with the theory of amplitude modulation.

Consider, for example, representing high-frequency local turbulent motions as a carrier signal $c(t) = \sin(4\pi t)$, and larger atmospheric motions with a higher mean wind speed as a modulating signal $m(t) = 2 + \sin(\pi t)$. The resultant amplitude-modulated signal $u(t) = m(t)c(t)$ and $m(t)$ are displayed in Fig. 2a. With $\hat{m}(\omega)$ and $\hat{u}(\omega)$ being the Fourier transform of $m(t)$ and $u(t)$, respectively, $\hat{u}(\omega)$ in Fig. 2b shows the mirroring of the energy content from $\hat{m}(\omega)$ around the base frequency of $c(t)$, 2 rad^{-1} $\pm$ 0.5 rad^{-1}. While the amplitude of the carrier signal has obviously been increased at the modulating signal's frequency (0.5 rad^{-1}), this influence is largely obscured in the Fourier transforms, with no energy actually contained at 0.5 rad^{-1}. Because of the broadband overlap of both low and high-frequency motions in the atmosphere, extracting a signal responsible for modulating high-frequency turbulence with Fourier methods is realistically unfeasible. For clarity, the mirroring effect on the Fourier transforms is proven in more generality in the document supplement.

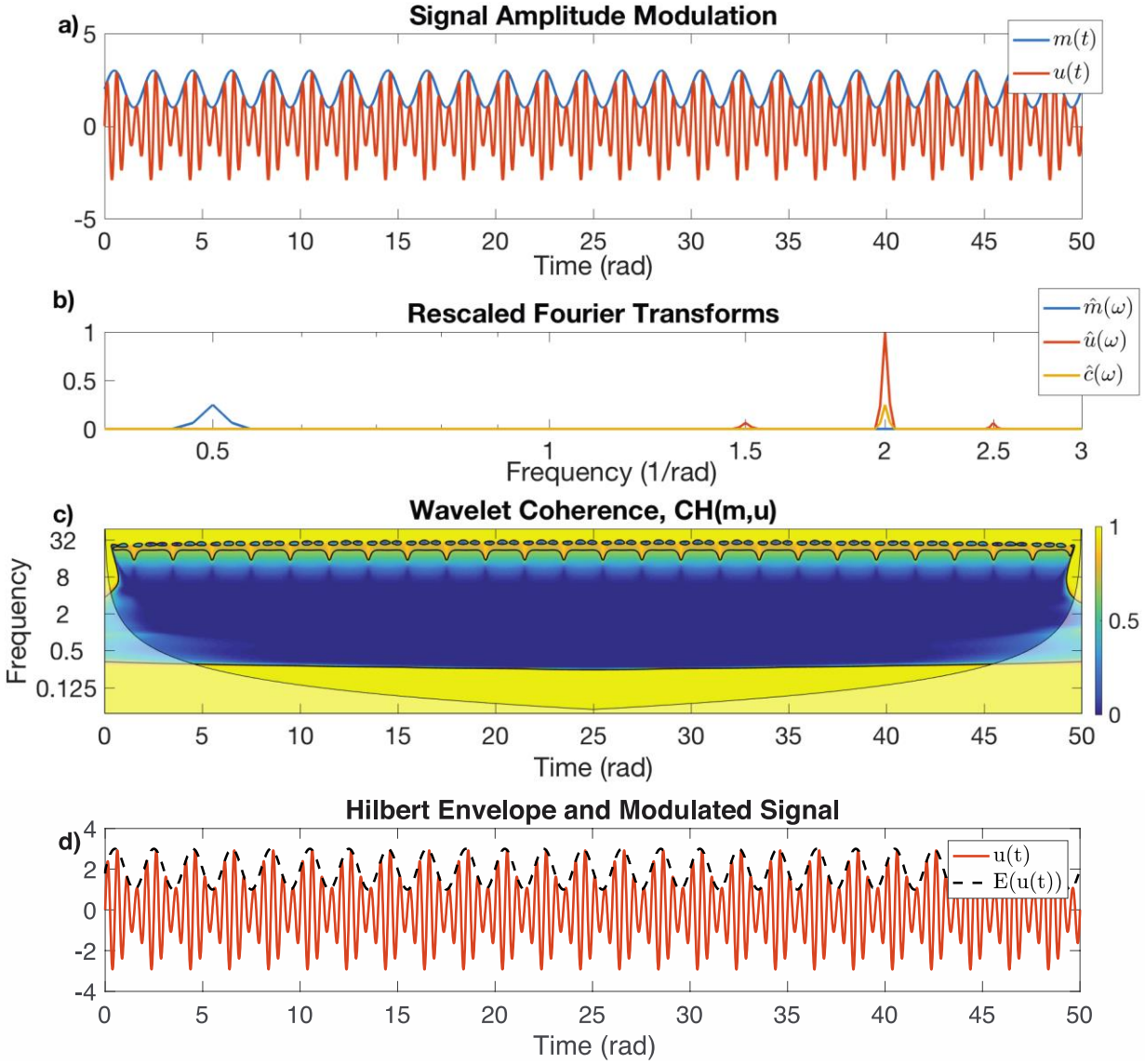

Figure 5-3: Example of amplitude modulation of high-frequency signal (a), Fourier transforms of modulating and modulated signals showing mirroring of modulating energy (b), wavelet coherence map of $CH_{n,s}(m,u)$ with no 0.5/radian coherence from $m(t)$ energy (c), and Hilbert transform recovered amplitude modulating signal (d).

Because of the translation of modulating signal energy away from its original frequency to each side of the carrier signal frequency, there is evidence of coupling in the wavelet coherence map of $m(t)$ and $u(t)$ at the frequencies of either the carrier (2 rad^{-1}) or modulating signals (0.5 rad^{-1}) ($CH_{n,s}(m,u) \approx 0$ in Fig. 5-3c). With sufficient frequency separation in the power spectra of

the carrier and modulating signals, however, the Hilbert transform can perfectly reconstruct the modulating signal. For a time series $x(t)$, define the Hilbert transform

$$\mathcal{H}[x(t)] = \tilde{x}(t) = \frac{PV}{\pi} \int_{-\infty}^{\infty} \frac{x(u)}{(t-u)} du = x(t) * \left(\frac{1}{\pi t}\right), \tag{5-3}$$

where PV is the Cauchy Principal Value and $*$ denotes standard convolution. The Hilbert transform can also be regarded as the imaginary part of the analytic function $z(t)$ with $Re(z) = x(t)$. Formally,

$$z(t) = x(t) + i\tilde{x}(t). \tag{5-4}$$

The modulus of $z(t)$ is called the envelope signal of $x(t)$, hereon written $E(x(t))$. Using the same modulating and carrier signals as in Fig. 5-3a, $E(u(t))$ is overlaid on $u(t)$ in Fig. 5-3d, and is identically the modulating signal $m(t)$. This reconstruction of modulating signals is proven in more generality in the document supplement.

Mathis et al. (2009a) showed that if one separates a sufficiently high Reynolds number streamwise wind signal, u, into low-frequency and high-frequency components, u_L and u_H, respectively, at an appropriate cutoff frequency, and then low-pass filters the envelope of the high-frequency signal, $E_L(u_H(t))$, one can identify to what degree passing large-scale motions modulate the high-frequency turbulence. This method identifies nonlinear effects of large scale motions on near-wall turbulence in the atmospheric surface layer that were missed in Fig. 5-3c. For the present study, it is proposed that the low-frequency component of streamwise wind speed, u_L, represents large eddies (modulating signal) that amplify the magnitude of high-frequency surface fluctuations (carrier signal), u_H. A correlation coefficient can then be defined that measures the degree of amplitude modulation, i.e. the influence of large-scale eddies on high frequency turbulence:

$$AM_{u,u} = \frac{\overline{u_L \, E_L(u_H)}}{\sqrt{\overline{u_L^2}}\sqrt{\overline{E_L(u_H)^2}}}, \tag{5-5}$$

where the overbar indicates temporal averaging. Note that because amplitude modulation inherently involves different scales of motions at different frequencies, AM intentionally does not account for a difference in mean or variance in the two time series. Furthermore, all signals were

standardized to have zero mean and unit variance prior to calculation of AM coefficients to account for different units and ranges of wind and snow signals. Background on amplitude modulation and the theory of Hilbert transforms can be found in Bendat and Piersol (2010).

5.2.4 Turbulence Characteristics

Turbulence statistics were calculated for each recording including, but not limited to, turbulence intensity, turbulence kinetic energy, friction velocity, drag coefficient (Lykossov and Wamser, 1995), dissipation length, energy flux, and several covariances. Reynolds stress time series were decomposed following quadrant analysis with a hole size of one (Lu and Willmarth, 1973). The percent of Reynolds stress contributed by each quadrant of motion above this threshold was then calculated. As well, the temporal occurrence of each quadrant motion was measured. As these values are all compact simplifications of the flow conditions, correlations between them and wavelet coherence or the degree of amplitude modulation across the recordings may provide useful corollaries for semi-deterministic modeling with lower computational cost. Notable correlations are presented in the results.

5.3 Results

5.3.1 Wavelet Coherence

Wavelet coherence was calculated for time series pairs of low-anemometer streamwise wind speed and blowing snow density as well as low-anemometer Reynolds stress and blowing snow density, $CH_{n,s}(\rho_{bs}, u_g)$ and $CH_{n,s}(\rho_{bs}, \tau)$ respectively, for all 23 recordings. Examples of raw wind (u_g and τ) and ρ_{bs} signals and their wavelet coherence maps ($CH_{n,s}$) from March 3 are shown in Fig. 5-4. Bold outlined regions of the coherence maps in Fig. 5-4c & 5-4d indicate coherent events at the 5% significance level.

As was typical for all recordings, there is much greater coherence between blowing snow density and streamwise wind speed in Fig. 5-4c than that measured with Reynolds stress (Fig. 5-4d). In Fig. 5-4, statistically significant regions cover 48% and 4% of the COI for $CH_{n,s}(\rho_{bs}, u_g)$ and $CH_{n,s}(\rho_{bs}, \tau)$, respectively. All but one recording exhibited $CH_{n,s}(\rho_{bs}, u_g)$ coherence at 5% significance for more than 5% of the scale-weighted area of the COI, with total coherent areas ranging from 4.6% to 49% over all nights. Only 10 out of the 23 recordings showed significant

coherence at the 5% level between τ and ρ_{bs} over more than 5% of the area of the COI. The significant percent of the COI ranged from 2 to 43% for $CH_{n,s}(\rho_{bs}, \tau)$. The average area of significant wind structures coupled with snow was 19% for u_g and 9% for τ over all recordings. Larger percentages of coherent areas indicate more consistent time-frequency coupling of streamwise wind speed with blowing snow across broader frequency bands, but both area averages also underscore the highly intermittent structure of natural blowing snow at this site.

Time-averaged $CH_{n,s}$ calculations, MCH_s, measured the mean coherence at each scale over an entire time series. The average MCH_s for the whole experiment is displayed in Fig. 5-5a with frequency ranges bin-averaged for clarity. One standard deviation is shaded surrounding the mean of both Fig. 5-5 plots. MCH_s provides similar information to magnitude-squared Fourier coherence with larger values indicating more coherence. Coherence monotonically increased with decreasing frequency between blowing snow and streamwise wind speed, whereas a distinct coherence peak was found between Reynolds stress and blowing snow for the bin 0.05-0.09 Hz. The measured coherence between the snow and either turbulence signal was equivalent above 0.35 Hz. As MCH_s is a time average of $CH_{n,s}$, the transient nature of intermittent blowing snow is not clearly captured.

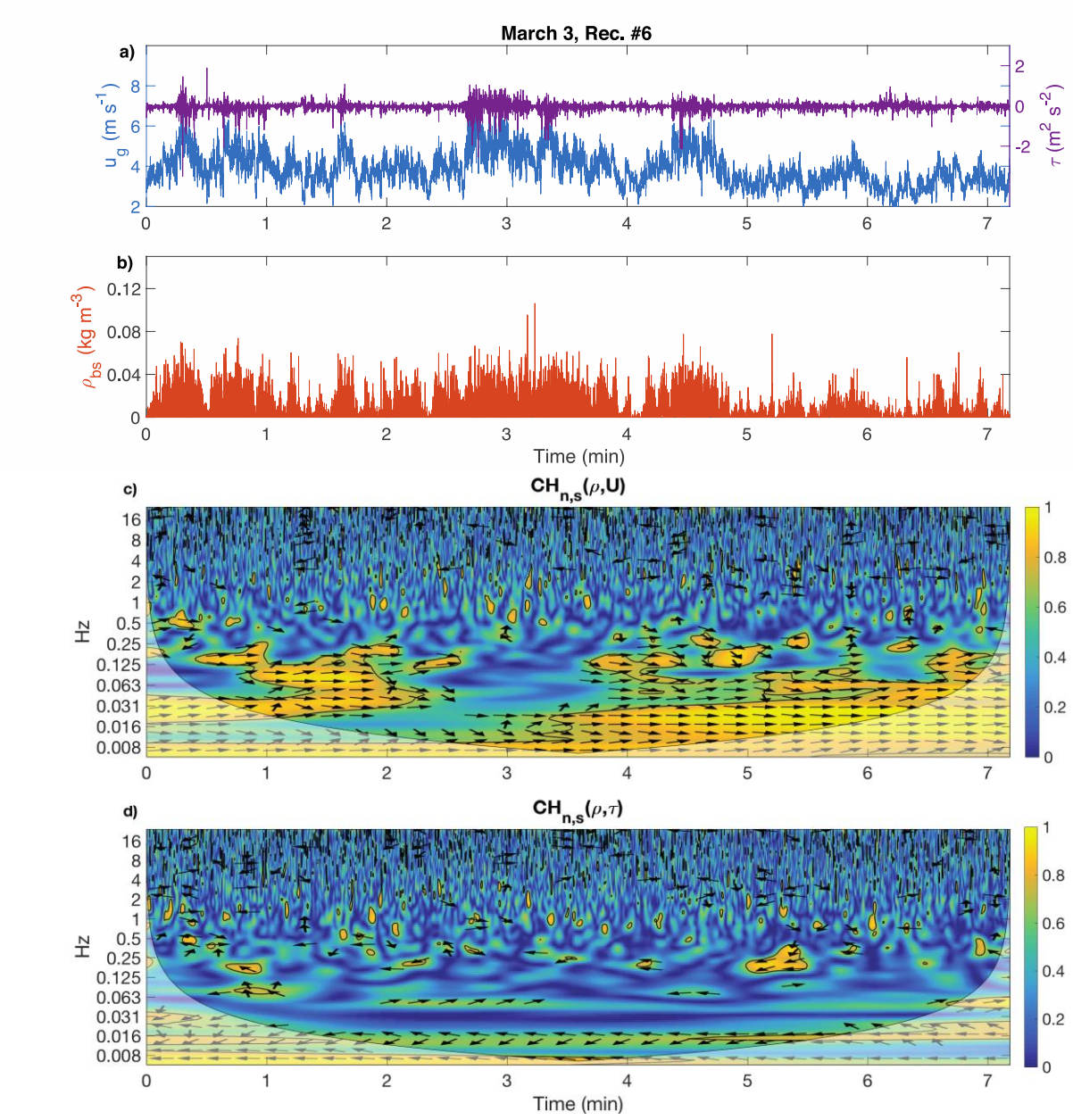

Figure 5-4: (a) Streamwise wind speed and Reynolds stress for 3 March 2016 recording #6 (22:12:54 to 22:20:06 MST). (b) Blowing snow density for the same recording. (c) Wavelet coherence for blowing snow and streamwise wind and (d) for blowing snow and Reynolds stress. In c) and d), bold lines surround 5% significance events. Arrows indicate the phase relationship of the two signals with in-phase pointing right, anti-phase pointing left, and 90° down being the wind leading the snow.

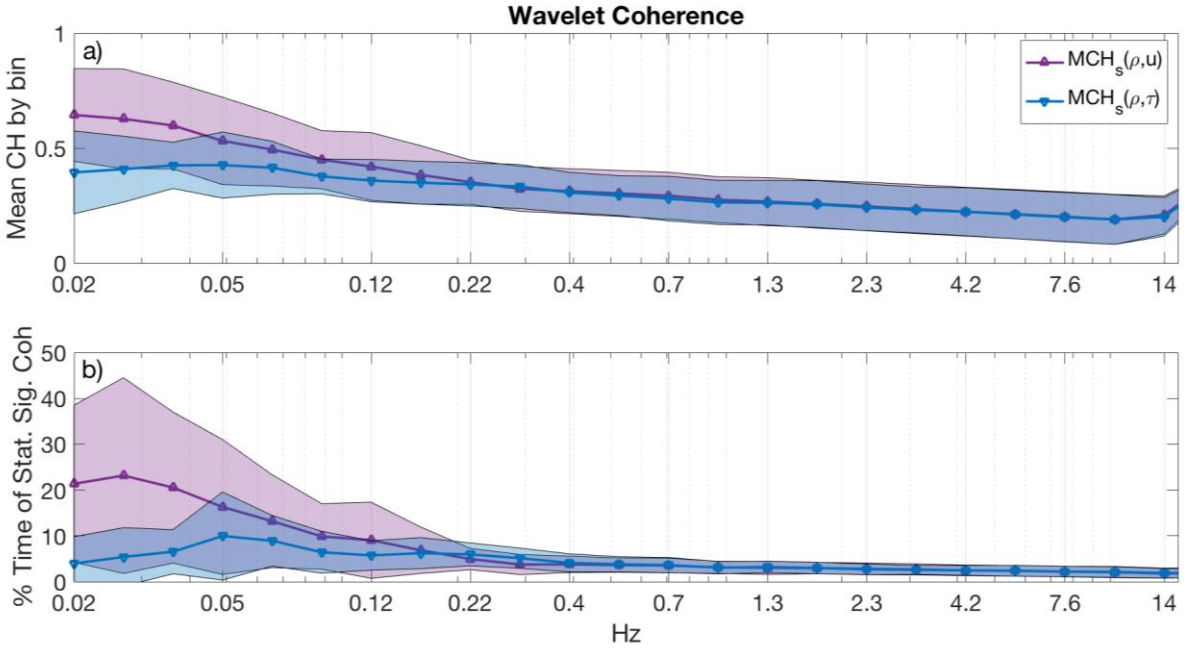

Figure 5-5: Frequency-binned $MCH_s(\rho_{bs}, \tau)$ and $MCH_s(\rho_{bs}, u_g)$ over all recordings (6a) and the percent of temporal occurrence of $CH(\rho_{bs}, u_g)$ and $CH(\rho_{bs}, \tau)$ values that were statistically significant at 5% for the same bins (6b). One standard deviation is shaded for all plots. Notice higher coherence at lower frequencies for $CH(\rho_{bs}, u_g)$ and general agreement of coherence for $f >$ 0.35 Hz.

In contrast, Fig. 5-5b displays the mean percent of time (inside the COI) with $CH_{n,s}(\rho_{bs}, u_g)$ and $CH_{n,s}(\rho_{bs}, \tau)$ at 5% statistical significance for the same frequency bins over all recordings. This uses the temporal localization of wavelets to present how often transient but significant coherence occurred. Interestingly, Fig. 5-5b shows there was always some statistically significant coupling in both pairs at all scales in the COI while low-frequency (<0.35 Hz) structures still dominated the bands of highest coherence. There was substantial low-frequency coherence below $f_c = 0.06\ Hz$ in $CH(\rho, u_g)$ that was not present in $CH(\rho, \tau)$, with significant coherence nearly four time more likely with streamwise wind speed. This is to be expected by the relatively low energy in τ at low frequencies (Hunt and Morrison, 2000) that provides little energy to the cross-wavelet transforms (Eq. 1). Again, there was general agreement in coherence of blowing snow with either wind signal at frequencies higher than 0.35 Hz.

The edge effects associated with the Morlet wavelet prevent resolving coherence of blowing snow with atmospheric motions larger than approximately half the length of a recording,

as they are outside the COI (Torrence and Compo, 1998). This is a typical issue with time-frequency decompositions and is a manifestation of using finite-length time series and a nonzero minimum area of Heisenberg boxes (Weyl, 1950). An analogous problem exists when resolving magnitude-squared coherence with Fourier methods where large Fast Fourier Transform windows allow lower frequency coherence measurements but introduce more signal noise (Biltoft and Pardyjak, 2009).

5.3.2 Amplitude Modulation

Wavelet coherence (Figs. 5-4 and 5-5) indicated that blowing snow responded most strongly to wind energy at long time scales (low frequencies) between one second and the limits of the COI. However, there was also coupling of ρ_{bs} to high-frequency u and τ fluctuations of unknown origin over shorter time scales (Fig. 5-5a, 5-5b). The analysis of Ellis (2006) indicates that the brief coherent structures responsible for intermittent sand transport in their study did not likely originate from surface instabilities. Thus, for all recordings, it was investigated whether the significant high-frequency coupling in Section 3.1 could be also be related to large scale structures. More precisely, was there evidence of amplitude modulation in high-frequency turbulence, blowing snow, and coherence signals during the passage of top-down penetrating structures?

The ability to quantify amplitude modulation with Hilbert transforms (Eq. 5-3 and 5-5) is sensitive to the cutoff frequency separating large scale and surface motions (Mathis et al., 2009a). The choice of scale separation in the current study is complicated by the topographical influence on turbulence spectra at the study site by the surrounding peaks (Mahrt and Gamage, 1987; Sievers et al., 2015). As well, both wind measurements were obtained relatively close to each other and near the snow surface, preventing identification of a distinct outer region peak as found by Hutchins and Marusic (2007a). However, a transition from self-similar behavior to an inertial subrange -5/3 slope was seen near the frequency $f = 0.06\,Hz$ in the averaged power spectra for each night (Fig. 5-6). There was also a transition to higher turbulence energy at the lower measurement height for frequencies above this threshold (Fig. 5-6). Using the mean wind speed at 2 m as a proxy for convective velocity, this frequency corresponded to eddy length scales

between 39 m and 67 m during the recordings. Average integral time scales for the streamwise wind series were also found to be of this order of magnitude at 33 $s = 0.03\ Hz^{-1}$. This is similar to a previous atmospheric boundary layer amplitude-modulation study that found the boundary layer depth ($\delta = 60$ m for their experiment) to be a suitable separating length scale (Mathis et al., 2009a). As there was no definitive measurement of the boundary layer depth at this mountain site, the cutoff frequency $f_c = 0.06\ Hz$ was chosen as a threshold to separate large-scale and small-scale motions. Varying the choice of threshold in the range from $f_c = 0.12$ to $0.03\ Hz$ did not affect the described analysis and results, though it did result in small variations in the degree of modulation, AM (Eq. 5-5).

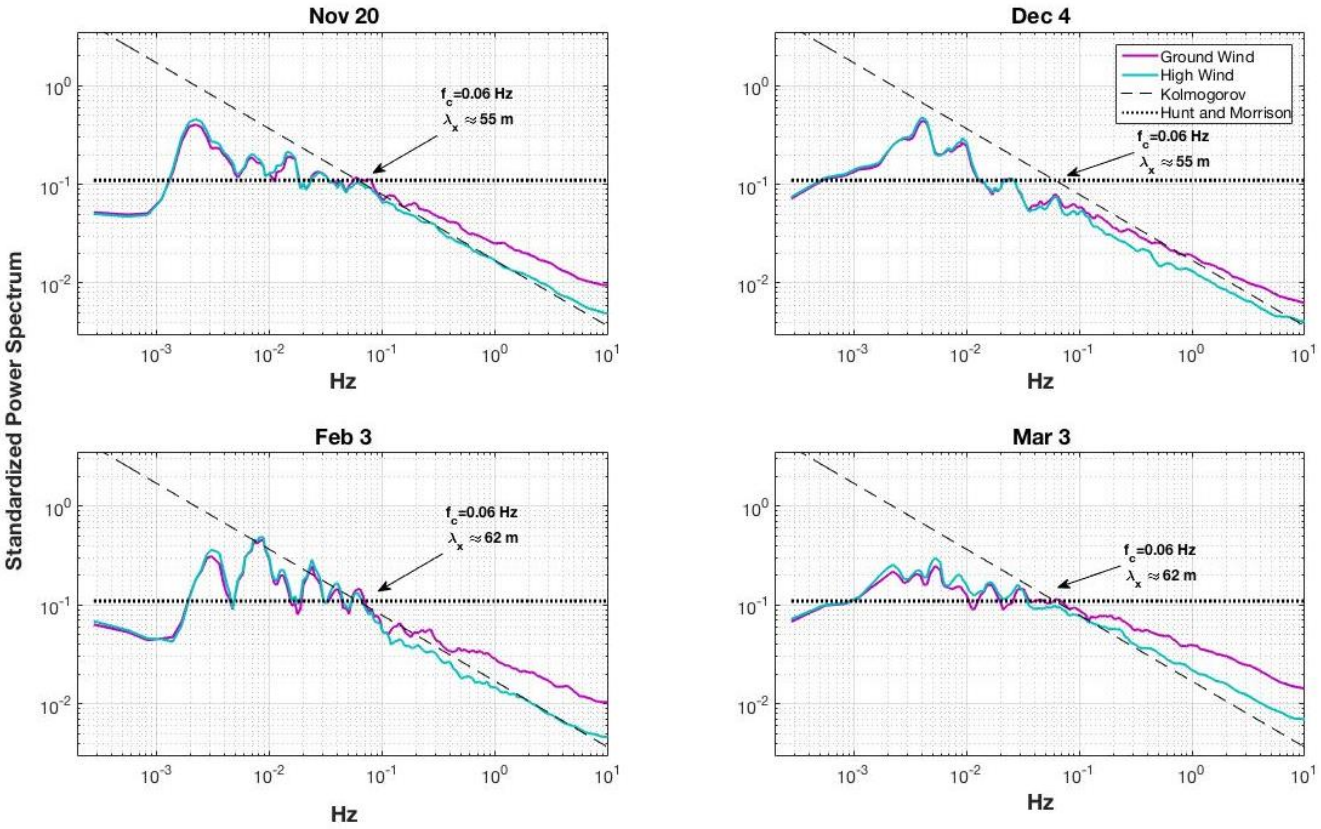

Figure 5-6: Standardized pre-multiplied power spectral density of streamwise wind speed for five hours at two measurement heights over four nights of recording. Self-similar (Hunt and Morrison, 2000) and -5/3 slope (Kolmogorov, 1941) lines overlaid to show transition and cutoff frequency $f_c = 0.06\ Hz$. Also note elevated high-frequency energy in ground wind signals above f_c. February 7 omitted for brevity.

The large motions defined by the low-pass filter in both the near-surface and upper anemometer streamwise wind signals, $u_{g,L}$ and $u_{h,L}$ respectively, were found to strongly modulate high-frequency near-surface turbulence,$u_{g,H}$. The coefficients AM_{u_h,u_g} and AM_{u_g,u_g}, as defined by Eq 5., were found to be typically greater than or equal to those found in previous modulation studies (Mathis et al., 2009a) and are detailed in Table 5-2. The consistently large AM values for either pair of turbulent wind signals ($AM \in [0.4 - 0.8]$) are convincing evidence of the influence of low-frequency large-scale events on high-frequency turbulence, and suggest that many near-surface turbulence bursts were not a purely local phenomenon. Amplitude modulation of ρ_{bs} by upper-anemometer large scale motions was also quantified and can be found in Table 5-2.

While the majority of recordings exhibited strong modulation (Table 5-2), there were several exceptions which are explained with quadrant analysis (Lu and Willmarth, 1973) in Section 4. These values are italicized in Table 5-2. Also of note, in contrast to the results of Hutchins and Marusic (2007a), there was inconsistent amplitude modulation of Reynolds stress signals.

	20 Nov							4 Dec						
Time (s)	571	282	643	*643*	734	557	731	571	571	*643*	864	864	864	864
$\boldsymbol{u_*}$ (m s^{-1})	0.29	0.24	0.31	*0.35*	0.44	0.27	0.36	0.37	0.42	*0.66*	0.49	0.39	0.57	1.00
$\boldsymbol{R_{u_h,u_g}}$	0.66	0.57	0.57	*0.03*	0.73	0.58	0.52	0.44	0.60	*0.19*	0.81	0.56	0.49	0.51
$\boldsymbol{R_{u_g,u_g}}$	0.68	0.56	0.58	*-0.10*	0.67	0.57	0.51	0.42	0.62	*0.13*	0.79	0.46	0.36	0.50
$\boldsymbol{R_{u_h,\rho}}$	0.3	0.75	0.46	*0.60*	0.79	0.75	0.40	0.34	0.29	*0.43*	0.30	0.54	0.32	0.34

	7 Dec		3 Feb				3 Mar		
Time (s)	1151	987	431	862	573	1149	432	432	*288*
$\boldsymbol{u_*}$ (m s^{-1})	0.53	0.3	0.25	0.23	0.25	0.31	0.16	0.18	*0.2*
$\boldsymbol{R_{u_h,u_g}}$	0.21	0.77	0.84	0.32	0.25	0.59	0.56	0.69	*0.05*
$\boldsymbol{R_{u_g,u_g}}$	0.19	0.78	0.85	0.26	0.22	0.58	0.60	0.72	*-0.01*
$\boldsymbol{R_{u_h,\rho}}$	0.04	0.71	0.70	0.74	0.59	0.70	0.77	0.95	*0.51*

Table 5-2: Amplitude modulation coefficients for each recording for blowing snow density by 2 m streamwise wind speed ($R_{u_h,\rho}$), ground streamwise wind speed by 2 m streamwise wind speed (R_{u_h,u_g}), and ground streamwise wind speed by ground streamwise wind speed (R_{u_g,u_g}).

Figure 5-7 displays an example of a time series of low-frequency upper anemometer wind speed and high-frequency envelopes for the same recording as in Fig. 5-4 ($AM_{u_h,u_g} = 0.69$, $AM_{u_h,\rho} = 0.95$). The raw wind and snow signals under analysis are shown in Fig. 5-7a. Figure 5-7b shows the low-pass filtered upper anemometer wind signal, $u_{h,L}$, the envelope of high-frequency blowing snow, $E_L(\rho_{bs,H})$, and the envelope of high-frequency near-surface turbulence, $E_L(u_{g,H})$, as well as purple dots during moments of extreme sweep Reynolds stress, $\{t \mid u'(t) > 0, w'(t) < 0, |u'(t)w'(t)| > rms(u'w')\}$ from quadrant analysis (Lu and Willmarth, 1973). For presentation clarity, all time series in Fig. 5-7b have been standardized to have zero mean and unit variance.

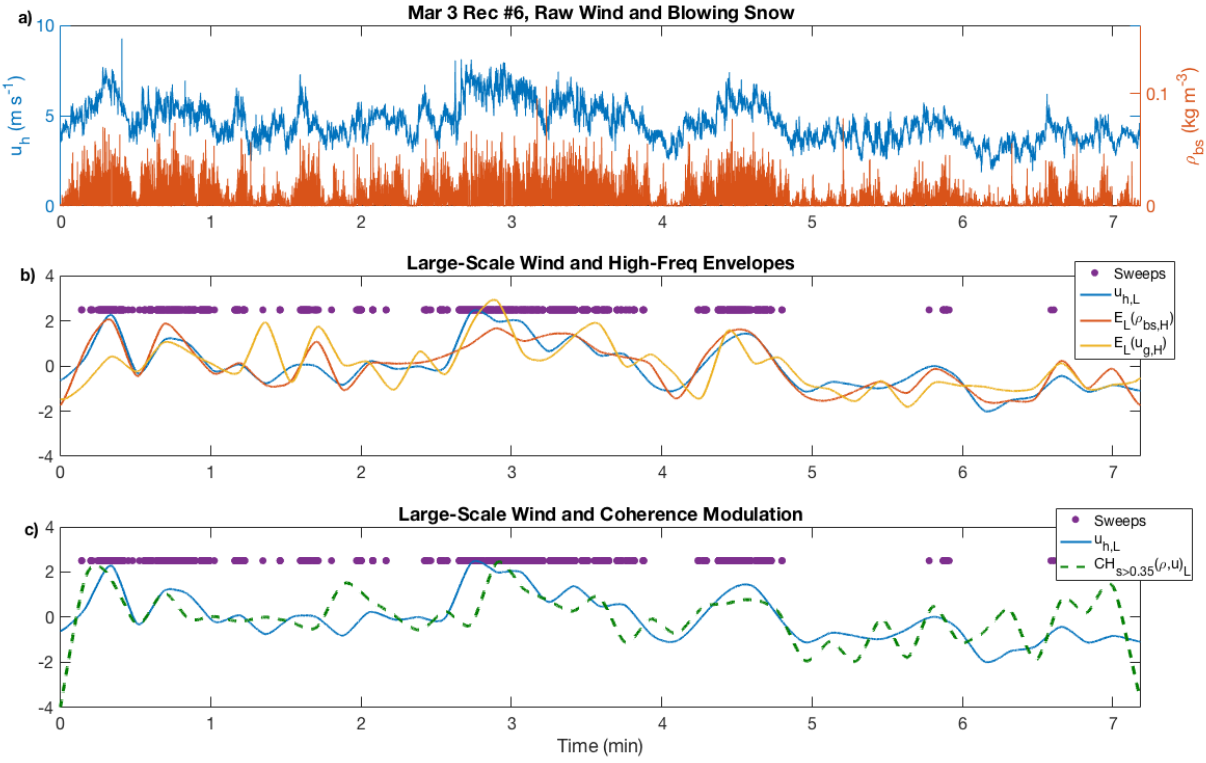

Figure 5-7: Amplitude modulation of high-frequency wind and blowing snow signals by large scale events. Subplot a displays raw wind and blowing snow signals. Notice correlation between low pass wind signal ($u_{h,L}$) and Hilbert transform envelopes of high pass wind and snow signals ($E_L(\rho_{bs,H})$ and $E_L(u_{g,H})$, 5-6 b). Low pass signal of high-frequency coherence ($CH_{n>0.35}(\rho, U)_L$) indicates many of the same low-frequency structures are generating periods of high frequency coherence (5-6 c). Sweep structures are marked by purple dots and coincide with the strongest excursions in u_L in subplots b-c. Y-values in 5-6 b-c are normalized and dimensionless.

Many local maxima in $E_L(\rho_{bs,H})$ and $E_L(u_{g,H})$ are in phase with the passage of energetic low-frequency events at the upper anemometer (e.g. 0 to 1 min, 2.5 to 5 min in Fig. 5-7b). In general, the same atmospheric motions that modulated near-surface turbulence were often responsible for enhancing high-frequency components of blowing snow. Disregarding three outlier recordings on 20 Nov, 3 Mar, and 4 Dec described in Section 5.4, there was strong linear correlation between $E_L(u_{g,H})$ and $E_L(\rho_{bs,H})$, resulting in an average correlation coefficient over all nights of 0.54.

The transient high-frequency coherence between wind and snow signals mentioned in Section 3.1 also appears to be connected to the passage of large scale motions. To illustrate this, each time step of $CH_{n,s}(\rho_{bs}, u_g)$ was scale-averaged over the Fourier frequencies greater than 0.35 Hz to obtain a mean coherency time series between only high-frequency components of snow and turbulence signals. This coherency time series was then low-pass filtered below the cutoff frequency $f_c = 0.06$ Hz to show the in- and out-of-phase relationship with large scale motions. This time series is displayed as a dashed green line ($CH_{s>0.35}(\rho, u)_L$) in Fig. 5-7c and is indicative of what was found in all recordings: many of the passing large motions that modulate high-frequency turbulence also coincide with stronger high-frequency coherence between wind and snow. This is also reflected in consistently high correlation coefficients between $CH_{s>0.35}(\rho, U)_L$ and $E_L(u_{g,H})$, with an average $r = 0.57$ over all recordings, as discussed more in Section 3.3. Thus, it was the passage of large-scale wind structures that was responsible for both high and low-frequency coherence between blowing snow transport and wind signals.

It is worth noting that, like the results of Baas (2006) and Liu et al. (2012), the snow transport signal maintained higher wavelet power spectral density than streamwise wind fluctuations at the upper end of the frequency spectrum, typically > 1 Hz, showing a possible inertial effect of snow particles and the presence of a near-surface rebound energy separate from that gained from the wind.

5.3.3 Connections with turbulence statistics

Statistical associations were examined between measurements of average coherence and amplitude modulation and turbulence descriptors for each recording to discern if certain

atmospheric conditions were more conducive to wind-snow coupling or amplitude modulation. Very few statistically significant correlations were found; for instance, no correlation was found with friction velocity, turbulence intensity, turbulence kinetic energy, or mean wind speed at either height. The strongest correlation discovered was between average high-frequency (>0.35 Hz) coherence and mean sonic temperature during the recordings ($r = 0.8$, P< 1e-5). That is, the warmer the temperature during the recording, the more high-frequency coherence between streamwise wind speed and blowing snow density that occurred. This may be a manifestation of entrainment of sensible heat into near-surface blowing snow. This association can also be explained by examination of the surface snow crystal habits coinciding with each temperature range. 20 Nov and 3 Feb were the two coldest nights with the most significantly wind-scoured snow surfaces and the lowest high-frequency coherence. 4 Dec was slightly warmer and also showed evidence of antecedent wind-scouring. However, on this evening there were more pockets of loose snow that could easily be available for transport and a slight increase in high-frequency coherence. 7 Dec and 3 Mar were the two warmest nights with fresh loose snow available on the surface for transport. Thus, it appears that for intermittent transport, the increased drag forces present on larger, unbroken grains, and increased availability of fresh snow for transport on the warm nights were more relevant for high-frequency blowing snow response than the presence of low-inertia small grain sizes. This transport initiation dependence on snow grain type is consistent with the findings of Guyomarc'h and Merindol (1998).

Further characterizing the relevant coherent turbulent structures is helpful for understanding the mechanisms in wind and snow transport modulation. For example, sweeps in Fig. 6b always coincide with local maxima of modulation envelopes or high-frequency coherence. This is further reflected by a fairly good correlation coefficient over the 23 recordings ($r \approx 0.6, P < 0.005$) between the percent of Reynolds stress generated by sweeps at the lower anemometer and the recording values of AM_{u_g,u_h}, AM_{u_g,u_g}, and $AM_{u_g,\rho}$. This connection is physically justified by the definition of sweeps as downward accelerating motions that could penetrate and modulate surface turbulence. The correlation was not as strong with upper anemometer sweeps ($r \approx 0.2 - 0.4$, $P < 0.06 - 0.25$) which suggests that surface eddy blocking may have prevented penetration all the way to the snow for some motions. Correlations with

quadrant two and quadrant one motions were not as prominent, but all three amplitude modulation coefficients were negatively correlated with the Reynolds stress contribution from inward motions $\{u'(t) < 0, w'(t) < 0\}$. There was no discernible relationship between average wavelet coherence in either frequency band and the presence of Reynolds stress from any quadrant motions. This is evidence of the difficulties encountered when describing turbulent two-phase flow with average statistical trends.

A weak positive correlation existed between mean blowing snow density and low-frequency coherence ($r = 0.43, P < 0.06$), indicating rates of transport increased with increasing low-frequency ($f < 0.35$ Hz) influence. A slightly more meaningful correlation ($r = 0.7, P < 0.0005$) was found between the temporal percent of a recording with measured blowing snow and low-frequency coherence. This indicated a shift to increased low-frequency coherence when blowing snow was occurring and particles responding to a wider spectrum of low-frequency fluctuations above threshold wind speeds.

As the snowpack deepened over the season and the lower anemometer became closer to the snow surface, the amount of unmeasured high-frequency turbulence energy increased. This is especially true of 3 March where low anemometer measurements occurred approximately 0.10 m above the snow surface and potentially 30% of high-frequency energy may have not been measured (van Boxel et al., 2004). It is suspected that the inclusion of additional high-frequency energy (e.g. with a hot-wire anemometer) would only enhance the already large high-frequency coherence values between turbulence and blowing snow transport $\left(CH_{s>0.35}(\rho_{bs}, u_g)\right)$ obtained on that night. As discussed above, the large coherence is most likely the result of increased drag with the fresh snow surface conditions, and not the absence of high-frequency wind measurements. Potential high-frequency losses for the two anemometers for each night of measurements are provided in the document supplement.

5.3.4 Wind-tunnel comparison

As the degree of amplitude modulation in turbulent boundary layers increases with increasing Reynolds number (Mathis et al., 2009a), understanding the contrasts between atmospheric flows at high Reynolds numbers and analogous wind tunnel experiments at low

Reynolds numbers is vital for understanding how and whether to extend laboratory-derived wind-snow transport relationships to natural terrain (e.g. Paterna et al. 2016). To highlight the significant role amplitude modulation played in both high- and low-frequency wind-snow coupling at FMSL, an analogous amplitude modulation analysis of wind-tunnel observations of streamwise wind fluctuations and streamwise blowing snow transport (Paterna et al., 2016) was performed. The degree of amplitude modulation was measured in nine 20-Hz time series of u' during blowing snow events, as well as modulation of directional blowing snow flux by wind, at a variety of cutoff frequencies ($f_c = 0.02 - 6.37$ Hz). As the Swiss Institute for Snow and Avalanche Research (SLF) wind tunnel where these data were collected has a 1 × 1 m cross-section, and an approximately 0.25 m deep logarithmic layer (Clifton et al., 2006), these separation scales encompass and exceed the largest eddies present in the boundary layer. Table 5-3 shows the results of the streamwise wind modulation analysis and is representative of the finding that amplitude modulation was not present in either signal ($AM_{u_g,\rho}$ and $AM_{u_g,u_g} \ll 1$, often negative). Thus, in the wind tunnel, the turbulent structures of which the wind was composed appear rather distinct from those found in the alpine outdoors for a subset of the friction velocities observed at FMSL.

f_c (Hz)	P (s)	Exp1	Exp2	Exp3	Exp4	Exp5	Exp6	Exp7	Exp8	Exp9
u_* (m s^{-1})		0.23	0.23	0.22	0.21	0.26	0.23	0.25	0.20	0.25
6.37	0.16	-0.01	-0.03	-0.04	0.00	0.02	0.04	0.03	0.06	0.03
3.18	0.31	-0.07	-0.07	-0.11	0.01	-0.03	0.00	-0.04	0.01	0.01
1.59	0.63	-0.16	-0.15	-0.15	-0.08	-0.06	-0.05	0.02	-0.04	-0.02
0.80	1.25	-0.17	-0.12	-0.10	-0.12	-0.09	-0.05	-0.03	-0.04	0.02
0.40	2.5	-0.11	-0.26	-0.28	-0.12	-0.10	-0.06	0.04	-0.09	-0.03
0.20	5.0	0.08	-0.25	-0.29	-0.16	-0.13	-0.09	-0.14	0.03	0.13
0.10	10.0	0.09	-0.08	-0.33	0.13	-0.09	-0.12	0.06	-0.42	0.15
0.05	20.0	0.08	0.03	-0.60	0.04	-0.08	-0.21	0.00	-0.85	-0.04
0.02	50.0	-0.25	-0.01	-0.84	-0.16	-0.02	-0.60	0.74	-0.94	0.55

Table 5-3: Streamwise amplitude modulation (AM_{u_g,u_g}) in SLF blowing snow wind tunnel experiment (Paterna et al., 2016) for a variety of cutoff frequencies, f_c, (and period P) over nine experiments. This indicates the absence of high-frequency turbulence amplitude for a wide variety of scale separations in a typical blowing snow wind tunnel experiment.

5.4 Discussion

The coupling of wind and near-surface snow saltation in the atmospheric surface layer proves to be complex with nonlinear momentum transfer over many time and length scales. Near-surface high-frequency turbulence was strongly modulated by passing large-scale low-frequency motions measured 160 cm above. These same large eddies were responsible for modulating the high-frequency components of the blowing snow density signal as seen by the strong correlation between the high-frequency envelopes generated by the streamwise wind and blowing snow signals. In the presence of the large-scale motions, wavelet coherence between wind and snow signals was strongest in the low-frequency range with significant high-frequency coherence being largely intermittent. However, high-frequency coherence peaks also coincided with passage of the same low-frequency motions. The question remains whether this coupling is the result of snow transport fluctuations responding to modulated high-frequency turbulence over short time scales, or if by the passage of large-scale events, the stochastic dynamics of surface impacts and rebound are amplified, resulting in a synchronous increase in high-frequency snow transport energy. As also noted by Jacob and Anderson (2017), amplitude modulation in nature may indeed play a crucial role in generating turbulent fluctuations sufficient to initiate blowing snow transport.

Two recordings with negligible turbulence modulation occurred on 20 Nov and on 3 Mar (italicized in Table 2). These recordings coincide with more positive Reynolds stress (τ) being generated by $u' < 0$ and $w' > 0$ (ejection) events than $u' > 0$ and $w' < 0$ (sweep) events. Ejections outweigh sweeps for only one other recording, 4 Dec #8, during which AM_{u_g,u_h} and AM_{u_g,u_g} were also less than average (0.19 and 0.13, respectively). Table 2 shows relatively low modulation coefficients for 7 Dec, #2 ($AM_{u_g,u_h} = 0.21$, $AM_{u_g,u_g} = 0.19$, and $AM_{u_g,\rho} = 0.04$), a recording that coincides with diminished presence of both sweeps and ejections and a relatively low total Reynolds stress. During these four recordings, the reduced presence of sweep events corresponds well with a decrease in large-scale motions penetrating to the surface and thus limited amplitude modulation. Somewhat counterintuitively, the spurious 20 Nov, 3 Mar, and 4 Dec recordings all maintained good snow-wind modulation coefficients, $AM_{u_g,\rho}$, adding another layer of complexity to the mechanics of near-surface momentum balance. Regardless, these data

support the role of sweeps as large-scale structures that modulate surface turbulence and snow transport.

In general, wavelet coherence and amplitude modulation analyses suggest a stronger dependence of snow transport on instantaneous wind speed than Reynolds stress, in agreement with recent aeolian sand studies (Sterk et al., 1998; Schönfedlt and von Löwis, 2003; Leenders et al. 2005). While the statistical testing of wavelet coherence does not determine a causal relationship, there is only a 5% probability that coherence peaks occur solely by chance. When limiting analysis to small scale motions at frequencies greater than 0.35 Hz, mean wavelet coherence (MCH_s) of blowing snow density and Reynolds stress was as strong as that with streamwise wind speed. This may indicate why Reynolds stress and friction velocity often scale with snow transport behavior in wind tunnels where large eddies are not present. However, Paterna et al. (2016) also documented high-frequency coupling between snow transport and streamwise wind speed for low-strength steady-state saltation. Here, in contrast to Paterna et al. (2016), there was no notable increase in low-frequency blowing snow energy caused by sediment transport decoupling from the wind as low-frequency energy and coherence dominated all FMSL recordings (Fig. 4). Closer examination of any decoupling as described by Paterna et al. (2016) is not possible with this dataset given the large temporal variability in transport in this gusty mountain environment. However, a connection exists between nights with a decrease in high-frequency coherence and the fragmentation of grains and reduction in particle drag. This fragmentation may prove to be an additional mechanism resulting in the decoupling noted during high-strength saltation by Paterna et al. (2016).

As modulation of near-surface turbulence by large-scale influences can also be manifested in fluctuations of Reynolds stress (Mathis et al., 2013), the amplitude modulation found indicates that common turbulence statistics, such as friction velocity (u_*), used to model blowing-snow transport are being strongly modified by large-scale motions. Interestingly, there was less evidence of amplitude modulation between low- and high-frequency bands of Reynolds stress than that found by Hutchins and Marusic (2007a). This may be caused by external environmental factors such as different surface roughness, momentum loss to snow transport, or considerably more complicated terrain and is subject for further investigation.

The analysis of turbulence mechanics in a wind tunnel blowing snow study showed negligible amplitude modulation when compared to the alpine observations, indicating an absence of the same magnitude of nonlinear momentum transfer that is found in nature. Thus, adapting wind-tunnel derived scaling relationships (e.g. Nishimura and Hunt, 2000; Clifton et al., 2006; Horender et al., 2013) to complex terrain is largely dependent on how topographically influenced motions, and their influence on surface turbulence statistics, can be represented as modifications of simpler cases. This has implications beyond the impact of wind fluctuations on models of steady-state blowing fluxes (e.g. Sørensen, 1997). For example, evidence of amplitude modulation has been found in the roughness sublayer (Anderson, 2016), the region represented by roughness lengths z_0 in log-law models. The common practice of modifying z_0 to accommodate a wind momentum deficit during blowing snow (Pomeroy and Gray, 1990; Liston and Sturm, 1998; Lehning et al., 2000) may also need to be reevaluated in this context.

Aksamit and Pomeroy (2017) showed that sweeps are responsible for considerable blowing snow initiation and surface transport, especially during intermittent transport conditions. Through the positive correlation of amplitude modulation coefficients and sweep generated Reynolds stress, the penetration of these large-scale structures also appears responsible for much of the near-surface turbulence modulation. Separating Reynolds stress into components of large scale modulation and purely local instability, as by Mathis et al. (2013), is the next step in reconciling scaling relationships derived in wind tunnels and the turbulent structures found in the ASL. The strong degree of amplitude modulation likely indicates that many of the largest near-surface turbulence events resulted from the passage of large scale motions and not local surface instabilities.

Further investigation with a wider span of measurement heights may permit implementation of turbulence modulation in driving a blowing snow initiation or transport model. Such an approach would be beneficial to delimit the necessary resolution of large eddy simulations. The eddies with length scales of 30-60 m that modulated the amplitude of near surface motions at FMSL are at the frontier of alpine blowing snow LES models (Vionnet et al., 2017). Further investigations may help realize statistically representative lower-boundary

conditions (Anderson, 2016) as well as improving wind-snow interactions in the saltation layer in LES.

5.5 Conclusions

This research examined how the structure of turbulence in the atmospheric surface layer affects near-surface blowing snow fluxes at a mountain site. The effects are multiscale and involve complex interactions between high- and low-frequency motions. Intermittent blowing snow transport responded to large low-frequency streamwise motions that modulated the amplitude of high-frequency turbulence. Because of this amplitude modulation, large-scale motions do not act simply as a shift in mean wind speed on local instabilities, but modify the dynamics of the surface momentum balance by increasing the amplitude of high-frequency turbulence. This modulation effect is important to characterizing turbulence for particle transport calculations, as the coherence between wind speed and snow transport signals also increases under footprint of these structures.

Large-scale sweep motions influenced near-surface turbulence and blowing snow fluxes across all measured frequencies. In light of the evidence of nonlinear momentum transfer across a wide spectrum of scales, determining the appropriate assumptions about the relative magnitude of structures and time scales for blowing snow transport is necessary for transport modeling. Future research to better understand near-surface turbulence amplitude modulation may permit reconciliation of the need for high-frequency near-surface streamwise velocity measurements in blowing snow models and the more standard and widely available low-frequency micrometeorological observations through near-surface turbulence modulation models. A clearer understanding of how specific turbulent structures affect near-surface turbulence will better characterize the differences between wind-tunnel and alpine blowing snow and provide insight for adapting steady-state, low-Reynolds-number scaling relationships to gusty natural conditions.

Continued observations of amplitude modulation over rough natural surfaces can help suggest improvements to surface interaction models for atmospheric large eddy simulations (Anderson, 2016) and to high resolution large eddy simulations of snow transport (e.g. Groot

Zwaaftink et al., 2014). Because the amplitude modulation in both the turbulence and blowing snow signals found in this outdoor setting is not present in wind tunnels, considerable advancement in the field of sediment transport in complex terrain will likely only come after appropriately addressing the nonlinear dynamics influencing near-surface turbulent motions and further investigating two-phase flow turbulence in outdoor boundary layers.

5.6 Acknowledgments, Samples, and Data

The authors acknowledge funding from the Canada Foundation for Innovation, the Natural Sciences and Engineering Research Council of Canada, the Changing Cold Regions Network, Canada Research Chairs, the Global Institute for Water Security and Alberta Agriculture and Forestry. The assistance of the Fortress Mountain Resort in logistics is gratefully noted. The authors would also like to express gratitude to Andreas Baas whose helpful comment improved this manuscript. Data are available at http://dx.doi.org/10.20383/101.010.

5.7 References

Aksamit, N. O., and J. W. Pomeroy (2016), Near-Surface Snow Particle Dynamics from Particle Tracking Velocimetry and Turbulence Measurements during Alpine Blowing Snow Storms, *Cryosph.*, *10*, 3043–3062, doi:10.5194/tc-10-3043-2016.

Aksamit, N. O., and J. W. Pomeroy (2017), Coherent Structures in the Atmospheric Surface Layer driving Blowing Snow Transport, *Boundary-Layer Meteorol.*, doi:10.1007/s10546-017-0318-2

Anderson, W. (2016), Amplitude modulation of streamwise velocity fluctuations in the roughness sublayer: evidence from large-eddy simulations, *J. Fluid Mech.*, *789*, 567–588, doi:10.1017/jfm.2015.744.

Baas, A. C. W., and D. J. Sherman (2005), Formation and behavior of aeolian streamers, *J. Geophys. Res.*, *110*, 1–15, doi:10.1029/2004JF000270.

Baas, A. C. W. (2006), Wavelet power spectra of aeolian sand transport by boundary layer turbulence, *Geophys. Res. Lett.*, *33*, 1–4, doi:10.1029/2005GL025547.

Baas, A. C. W. (2006), Wavelet power spectra of aeolian sand transport by boundary layer turbulence, *Geophys. Res. Lett.*, *33*, 1–4, doi:10.1029/2005GL025547.

Baas, A. C. W. (2008), Challenges in aeolian geomorphology: Investigating aeolian streamers, *Geomorphology*, *93*(1–2), 3–16, doi:10.1016/j.geomorph.2006.12.015.

Bauer, B. ., J. Yi, S. Namikas, and D. Sherman (1998), Event detection and conditional averaging in unsteady aeolian systems, *J. Arid Environ.*, *39*, 345–375.

Bauer, B. O., I. J. Walker, A. C. W. Baas, D. W. T. Jackson, C. M. Neuman, G. A. Hesp, and F. S. W. Patrick (2013), Critical Reflections on the Coherent Flow Structures Paradigm in Aeolian Geomorphology, in *Coherent Flow Structures at Earth's Surface*, edited by J. G. Venditti, J. L. Best, M. Church, and R. J. Hardy, pp. 111–134, Wiley Blackwell, West Sussex, UK.

Bendat, J. S., and A. G. Piersol (2010), *Random Data: Analysis and Measurement Procedures*, Fourth., John Wiley & Sons, Inc, Hoboken, New Jersey.

Biltoft, C. a., and E. R. Pardyjak (2009), Spectral coherence and the statistical significance of turbulent flux computations, *J. Atmos. Ocean. Technol.*, *26*(2), 403–410, doi:10.1175/2008JTECHA1141.1.

Bintanja, R. (1998), The interaction between drifting snow and atmospheric turbulence, *Ann. Glaciol.*, *26*, 167–173.

Bintanja, R. (2000), Snowdrift suspension and atmospheric turbulence. Part I: Theoretical background and model description, *Boundary-layer Meteorol.*, *95*, 343–368.

Bisantino, T., F. Gentile, P. Milella, and G. T. Liuzzi (2010), Effect of Time Scale on the Performance of Different Sediment Transport Formulas in a Semiarid Region, *J. Hydraul. Eng.*, *136*(1), 56–61, doi:10.1061/(ASCE)HY.1943-7900.0000125.

Chapman, C., I. J. Walker, P. A. Hesp, B. O. Bauer, R. G. D. Davidson-Arnott, and J. Ollerhead (2013), Reynolds stress and sand transport over a foredune, *Earth Surf. Process. Landforms*, *38*(14), 1735–1747, doi:10.1002/esp.3428.

Clifton, A., J. D. Rüedi, and M. Lehning (2006), Snow saltation threshold measurements in a drifting-snow wind tunnel, *J. Glaciol.*, *52*(179), 585–596, doi:10.3189/172756506781828430.

Daubechies, I. (1992), *Ten Lectures on Wavelets*, Society for Industrial and Applied Mathematics, Philadelphia, PA.

Diplas, P., C. L. Dancey, A. O. Celik, M. Valyrakis, K. Greer, and T. Akar (2008), The Role of Impulse on the Initiation of Particle Movement Under Turbulent Flow Conditions, *Science (80-.).*, *322*(5902), 717–720, doi:10.1126/science.1158954.

Dyunin, A. K., and V. Kotlyakov (1980), Redistribution of snow in the mountains under the effect of heavy snow-storms, *Cold Reg. Sci. Technol.*, *3*, 287–294.

Ellis, J. T. (2006), Coherent Structures and Aeolian Saltation, Texas A&M.

Foufoula-Georgiou, E., and P. Kumar (1994), *Wavelets in Geophysics*, Academic Press, San Diego, USA.

Freitag, D. R., and T. McFadden (1997), *Introduction to Cold Regions Engineering*, American Society of Civil Engineers, New York, NY.

Gordon, M., S. Savelyev, and P. a. Taylor (2009), Measurements of blowing snow, part II: Mass and number density profiles and saltation height at Franklin Bay, NWT, Canada, *Cold Reg. Sci. Technol.*, *55*(1), 75–85, doi:10.1016/j.coldregions.2008.07.001.

Grinsted, a., J. C. Moore, and S. Jevrejeva (2004), Application of the cross wavelet transform and wavelet coherence to geophysical time series, *Nonlinear Process. Geophys.*, *11*(5/6), 561–566, doi:10.5194/npg-11-561-2004.

Groot Zwaaftink, C. D., M. Diebold, S. Horender, J. Overney, G. Lieberherr, M. B. Parlange, and M. Lehning (2014), Modelling Small-Scale Drifting Snow with a Lagrangian Stochastic Model Based on Large-Eddy Simulations, *Boundary-Layer Meteorol.*, *153*(1), 117–139, doi:10.1007/s10546-014-9934-2.

Guyomarc'h, G., and L. Mérindol (1998), Validation of a Forecasting Application of Blowing Snow Periods, *Ann. Glaciol.*, *26*, 138–143.

Helgason, W., and J. W. Pomeroy (2012), Characteristics of the Near-Surface Boundary Layer within a Mountain Valley during Winter, *J. Appl. Meteorol. Climatol.*, *51*(3), 583–597, doi:10.1175/JAMC-D-11-058.1.

Horender, S., C. D. Groot Zwaaftink, B. Walter, and M. Lehning (2013), Intermittent drifting snow - combining experimental and model studies., in *Proceedings International Snow Science Workshop*, pp. 104–107, Grenoble Chamonix Mont-Blanc.

Hunt, J. C. R., and J. F. Morrison (2000), Eddy structure in turbulent boundary layers, *Eur. J. Mech. B-Fluids*, *19*, 673–694, doi:10.1016/S0997-7546(00)00129-1.

Hutchins, N., and I. Marusic (2007), Evidence of very long meandering features in the logarithmic region of turbulent boundary layers, *J. Fluid Mech.*, *579*, 1–28, doi:10.1017/S0022112006003946.

Hutchins, N., and I. Marusic (2007), Large-scale influences in near-wall turbulence, *Philos. Trans. R. Soc. A Math. Phys. Eng. Sci.*, *365*(1852), 647–664, doi:10.1098/rsta.2006.1942.

Jacob, C., and W. Anderson (2017), Conditionally Averaged Large-Scale Motions in the Neutral Atmospheric Boundary Layer : Insights for Aeolian Processes, *Boundary-Layer Meteorol.*, *162*(1), 21–41, doi:10.1007/s10546-016-0183-4.

Kaimal, J. C., and J. J. Finnigan (1994), *Atmospheric boundary layer flows: their structure and measurement*, Oxford University Press, New York, NY.

Kok, J. F., E. J. R. Parteli, T. I. Michaels, and D. B. Karam (2012), The physics of wind-blown sand and dust, *Reports Prog. Phys.*, *75*(10), doi:10.1088/0034-4885/75/10/106901.

Kolmogorov, A. (1941), The local structure of turbulence in incompressible viscous fluid for very large Reynolds numbers, *Dokl. Akad. Nauk SSSR*, 9–13.

Leenders, J. K., J. H. van Boxel, and G. Sterk (2005), Wind forces and related saltation transport, *Geomorphology*, *71*, 357–372, doi:10.1016/j.geomorph.2005.04.008.

Lehning, M., J. Doorschot, and P. Bartelt (2000), A snowdrift index based on SNOWPACK model calculations, *Ann. Glaciol.*, *31*(August 2015), 382–386, doi:10.3189/172756400781819770.

Li, L., and J. W. Pomeroy (1997), Estimates of Threshold Wind Speeds for Snow Transport Using Meteorological Data, *J. Appl. Meteorol.*, *36*, 205–213.

Liston, G., and M. Sturm (1998), A snow-transport model for complex terrain, *J. Glaciol.*, *44*(148), 498–516.

Liu, J., Y. Wang, and B. Yang (2012), Wavelet packet analysis of particle response to turbulent fluctuation, *Adv. Powder Technol.*, *23*(3), 305–314, doi:10.1016/j.apt.2011.04.002.

Liu, J., Y. Wang, and Y. Zhang (2009), Stationary wavelet-based analysis and simulation of unsteady wind in aeolian sand transport, in *ICEMI 2009 - Proceedings of 9th International Conference on Electronic Measurement and Instruments*, pp. 3789–3794.

Liu, P. C. (1994), Wavelet spectrum analysis and ocean wind waves, in *Wavelets in Geophysics*, edited by E. Foufoula-Georgiou and P. Kumar, pp. 151–166, Academic Press, San Diego.

Lu, S. S., and W. W. Willmarth (1973), Measurements of the structure of Reynolds stress in a turbulent boundary layer, *J. Fluid Mech.*, *60*(3), 481–511.

Lykossov, V. N., and C. Wamser (1995), Turbulence intermittency in the atmospheric surface layer over snow-covered sites, *Boundary-Layer Meteorol.*, *72*(4), 393–409, doi:10.1007/BF00709001.

Mahrt, L., and N. Gamage (1987), Observations of Turbulence in Stratified Flow, *J. Atmos. Sci.*, *44*(7), 1106–1121, doi:10.1175/1520-0469(1987)044<1106:OOTISF>2.0.CO;2.

Mallat, S. (2008), *A wavelet tour of signal processing: the sparse way*, Elsevier.

Marusic, I., R. Mathis, and N. Hutchins (2010), Predictive model for wall-bounded turbulent flow. *Science (80-.).*, **329**, 193–196, doi:10.1126/science.1188765.

Mathis, R., N. Hutchins, and I. Marusic (2009), Large-scale amplitude modulation of the small-scale structures in turbulent boundary layers, *J. Fluid Mech.*, *628*, 311–337, doi:10.1017/S0022112009006946.

Mathis, R., N. Hutchins, and I. Marusic (2011), A predictive inner–outer model for streamwise turbulence statistics in wall-bounded flows, *J. Fluid Mech*, *681*, 537–566, doi:10.1017/jfm.2011.216.

Mathis, R., I. Marusic, S. I. Chernyshenko, and N. Hutchins (2013), Estimating wall-shear-stress fluctuations given an outer region input, *J. Fluid Mech.*, *715*, 163–180, doi:doi:10.1017/jfm.2012.508.

Mathis, R., J. P. Monty, N. Hutchins, and I. Marusic (2009), Comparison of large-scale amplitude modulation in turbulent boundary layers, pipes, and channel flows, *Phys. Fluids*, *21*(11), 1–4, doi:10.1063/1.3267726.

Naaim-Bouvet, F., M. Naaim, H. Bellot, and K. Nishimura (2011), Wind and drifting-snow gust factor in an Alpine context, *Ann. Glaciol.*, *52*(58), 223–230, doi:10.3189/172756411797252112.

Nemoto, M., and K. Nishimura (2004), Numerical simulation of snow saltation and suspension in a turbulent boundary layer, *J. Geophys. Res. Atmos.*, *109*(18), doi:10.1029/2004JD004657.

Nemoto, M., K. Nishimura, S. Kobayashi, and K. Izumi (2004), Numerical study of the time development of drifting snow and its relation to the spatial development, *Ann. Glaciol.*, *38*, 343–350, doi:10.3189/172756404781815202.

Nishimura, K., and J. C. R. Hunt (2000), Saltation and incipient suspension above a flat particle bed below a turbulent boundary layer, *J. Fluid Mech.*, *417*, 77–102, doi:10.1017/S0022112000001014.

Otsu, N. (1979), A Threshold Selection Method from Gray-Level Histograms, *IEEE Trans. Syst. Man. Cybern.*, *SMC-9*(1), 62–66.

Paterna, E., P. Crivelli, and M. Lehning (2016), Decoupling of mass flux and turbulent wind fluctuations in drifting snow, *Geophys. Res. Lett.*, 1–7, doi:10.1002/2016GL068171.Received.

Pomeroy, J. W., D. M. Gray, and P. G. Landine (1993), The Prairie Blowing Snow Model : characteristics, validation, operation, *J. Hydrol.*, *144*, 165–192.

Pomeroy, J. W., and D. Gray (1990), Saltation of snow, *Water Resour. Res.*, *26*(7), 1583–1594.

Scarchilli, C., M. Frezzotti, P. Grigioni, L. De Silvestri, L. Agnoletto, and S. Dolci (2010), Extraordinary blowing snow transport events in East Antarctica, *Clim. Dyn.*, *34*(7), 1195–1206, doi:10.1007/s00382-009-0601-0.

Schönfeldt, H.-J., and S. von Löwis (2003), Turbulence-driven saltation in the atmospheric surface layer, *Meteorol. Zeitschrift*, *12*(5), 257–268, doi:10.1127/0941-2948/2003/0012-0257.

Schweizer, J., B. Jamieson, and M. Schneebeli (2003), Snow avalanche formation, *Rev. Geophys.*, *41*(4), doi:10.1029/2002RG000123.

Sievers, J., T. Papakyriakou, S. Larsen, M. M. Jammet, S. Rysgaard, M. K. Sejr, and L. L. Sørensen (2015), Estimating local atmosphere-surface fluxes using eddy covariance and numerical Ogive optimization, *Atmos. Chem. Phys.*, *15*(4), 2081–2103, doi:10.5194/acp-15-2081-2015.

Sørensen, M. (1997), On the effect of time variability of the wind on rates of aeolian sand transport, *Aarhus Geosci.*, *7*, 73–77.

Sterk, G., a. F. G. Jacobs, and J. H. Van Boxel (1998), The effect of turbulent flow structures on saltation sand transport in the atmospheric boundary layer, *Earth Surf. Process. Landforms*, *23*(10), 877–887.

Stout, J., and T. Zobeck (1997), Intermittent saltation, *Sedimentology*, *44*, 959–970.

Torrence, C., and G. P. Compo (1998), A practical guide to wavelet analysis, *Bull. Am. Meteorol. Soc.*, *79*(1), 61–78.

Torrence, C., and P. J. Webster (1999), Interdecadal Changes in the ENSO – Monsoon System, *J. Clim.*, *12*(8), 2679–2690, doi:10.1175/1520-0442(1999)012<2679:ICITEM>2.0.CO;2.

Valyrakis, M., P. Diplas, and C. Dancey (2010), Role of instantaneous force magnitude and duration on particle entrainment, *J. Geophys. …*, *115*, F02006, doi:10.1029/2008JF001247.

van Boxel, J. ., G. Sterk, and S. . Arens (2004), Sonic anemometers in aeolian sediment transport research, *Geomorphology*, *59*(1–4), 131–147, doi:10.1016/j.geomorph.2003.09.011.

Venditti, J. G., and S. J. Bennett (2000), Spectral analysis of turbulent flow and suspended sediment transport over fixed dunes, *J. Geophys. Res.*, *105*(C9), 22,035-22,047.

Vionnet, V., E. Martin, V. Masson, C. Lac, F. N. Bouvet, and G. Guyomarc'h (2017), High-resolution large eddy simulation of snow accumulation in alpine terrain, *J. Geophys. Res. Atmos.*, doi:10.1002/2017JD026947.

Wiggs, G. F. S., and C. M. Weaver (2012), Turbulent flow structures and aeolian sediment transport over a barchan sand dune, *Geophys. Res. Lett.*, *39*(5), 1–7, doi:10.1029/2012GL050847.

Xuan, J. (2004), Turbulence factors for threshold velocity and emission rate of atmospheric mineral dust, *Atmos. Environ.*, *38*(12), 1777–1783, doi:10.1016/j.atmosenv.2003.12.030.

CHAPTER 6
CONCLUSIONS

6.1 Concluding Remarks

This thesis analyzed near-surface snow particle motions and the role of turbulent wind fluctuations and coherent structures driving blowing snow in mountainous terrain. By the nature and location of the two-way coupling of wind and snow, it is of paramount importance to understand and characterize turbulence behaviour in complex mountainous terrain, and survey the impact on snow redistribution. The research presented in this thesis has added to this body of knowledge using unique high frequency observations of particle motions and turbulence near the snow surface by the first application of PTV to blowing snow in a natural environment. The main conclusions with regards to the objectives in Chapter 1 can be summarized as follows:

Objective 1) Determine snow particle motion response to time dependent atmospheric surface layer winds at varying heights in the saltation layer.

Commonly assumed uniform velocity profiles and constant rates of particle entrainment are inconsistent with the time-resolved blowing snow velocities measured with the environmental PTV. Chapter 2 and 3 indicated that creep plays a large role in particle motion initiation. In the intermittent conditions present, the onset of blowing snow transport always began with grains rolling on the surface, eventually bouncing into saltation as the drag forces increased and particles accelerated sufficiently. The creep motion on the surface often occurred below previously reported transport thresholds and appeared to mobilize particles as an active reservoir of motion, ready for more energetic transport. As well, the tumbling motion at low wind speeds dislodged particles, enabling them to become mobilized while not initiating a full splash regime.

Chapter 3 indicated that in the first 3 cm of the snow surface, a linear particle velocity profile was present with slope depending on the concurrent wind conditions. Mass concentration was always greatest immediately above the surface, even though average particle velocity was

lowest in that area. Velocity and concentration profiles were also time dependent, evolving with the onset and decline of wind gusts on second time scales.

Objective 2) Identify coherent turbulence structures relevant to saltation initiation and particle entrainment.

Chapter 3 and Chapter 4 showed that sweeps and ejections played important, yet distinct, roles in blowing snow initiation and transport. The VITA+LEVEL analysis of Chapter 4 indicated that sweeps were most responsible for both initiation and sustained transport, while ejections were unable to initiate transport but enhanced vertical dispersion of grains if there was antecedent blowing snow. Strong sweeps also enhanced vertical transport of grains, largely because of the enhanced horizontal acceleration of particles during sweeps, which was translated into vertical velocity upon impact with the uneven snow surface.

Inward motions (Q3: $u' < 0, w' < 0$) appeared to not contribute to blowing snow in any distinct way. Outward motions (Q`: $u' > 0, w' > 0$) were difficult to differentiate from sweeps as strong in-rush sweep motions and highly autocorrelated periods of $u' > 0$ often occurred with w' fluctuating around zero. As suggested by Shih et al. (2017), this is likely a result of the interaction between the overarching sweep motion and the bed surface, and is not a unique outward interaction mechanism.

Objective 3) Improve understanding of mechanics and origins of near-surface turbulence structures most responsible for blowing snow transport.

In Chapter 5, blowing snow was found to respond to wind structures across a full spectrum of motions from 25 Hz to 1/30 Hz. The strongest coherence was typically found at lower frequencies with spontaneous bursts of statistically significant coherence at sub second frequencies. After the onset of transport, snow grains typically responded to a wider spectrum of motions. That is, prior to initiation, short gusts were not always sufficient to mobilize grains, but during transport, grains could more easily respond to short gusts. Snow surface characteristics

played a strong role in the ability to obtain wavelet coherence between blowing snow and wind. Turbulence-snow coupling was much more sporadic in the near-surface over wind-hardened snowpacks with fine grains. When surfaces were composed of larger, less cohesive, fresh snowfall, turbulence-snow coupling was much more obvious with very short lag times.

Interestingly, the high frequency coherence was found to be present most often under the passage of large scale superstructures associated with advection of non-local turbulence. That is, the dominant motions responsible for wind-snow coupling over all frequencies were strong low-frequency motions. Thus, outer-layer atmospheric motions appear to be most relevant for transport in intermittent conditions. It is noted that these motions are strongly affected by the regional mountain terrain that surrounded the study site. Inner-layer turbulence characteristics may be the incorrect method for obtaining turbulence measurements to drive blowing snow models and the regional aspect of outer-layer motions means that blowing snow transport, even in a locally level site, can be affected by terrain-induced turbulence motions.

6.2 Concluding Discussion

The majority of blowing snow fluxes measured in this field campaign could be linked to a driving turbulent coherent structure. The presence of such structures had long term effects on mean transport velocity and concentration profiles. Blowing snow responded at the snow surface to turbulent gusts with very short lag times and for as short as sub-second durations. While this complex coupling of turbulent wind and snow transport may seem like a daunting conclusion (modeling turbulence in complex terrain is already fraught with great difficulty) connections to longer timescale turbulent structures provide a hopeful way forward. A semi-deterministic approach may soon be possible, connecting time-dependent entrainment and flux with coherent structures. It should be noted that these coherent structures are likely influenced by regional wind flow characteristics and were remarkably strong and variable in this mountain environment. Enhanced variability of wind flow and advection of turbulence in this environment has been noted by others (Helgason and Pomeroy, 2005).

The research presented here makes no effort to disprove previous theories of blowing snow transport. However, the findings discussed in the previous chapters make clear one

pertinent discrepancy with current methods: gust-driven snow transport is coupled with very specific turbulent atmospheric structures. The presence and characteristics of gusts affect the mechanisms of transport (Chapter 2 and 3) and the blowing snow concentration and velocity profiles (Chapter 3). Blowing snow responds to specific turbulent bursts over very short timescales (Chapter 4) and transport dynamics are driven by a wide spectrum of motions in a nonlinear fashion (Chapter 5). In the alpine environment, determining a time-averaged variable that can represent the complexity of this coupling has not yet been achieved. Blowing snow is shown here to respond preferentially to specific quadrants of motion, however, u_*, as derived from time-averaged Reynolds stress, treats all turbulent motions with the same magnitude Reynolds stress equally. This is now shown to be conceptually incorrect. In Chapter 4 it was clearly shown that large Reynolds stress is often a necessary, but not sufficient condition for blowing snow transport. Findings of amplitude modulation from large scale atmospheric motions in near-surface turbulence in Chapter 5 also suggest a new approach to parameterizing alpine blowing snow transport may be prudent.

In aeolian sand transport models, many of the same turbulence-related complexities exist and are the focus of active research. Transport intermittency itself remains difficult to quantify (Sherman et al., 2017), as does its effect on particle velocity profiles (Bauer and Davidson-Arnott, 2014). In order to address spatio-temporal variability of the wind field, DNS and LES-coupled sand saltation models are typically needed (e.g. Duran et al., 2014; Dupont et al. 2014). However, friction velocity-based models are still capable of providing insight into difficult-to-measure processes such as sand redistribution around vegetation, supply-limited sand transport (such as on wet beaches), and sand transport on Mars (de Vries et al., 2014; Webb et al., 2014; Sullivan and Kok, 2017). Advances in intermittency and surface momentum balance in aeolian modeling are currently dependent on enhanced physical understanding of the natural processes.

Adapting PTV methods to outdoor snow (or sand) particle tracking to improve this physical understanding involves considerable but not insurmountable challenges. One reason that scaling relationships were not evident across multiple nights in the current experimental data set were the difficulties involved in collecting enough data to accurately represent the influence of each snow type. For example, the slope α of the linear velocity profiles in Chapter 3 varied not

only with turbulence characteristics, but with snow surface conditions. The implementation of a 2D light plane for particle velocity measurements was incredibly labour-intensive. As the wind directions shifted, the camera-laser frame needed to be constantly adjusted, camera lens cleaned, and camera refocused. This consumed many hours of the collection period, without producing very long periods of recording. The amount of data that needed to be discarded was significant, with only one third of the recording nights resulting in useable data. Expanding the data set with the collection methods introduced in this thesis will undoubtedly improve our understanding, and improvements to the method are suggested in Section 6.3

This research suggests that it will be difficult to improve the performance of blowing snow models that are driven by low time resolution data (e.g. a cup or propeller anemometer responding at 0.05 Hz on a 5 m mast) without additional parameterizations accounting for gusts. For example, an intensive short-term study with high-frequency (e.g. sonic or hot-wire) anemometry could provide a better understanding of how amplitude modulation affects snow transport at a given site. With these relationships in hand, there is hope for synthesizing high frequency turbulence signals from measurements of large scale motions, even when the three-dimensional, high resolution aspects of turbulence are no longer measurable. At this point a relative bursting frequency or an outer scale analog may provide long-term statistical insight into the sweep-ejection processes, and how to recalibrate a gust-factor with that insight. This could most likely assume the structure of the Chepil (1959) model using the ratio of mean to maximum wind speed via standard deviations. The Chepil (1959) ratio was an attempt to incorporate the influence of "turbulent impulses" in soil transport models. Quantifying the influence of these impulses was largely the focus of this study, though improved predictive capabilities will likely only come through a shift in modeling methodology towards including enhanced descriptions of wind and temporal variability in transport mechanics.

6.3 Outlook

Recently, blowing snow research has predominantly focused on either increasing complexity of terrain over which existing blowing snow models are run (Vionnet et al., 2017), or improving the understanding of aspects of equilibrium grain saltation in wind tunnels or

numerical simulations (Comola and Lehning, 2017; Comola et al., 2017; Niiya and Nishimura, 2017; Paterna et al., 2017). While these appear to be fundamentally different questions, the present research provides a way forward to improve the coupling of these intrinsically connected aspects of blowing snow models for natural environments at the scales of relevance.

All chapters in this thesis suggest that the non-steady winds commonly found in mountainous terrain greatly influence the necessary complexity to accurately describe the snow surface response: the steady-state and fully-developed flow conditions that are assumed by many blowing snow models were never observed. The predictive capabilities of blowing snow models in complex terrain may improve as wind components of transport models improve in accuracy, and the coupling of snow transport with LES shows great promise. For example, the eddies resolved by Vionnet et al. (2017) are precisely in the range found responsible for amplitude modulation of turbulence and transport in Chapter 5. Thus, statistical approaches to represent high frequency surface motions (e.g. Mathis et al., 2016) may be a viable avenue. Amplitude modulation is a potential bridge between the smallest eddies resolved by the LES and the "subgrid" and surface turbulence that is immediately affecting the time-dependent nature of entrainment and transport. However, high-resolution surface measurements must also be coupled with snow depth and flux and wind measurements at larger length scales to facilitate any meaningful model validation.

Furthermore, a necessary shift away from equilibrium initiation and transport models can only come after increased understanding of the initiation and transport in natural conditions, such as through environmental PTV. For a better understanding of the surface dynamics of blowing snow, there is great opportunity with blowing snow PTV. Because of the labour intensive-nature of environmental PTV, some questions are more suitably addressed in wind tunnels. For example, a constant wind speed and constant wind direction provides a great advantage for investigating splash and fracturing mechanisms (Comola and Lehning, 2017; Comola et al., 2017). The impetus then is to be able to accurately adapt these wind-tunnel snow models to natural snowpacks with natural snow bonds. Environmental PTV would help facilitate calibrating the parameters of these surface momentum balance models to other climates with different snowpacks.

This research was the first investigation of the utility of environmental PTV for blowing snow and so is fundamentally exploratory. As such, there is still much room for integrating PTV as a component of more comprehensive outdoor blowing snow studies. For example, coupling PTV measurements with an array of snow particle counters, snow surveys, and meteorological measurements at a well-established study site could help facilitate the inclusion and physical verification of complex particle motion models (e.g. Nemoto and Nishimura, 2004; Nemoto et al., 2004; Comola et al., 2017) with large scale effects of snow transport. Of note, the inclusion of creep modes of transport measured in Chapter 2 and 3 could allow for lower mean transport thresholds and implementation of a continuum of transport motions as by Nemoto and Nishimura (2004). Mass flux in the creep layer was found to be a considerable component of transport in the lowest 30 mm, and also behaved as a reservoir of particles readily available to be transported into saltation and suspension. Behaving as an intermediary stage between "at-rest" and "in-saltation," the addition of a creep flux may help improve physical accuracy of blowing snow models in intermittent conditions and also explain some of the snow redistribution in mountains that is observed at wind speeds that are considered below the classical threshold condition for transport.

No recent work has focused on advancing the physics of coupling turbulence to blowing snow transport in natural conditions. This is an avenue with great promise using the observation and analytical methods described in this thesis. Much work should be continued in understanding the scales at which wind speeds can be characterised for transport in complex terrain. With the common absence of a spectral gap, and the non-linear dependence of mass flux on wind gusts, time-averaged wind characterisations are ill-suited for complex terrain. However, a semi-deterministic, coherent structure-based approach may provide a middle ground. High-frequency, multi-dimensional data provides greater hope for progress in understanding and modelling alpine blowing snow.

As an instrument for flux measurements, significant improvements can be made to the blowing snow PTV method. The use of multiple upward-pointing cameras for 3D-PTV as by Rosi et al. (2014) or Toloui et al (2014) would greatly enhance the capabilities of blowing snow velocity measurements in the outdoors and may minimize the experiment down time currently caused by reorienting and refocusing the 2D camera-laser frame in the streamwise direction as wind

direction shifts. Multiple camera methods may be best reserved for recording upper layers of saltation and suspension as to avoid the complications of measuring white snow motion in front of a white background. Natural variability in spanwise wind fluctuations and the stochastic 3D nature of particle rebound could then also be accounted for and allow longer particle tracks and more accurate velocity measurements.

6.4 References

Bauer, B. O., and R. G. D. Davidson-Arnott (2014), Aeolian particle flux profiles and transport unsteadiness, *J. Geophys. Res. F Earth Surf.*, 1–27, doi:10.1002/2013JF003000.Received.

Chepil, W. S., 1959: Equilibrium of soil grains at the threshold of movement by wind. *Soil Sci. Soc. Am. J.*, **23**, 422–428.

Comola, F., and M. Lehning, 2017: Energy and momentum conserving model of splash entrainment in sand and snow saltation. *Geophys. Res. Lett.*, doi:10.1002/2016GL071822.

Comola, F., J. F. Kok, J. Gaume, E. Paterna, and M. Lehning, 2017: Fragmentation of wind-blown snow crystals. *Geophys. Res. Lett.*, **44**, 4195–4203, doi:10.1002/2017GL073039.

De Vries, S., J. S. M. van Thiel de Vries, L. C. van Rijn, S. M. Arens, and R. Ranasinghe (2014), Aeolian sediment transport in supply limited situations, *Aeolian Res.*, *12*, 75–85, doi:10.1016/j.aeolia.2013.11.005.

Duran, O., P. Claudin, and B. Andreotti (2014), Direct numerical simulations of aeolian sand ripples, *Proc. Natl. Acad. Sci.*, *111*(44), 15665–15668, doi:10.1073/pnas.1413058111.

Dupont, S., G. Bergametti, and S. Simoëns (2014), Modeling aeolian erosion in presence of vegetation, *J. Geophys. Res. Earth Surf.*, *119*, 168–187, doi:10.1002/2013JF002875.

Mathis, R., I. Marusic, O. Cabrit, N. L. Jones, and G. N. Ivey, 2016: Reconstruction ofWall Shear-Stress Fluctuations in a Shallow Tidal River. *Progress in Wall Turbulence II*, M.S. et Al., Ed., Vol. 23 of, Springer International Publishing.

Nemoto, M., K. Nishimura, S. Kobayashi, and K. Izumi, 2004: Numerical study of the time development of drifting snow and its relation to the spatial development. *Ann. Glaciol.*, **38**, 343–350, doi:10.3189/172756404781815202.

Nemoto, M., and K. Nishimura, 2004: Numerical simulation of snow saltation and suspension in a turbulent boundary layer. *J. Geophys. Res. Atmos.*, **109**, doi:10.1029/2004JD004657.

Niiya, H., and K. Nishimura, 2017: Spatiotemporal structure of aeolian particle transport on flat surface. *J. Phys. Soc. Japan*, **86**, doi:10.7566/JPSJ.86.054402.

Paterna, E., P. Crivelli, and M. Lehning, 2017: Wind tunnel observations of weak and strong snow saltation dynamics. *J. Geophys. Res. Earth Surf.*, doi:10.1002/2016JF004111.

Rosi, G. a., M. Sherry, M. Kinzel, and D. E. Rival (2014), Characterizing the lower log region of the atmospheric surface layer via large-scale particle tracking velocimetry, *Exp. Fluids*, *55*(5), 10, doi:10.1007/s00348-014-1736-2.

Sherman, D. J., B. LI, J. T. Ellis, and C. Swann (2017), Intermittent Aeolian Saltation: A Protocol For Quantification, *Geogr. Rev.*, 1–19, doi:10.1111/gere.12249.

Sullivan, R., and J. F. Kok (2017), Aeolian saltation on Mars at low wind speeds, *J. Geophys. Res. Planets*, *122*, 2111–2143, doi:10.1002/2017JE005275.

Toloui, M., S. Riley, J. Hong, K. Howard, L. P. Chamorro, M. Guala, and J. Tucker (2014), Measurement of atmospheric boundary layer based on super-large-scale particle image velocimetry using natural snowfall, *Exp. Fluids*, *55*(5), 14, doi:10.1007/s00348-014-1737-1.

Vionnet, V., E. Martin, V. Masson, C. Lac, F. N. Bouvet, and G. Guyomarc'h, 2017: High-resolution large eddy simulation of snow accumulation in alpine terrain. *J. Geophys. Res. Atmos.*, doi:10.1002/2017JD026947.

Webb, N. P., G. S. Okin, and S. Brown (2014), The effect of roughness elements on wind erosion: The importance of surface shear stress distribution, *J. Geophys. Res. Atmos.*, *119*, 1–19, doi:10.1002/2014JD021491.

APPENDIX – DATA AVAILABILITY

The data processed in this thesis is hosted on a publicly accessible server at the University of Saskatchewan at the following URL:

http://giws.usask.ca/datasets/aksamit/Aksamit_ThesisData.zip

The archive consists of two folders, "PTV_Tecplots" and "SnowDensity_Wind." The two folders contain .txt files, indexed in a consistent *Month-Day-Experiment #* format.

Columns in the PTV text files follow the included headers: Particle Identification Number, Time step (frame), x-coordinate (mm), y-coordinate (mm), horizontal velocity (m s^{-1}), vertical velocity (m s^{-1}). The coordinate system origin is located at the bottom left corner of each recording frame. The orientation of the illumination plane is always parallel to the streamwise wind direction during the recording.

Columns in the blowing snow density and wind files follow the accompanying header: Volumetric density of suspended particles in a given frame (kg m^{-3}), x-direction wind speed at the lower anemometer, x-direction wind speed at the upper anemometer, y-direction wind speed at the lower anemometer, y-direction wind speed at the upper anemometer, z-direction wind speed at the lower anemometer, z-direction wind speed at the upper anemometer. The orientation of both CSAT3 anemometers follow the right-hand-rule, as indicated in the Campbell Scientific with positive x-direction wind speeds being southerly. The anemometer heights above the snow surface fluctuated with fluctuating snow depth. The recording heights never fluctuated more than 5 cm during any one night of recording and are approximated as follows:

Date	Upper Anemometer (cm)	Lower Anemometer (cm)
23 Mar 2015	200	40
20 Nov 2015	150	20
4 Dec 2015	170	40
7 Dec 2015	170	40
3 Feb 2016	155	25
3 Mar 2016	140	10

Table A-1: Sonic anemometer measurement heights for each night of recording.